Luminescence Spectroscopy of Er^{3+} Doped Inorganic Nanocrystals – An Investigation into their Upconversion Properties

Fiorenzo Vetrone

A Thesis

in

The Department

of

Chemistry and Biochemistry

Presented in Partial Fulfillment of the Requirements
for the Degree of Doctor of Philosophy at
Concordia University
Montreal, Quebec, Canada

May 2005

Your file Votre référence
ISBN: 0-494-04038-6
Our file Notre référence
ISBN: 0-494-04038-6

ABSTRACT

Luminescence Spectroscopy of Er^{3+} Doped Inorganic Nanocrystals – An Investigation into their Upconversion Properties

Fiorenzo Vetrone, Ph.D.
Concordia University, 2005

This thesis presents a detailed investigation into the spectroscopic properties of inorganic nanocrystals doped with trivalent rare earth ions. We focus on their upconversion luminescence, emission of radiation at higher energy than the pump wavelength, and evaluate the fundamental mechanisms of upconversion in the nanocrystal.

We evaluate the spectroscopic properties of sesquioxide nanocrystals doped with trivalent erbium ($M_2O_3:Er^{3+}$, where M = Y, Lu, or Sc) prepared by the propellant synthesis technique. Characteristic green, red, and near-infrared Er^{3+} emission is observed following excitation with 488 nm in all samples under investigation. The overall luminescence intensity of the sesquioxide nanocrystals is lower compared to the microcrystalline material (bulk) as a result of the presence of high vibrational energies, 1500 and 3350 cm^{-1}, due to adsorbed CO_3^{2-} and OH^- anions, respectively, which significantly increase the rate of multiphonon relaxation. The garnet ($Gd_3Ga_5O_{12}:Er^{3+}$) nanocrystals, however, have considerably less surface adsorbed species, which consequently increases the luminescence intensity drastically.

The upconversion of red (λ_{exc} = 650 nm) and near-infrared (λ_{exc} = 800 or 980 nm) radiation into UV, blue, green, and red emission is studied for Er^{3+} ions doped in various sesquioxide (Y_2O_3, Lu_2O_3, and Sc_2O_3) and garnet ($Gd_3Ga_5O_{12}$) nanocrystals over a wide

range of temperatures and dopant concentration is investigated. We present, for the first time, upconversion in a trivalent rare earth (RE^{3+}) doped nanocrystalline material, specifically $Y_2O_3:Er^{3+}$. We show that replacing the Y^{3+} cation has significant consequences on the upconversion. The upconverted luminescence of $Lu_2O_3:Er^{3+}$ nanocrystals have intensities that are 100× greater compared to identically doped nanocrystalline $Y_2O_3:Er^{3+}$. Furthermore, $Sc_2O_3:Er^{3+}$ nanocrystals show an enhanced red emission, which is greater than $Y_2O_3:Er^{3+}$ nanocrystals (with identical Er^{3+} concentration) due to the smaller unit cell resulting in increased interaction between Er^{3+} ions. The upconversion is observed to be dependent on the method of preparation. We explore nanocrystalline $Y_2O_3:Er^{3+}$ prepared via the propellant synthesis technique and a controlled hydrolysis synthesis (or wet chemical synthesis) where we observed quite diverse upconversion behavior attributed to the vastly different morphological properties of the two different nanocrystalline materials. Additionally, we investigate the effect of Yb^{3+} co-doping on the upconversion luminescence of $Y_2O_3:Er^{3+}$ nanocrystals prepared via the two distinct synthesis routes, and observe a significant change in the mechanisms of upconversion. In the sesquioxides, the upconversion properties of the nanocrystalline material are diverse from the bulk counterpart.

Finally, we attempt to ascertain if any spectroscopic changes occur in nanosized $Lu_2O_3:Nd^{3+}$, $Y_2O_3:Sm^{3+}$ and $Y_2O_3:Dy^{3+}$ prepared via combustion synthesis. In all cases, the size of the particles affects the luminescence behavior.

ACKNOWLEDGEMENTS

I am, and will forever be, indebted to my thesis supervisor, Prof. John A. Capobianco for all his help and invaluable guidance throughout the course of this degree. I thank him for his enthusiasm, advice, and effort, which helped make this thesis a reality. I thank him for forcing the very best out of me and at all times encouraging free thinking. I am grateful for the intellectual freedom he granted and the latitude to take the research in whatever direction I saw fit. I thank him for sending me to innumerable international conferences, which undoubtedly helped me become a well-rounded scientist. Our travels have taken us to San Francisco, Philadelphia and Verona. I take with me great memories of our trip to Italy, traveling by train through the Alps and proving that this thesis reflects not only the scientific endeavor but the many friends acquired along the way. I would like to express my thanks for the complete graduate education I have received under your supervision. I could not have asked for a better mentor, both as a scientist and a person. It was an honor to work both for you and with you.

I would like to thank the members of my research committee, Prof. Peter H. Bird and Prof. Heidi M. Muchall for helpful suggestions throughout the course of this degree and for serving on my thesis committee. I would like to express my sincere appreciation to Prof. Christian Reber (Université de Montréal) for taking the time to go through this thesis given the exceptionally difficult circumstances.

This thesis would never have seen the light of day without the dedication of two wonderful scientists, Prof. Marco Bettinelli and Dr. Adolfo Speghini from L'Università di Verona. Their unprecedented mastery of the synthesis of rare earth doped nanocrystals

and relentless pursuit of scientific excellence have significantly pushed the envelope and advanced the body of knowledge of these novel materials. Ours is a collaboration in the truest sense of the word and any successes I have had would never have been possible without these two great researchers whom I now have the pleasure of calling friends. I wholeheartedly thank Prof. Bettinelli and Dr. Speghini for their excellent and warm-hearted hospitality during my two visits to Verona. Over the years, I have had the pleasure and the privilege of working very closely with these two gentlemen and they have put tremendous time, effort, and resources into this project. Words cannot express my gratitude for all your help, for your contributions to this thesis and other projects we've worked on, for your patience, for all your generosity, but above all, I thank you for your friendship. May we continue to work together in the future.

I would like to sincerely and wholeheartedly thank Prof. Chris G. Morgan (University of Salford). When we initiated this project, we had only technological aspirations for these nanocrystalline materials. After our meetings in Verona, over a couple of glasses of Valpolicella, I began to see a whole new world for these nanomaterials as biological labels, and as a result, has completely reshaped my outlook on research. I hope that we can continue to work together on these upconverting nanoparticles.

From the bottom of my heart, I thank the current members of the Lanthanide Research Group; John-Christopher Boyer, Sean R. Hughes, and Rafik Naccache. We started out as lab mates and somewhere along the way became friends. Who else but friends would put up with my many moods, especially in the early morning before my

first cup of coffee. I have great memories of time spent in the dark with these gentlemen with the soothing hum of the laser and the tick, ticking of the monochromator in the background. Some of my favorite memories include the "awakening" experience with JCB, SRH and the years of "cripplage", and RN's "elusiveness". I've no doubt that many years down the road we will look back fondly upon these memories and a smile will cross our faces. Who knows what the future has in store for us or where our paths will lead us, but hopefully, I can continue to work with these great scientists.

I wholeheartedly acknowledge Prof. Louis Cuccia (Concordia University) for the use of his laboratory facilities and allowing me to pick his brain. I thank him for his friendship, fantastic discussions on science and Formula 1, and encouragement throughout the writing of this thesis.

A sincere thank you to Prof. Nick Serpone (Concordia University and Università di Pavia) for insightful discussions on semiconductor nanocrystals while preparing for my literature seminar and for the generous use of his equipment to obtain the reflectance data. I would like to express my thanks to Prof. George Dénès for always being willing to entertain my questions on the many facets of crystallography and X-ray diffraction.

I wish to acknowledge some former members of the Capobianco lab. Dr. Tania Peres for introducing me to Dr. Capobianco's research and showing me the ropes during my formative years. A sincere thank you to Dr. Pierre-Paul Proulx for parting upon me his many insights on the spectroscopy of rare earth doped materials and for allowing us access to his equipment at the Canadian Space Agency. A warm thank you to my friend

Dr. Andrea A. Romeo for being there when needed and his willingness to always lend a out a helping hand.

A general thank you to all those at Concordia University who over the years made the Department of Chemistry and Biochemistry a wonderful place to pursue a Ph.D. I am grateful to the many graduate students, past and present, whom I have had the privilege of knowing and working with. A heartfelt thank you to Dr. Angelo Filosa for the memorable coffee breaks and the many laughs over the years. Thank you to my friend and fellow graduate student Nabil Al-Yassir for his company on weekends and during the wee hours of the morning and of course, for the many heated political debates.

I would like to express my gratitude to the entire secretarial staff of the Department of Chemistry and Biochemistry; Carole Coutts, Donna Gordon, Lisa Montesano, and Kathy Usas, for all their help all through the many long years of graduate school. Thank you also to Lori Dupuis for all she's done and especially for putting up with my endless phone calls.

A big thank you to Miriam Posner (Concordia University) for her ability and willingness to take care of the innumerable logistical problems, which inevitably arose during my years here. Thank you to the technical staff of the Department of Chemistry and Biochemistry especially Mr. Franco Nudo and Mr. Kai Lee for making my T.A.'s enjoyable and for their willingness to help with this project by allowing me to use departmental facilities.

There are a few people whom I met during my stay at L'Università di Verona that deserve my thanks. I thank Prof. C. K. Jayasankar (Sri Venkateswara University) for

valuable discussions on crystal field theory and Prof. Colin D. Flint (Birkbeck College, University of London) for the wonderful breakfast conversations. You now have 101 airports where someone will buy you a beer. I am grateful to Erica Viviani (Università di Verona) for preparing many of the samples studied in this thesis. Finally, I would like to acknowledge the late Prof. Gino Tessari (Università di Verona). It was his foresight that introduced us to nanocrystalline Y_2O_3.

I would like to express my appreciation to Prof. Stefano Polizzi (Università Ca' Foscari Venezia) for providing much of the characterization data presented in this thesis.

I would be remiss if I did not acknowledge my close friends (affectionately known as *The Old Boys*). There are of course too many to list, but I have no doubts they know who they are. Every Friday night for the last decade or so, we have gone into battle together, where our battlefields were the soccer pitches, our ammunition a lone soccer ball. On those nights, they provided an environment where for a few precious moments, science was merely a hazy, foggy memory. I thank you.

I will forever be grateful to the entire Sasso family for their support and understanding throughout the course of this degree.

As I write the acknowledgements for this thesis, I overwhelmed with bittersweet emotions. On the one hand, I am elated that it is now complete and I can begin the next chapter of my life. On the other, I am gut-wrenchingly heartbroken that the three people for whom this thesis meant the world, are not here to witness the end. My grandfather, Pasquale Di Francesco, and my mother and father (Angelina Di Francesco and Giuseppe

Vetrone). This thesis has come to completion but I have lost many loved ones along the way.

To my grandfather and best friend, Pasquale Di Francesco. You came to this country with nothing, made a life and raised a family. The word quit was simply not part of your vocabulary. You taught me all about responsibility and accountability and are one of the major reasons I am writing these acknowledgements today.

To my beloved mother, Angelina Di Francesco. If it was not for your belief in me, I would not be at this juncture. No matter how badly I messed things up, no matter how many mistakes I committed, I could always count on your unconditional love and support. You always believed that I could, and would, reach my potential. You taught me the true meaning of strength and courage and although you are not here to see me enter this new chapter, I have no doubts that you are looking down with a smile on your face and pride in your heart.

To my dear father, Giuseppe Vetrone. Your quiet encouragement meant the world to me. It was your hard work and your innumerable sacrifices that put me through graduate school. Unfortunately, you passed only weeks before completion of my Ph.D. but I know that you are looking down with pride at your son's accomplishments. Please know that I am as proud of you, for everything you've accomplished, as you are of me.

I thank my sister, Maria Antonietta Vetrone, for being the strength, which I draw upon. You have supported me in many, many ways and this Ph.D. is as much yours as it is mine.

Finally, I will aspire to thank Enza Sasso but surely I will fail since there are no words that can accurately describe how I truly feel. Ours has been a long and arduous journey and without exception she was always there for me. I thank her for her unwavering support and unconditional love throughout the many (and sometimes long) years of graduate school. I am forever grateful for her patience and understanding of my crazy Ph.D. lifestyle, which resulted in many a late night. Without her in my life this degree would never have come to be. Whatever I have accomplished pales in comparison to having you in my life. That is by far, my greatest achievement and know that I will always love you.

To my mother and father
Angelina Di Francesco (December 30, 1946 December 31, 2003)
Giuseppe Vetrone (April 10, 1944 - February 21, 2005)

To my grandfather
Pasquale Di Francesco (December 23, 1910 - June 14, 2002)

To my sister
Maria Antonietta Vetrone

For giving me the strength to start this thesis

And

To Enza Sasso

For giving me the courage to finish it

"If I have seen further, it is by standing on the shoulders of giants"

Sir Isaac Newton, *Letter to Robert Hooke, February 5, 1765*

TABLE OF CONTENTS

List of Figures xix

List of Tables xxviii

CHAPTER 1

1. Introduction ..... **- 1 -**

1.1. The Rare Earth Elements ..... - 1 -

1.1.1. History and Discovery of the Rare Earths ..... - 1 -

1.1.2. The Rare Earths and the Periodic Table ..... - 5 -

1.2. History of Spectroscopy ..... - 8 -

1.2.1. The Origins of Spectroscopy ..... - 8 -

1.2.2. Rare Earth Spectroscopy ..... - 11 -

1.3. The Rare Earth Elements in the Modern Times ..... - 18 -

1.3.1. Luminescence and Phosphors ..... - 19 -

1.4. Inorganic Nanocrystalline Materials ..... - 24 -

CHAPTER 2

2. Background ..... **- 28 -**

2.1. Nanophosphors ..... - 28 -

2.2. The Phenomenon of Upconversion ..... - 32 -

2.2.1. Excited State Absorption (ESA) ..... - 33 -

2.2.2. Upconversion Involving Energy Transfer ..... - 34 -

2.2.3. Photon Avalanche (PA) ..... - 36 -

2.3. Suitability of the Erbium ion (Er^{3+}) for Upconversion ..... - 37 -

2.4. Upconverting Nanoparticles for Upconversion Based FRET Assays ..... - 40 -

2.5. Statement of the Problem ..... - 46 -

CHAPTER 3

3. Theory ..... **- 48 -**

3.1. Hamiltonian of the Free Ion ..... - 48 -

3.1.1. Electrostatic (Coulomb) Interaction ..... - 51 -

3.1.2. Spin-Orbit Interaction ..... - 53 -
3.2. The Crystal Field Effect ..... - 55 -
3.3. Selection Rules ..... - 57 -
3.4. Intensity Calculation and the Judd-Ofelt Theory ..... - 61 -
3.4.1. Induced Electric Dipole Transitions ..... - 63 -
3.4.2. Magnetic Dipole Transitions ..... - 64 -
3.4.3. Fluorescence Parameters for RE^{3+} Doped Materials ..... - 66 -
3.5. Energy Transfer ..... - 67 -
3.5.1. Multipolar Interaction ..... - 70 -
3.5.2. Exchange Interaction ..... - 72 -
3.5.3. Upconversion by Energy Transfer ..... - 74 -

CHAPTER 4

4. Experimental ..... - 75 -
4.1. Sample Preparation ..... - 75 -
4.1.1. Propellant Synthesis ..... - 75 -
(i) Sesquioxide Nanocrystals ..... - 78 -
(ii) Garnet Nanocrystals ..... - 80 -
4.1.2. Controlled Hydrolysis Procedure ..... - 81 -
4.1.3. Synthesis of Bulk Sesquioxides ..... - 83 -
4.2. Characterization ..... - 84 -
4.2.1. Scanning Electron Microscopy (SEM) ..... - 84 -
4.2.2. Transmission Electron Microscopy (TEM) ..... - 84 -
4.2.3. X-ray Diffraction ..... - 84 -
4.3. Spectroscopy ..... - 87 -
4.3.1. Fourier Transform Infrared Spectroscopy (FTIR) ..... - 87 -
4.3.2. Reflectance Spectroscopy ..... - 87 -
4.3.3. Luminescence Spectroscopy ..... - 87 -
4.3.4. Lifetime Measurements ..... - 89 -
4.3.5. Power Dependence Studies ..... - 89 -
4.3.6. Low Temperature ..... - 89 -
4.3.7. Raman Spectra ..... - 89 -

CHAPTER 5

5. Morphology and Structure ..... - 96 -

5.1. Transmission Electron Microscopy (TEM) and Scanning Electron Microscopy (SEM) ..... - 96 -

5.1.1. Sesquioxide and Garnet Nanocrystals Prepared Via Propellant Synthesis ..... - 96 -

5.1.2. Sesquioxide Nanocrystals Prepared Via Wet Chemical Synthesis ..... - 100 -

5.2. X-ray Diffraction ..... - 102 -

5.2.1. Sesquioxides ..... - 102 -

5.2.2. Garnets ..... - 104 -

CHAPTER 6

6. Results and Discussion of the Spectroscopic Investigation ..... - 108 -

6.1. An Investigation of $Y_2O_3:Er^{3+}$ and $Y_2O_3:Er^{3+}$, Yb^{3+} Nanocrystals Prepared Via Propellant Synthesis ..... - 109 -

6.1.1. Reflectance Spectroscopy ..... - 109 -

6.1.2. Emission Spectroscopy of $Y_2O_3:Er^{3+}$ Nanocrystals ..... - 114 -

6.1.3. Decay Times of Bulk and Nanocrystalline $Y_2O_3:Er^{3+}$ (λ_{exc} = 488 nm) ..... - 117 -

6.1.4. Consequence of Adsorbed Surface Species ..... - 120 -

6.1.5. Concentration Dependence of the Luminescence Properties in $Y_2O_3:Er^{3+}$ ..... - 123 -

6.1.6. Anti-Stokes (Upconversion) Luminescence Spectroscopy Following Excitation into the $^4I_{9/2}$ Level (λ_{exc} = 815 nm) ..... - 126 -

6.1.7. Comparison of the Stokes (λ_{exc} = 488 nm) and Upconversion (λ_{exc} = 815 nm) Spectra ..... - 133 -

6.1.8. Anti-Stokes (Upconversion) Luminescence Spectroscopy Following Excitation into the $^4I_{11/2}$ Level (λ_{exc} = 980 nm) ..... - 141 -

6.1.9. Effect of Yb^{3+} Co-doping on the Upconversion Emission in Nanocrystalline $Y_2O_3:Er^{3+}$ ..... - 155 -

6.1.10. Significance of Yb^{3+} Concentration on the Upconversion Mechanisms in Co-doped $Y_2O_3:Er^{3+}$, Yb^{3+} Nanocrystals ..... - 169 -

6.2. Luminescence Properties of Erbium Doped Nanocrystalline Yttrium Oxide Prepared Via The Controlled Hydrolysis Procedure ..... - 186 -

6.2.1. Reflectance and Emission Spectroscopy ..... - 186 -

6.2.2. Upconversion Luminescence Spectroscopy Following Excitation into the $^4F_{9/2}$ State (λ_{exc} = 650 nm) - 196 -

6.2.3. Upconversion Luminescence Spectroscopy Following Excitation into the $^4I_{9/2}$ State (λ_{exc} = 800 nm) - 201 -

6.3. Upconversion Spectroscopy of Bulk and Nanocrystalline $Lu_2O_3:Er^{3+}$ - 209 -

6.3.1. Visible Emission Spectroscopy and Decay Time Measurements in $Lu_2O_3:Er^{3+}$ - 209 -

6.3.2. Near-Infrared Emission Spectroscopy - 215 -

6.3.3. Upconversion Upon Excitation into the $^4F_{9/2}$ Manifold (λ_{exc} = 650 nm) - 217 -

6.3.4. Upconversion Upon Excitation into the $^4I_{9/2}$ Manifold (λexc = 804 nm) - 217 -

6.3.5. Temperature Dependence of the Transition Probabilities - 221 -

6.3.6. Mechanisms of Upconversion - 224 -

6.3.7. Upconversion Upon Excitation into the $^4I_{11/2}$ Manifold (λ_{exc} = 980 nm) - 227 -

6.3.8. Blue Upconversion in $Lu_2O_3:Er^{3+}$ - 234 -

6.3.9. Temperature Dependence of the Upconversion Luminescence - 237 -

6.4. Comparative Analysis of the Upconversion (Anti-Stokes) Emission of Nanocrystalline $Sc_2O_3:Er^{3+}$ - 241 -

6.4.1. Stokes (λ_{exc} = 488 nm) and Anti-Stokes Emission Spectroscopy of $Sc_2O_3:Er^{3+}$ Nanocrystals (λ_{exc} = 980 nm) - 241 -

6.4.2. Elucidation of the Mechanism of Upconversion – Power Study and Upconversion Decay Times - 245 -

6.4.3. Enhancement of Red Emission ($^4F_{9/2} \rightarrow {}^4I_{15/2}$) – Comparison to $Y_2O_3:Er^{3+}$ - 248 -

6.5. Luminescence Spectroscopy and NIR-to-Visible Upconversion of $Gd_3Ga_5O_{12}:Er^{3+}$ Nanocrystals - 252 -

6.5.1. Visible and NIR Emission in $Gd_3Ga_5O_{12}:Er^{3+}$ Nanocrystals (λ_{exc} = 488 nm) - 252 -

6.5.2. Efficient NIR-to-Visible Upconversion in GGG:Er^{3+} Nanocrystals (λ_{exc} = 800 nm) - 258 -

6.6. Laser Spectroscopy of Sesquioxide Nanocrystals Doped With Other Rare Earth Ions - 266 -

6.6.1. Spectroscopic Properties of $Lu_2O_3:Nd^{3+}$ and the *X* Parameter - 266 -

6.6.2. Effect of the Surrounding Media on the Decay Times of Nanocrystalline $Y_2O_3:Sm^{3+}$ - 271 -

6.6.3. Decay Times of Nanocrystalline $Y_2O_3:Dy^{3+}$ Using the Inokuti – Hirayama Model ..... - 277 -

CHAPTER 7

7. Conclusion ..... - 282 -

CHAPTER 8

8. Future Work ..... - 294 -

CHAPTER 9

9. References ..... - 298 -

LIST OF FIGURES

CHAPTER 1

1.1 Periodic table of the elements with the rare earth series (and similar ions) expanded for clarity.....- 5 -

1.2 Sir Isaac Newton's experimental set-up used to separate the colors of sunlight.....- 9 -

1.3 The initial Bunsen-Kirchoff spectroscope invented by Bunsen and Kirchoff in 1861..... - 10 -

1.4 A more modern spectroscope, circa 1880.....- 10 -

1.5 Observed energy levels of the rare earth ions in the $LaCl_3$ structure.....- 17 -

CHAPTER 2

2.1 Simplified schematic representation of the excited state absorption process.....- 34 -

2.2 Simplified schematic representation of the cross-relaxation upconversion process.....- 35 -

2.3 Simplified schematic representation of the energy transfer upconversion process.....- 35 -

2.4 Simplified schematic representation of the photon avalanche upconversion process.....- 36 -

2.5 Energy level diagram of the tripositive erbium ion. Asterisks (*) point out the NIR excited states, which can act as intermediate states (population reservoirs) in the various upconversion processes.....- 39 -

2.6 Schematic representation of the conventional FRET process.....- 41 -

2.7 Schematic representation of the upconversion FRET process.....- 43 -

2.8 Emission spectrum of a typical Er^{3+} doped inorganic material. Note the total absence of emission in the region centered around 600 nm.....- 44 -

CHAPTER 3

3.1 Effect of inclusion of successive terms in the atomic Hamiltonian for the $4f^{11}$ configuration (Er^{3+})..... - 56 -

3.2 Representation of the Coulomb interaction between two atoms (*A* and *B*) in a resonant energy transfer process..... - 68 -

3.3 Spectral overlap (shaded region) between the Donor emission (in blue) and the acceptor absorption bands (in red)..... - 70 -

CHAPTER 4

4.1 Structure of the surface modifiers used in the controlled hydrolysis procedure (A) β-alanine and (B) Tween®80 (polyoxyethylene (20) sorbitan monooleate)..... - 82 -

4.2 Schematic representation of the Lanthanide Research Group laser spectroscopy laboratory. A more specific explanation of each optical table is shown in the subsequent pages..... - 90 -

CHAPTER 5

5.1 SEM micrographs of Y_2O_3 nanocrystals prepared via propellant synthesis..... - 96 -

5.2 SEM micrograph of Lu_2O_3 nanocrystals prepared via propellant synthesis..... - 97 -

5.3 SEM micrographs of Sc_2O_3 nanocrystals prepared via propellant synthesis..... - 97 -

5.4 SEM micrographs of $Gd_3Ga_5O_{12}$ nanocrystals prepared via propellant synthesis..... - 97 -

5.5 TEM micrographs of Y_2O_3 nanocrystals prepared via propellant synthesis..... - 98 -

5.6 TEM micrographs of Sc_2O_3 nanocrystals prepared via propellant synthesis..... - 98 -

5.7 TEM micrographs of Lu_2O_3 nanocrystals prepared via propellant synthesis..... - 99 -

5.8 TEM micrographs of $Gd_3Ga_5O_{12}$ nanocrystals prepared via propellant synthesis..... - 99 -

5.9 SEM micrographs of Y_2O_3 nanocrystals synthesized via a controlled hydrolysis procedure.....- 100 -

5.10 TEM micrographs of Y_2O_3 nanocrystals synthesized via a controlled hydrolysis procedure.....- 101 -

5.11 Pictorial representation of the C_2 and C_{3i} cation sites of the cubic Y_2O_3 Lattice.....- 102 -

5.12 Pictorial representation of the polyhedra of the garnet structure showing: one dodecahedron (• A ions), one octahedron (• B ions), and one tetrahedron (• C ions).....- 105 -

5.13 XRD patterns of the different Y_2O_3 samples. (a) Commercial Y_2O_3 (Aldrich, 99.99 %) (b) Y_2O_3:Er^{3+} synthesized via combustion synthesis and (c) Y_2O_3:Er^{3+} synthesized via the controlled hydrolysis procedure. All peaks normalized to the 222 reflection.....- 106 -

5.14 XRD pattern of the nanocrystalline Sc_2O_3 sample obtained by propellant synthesis. Inset: (222) peaks for the 10 mol% Er^{3+} doped (□) and undoped (■) nanocrystalline Sc_2O_3 showing the peak shifts and the different profile width. The (222) peak is not shown entirely in the full spectrum (see inset).....- 107 -

CHAPTER 6

6.1 Reflectance spectrum of nanocrystalline Y_2O_3:Er^{3+} (10 mol%) showing transitions from the $^4I_{15/2}$ ground state to the various Er^{3+} excited states: (a) $^4F_{9/2}$, (b) $^4S_{3/2}$, (c) $^2H_{11/2}$, (d) $^4F_{7/2}$, (e) $^4F_{5/2}$, (f) $^4F_{3/2}$, (g) $^2H_{9/2}$, (h) $^4G_{11/2}$, (i) $^2G_{9/2}$.....- 112 -

6.2 Reflectance spectrum of bulk Y_2O_3:Er^{3+} (10 mol%) showing transitions from the $^4I_{15/2}$ ground state to the various Er^{3+} excited states: (a) $^4F_{9/2}$, (b) $^4S_{3/2}$, (c) $^2H_{11/2}$, (d) $^4F_{7/2}$, (e) $^4F_{5/2}$, (f) $^4F_{3/2}$, (g) $^2H_{9/2}$, (h) $^4G_{11/2}$, (i) $^2G_{9/2}$.....- 113 -

6.3. Room temperature luminescence of nanocrystalline and bulk Y_2O_3:Er^{3+} (10 mol%) upon excitation at 488 nm. (i) $^2H_{11/2} \rightarrow {}^4I_{15/2}$ (ii) $^4S_{3/2} \rightarrow {}^4I_{15/2}$ (iii) $^4F_{9/2} \rightarrow {}^4I_{15/2}$. Inset: (iv) $^4I_{9/2} \rightarrow {}^4I_{15/2}$ (v) $^4S_{3/2} \rightarrow {}^4I_{13/2}$.....- 116 -

6.4. Diffuse reflectance spectra of nanocrystalline Y_2O_3:Er^{3+} (10 mol%) following sequential heat treatment: (a) 800 °C for 17 h (b) 1000 °C for 65 h (c) bulk Y_2O_3:Er^{3+} (10 mol%) sample shown for comparison. Inset: Diffuse reflectance spectrum of nanocrystalline Y_2O_3:Er^{3+} (1 mol%) following heat treatment under an N_2 flow (2 liters/minute) for 2 hours at 700 °C.....- 122 -

6.5. Room temperature luminescence of nanocrystalline $Y_2O_3:Er^{3+}$ (1, 2, 5, and 10 mol%) upon excitation at 488 nm. (i) $^2H_{11/2} \rightarrow {}^4I_{15/2}$ (ii) $^4S_{3/2} \rightarrow {}^4I_{15/2}$ (iii) $^4F_{9/2} \rightarrow {}^4I_{15/2}$. Inset: (iv) $^4I_{9/2} \rightarrow {}^4I_{15/2}$ (v) $^4S_{3/2} \rightarrow {}^4I_{13/2}$ ..... - 124 -

6.6. Room temperature luminescence of bulk $Y_2O_3:Er^{3+}$ (1, 2, 5, and 10 mol%) upon excitation at 488 nm. (i) $^2H_{11/2} \rightarrow {}^4I_{15/2}$ (ii) $^4S_{3/2} \rightarrow {}^4I_{15/2}$ (iii) $^4F_{9/2} \rightarrow {}^4I_{15/2}$. Inset: (iv) $^4I_{9/2} \rightarrow {}^4I_{15/2}$ (v) $^4S_{3/2} \rightarrow {}^4I_{13/2}$ ..... - 125 -

6.7. Upconverted emission of Er^{3+} doped Y_2O_3 nanocrystals (1, 2, 5, and 10 mol%) at room temperature, showing (i) $^2H_{11/2} \rightarrow {}^4I_{15/2}$ (ii) $^4S_{3/2} \rightarrow {}^4I_{15/2}$ (iii) $^4F_{9/2} \rightarrow {}^4I_{15/2}$, λ_{exc} = 815 nm ..... - 128 -

6.8. Upconverted emission of bulk Er^{3+} doped Y_2O_3 (1, 2, 5, and 10 mol%) at room temperature, showing (i) $^2H_{11/2} \rightarrow {}^4I_{15/2}$ (ii) $^4S_{3/2} \rightarrow {}^4I_{15/2}$ (iii) $^4F_{9/2} \rightarrow {}^4I_{15/2}$, λ_{exc} = 815 nm ..... - 129 -

6.9. Upconverted emission of bulk $Y_2O_3:Er^{3+}$ (1, 2, 5, and 10 mol%) at room temperature, showing (i) $^4F_{5/2} \rightarrow {}^4I_{15/2}$ (ii) $^2P_{3/2} \rightarrow {}^4I_{11/2}$ (iii) $^4F_{7/2} \rightarrow {}^4I_{15/2}$, λ_{exc} = 815 nm ..... - 130 -

6.10. Graph of the ratio of the integrated areas of the ($^2H_{11/2}$, $^4S_{3/2}$) $\rightarrow {}^4I_{15/2}$ and $^4F_{9/2} \rightarrow {}^4I_{15/2}$ bands [($^2H_{11/2}$, $^4S_{3/2}$) / $^4F_{9/2}$] versus Er^{3+} concentration for the nanocrystalline material ..... - 131 -

6.11. Graph of the ratio of the integrated areas of the ($^2H_{11/2}$, $^4S_{3/2}$) $\rightarrow {}^4I_{15/2}$ and $^4F_{9/2} \rightarrow {}^4I_{15/2}$ bands [($^2H_{11/2}$, $^4S_{3/2}$) / $^4F_{9/2}$] versus Er^{3+} concentration for the bulk material ..... - 132 -

6.12. Power study of the $^4F_{9/2} \rightarrow {}^4I_{15/2}$ transition in 10 mol% bulk $Y_2O_3:Er^{3+}$ (λ_{exc} = 815 nm). Inset: Power dependence of the upconversion luminescence intensity observed with 815 nm excitation. (a) 650 mW (b) 240 mW (c) 70 mW ..... - 137 -

6.13. Energy level diagram of Er^{3+} ions in Y_2O_3 showing the ($^4I_{9/2}$, $^4I_{11/2} \rightarrow {}^4I_{13/2}$, $^4F_{9/2}$) ion-pair process responsible for directly populating the $^4F_{9/2}$ level (λ_{exc} = 815 nm) ..... - 138 -

6.14. Energy level diagram of Er^{3+} ions in Y_2O_3 showing the ($^4I_{9/2}$, $^4I_{11/2} \rightarrow {}^4I_{13/2}$, $^4F_{9/2}$) ion-pair process responsible for directly populating the $^4F_{9/2}$ level (λ_{exc} = 815 nm) ..... - 139 -

6.15. Room temperature luminescence of nanocrystalline $Y_2O_3:Er^{3+}$ upon excitation at 980 nm. (i) $^2H_{11/2} \rightarrow {}^4I_{15/2}$ (ii) $^4S_{3/2} \rightarrow {}^4I_{15/2}$ (iii) $^4F_{9/2} \rightarrow {}^4I_{15/2}$ ..... - 146 -

6.16. Room temperature luminescence of bulk $Y_2O_3:Er^{3+}$ upon excitation at 980 nm. (i) $^2H_{11/2} \rightarrow {}^4I_{15/2}$ (ii) $^4S_{3/2} \rightarrow {}^4I_{15/2}$ (iii) $^4F_{9/2} \rightarrow {}^4I_{15/2}$ ..... - 147 -

6.17. Upconverted blue emission of bulk $Y_2O_3:Er^{3+}$ at room temperature, showing (i) $^4F_{5/2} \rightarrow {}^4I_{15/2}$ (ii) $^2P_{3/2} \rightarrow {}^4I_{11/2}$ (iii) $^4F_{7/2} \rightarrow {}^4I_{15/2}$ (λ_{exc} = 980 nm)..... - 148 -

6.18. Schematic representation of the excited state absorption (ESA) and energy transfer upconversion (ETU) mechanisms. The $^4F_{7/2} \rightarrow {}^4F_{9/2}$ and $^4F_{9/2} \leftarrow {}^4I_{11/2}$ cross-relaxation (CR) process responsible for populating the $^4F_{9/2}$ state is also shown..... - 153 -

6.19. Schematic representation of the 3 step phonon-assisted energy transfer (PET) upconversion process responsible for populating the $^2P_{3/2}$ state. Note: Only the relevant energy levels of the Er^{3+} ions are shown for simplicity..... - 154 -

6.20. Room temperature Stokes luminescence of nanocrystalline $Y_2O_3:Er^{3+}$, Yb^{3+} (1 mol% Er^{3+} and 1 mol% Yb^{3+}) prepared via propellant synthesis following excitation with 488 nm. Inset: Room temperature Stokes luminescence of bulk $Y_2O_3:Er^{3+}$, Yb^{3+} (1 mol% Er^{3+} and 1 mol% Yb^{3+}) (i) $^2H_{11/2}$, $^4S_{3/2} \rightarrow {}^4I_{15/2}$ (ii) $^4F_{9/2} \rightarrow {}^4I_{15/2}$ (iii) $^4I_{9/2} \rightarrow {}^4I_{15/2}$ (iv) $^4S_{3/2} \rightarrow {}^4I_{13/2}$..... - 158 -

6.21. Near-infrared Stokes luminescence of the $^4I_{11/2} \rightarrow {}^4I_{15/2}$ transition in bulk (a) $Y_2O_3:Er^{3+}$ (1 mol% Er^{3+}) and (b) $Y_2O_3:Er^{3+}$, Yb^{3+} (1 mol% Er^{3+} and 1 mol% Yb^{3+}) following excitation with 488 nm. Emission from the $^2F_{5/2} \rightarrow {}^2F_{7/2}$ transition denoted with an asterisk (*)..... - 159 -

6.22. Room temperature upconversion (anti-Stokes) luminescence of nanocrystalline $Y_2O_3:Er^{3+}$, Yb^{3+} (1 mol% Er^{3+} and 1 mol% Yb^{3+}) prepared via propellant synthesis following excitation with 978 nm. (i) $^2H_{11/2}$, $^4S_{3/2} \rightarrow {}^4I_{15/2}$ (ii) $^4F_{9/2} \rightarrow {}^4I_{15/2}$..... - 163 -

6.23. Room temperature anti-Stokes luminescence of bulk $Y_2O_3:Er^{3+}$, Yb^{3+} (1 mol% Er^{3+} and 1 mol% Yb^{3+}) following excitation with 978 nm. Inset: Room temperature anti-Stokes luminescence of bulk $Y_2O_3:Er^{3+}$, Yb^{3+} following excitation with 1064 nm. (i) $^2H_{11/2}$, $^4S_{3/2} \rightarrow {}^4I_{15/2}$ (ii) $^4F_{9/2} \rightarrow {}^4I_{15/2}$..... - 164 -

6.24. Study of the upconversion luminescence of the $^2H_{11/2}$, $^4S_{3/2} \rightarrow {}^4I_{15/2}$ transitions in bulk $Y_2O_3:Er^{3+}$, Yb^{3+} following excitation with 978 nm as a function of pump power; (a) 320 mW (b) 215 mW (c) 115 mW (d) 60 mW (e) 25 mW. Inset: Power dependence of the $^2H_{11/2}$, $^4S_{3/2} \rightarrow {}^4I_{15/2}$ anti-Stokes luminescence intensity of bulk $Y_2O_3:Er^{3+}$, Yb^{3+} observed following 978 nm excitation..... - 165 -

6.25. Schematic representation of the Yb^{3+} to Er^{3+} energy transfers responsible for population of the $^4F_{7/2}$ state as well as the ($^4F_{7/2}$, $^4I_{11/2}$) $\rightarrow$ ($^4F_{9/2}$, $^4F_{9/2}$) ion-pair process and the phonon-assisted energy transfer process responsible for directly populating the $^4F_{9/2}$ state in $Y_2O_3:Er^{3+}$, Yb^{3+} following 978 nm excitation..... - 168 -

6.26. Visible emission spectra of nanocrystalline $Y_2O_3:Er^{3+}$, Yb^{3+} (λ_{exc} = 488 nm) showing the (i) $^2H_{11/2}$, $^4S_{3/2} \rightarrow {}^4I_{15/2}$ and (ii) $^4F_{9/2} \rightarrow {}^4I_{15/2}$ transitions.....- 171 -

6.27. Schematic representation of the process responsible for the red enhancement following excitation of nanocrystalline $Y_2O_3:Er^{3+}$, Yb^{3+} with 488 nm.....- 172 -

6.28. Upconversion spectra of nanocrystalline $Y_2O_3:Er^{3+}$, Yb^{3+} (λ_{exc} = 978 nm) showing the (i) $^2H_{11/2}$, $^4S_{3/2} \rightarrow {}^4I_{15/2}$ and (ii) $^4F_{9/2} \rightarrow {}^4I_{15/2}$ transitions.....- 176 -

6.29. Schematic representation of the various upconversion mechanisms in nanocrystalline $Y_2O_3:Er^{3+}$, Yb^{3+} following excitation with 978 nm.....- 177 -

6.30. Power dependence of the green ($^4S_{3/2} \rightarrow {}^4I_{15/2}$) upconverted luminescence in nanocrystalline $Y_2O_3:Er^{3+}$, Yb^{3+} (Er1Yb1) following excitation with 978 nm. Inset: Graph of $\ln(I_{vis})$ versus $\ln(I_{NIR})$ for the Er1Yb1 and Er1Yb10 samples for the $^4S_{3/2} \rightarrow {}^4I_{15/2}$ transition.....- 178 -

6.31. Comparison of the upconversion spectra of (a) bulk $Y_2O_3:Er^{3+}$, Yb^{3+} (BErYb), and (b) nanocrystalline $Y_2O_3:Er^{3+}$, Yb^{3+} (Er1Yb1) showing the (i) $^2H_{11/2}$, $^4S_{3/2} \rightarrow {}^4I_{15/2}$ and (ii) $^4F_{9/2} \rightarrow {}^4I_{15/2}$ transitions (λ_{exc} = 978 nm).....- 184 -

6.32. Upconversion spectrum of nanocrystalline $Y_2O_3:Er^{3+}$, Yb^{3+} (1 mol% Er^{3+} and 10 mol% Yb^{3+}) showing the (i) $^4G_{11/2} \rightarrow {}^4I_{15/2}$ and (ii) $^2H_{9/2} \rightarrow {}^4I_{15/2}$ transitions following excitation with 978 nm.....- 185 -

6.33. Reflectance spectrum of nanocrystalline $Y_2O_3:Er^{3+}$ (10 mol%) prepared via the controlled hydrolysis procedure showing transitions from the $^4I_{15/2}$ ground state to the various Er^{3+} excited states: (a) $^4F_{9/2}$, (b) $^4S_{3/2}$, (c) $^2H_{11/2}$, (d) $^4F_{7/2}$, (e) $^4F_{5/2}$, (f) $^4F_{3/2}$, (g) $^2H_{9/2}$, (h) $^4G_{11/2}$, (i) $^2G_{9/2}$.....- 188 -

6.34. 77 K luminescence spectra showing the $^4S_{3/2} \rightarrow {}^4I_{15/2}$ transition in (a) bulk and (b) nanocrystalline 10 mol% $Y_2O_3:Er^{3+}$ (λ_{exc} = 488 nm).....- 189 -

6.35. Room temperature luminescence spectrum of nanocrystalline $Y_2O_3:Er^{3+}$ (a) 1 mol% and (b) 10 mol% as well as (c) 10 mol% bulk $Y_2O_3:Er^{3+}$ shown for comparison (λ_{exc} = 488 nm). (i) $^2H_{11/2} \rightarrow {}^4I_{15/2}$ (ii) $^4S_{3/2} \rightarrow {}^4I_{15/2}$ (iii) $^4F_{9/2} \rightarrow {}^4I_{15/2}$.....- 193 -

6.36. Diffuse reflectance spectrum of $Y_2O_3:Er^{3+}$ nanocrystals (10 mol%) prepared via wet chemical synthesis.....- 194 -

6.37. Decay curves of the $^4S_{3/2} \rightarrow {}^4I_{15/2}$ transition in 1 and 10 mol% $Y_2O_3:Er^{3+}$ nanocrystals following excitation with 488 or 800 nm.....- 195 -

6.38. Upconversion luminescence spectrum of nanocrystalline $Y_2O_3:Er^{3+}$ (a) 1 mol% and (b) 10 mol% as well as (c) 10 mol% bulk $Y_2O_3:Er^{3+}$ shown for comparison (λ_{exc} = 650 nm). (i) $^2H_{11/2} \rightarrow {}^4I_{15/2}$ (ii) $^4S_{3/2} \rightarrow {}^4I_{15/2}$.....- 198 -

6.39. Upconversion power studies of 1 and 10 mol% nanocrystalline $Y_2O_3:Er^{3+}$ prepared via wet chemical synthesis..... - 199 -

6.40. Schematic representation of the 650 nm upconversion mechanism(s) in bulk and nanocrystalline $Y_2O_3:Er^{3+}$..... - 200 -

6.41. Upconversion luminescence spectrum of nanocrystalline $Y_2O_3:Er^{3+}$ (a) 1 mol% and (b) 10 mol% as well as (c) 10 mol% bulk $Y_2O_3:Er^{3+}$ shown for comparison (λ_{exc} = 800 nm). (i) $^2H_{11/2} \rightarrow {}^4I_{15/2}$ (ii) $^4S_{3/2} \rightarrow {}^4I_{15/2}$ (iii) $^4F_{9/2} \rightarrow {}^4I_{15/2}$..... - 206 -

6.42. Schematic representation of the 800 nm upconversion mechanism(s) in bulk and nanocrystalline $Y_2O_3:Er^{3+}$..... - 207 -

6.43. Room temperature upconversion (anti-Stokes) luminescence of nanocrystalline $Y_2O_3:Er^{3+}$, Yb^{3+} (1 mol% Er^{3+} and 1 mol% Yb^{3+}) prepared via the controlled hydrolysis procedure (λ_{exc} = 978 nm). (i) $^2H_{11/2}$, $^4S_{3/2} \rightarrow {}^4I_{15/2}$ (ii) $^4F_{9/2} \rightarrow {}^4I_{15/2}$..... - 208 -

6.44. Room temperature luminescence of (a) nanocrystalline and (b) bulk $Lu_2O_3:Er^{3+}$ (1 mol%) following 488 nm excitation. (i) $^2H_{11/2} \rightarrow {}^4I_{15/2}$ (ii) $^4S_{3/2} \rightarrow {}^4I_{15/2}$ (iii) $^4F_{9/2} \rightarrow {}^4I_{15/2}$ Inset: (iv) $^4I_{9/2} \rightarrow {}^4I_{15/2}$ (v) $^4S_{3/2} \rightarrow {}^4I_{13/2}$..... - 209 -

6.45. Diffuse reflectance medium-infrared (MIR) spectrum of nanocrystalline $Lu_2O_3:Er^{3+}$ (1 mol%)..... - 213 -

6.46. Raman spectrum of (a) commercial and (b) nanocrystalline undoped Lu_2O_3..... - 214 -

6.47. NIR luminescence of bulk $Lu_2O_3:Er^{3+}$ (1 mol%) upon excitation at 488 nm. Inset: NIR luminescence of $Lu_2O_3:Er^{3+}$ (1 mol%) nanocrystals upon excitation at 488 nm. (i) $^4I_{11/2} \rightarrow {}^4I_{15/2}$ (ii) $^4S_{3/2} \rightarrow {}^4I_{11/2}$ (iii) $^4I_{13/2} \rightarrow {}^4I_{15/2}$..... - 216 -

6.48. Upconversion luminescence of (a) nanocrystalline and (b) bulk $Lu_2O_3:Er^{3+}$ (1 mol%) following excitation with 650 nm. (i) $^2H_{11/2} \rightarrow {}^4I_{15/2}$ (ii) $^4S_{3/2} \rightarrow {}^4I_{15/2}$ (iii) $^4F_{5/2} \rightarrow {}^4I_{15/2}$ (iv) $^2P_{3/2} \rightarrow {}^4I_{15/2}$ (v) $^4F_{7/2} \rightarrow {}^4I_{15/2}$..... - 219 -

6.49. Upconversion luminescence of (a) nanocrystalline and (b) bulk $Lu_2O_3:Er^{3+}$ (1 mol%) following excitation with 804 nm. (i) $^2H_{11/2} \rightarrow {}^4I_{15/2}$ (ii) $^4S_{3/2} \rightarrow {}^4I_{15/2}$ (iii) $^4F_{9/2} \rightarrow {}^4I_{15/2}$ (iv) $^4F_{5/2} \rightarrow {}^4I_{15/2}$ (v) $^2P_{3/2} \rightarrow {}^4I_{15/2}$ (vi) $^4F_{7/2} \rightarrow {}^4I_{15/2}$..... - 220 -

6.50. Upconversion luminescence spectra of bulk $Lu_2O_3:Er^{3+}$ at different temperatures (λ_{exc} = 804 nm): (a) 78 K, (b) 120 K, (c) 140 K, (d) 180 K, (e) 240 K, (f) 298 K. (i) $^2H_{11/2} \rightarrow {}^4I_{15/2}$ (ii) $^4S_{3/2} \rightarrow {}^4I_{15/2}$ (iii) $^4F_{9/2} \rightarrow {}^4I_{15/2}$. The intensities of emission are normalized to green ($^4S_{3/2} \rightarrow {}^4I_{15/2}$) transition..... - 223 -

6.51. Energy level diagram of Er^{3+} ions in Lu_2O_3 showing the three photon upconversion process responsible for populating the $^4G_{7/2}$ level (λ_{exc} = 804 nm)..... - 226 -

6.52. Room temperature upconversion luminescence of (a) nanocrystalline and (b) bulk $Lu_2O_3:Er^{3+}$ following 980 nm excitation. (i) $^2H_{11/2} \rightarrow {}^4I_{15/2}$ (ii) $^4S_{3/2} \rightarrow {}^4I_{15/2}$ (iii) $^4F_{9/2} \rightarrow {}^4I_{15/2}$. Inset: (iv) $^4F_{5/2} \rightarrow {}^4I_{15/2}$ (v) $^2P_{3/2} \rightarrow {}^4I_{11/2}$ (vi) $^4F_{7/2} \rightarrow {}^4I_{15/2}$..... - 230 -

6.53. Power dependence of the green and red upconversion luminescence intensity of nanocrystalline $Lu_2O_3:Er^{3+}$ observed following 980 nm excitation..... - 231 -

6.54. Schematic representation of the ESA and ETU processes in bulk and nanocrystalline $Lu_2O_3:Er^{3+}$. Note: only the relevant Er^{3+} energy levels are shown..... - 232 -

6.55. Power dependence of the blue upconversion luminescence intensity of bulk $Lu_2O_3:Er^{3+}$ observed following 980 nm excitation..... - 236 -

6.56. Upconversion luminescence spectra of nanocrystalline $Lu_2O_3:Er^{3+}$ at different temperatures (λ_{exc} = 980 nm): (a) 77 K, (b) 100 K, (c) 130 K, (d) 160 K, (e) 190 K, (f) 220 K, (g) 250 K, (h) 298 K. (i) $^2H_{11/2} \rightarrow {}^4I_{15/2}$ (ii) $^4S_{3/2} \rightarrow {}^4I_{15/2}$ (iii) $^4F_{9/2} \rightarrow {}^4I_{15/2}$. The intensities of emission are normalized to green ($^4S_{3/2} \rightarrow {}^4I_{15/2}$) transition..... - 240 -

6.57. Stokes emission spectra of nanocrystalline Sc_2O_3 doped with (a) 0.1 mol%, (b) 1 mol%, (c) 10 mol% Er^{3+} following excitation with 488 nm. Shown are the (i) $^2H_{11/2} \rightarrow {}^4I_{15/2}$ (ii) $^4S_{3/2} \rightarrow {}^4I_{15/2}$ (iii) $^4F_{9/2} \rightarrow {}^4I_{15/2}$ transitions..... - 243 -

6.58. Upconversion emission spectra of nanocrystalline Sc_2O_3 doped with (a) 0.1 mol%, (b) 1 mol%, (c) 10 mol% Er^{3+} following excitation with 980 nm. Shown are the (i) $^2H_{11/2} \rightarrow {}^4I_{15/2}$ (ii) $^4S_{3/2} \rightarrow {}^4I_{15/2}$ (iii) $^4F_{9/2} \rightarrow {}^4I_{15/2}$ transitions..... - 244 -

6.59. Power dependence study of the $^4F_{9/2} \rightarrow {}^4I_{15/2}$ upconverted emission following excitation with 980 nm. (a) 210 mW (b) 135 mW (c) 80 mW (d) 45 mW (e) 10 mW. Inset: Graph of ln (Intensity) versus ln (Power) (slope n = 2)..... - 246 -

6.60. Schematic representation of the different mechanisms responsible for the anti-Stokes emission..... - 251 -

6.61. Emission spectrum of nanocrystalline $GGG:Er^{3+}$ doped with (a) 1 mol% and (b) 5 mol% Er^{3+} following excitation with 488 nm and showing the following transitions: (i) $^2H_{11/2} \rightarrow {}^4I_{15/2}$ (ii) $^4S_{3/2} \rightarrow {}^4I_{15/2}$ (iii) $^4F_{9/2} \rightarrow {}^4I_{15/2}$. Inset: (iv) $^4I_{9/2} \rightarrow {}^4I_{15/2}$ (v) $^4S_{3/2} \rightarrow {}^4I_{13/2}$..... - 255 -

6.62. NIR emission spectrum of nanocrystalline GGG:Er^{3+} doped with (a) 1 mol% and (b) 5 mol% Er^{3+} following excitation with 488 nm and showing the following transitions: (i) $^4I_{11/2} \rightarrow {}^4I_{15/2}$ (ii) $^4S_{3/2} \rightarrow {}^4I_{11/2}$ (iii) $^4I_{13/2} \rightarrow {}^4I_{15/2}$ ..... - 256 -

6.63. Medium-Infrared (MIR) reflectance spectra of nanocrystalline (a) GGG:Er 1 mol%, (b) Y_2O_3:Eu 1 mol%, and (c) Y_2O_3:Er 1 mol% ..... - 257 -

6.64. Upconversion spectrum of nanocrystalline gadolinium gallium garnet doped with (a) 1 mol% and (b) 5 mol% Er^{3+} following excitation with 800 nm and showing the following transitions: (i) $^2H_{11/2} \rightarrow {}^4I_{15/2}$ (ii) $^4S_{3/2} \rightarrow {}^4I_{15/2}$ (iii) $^4F_{9/2} \rightarrow {}^4I_{15/2}$. Inset: (iii) $^4F_{7/2} \rightarrow {}^4I_{15/2}$ ..... - 260 -

6.65. Power dependence of the upconverted (i) $^2H_{11/2} \rightarrow {}^4I_{15/2}$ and (ii) $^4S_{3/2} \rightarrow {}^4I_{15/2}$ emission in nanocrystalline gadolinium gallium garnet doped 1 mol% Er^{3+} following excitation with 800 nm. (a) 750 mW (b) 580 mW (c) 360 mW (d) 180 mW (e) 84 mW. Inset: Graph of $\ln(I_i)$ versus $\ln(I_o)$ yielding slopes of approximately 2 for both transitions ..... - 261 -

6.66. Diagram showing the excited state absorption and energy transfer upconversion mechanisms in nanocrystalline GGG:Er^{3+} following excitation with 800 nm into the $^4I_{9/2}$ state. Also shown is the $(^4I_{9/2}, {}^4I_{11/2}) \rightarrow (^4I_{13/2}, {}^4F_{9/2})$ ion pair process responsible for $^4F_{9/2}$ state ..... - 265 -

6.67. NIR luminescence spectra of (a) nanocrystalline and (b) bulk $Lu_2O_3:Nd^{3+}$, showing (i) $^4F_{3/2} \rightarrow {}^4I_{9/2}$, (ii) $^4F_{3/2} \rightarrow {}^4I_{11/2}$, (iii) $^4F_{3/2} \rightarrow {}^4I_{13/2}$ and (iv) $^4F_{3/2} \rightarrow {}^4I_{15/2}$ (λ_{exc} = 488 nm) ..... - 268 -

6.68. Visible emission spectrum of (a) 0.1 and (b) 1 mol% nanocrystalline $Y_2O_3:Sm^{3+}$ following excitation with 476.5 nm at room temperature. Inset: Visible emission spectrum of 1 mol% bulk $Y_2O_3:Sm^{3+}$ (λ_{exc} = 476.5 nm). (i) $^4G_{5/2} \rightarrow {}^6H_{5/2}$ (ii) $^4G_{5/2} \rightarrow {}^6H_{7/2}$ (iii) $^4G_{5/2} \rightarrow {}^6H_{9/2}$ (iv) $^4G_{5/2} \rightarrow {}^6H_{11/2}$ ..... - 273 -

6.69. Dependence of the $^4G_{5/2}$ decay time of nanocrystalline $Y_2O_3:Sm^{3+}$ (1 mol%) on the index of refraction of the medium surrounding the nanocrystals as a function of different filling factors (x) following excitation with 476.5 nm at room temperature ..... - 276 -

6.70. Visible emission spectrum of 1 mol% nanocrystalline $Y_2O_3:Dy^{3+}$ following excitation with 457.9 nm at room temperature. (i) $^4F_{9/2} \rightarrow {}^6H_{15/2}$ (ii) $^4F_{9/2} \rightarrow {}^6H_{13/2}$ (iii) $^4F_{9/2} \rightarrow {}^6H_{11/2}$ (iv) $^4F_{9/2} \rightarrow {}^6H_{9/2} + {}^6F_{11/2}$ (v) $^4F_{9/2} \rightarrow {}^6H_{7/2} + {}^6F_{9/2}$ ..... - 278 -

6.71. Results of the single exponential and Inokuti-Hirayama fits to the decay curve of the $^4F_{9/2}$ emission in nanocrystalline $Y_2O_3:Dy^{3+}$ ..... - 281 -

LIST OF TABLES

CHAPTER 1

1.1 Ground state electronic configurations of the rare earth elements..... - 6 -

CHAPTER 4

4.1 Different fuels used with stoichiometric amounts of $Y(NO_3)_3 \cdot 6H_2O$ in the combustion reaction from ref [205]..... - 78 -

4.2 List of sesquioxide nanocrystalline samples studied prepared by propellant synthesis..... - 79 -

4.3 List of starting materials used in the propellant synthesis of the sesquioxides..... - 79 -

4.4 List of garnet nanocrystalline samples studied prepared by propellant synthesis..... - 80 -

4.5 List of nanocrystalline samples studied prepared by the controlled hydrolysis procedure..... - 82 -

4.6 List of bulk sesquioxide samples studied..... - 83 -

CHAPTER 5

5.1 Average crystallite dimensions, $\langle D \rangle_v$, obtained from two pairs of reflections (222/444 and 400/800) for all sesquioxide nanocrystals under investigation..... - 104 -

CHAPTER 6

6.3 Decay times obtained from an exponential fit of the room temperature decay curves for the $^4S_{3/2} \rightarrow {}^4I_{15/2}$ transition upon 488 nm excitation..... - 119 -

6.4 Room temperature decay time constants (τ_m) for nanocrystalline $Y_2O_3:Er^{3+}$ following excitation with 980 nm..... - 143 -

6.5 List of the bulk and nanocrystalline $Y_2O_3:Er^{3+}$, Yb^{3+} samples investigated..... - 169 -

6.6 Decay time constants, τ_m, of nanocrystalline $Y_2O_3:Er^{3+}$, Yb^{3+} following excitation with 488 nm into the $^4F_{7/2}$ state of Er^{3+} ..... - 174 -

6.7 Decay time constants, τ_m, of nanocrystalline $Y_2O_3:Er^{3+}$, Yb^{3+} following excitation with 978 nm into the $^2F_{5/2}$ state of Yb^{3+} ..... - 179 -

6.8 Effective decay time constants, τ_m, of the $^4S_{3/2}$ state in $Y_2O_3:Er^{3+}$ nanocrystals prepared via the controlled hydrolysis procedure (0.1, 1, and 10 mol% Er^{3+}) following excitation with 488, 650, or 800 nm ..... - 192 -

6.9 Room temperature decay times for bulk and nanocrystalline $Lu_2O_3:Er^{3+}$ obtained from an exponential fit of the decay curves upon 488 excitation ..... - 211 -

6.10 Decay times for bulk $Lu_2O_3:Er^{3+}$ as a function of temperature obtained from an exponential fit of the decay curves upon 488 excitation ..... - 222 -

6.11 Room temperature decay times for bulk and nanocrystalline $Lu_2O_3:Er^{3+}$ obtained from an exponential fit of the decay curves upon 980 excitation ..... - 233 -

6.12 Decay times of bulk and nanocrystalline $Lu_2O_3:Er^{3+}$ for the $^4S_{3/2} \rightarrow {}^4I_{15/2}$ and $^4F_{9/2} \rightarrow {}^4I_{15/2}$ transitions upon 980 nm excitation at various temperatures ..... - 239 -

6.13 Effective decay time constants, τ_m, of the $^4S_{3/2}$ emitting state in $Sc_2O_3:Er^{3+}$ nanocrystals ..... - 245 -

6.14 Decay times of nanocrystalline $GGG:Er^{3+}$ following excitation with 488 nm. In the case of the 5 mol% doped sample, the values of the decay time constant, τ_m, are reported ..... - 254 -

6.15 Decay times of nanocrystalline $GGG:Er^{3+}$ following excitation with 800 nm. In the case of the 5 mol% doped sample, the values of the decay time constant, τ_m, are reported ..... - 259 -

6.16 Decay times of bulk and nanocrystalline $Y_2O_3:Sm^{3+}$ following excitation with 476.5 nm ..... - 272 -

6.17 Decay times of the $^4F_{9/2}$ state of $Y_2O_3:Dy^{3+}$ nanocrystals following excitation with 457.9 nm ..... - 277 -

CHAPTER 1

1. Introduction

1.1. The Rare Earth Elements

"These elements (rare earths) perplex us in our researches, baffle us in our speculations and haunt us in our dreams. They stretch like an unknown sea before us - mocking, mystifying and murmuring strange revelations and possibilities"

Sir William Crooke (1887)

1.1.1. History and Discovery of the Rare Earths

The rare earth elements are the fourteen elements that follow lanthanum in the periodic table. The term rare earth was first suggested by Finnish chemist Johan Gadolin in 1794, however despite their name, the rare earths are neither particularly rare nor are they earths. In fact, each rare earth is more common in the earth's crust than the precious metals, silver, gold, or platinum by several orders of magnitude [1, 2]. Rare earths are never found as free metals in the earth's crust but rather in naturally occurring minerals, which generally consist of mixtures of various rare earths and non-metals.

The discovery of the rare earths, now aptly known as the lanthanides, a name derived from the Greek; to lie hidden or concealed, tells a remarkable tale of discovery (or mis-discovery) and puzzlement. The saga begins in Sweden in 1787 in a town called Ytterby in Stockholm's archipelago. An amateur geologist and Swedish artillery officer, Lieutenant Karl Axel Arrhenius, discovered a dense black mineral, which he named ytterbite after the feldspar quarry in which it was found [3]. In 1794 while studying the rare mineral, Gadolin discovered a new earth, which he named ytterbia and later shortened to yttria [4]. In 1803 this mineral, which eventually became known as gadolinite, yielded another earth named cerium after the asteroid Ceres through the work

of Swedish chemists Jöns Jacob Berzelius and Wilhelm Hisinger and independently by German chemist Martin Klaproth [2].

Some time later, the British chemist, Sir Humphry Davy, proved that the earths were not elements but in fact oxides of the elements yttrium and cerium [2]. Forty years into the future, Swedish chemist Carl Gustav Mosander showed that the yttria and ceria earths were in fact oxides of mixtures of elements [4]. The two new oxides found in yttria were named erbia and terbia (again derived from Ytterby) while the oxides found in ceria were named lanthana and didymia [2]. Mosander was the first chemist to actually extract the rare earth metals from their respective oxides, although the rudimentary equipment used resulted in a rather impure form. In the mid-1850s, there was sizeable debate and bewilderment over the results of further isolation of the rare earths with different laboratories each naming the earths. The level of confusion reached such an epic level that in 1860, a consensus was reached by scientists of the day, to interchange the names of erbia and terbia [2].

Over the next century, fractionation of the rare earths was being investigated widely. Didymia was shown to be a mixture of the oxides of samarium (Paul Emile Lecoq de Boisbaudran, 1879), praseodymium (Carl Auer von Welsbach, 1885), neodymium (Carl Auer von Welsbach, 1885) and europium (Eugene Demarcay, 1896) [5]. Terbia and erbia yielded the oxides of ytterbium (Jean-Charles-Galinard de Marignac, 1878), holmium (Per Theodor Cleve, 1878), thulium (Per Theodor Cleve, 1879), dysprosium (Paul Emile Lecoq de Boisbaudran, 1886) and lutetium (Georges Urbain, 1907) [5]. The name lutetium was universally accepted by scientists except those in Germany who referred to it as cassiopeium, until the 1950s when the name was agreed

internationally [2]. To add to the confusion, what was renamed erbia in 1860 reverted back to terbia in 1877 and terbia once again became erbia. However, Mosander is credited with discovering what we now know as erbium and terbium in 1843 and 1878, respectively. In 1880, the Swiss chemist Jean-Charles-Galinard de Marignac discovered gadolinium by separating gadolinia from the mineral samarskite (not gadolinite) but did not name it. Some years later, French chemist Paul Emile Lecoq de Boisbaudran produced a pure form of the earth and with Marignac's approval named it in honor of Gadolin [5].

By this time, all the rare elements were known with the exception of number 61, the element between neodymium and samarium. However, its existence was predicted in 1902 by John Branner and was initially confirmed by British physicist Henry Moseley in 1914 [6]. In 1941, new radioactivities, which were thought to be those of element 61, were produced by irradiating neodymium and praseodymium with neutrons, deuterons, and alpha particles [7]. In 1942, Chien Shiung Wu, Emilio Gino Segrè, and Hans Albrecht Bethe, confirmed the formation this new element but chemical proof was lacking due to the difficulty in separating the rare earths from each other at that time [8]. In 1945, chemists Jacob Marinsky, Larry Glendenin, and Charles Coryell produced element 61 by both uranium fission and neutron bombardment of neodymium [7]. Using ion-exchange chromatography, they made the first chemical identification of two radioisotopes of element 61. The existence of element 61 was announced at the American Chemical Society meeting in 1947 by Marinsky and Glendenin, the two year gap between discovery and announcement due to the scientists being too busy with defense-related chemistry during the war [9]. In 1948, they proposed the name

promethium for the newly discovered element, after Prometheus, the Titan in Greek mythology who stole fire from the heavens and in 1949, was accepted by the international union of chemistry [9]. Searches for promethium on earth have been fruitless, and it now appears that promethium is completely missing from the earth's crust. Appositely, promethium has been detected in the spectrum of a star in the constellation Andromeda [10].

1.1.2. The Rare Earths and the Periodic Table

The discovery of these elements was major concern for chemists of the early twentieth century since they could not be squeezed into the original periodic table proposed by Russian chemist Dmtri Mendeleev in 1869. In fact Mendeleev himself suggested that the discovery of the lanthanides "broke" his periodic table [11]. Resolution of this puzzle had to wait until the early 1900s when an understanding of atomic structure was developed. The answer was to isolate these 14 elements below the main body of the periodic table (Figure 1.1).

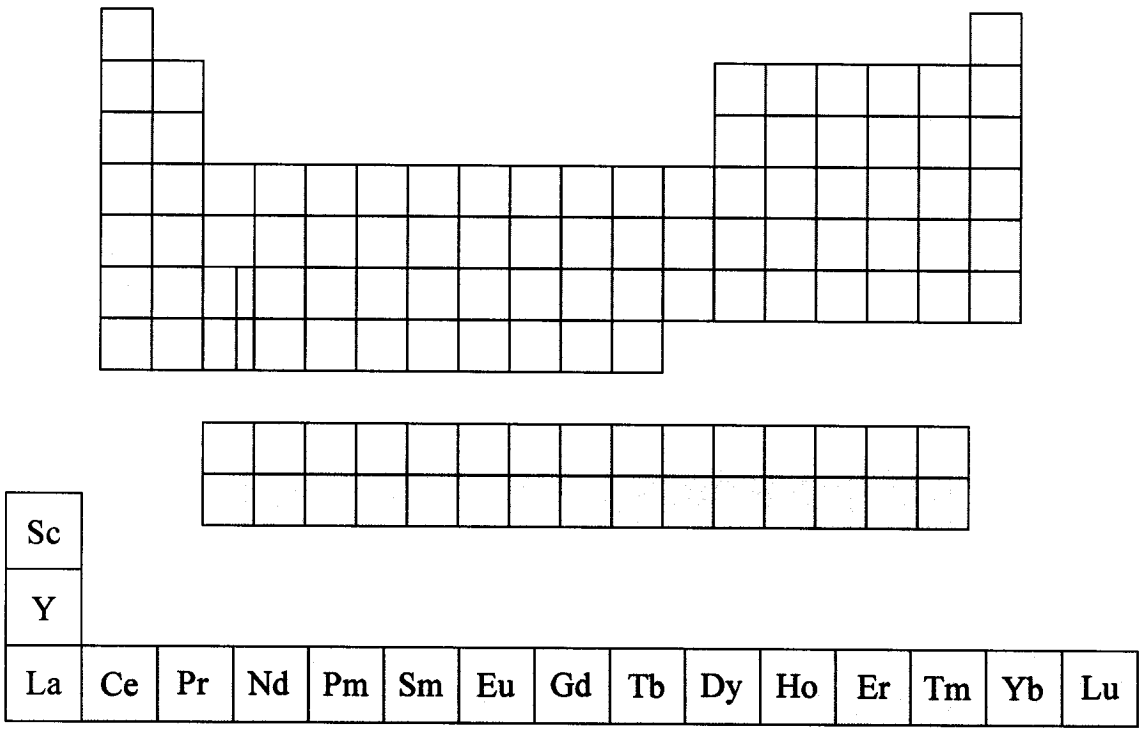

Figure 1.1: Periodic table of the elements with the rare earth series (and similar ions) expanded for clarity.

The rare earth elements correspond to the filling of the 4*f* orbitals. However, also shown in Figure 1.1 are the elements from Group 3; scandium, yttrium, lanthanum, which although not members of the rare earth series have very similar chemical properties and generally occur with the rare earths in the natural minerals. There is discord amongst chemists as to which elements actually belong to the rare earth series. Many claim cerium to lutetium, whereas there are voices, which say lanthanum to ytterbium. The problem becomes apparent when looking at the electron configurations [12] (Table 1.1)

Table 1.1: Ground state electronic configurations of the rare earth elements.

Atomic Number	Element	Symbol	Electronic Configuration	
			Atom	RE^{3+}
57	Lanthanum	La	[Xe] $6s^2\ 4f^0\ 5d^1$	[Xe] $4f^0$
58	Cerium	Ce	[Xe] $6s^2\ 4f^1\ 5d^1$	[Xe] $4f^1$
59	Praseodymium	Pr	[Xe] $6s^2\ 4f^3$	[Xe] $4f^2$
60	Neodymium	Nd	[Xe] $6s^2\ 4f^4$	[Xe] $4f^3$
61	Promethium	Pm	[Xe] $6s^2\ 4f^5$	[Xe] $4f^4$
62	Samarium	Sm	[Xe] $6s^2\ 4f^6$	[Xe] $4f^5$
63	Europium	Eu	[Xe] $6s^2\ 4f^7$	[Xe] $4f^6$
64	Gadolinium	Gd	[Xe] $6s^2\ 4f^7\ 5d^1$	[Xe] $4f^7$
65	Terbium	Tb	[Xe] $6s^2\ 4f^9$	[Xe] $4f^8$
66	Dysprosium	Dy	[Xe] $6s^2\ 4f^{10}$	[Xe] $4f^9$
67	Holmium	Ho	[Xe] $6s^2\ 4f^{11}$	[Xe] $4f^{10}$
68	Erbium	Er	[Xe] $6s^2\ 4f^{12}$	[Xe] $4f^{11}$
69	Thulium	Tm	[Xe] $6s^2\ 4f^{13}$	[Xe] $4f^{12}$
70	Ytterbium	Yb	[Xe] $6s^2\ 4f^{14}$	[Xe] $4f^{13}$
71	Lutetium	Lu	[Xe] $6s^2\ 4f^{14}\ 5d^1$	[Xe] $4f^{14}$

While most periodic tables list lutetium as a lanthanide, its electronic configuration (as an element) fits the pattern of the third transition series. The 15 elements from lanthanum to

lutetium share common chemical features, which explains why it took more than a century from initial discovery to complete isolation. Thus, it is logical to group them together. However, from a spectroscopic viewpoint, the elements from cerium to ytterbium (with the exception of promethium) are of interest due to their unfilled $4f$ shell.

1.2. History of Spectroscopy

And God said, Let there be light: and there was light.
Genesis 1:3

1.2.1. The Origins of Spectroscopy

Light is undoubtedly at the core of spectroscopy and in tracing the history of this science, it can be said that its foundations were laid with the utterance of the above words. However, its physical understanding was forced to wait eons and came to light with the arrival of Sir Isaac Newton. Newton allowed sunlight from a small, circular hole to fall on a prism, producing a rainbow of color. Although the production of a rainbow by a clear crystal was known to the ancients, it was Newton (in 1666) who showed that white light from the sun could be dispersed into a continuous series of colors. He proved that the colors did not originate in the crystal, but rather were the components of sunlight. This array of colors he called a spectrum and subsequently put forth his theory in the 1704 book "Opticks" [13]. According to Newton and contrary to beliefs of the era, light was composed of tiny particles (corpuscles) that were emitted by luminous bodies. In his eulogy, following the death of Sir Isaac Newton, the poet Alexander Pope highlighted Newton's accomplishments in the field of optics:

> *"Nature and Nature's laws lay hid in night;*
> *God said, 'Let Newton be!' and all was light."*
> **Alexander Pope (1727)**

The spectral nature of light was present in the rainbow since the dawn of time but it was beyond the ability of primitive man to recognize its significance. Newton's studies led him to unweave the mystery and essentially spoil the poetic beauty of the rainbow.

Scientific understanding of the colors of the rainbow inspired Keats to pen his well known lines [14]:

> *"Do not all charms fly at the mere touch of cold philosophy? There was an awful rainbow once in heaven: we know her woof, her texture; she is given in the dull catalogue of common things. Philosophy will clip an angel's wings, conquer all mysteries by rule and line, empty the haunted air, and gnome mine unweave a rainbow."*
>
> **John Keats (1820)**

Isaac Newton used an instrument with a small circular aperture to define the beam of light and a lens to collimate the beam. It was then directed to a glass prism, which dispersed it onto a small screen that displayed the spectrum (Figure 1.2).

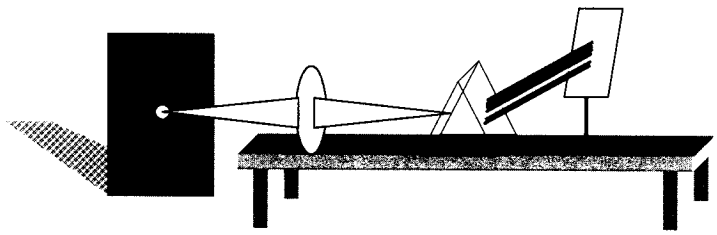

Figure 1.2: Sir Isaac Newton's experimental set-up used to separate the colors of sunlight.

This rudimentary instrument was the foundation of the modern spectroscope and Newton's analysis of sunlight unleashed the scientific pursuit of what we refer today as the science of spectroscopy.

In the 19th century, the science of spectroscopy advanced by leaps and bounds with the invention of the spectroscope. In 1861, Prussian physicist Gustav Robert Kirchoff and German chemist Robert Wilhelm Eberhard von Bunsen pieced together the first spectroscope. The initial Bunsen-Kirchoff spectroscope (Figure 1.3) was made of

nothing more than a cigar box, prism, two obsolete telescopes and a flame (from a Bunsen burner) [15].

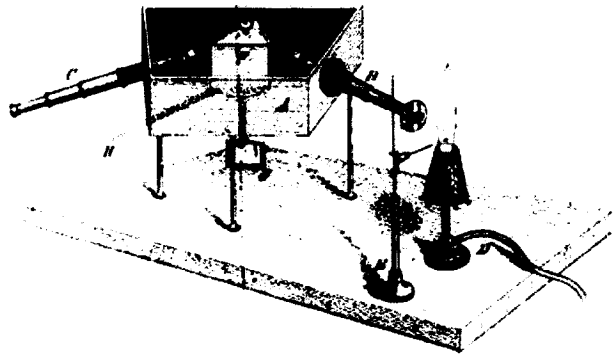

Figure 1.3: The initial Bunsen-Kirchoff spectroscope invented by Bunsen and Kirchoff in 1861.

The instrument was of tremendous importance in chemical analysis, especially in the discovery of new elements by yielding a unique spectrum for each element. By the late 1880's the spectroscope was refined to include a collimator, adjustable slit, a prism for comparison of spectra, a second collimator with a photographed millimeter scale, and a telescope for examining the rays from the former two. The prism, which was of made of flint-glass, was enclosed in a strong metal box (Figure 1.4) [16].

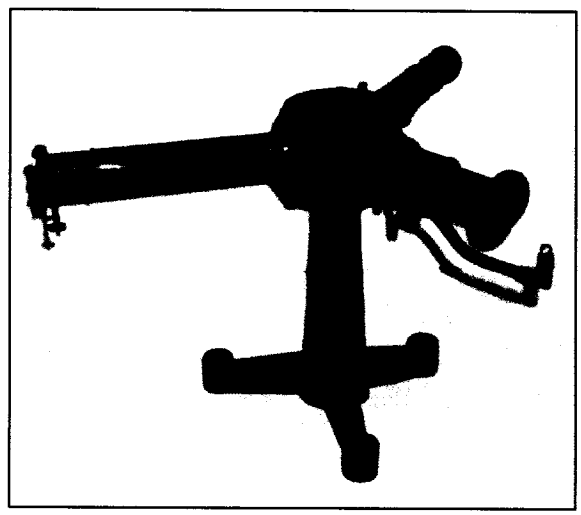

Figure 1.4: A more modern spectroscope, circa 1880.

The invention of the spectroscope transcended science and made its way to literary circles. In *Our Mutual Friend*, written in 1865, Charles Dickens imagined a "moral spectroscopy" whereby the inhabitants of remote galaxies and stars might analyze the light from the Earth to gauge its good and evil, the moral spectrum of its inhabitants [17, 18].

Of course, the complete and entire history of spectroscopy is vast. We will thus henceforth only focus on the history of rare earth spectroscopy.

1.2.2. Rare Earth Spectroscopy

Spectroscopic studies of the rare earths began a few years following the development of spectral analysis by Bunsen and Kirchoff. In his studies on didymium sulfate octahydrate (1866), Bunsen observed absorption spectra that were dependent upon the direction of the crystals with respect to the excitation light [19]. Using light polarized in different orientations, unique absorption spectra were obtained for given crystallographic directions. In 1888, French physicist Henri Becquerel who along with Pierre and Marie Curie discovered radioactivity, thoroughly examined this phenomenon using many rare earth containing minerals. Becquerel recognized the appearance and disappearance of structure in these minerals because of the sharpness of the absorption bands [20]. Roughly two decades into the future, his son Jean Becquerel examined the spectra of these minerals at low temperatures and observed a relationship between the width of the absorption lines and temperature. Along with his co-workers, they noticed a refinement of the bands into sharp lines when the material was cooled to liquid air temperature (85 K) [21], sharper lines when the temperature was lowered to liquid

hydrogen (20 K) [22], and sharper still at liquid helium temperatures (4 K) [23]. They recognized that the absorption spectra consisted not of bands but of lines approximating in sharpness the absorption lines of gases. A link between the structure of the rare earth ion and the observed absorption spectrum could not be established with absolute certainty due to the doubtful identity of the rare earth ion contained in the mineral studied. Many of the minerals under investigation contained a combination of rare earths and thus complicated the analysis. A considerable amount of experimental evidence was collected but little progress was made in understanding the phenomena due to the lack of a solid theoretical foundation. In the course of his studies, Becquerel also discovered a Zeeman effect from these crystals and became interested in their magnetic orientation [24].

The fundamental theory of rare earth spectra began to gain momentum with the advent of the Bohr Theory (1913) and later with the dawn of quantum mechanics in 1925. The mid to late 1920's was a remarkable time in the study of rare earths. Friedrich Hund studied the magnetic properties of the rare earths and successfully predicted the ground states of the trivalent ions [25]. Shortly thereafter in 1929, Hans Bethe and Hendrik A. Kramers made possible the interpretation of rare earth spectra. Bethe introduced group theory (*gruppen pest*) to the study of the rare earths and laid the foundation for the study of energy states in crystals, essentially giving birth to the crystal field theory [26, 27]. He derived the number and symmetry characteristics of the component levels, which arise for a given atomic energy level after it's embedded in fields of various crystallographic symmetries. Bethe showed that the observed splitting of the absorption lines in the electric crystalline field was directly related to the symmetry of the field. Meanwhile, Kramers [28] (1929) made use of the recently developed quantum theory to interpret the

results of these experiments and made a significant discovery. He noticed that the electrical fields of the lattice do not remove the degeneracy coming from the spin of the electrons and proved that in an odd electron system, every level must remain at least doubly degenerate (Kramer's degeneracy). The degeneracy of these levels can be removed by an externally applied magnetic field. Today, the trivalent rare earth ions with odd $4f$ electrons are commonly referred to as Kramers ions [29].

John H. Van Vleck and Amelia Frank resolved the inconsistencies between theory and experiment for Eu^{3+}, which at the time, marred Hund's rare earth theory (1929) [30]. The findings continued on into the 1930's where in 1932, Van Vleck published his comprehensive book on magnetic susceptibilities [31]. In their 1932 paper, William G. Penney and Robert Schlapp initiated practical crystal field calculations [32]. By making use of Eugene P. Wigner's recently published *Gruppentheorie* [33], Penney and Schlapp's crystal field theory was extended by Amelia Frank (1932 and 1935) to include *J*-mixing [34, 35]. Frank applied the crystal field theory of Penney and Schlapp to the magnetic susceptibilities of Eu^{3+} and Sm^{3+}. She explored the effects of a breakdown to lower symmetry, from cubic to rhombic, and in her short life can be considered one of the unsung protagonists of crystal field theory [36].

As early as 1929, Simon Freed and Frank H. Spedding [19, 37, 38] had initiated detailed studies of the low temperature absorption spectra of rare earth salts and outlined reasons why the sharp absorption spectra of the rare earths in the solid state would resemble the line spectra of the ions in the gaseous state. Freed and Spedding observed that there existed large groups of lines clustered closely together separated by larger intervals. Some of these clusters disappeared at low temperatures allowing them to

identify the presence of low lying levels, which were significantly populated at higher temperatures. Freed and Spedding recognized that these cluster of closely spaced lines arose from the crystal splitting of the free atom states. However, they speciously suggested that the sharp line spectra were due to $4f-5d$ or $4f-6s$ transitions [39].

In 1937, Bethe and Spedding collaborated on the absorption spectrum of $Tm_2(SO_4)_3 \cdot 8H_2O$ and observed sharp bands of weak intensity, which led them to speculate that they were due to forbidden transitions [40]. They surmized that the absorption bands were the result of a rearrangement within the $4f$ shell and suggested three possible types of transitions:

(i) Quadrupole transitions

(ii) Dipole transitions caused by a natural lack of symmetry of the crystalline field

(iii) Dipole transitions caused by coupling with crystal vibrations

Simultaneously, Van Vleck published his seminal paper entitled, "*The Puzzle of Rare-Earth Spectra in Solids*" and arrived to similar conclusions as Bethe and Spedding [41]. He opined that the forbidden lines violated the Laporte rule and proposed mechanisms by which the $4f-4f$ configuration intensities could be observed. He supposed they were due to a variety of effects such as quadrupole radiation, magnetic dipole radiation, and radiation created by crystalline fields in which the mandatory departures from a center of symmetry are either present at the equilibrium position or caused by atomic vibrations. John Van Vleck calculated the crystal field splitting of the ground states under the assumption that the rare earth ions were essentially free ions (with a Russell-Saunders ground state term) in a static electric field produced by the surrounding lattice. By 1940,

the studies of Bethe, Spedding and Van Vleck were the root for further studies by a growing number of scientists and budding interest in the field.

As with many other fields, the epoch following the Second World War saw foremost developments in both experiment and theory that significantly hastened the understanding of the rare earths and many of their perplexing attributes. A major advancement was achieved in 1949 with Giulio Racah's application of group theory and tensor operators to the problems of complex spectra [42]. He fashioned the tools required to perform detailed spectroscopic calculations for systems involving the multitudinous states of the $4f$ shell in the meanwhile revolutionizing the entire subject of rare earth spectroscopy.

Roger Elliott and Kenneth Stevens used electron paramagnetic resonance techniques to obtain more precise data for the ground state crystal field splitting [43, 44]. The "Stevens Method of Equivalent Operators" was born with the supposition that the crystal field perturbations were infinitesimal compared to the spin orbit coupling, which allows the ground state to be considered as an isolated multiplet of constant J. The underlying assumption in the Stevens' operator equivalents method is that the crystal field interacts only within the separate free ion J-manifolds (i.e. no J-mixing). This premise holds true when the separations between J levels are large in comparison to the crystal field splittings. The assumption however, breaks down in the case of strong crystal fields or where the free ions are mixed and thus, the J-mixing must be included in any calculation. This was accomplished by a number of researchers in the years between 1959 to 1962 [45-47].

Gerhard H. Dieke and co-workers provided necessary and numerous experimental data on the spectra of rare earth doped crystals. Dieke identified many of the free ion levels of the rare earths and led to the landmark publication of his book, "*Spectra and Energy Levels of Rare Earth Ions in Crystals*" [48]. The combination of their theoretical and experimental work is summarized in Figure 1.5:

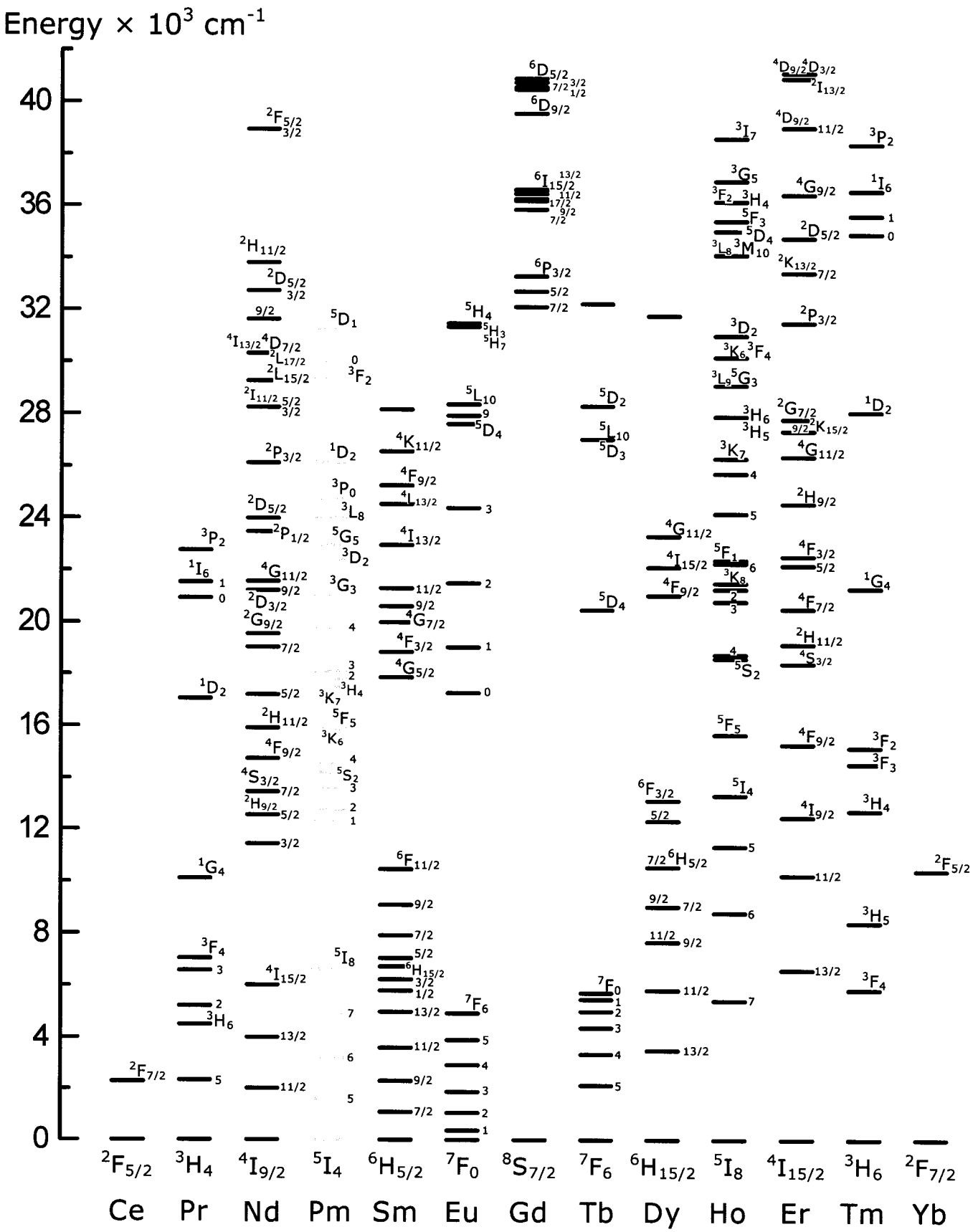

Figure 1.5: Observed energy levels of the rare earth ions in the $LaCl_3$ structure.

1.3. The Rare Earth Elements in the Modern Times

"Lanthanum has only one important oxidation state in aqueous solution, the +3 state. With few exceptions, this tells the whole boring story about the other 14 Lanthanides"

G. C. Pimentel and R. D. Sprately (1971)

During the middle of the previous century, the rare earth elements ascended from simple scientific curiosity to technological relevance. Their beauty and usefulness lies in the fact that they are very similar from a chemical point of view although their individual physical properties, such as color, luminescent behavior, and nuclear magnetic properties, make them quite diverse. The major chemical use is undoubtedly in the petroleum industry as a cracking catalyst used to refine crude oil into gasoline and other valuable fuels [49]. The automotive industry also makes use of the chemical properties of these elements in catalytic converters and alloys for magnets used in such important vehicle systems as anti-lock braking systems and air bags [50]. However, the majority of the applications of the rare earths exploit their physical properties. They were originally used to turn ordinary glass into eye catching masterpieces containing vivid colors that are displayed at some of the world's most historic landmarks [51]. Today, they have many interesting applications spanning a number of industries. Clinical diagnostics is facilitated in the medical community by Gd^{3+} where it is used as a contrasting agent in magnetic resonance imagining (MRI) [52]. The Eu^{3+} ion protects the European Community's currency, the Euro, from counterfeiting by making use of its characteristic luminescence in the red, green, and blue regions following UV excitation [53].

Following the advent of the laser [54-57] by Townes, Schawlow, and Maiman, the 1960's witnessed a boom in the development of solid state lasers by utilizing the luminescence of rare earth ions in glasses and crystals. Without doubt, the most

important success from this era is the Nd:YAG laser, which is still commonly used today. In the domain of telecommunications, the 1500 nm window is the wavelength of choice, which fortuitously coincides with the 1535 nm $4f-4f$ $^4I_{13/2} \rightarrow {}^4I_{15/2}$ transition of the Er^{3+} ion [58]. As a result, the development of the erbium doped fiber amplifier (EDFA) in the 1980's allowed the transmission and amplification of signals in the 1530-1560 nm region [59]. The EDFA eliminated the need for expensive optical to electrical conversion and offered several advantages over conventional amplification such as the capability to produce gain at several wavelengths, a necessary requisite for wavelength division multiplexing (WDM) [60]. The rare earths also had a mammoth impact on the lighting and imaging industries where rare earth doped phosphors are extensively used in a variety of devices such as energy saving trichromic fluorescent lamps and the cathode ray tube [61]. A more detailed discussion of rare earth doped phosphors is presented in the subsequent section.

1.3.1. Luminescence and Phosphors

Luminescence, the emission of light by a material after it has been exposed to UV, visible, IR radiation, electron bombardment, X-rays, or some other method of excitation, has mesmerized people since ancient times [62]. Fascination with phosphorescence and luminescence originated from the mysterious fact that an apparently imperceptible power source could somehow produce discernible light. Inorganic luminescent materials, phosphors, have been known since approximately the 10^{th} century in China and Japan as well as since the end of the middle ages in Europe [63]. In approximately 1600 AD, the Stone of Bologna peaked Galilei's interest by emitting a

persistent yellow-orange light when exposed to sunlight [64]. Although the physical processes were unfamiliar to him, he excluded mystery as the origin of the phenomenon. By the end of the 19th century, luminescent materials were used mainly for decorative purposes. During WWII, research on luminescent devices was intensified, however at that time, the devices were monochromatic and thus contained only a single phosphor [64]. In 1964, $YVO_4:Eu^{3+}$ was successfully proposed as a red phosphor for color television tubes and subsequently for fluorescent lamps [65]. This was the start of the now overwhelming role of rare earth ion luminescence in commercial phosphors.

Today, the commercial applications of rare earth luminescence are ubiquitous, with light emitting materials being extensively deployed in everyday commodities such as lamps, television screens, and computer and cell phone displays. From the early black and white television sets on which the British Broadcasting Corporation (BBC) transmitted its first television signal to the public in 1936 [66], to the state of the art high definition televisions, from Thomas Edison's first light bulb to the modern compact fluorescence bulb, technology has advanced tremendously and the rare earths have been there at each step of the way [67]. However, before discussing where we are headed with rare earth doped phosphors, it is of utmost importance that we revisit their storied past.

Rare earth doped phosphors have been classically employed in trichromic fluorescent lamps. In fact, of all the artificially generated photons on earth, approximately 90% originate from discharge lamps [68]. A fluorescent lamp is a gaseous discharge light source where light is produced by passing an electric arc between tungsten cathodes in a glass tube filled with mercury vapor and rare gases [69]. The arc excites the mercury vapor, which generates UV photons. The RE^{3+} phosphor coating

converts the UV emission into visible light, most often white light. The white light is made by mixing a trio of red, blue, and green emitting (RBG) rare earth phosphors [64]. These tri-phosphor blends are classically, $Y_2O_3:Eu^{3+}$ (red-emitting), $CeMgAl_{11}O_{19}:Tb^{3+}$ (green-emitting) and $BaMgAl_{11}O_{19}:Eu^{2+}$ (blue-emitting) [70]. The color can be varied by changing the proportion of each phosphor.

The cathode ray tube (CRT) is still the most commonly used display device in the world today found in millions of television sets across the globe. A basic CRT utilizes a heated cathode, two sets of anodes (focusing and accelerating) and steering coils to produce and direct electrons at phosphors coated onto a screen to generate light and thus a picture [71]. The commercial phosphors utilized in the majority of current CRTs are micrometer in size due to problems encountered such as decreased luminescence as one goes to smaller particle sizes. If it were possible to produce smaller spherical particles in the nanometer range with luminescent properties similar to or improved over their current micrometer counterparts, then these particles could be easily processed into smaller pixels than those currently used in conventional cathode ray tube (CRT) screens. This opens up the possibility of higher resolution which is desirable for the future of high definition television (HDTV) [72].

After more than a half century of extensive research on luminescent materials applied in lamps and displays, tens of thousands of phosphor mixtures have been synthesized but only approximately 50 materials exhibit properties that are sufficient for technological applications and these compounds are obtained with almost ideal physical properties [73]. However, the search for novel rare earth doped materials is still of utmost importance for tomorrow's fields of light generation for displays and illumination.

Current phosphor research is best organized by the excitation source. For example, luminescent materials in plasma display panels (PDP) in which the phosphor powders are excited by vacuum ultraviolet (VUV) photons (145 – 180 nm) and field emission displays (FED) in which the luminescent material in bombarded by low energy electrons emitted by microtips [74].

Plasma Display Panels (PDP) are a new generation of large flat panel displays. PDPs are based on multiple micro-discharges working on the same basic principles as the fluorescent tubes mentioned above. These PDP modules consist of a cell structure where a combination of gases is confined. Each cell has electrodes that enable gas ionization under an electric field. The UV rays that are created from this plasma gas excite a phosphor layer that converts them into red, green or blue color. PDP is the only technology able to provide direct view displays with diagonals in the range 30 to 65 inches, which can be viewed under room-light or sunlight conditions. The high energy UV photons (147 nm, 8.5 eV) that impinge on the phosphor powders cause reduction in luminous efficiency of the display over time because of radiation damage induced in the material [75]. Thus, oxide phosphors were found to be optimal for plasma panel display (PDP) devices compared to other conventional sulfide based phosphors which suffer from this type of degradation.

The field emission display (FED) has been recognized as one of the most promising technologies for flat panel display. The FED functions on similar principals to the CRT as a beam of electrons are utilized to excite the phosphors, which then emit light. However, they differ in that the FED uses multiple electron emitters for each pixel arranged in a grid [76]. This technology eliminates the beam steering system of the CRT

and allows screens to be manufactured as thin as 10-20 mm. FEDs also have several advantages over the current choice for flat panel displays LCDs: they require no back light, are very light, have a wide viewing angle, short response time, very high contrast ratio and excellent color properties [70].

1.4. Inorganic Nanocrystalline Materials

"If I were asked for an area of science and engineering that will most likely produce the breakthroughs of tomorrow, I would point to nanoscale science and engineering."
Neal Lane (1998)

The scientific community will irrefutably remember the twentieth century for the advancement of nanoscience, science at the nanometer level, which has led to an unprecedented understanding and control over the fundamental building blocks of nature and fulfilling the predications made by Richard Feynman in December of 1959 [77, 78]. In his prophetic talk entitled, "*There's Plenty of Room at the Bottom*" given at the annual meeting of the American Physical Society at the California Institute of Technology, Feynman envisioned nanotechnology (and nanoscience) long before the conception of nano. Recent progress in nanoscience has yielded the ability to not only study but manipulate these building blocks, atoms and molecules, from which all things are made. This knowledge will no doubt one day change the way most things known to man are created and allowing limitless possibilities for new innovation.

In the realm of materials science, the natural (and necessary) march towards the nanoscale has opened up new and exciting opportunities. In fact, materials science sits at the cusp of a new and wonderful beginning as it proceeds headlong into the nanoworld. Many things that were once believed unattainable are now easily within our grasp and the field is quickly burgeoning and adapting. The interest in these nanomaterials has carried over to the field of luminescence where over the last few years, much of the research has shifted from bulk glasses and crystals to nanometer sized phosphors. Nanocrystals (or nanoparticles), as they are more commonly known, typically have particle diameters of

100 nm or less, and have been shown to exhibit particle-size-dependent phenomenon in a wide variety of materials from semiconductors to insulators [79, 80].

Over the past two decades, using size control to tailor the characteristics of semiconductor materials has been widely demonstrated [81]. It was shown that the optical properties of these materials could be changed by varying the particle size, thus stimulating a great deal of interest in both basic [82] and applied research [83]. In the early 1990's, Bhargava reported [84-86] that nanocrystalline ZnS:Mn^{2+} could yield high luminescence efficiencies and a spectacular lifetime shortening, which suggested that doped semiconductor nanoparticles formed a new class of luminescent materials for various applications. This effect was in part due to a change in the band structure of the semiconductor as the particle size was decreased. This quantum confinement effect [79], as it became known, leads to an increase in the band gap causing the edges of the bands to split into discrete energy levels [87] and results in a blue shifted optical spectrum. Those findings were subsequently critically reviewed by Bol and Meijerink [88, 89] who showed substantial misinterpretation of the experimental results. However, this did not stem the tide and a myriad of papers on the quantum size effects in nanocrystalline semiconductors have since appeared.

The interest in nanoparticles was not only limited to semiconductor materials. Shortly thereafter, many papers appeared on nanocrystalline insulating materials doped with rare earth ions [90-97]. As we discussed in the preceding section, microcrystalline powder phosphors find uses in numerous lighting and display applications; particularly the cathode ray tube (CRT) used in conventional television sets. The resolution of images on a CRT display is related closely to the particle size of the phosphors and thus,

smaller particles are favorable for higher resolution [98]. However, reducing the size of a conventionally synthesized phosphor resulted in a decrease in the luminescence efficiency [98]. As many electronic display devices are being reduced in size, the development of these phosphors with nanometric particle sizes has become vital. An excellent example is the development of flat panel displays where design constraints severely limit the amount of excitation power available for the excitation of phosphors [99]. Consequently, there is an ongoing search for luminescing materials with increased efficiency and smaller size. Recently, synthesis techniques were developed, which could synthesize nanosized phosphors and it was therefore a logical extension to study these nanophosphors in the hopes of replacing the currently used microcrystalline phosphors.

There are two main reasons for the change in the electronic properties of these nanoparticles. The first is the quantum size effect observed in semiconductor nanocrystals and is a consequence of the strong reduction of quantum mechanical allowed states in a small particle, seen in an increased band gap [100]. In insulating nanocrystals, the band gaps are very large and the electronic energy levels of the dopant ion reside within that band gap [101]. Consequently, quantum confinement is not observed in these materials. Secondly, nanocrystalline materials posses a large surface/volume ratio and result in a number of observed size effects. The large surface-to-volume ratio of nanometer-size particles determines the structure and chemistry of the particles, which in turn dictates the structural, electronic, and optical properties of the materials [102].

In recent times, there has been considerable attention focused on nanometer sized rare earth doped phosphors, since it has been shown that a reduction in particle diameter

results in many interesting size induced effects. Exploiting these size effects in rare earth doped nanocrystals is of utmost interest and is fueled by their potential as efficient display phosphors for opto-electronics applications as a result of their enhanced optical properties.

CHAPTER 2

2. Background

2.1. Nanophosphors

The generation of light by single crystals doped with rare earth ions is well known. While these single crystals are one of the most common ways to create light, several limitations exist. For example, the formation of large defect free crystals can be time-consuming and the specialized equipment required for their production is quite costly. A simpler and more cost effective method to obtain phosphors is to use a solid state reaction or precipitation method to produce powders with crystal sizes in the micrometer range (6 – 10 μm). Such luminescent materials synthesized via conventional means were ground down mechanically to attain the desired smaller particles. However, the reduction in the particle size achieved by mechanically grinding techniques had little or no control over the particle morphology and ultimately resulted in a decrease of the luminescence efficiency [103]. Grinding of the particles results in the formation of a surface dead layer, which provides non-radiative recombination routes thereby lowering the luminescence efficiency [104]. The development of facile techniques to synthesize the crystals directly in the nanometer regime has eliminated the need for such practices and has inspired a wealth of new possibilities. Novel display and imaging devices with reduced dimensions are currently being developed, which require new and improved luminescent materials. However, the existing commercial phosphors are very much limited due to their large particle sizes, making them inadequate to meet the needs of these new smaller devices and thus, the development of phosphors with nanometric particle sizes has become paramount.

For many of these initial studies, nanocrystalline $Y_2O_3:RE^{3+}$ has been the material of choice owing to its favorable physical properties and ease of synthesis in the nanometer regime. The optical properties of yttrium oxide (single crystal and microcrystalline) doped with rare earth ions are very well known. Yttria is a favorable host for rare earth ion substitution for a myriad of reasons, but, perhaps the most important property of all is that yttrium oxide possesses low vibrational (phonon) energies (approximately 600 cm^{-1}, maximum) [105, 106]. In fact, the dominant phonon energy is 380 cm^{-1}, which is one of the smallest phonon energies among the oxides [107]. This relatively small vibrational energy allows for efficient radiative transitions between electronic energy levels of the rare earth ions. In nanocrystalline form, the intensity of the rare earth luminescence [108] and lifetime of the excited states [109], have been shown to be inversely proportional to the size of the particles in this host.

In the early 1990's, Bhargava and co-workers studied the optical properties of Tb^{3+} doped Y_2O_3 nanocrystals and showed that a decrease in particle size, from 10 to 4 nm, resulted in the corresponding increase of the photoluminescent efficiency of the characteristic green $^5D_4 \rightarrow {}^7F_5$ emission. They showed that the light output per Tb^{3+} ion in the doped nanocrystalline Y_2O_3 phosphor was higher than in the standard microcrystalline $LaOBr:Tb^{3+}$ phosphor [108]. The increase in the efficiency varied as the square of the particle size (D) [87] as was expected from the semiconductor quantum confinement model ($1/D^2$) [110]. They proposed that the excited states of the localized terbium atoms in yttria could be strongly modulated as a result of quantum confinement in the nanocrystals, which could lead to changes in the overlap of wave functions with other atoms in the particle. Due to this modulation effect, the dopant terbium ions could

interact more readily with the host lattice compared to a bulk sample, which could lead to changes in both the electronic structure and transition probabilities. Furthermore, the authors showed that the green Tb^{3+} emission peak of the nanocrystalline phosphor was shifted by 2 nm compared to the standard phosphor and again attributed it to the quantum confinement of the dopant ion. However, the authors failed to report that the shift of 2 nm may occur because the Tb^{3+} ions experience different crystal field effects from the two different hosts. Konrad and co-workers [111] later disproved the presence of quantum confinement in nanocrystalline Y_2O_3 and determined that the size effects were caused by an increase in the lattice relaxation energy of the excited state.

Around the same time, Tissue et al. carried out a thorough investigation on nanophase monoclinic $Y_2O_3:Eu^{3+}$ synthesized via a laser-heated vaporization-condensation technique and observed a number of size effects in the spectroscopy of this material. However most notably, they discerned that the lifetime of the characteristic red Eu^{3+} emission was particle size dependent [112-115]. These initial findings and subsequent research by a number of other investigators had an immense impact on the imaging and display industries where polycrystalline $Y_2O_3:Eu^{3+}$ and $Y_2O_3:Tb^{3+}$ are common phosphors and used frequently in fluorescent lighting and display devices. Thus, these ground-breaking studies fostered a great deal of interest from the scientific community. As a result, towards the end of the 20^{th} century and into the new millennium, there has been a renaissance in the study of rare earth doped powder phosphors where modern day scientists are investigating the luminescence properties of these crystalline materials in the nanometer scale, with particle sizes under the 100-nm threshold for advanced phosphor and photonic applications. These enhanced properties have important

implications in the technological domain where many of today's standard devices are smaller than their predecessors. Consequently, there exists a need for new, far more efficient emissive materials with smaller sizes, in order to meet the demand of current technology.

2.2. The Phenomenon of Upconversion

Recently, considerable attention has been given to trivalent rare earth (RE^{3+}) doped phosphors with particle sizes in the nanometer regime [116, 117]. The bulk of the research has focused primarily on their Stokes luminescence properties, studying the emission of radiation at lower energy than the exciting wavelengths. The interest stems from the remarkable particle-size-dependent phenomena that can be exhibited by these nanosized phosphors, which is believed will make a massive technological impact. In contrast however, many fewer studies have appeared on upconversion nanocrystalline phosphors, which provide the emission of radiation at higher energy than the excitation wavelength (see for example [93, 97, 118-131]).

The phenomenon of upconversion has been studied extensively over the past few years in rare earth doped glasses [132-134] and crystals and it is an important process for the generation of visible light from near infrared radiation. Upconversion is defined as the optical illumination of a transition metal, rare earth, or sometimes actinide ion-doped material, which produces a population in an excited state, whose energy exceeds that of the pump photon [135-140]. An upconverting phosphor is excited by near infrared (NIR) light directly, leading to visible (or UV) emission. The most common mechanism involves excitation of an ion by an NIR photon to populate an intermediate excited state having a relatively long lifetime that can be further excited by another NIR photon to the higher energy emissive state. In the strictest sense, the (up)conversion of infrared radiation to visible has generated much of the current interest in upconversion as advances in both solid state lasers and semiconductor laser diodes have resulted in highly efficient and inexpensive sources of NIR radiation [141] making inorganic upconversion

phosphors attractive for commercial applications. A condition for efficient upconversion is that the absorbing ion must have a metastable state that is intermediate in energy between the ground state and the emitting state [137]. This intermediate state acts as a population reservoir. The requirements for efficient upconversion make rare earth ion-doped solid state crystals ideal for this application. RE^{3+} ions such as Pr^{3+}, Nd^{3+}, Sm^{3+}, Dy^{3+}, Ho^{3+}, Er^{3+}, and Tm^{3+} ions are particularly suited for upconversion as they posses several excited states with long-lived lifetimes that are well matched to the emission wavelengths of several efficient pump laser sources. Co-doping with the Yb^{3+} ion has been shown to improve the upconversion efficiency in singly doped systems, due to its high absorption cross-section in the NIR (circa 980 nm) and efficient energy transfer rates [142]. Furthermore, co-doping with Yb^{3+} can result in upconversion where normally it is not possible in the single ion [143].

Upconversion is well known to occur via three distinct mechanisms [144-146]which are highlighted briefly below.

2.2.1. Excited State Absorption (ESA)

Excited state absorption, also known as sequential absorption of photons, is one of the best known models of upconversion. Originally discussed by Bloembergen as the basis for an infrared quantum counter [144], it involves only a single ion and is, in most cases, the only upconversion process which occurs in materials having low rare earth dopant concentrations. In this process, an incoming photon from the pump beam will bring the ion to a long-lived intermediate excited level (2) and a second photon from the pump beam promotes it to the upper emitting level (3) (Figure 2.1).

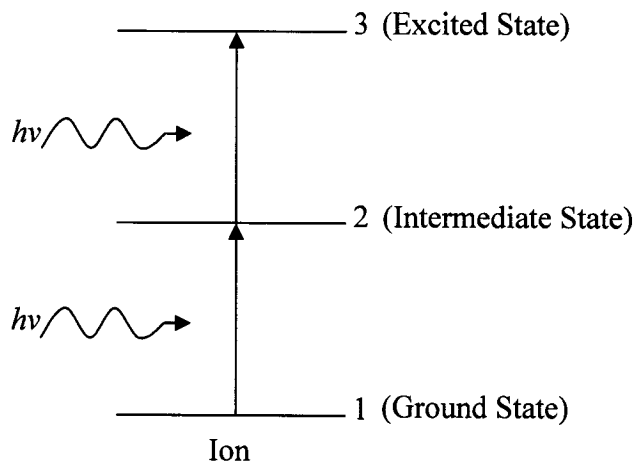

Figure 2.1: Simplified schematic representation of the excited state absorption process.

2.2.2. Upconversion Involving Energy Transfer

Upconversion by energy transfer between excited ions was studied extensively in the mid 1960's [145]. The pioneering contributions by Auzel resulted in the observation of the ATPE effect (addition de photon par transferts d'energie), which was later termed energy transfer upconversion (ETU) [147]. Schemes of upconversion via energy transfer involve two neighboring ions in close proximity and thus are usually the dominant mechanisms in materials with high concentrations of dopant ions. There are two well known upconversion mechanisms, which involve energy transfer. The first, cross-relaxation (CR) usually occurs between identical dopant ions (singly doped systems) and proceeds according to a scheme where the two identical ions in close proximity are both excited from the ground state (1) to an intermediate level (2) by the pump laser (ground state absorption, GSA) and are coupled by a non-radiative process in which one ion returns to the ground state while the other is promoted to the upper level (3) (Figure 2.2).

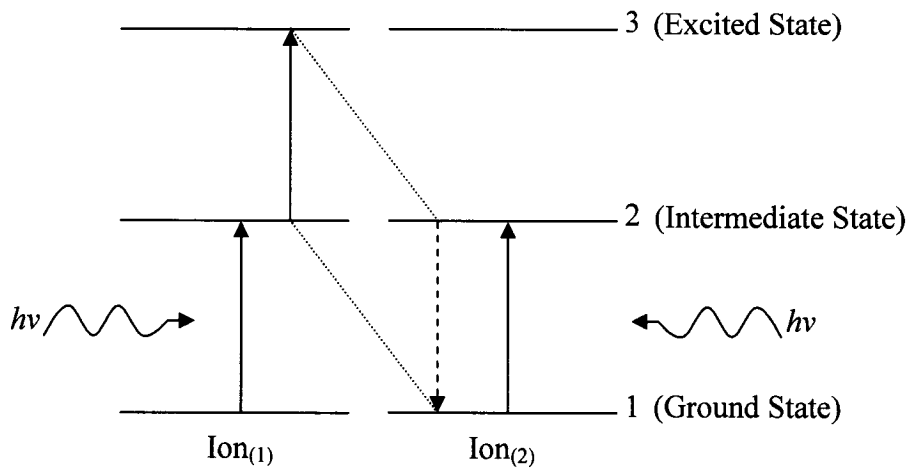

Figure 2.2: Simplified schematic representation of the cross-relaxation upconversion process.

On the other hand ETU, which normally occurs in co-doped materials, involves the successive transfers of energy from a donor ion ($Ion_{(D)}$) to an acceptor ion ($Ion_{(A)}$). Thus, the donor ions are excited to their intermediate states via GSA. An excited donor ion ($Ion_{(D1)}$) transfers its energy to the acceptor thereby promoting it to the intermediate state. Subsequently, a second energy transfer ($Ion_{(D2)}$) promotes the acceptor ion to the emitting state (Figure 2.3).

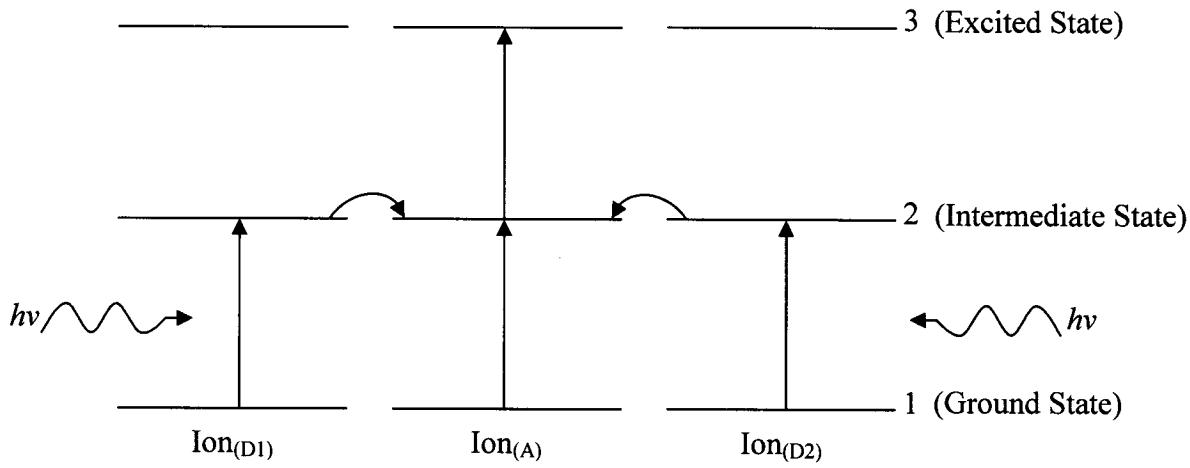

Figure 2.3: Simplified schematic representation of the energy transfer upconversion process.

2.2.3. Photon Avalanche (PA)

Photon avalanche, the least common of the upconversion schemes, is among the most efficient and is produced by absorption from an excited state of the rare earth ion [137]. In this scheme, the pump laser wavelength is resonant with a transition from the intermediate metastable level 2 to a higher excited state 4 and not from the ground level 1 to the intermediate state [136]. The absorption of the pump photons directly populates the higher excited state, during which an energy transfer process is responsible for replenishing the population in the intermediate excited state. The fundamental nature of the avalanche process is that one ion initially in the metastable state produces two ions in this state as a result of photon absorption and ensuing energy transfer. Under appropriate pumping conditions two ions can produce four in the metastable state, four can produce eight, the eight sixteen, etc. and gives rise to an avalanche of ion population in the intermediate state. The avalanche process requires minimum pump intensity and is characterized by a pump threshold, which if not achieved, will result in inefficient upconversion [148].

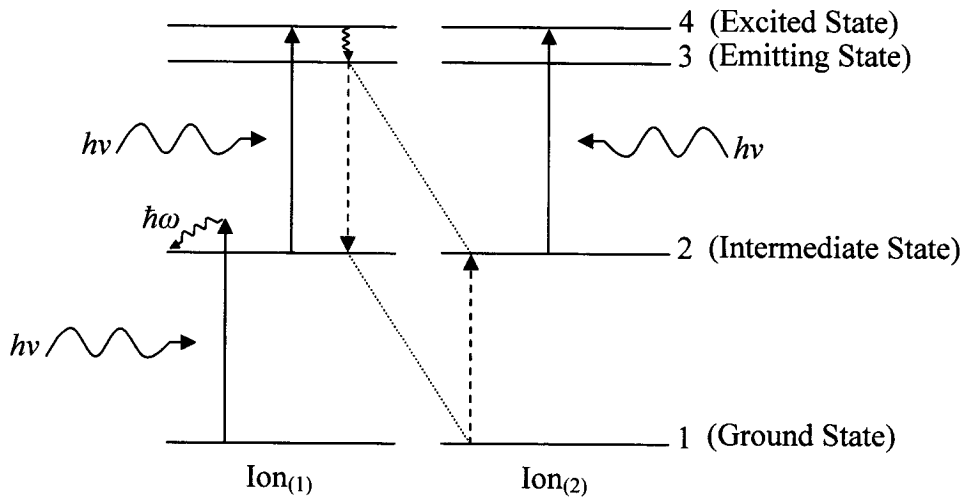

Figure 2.4: Simplified schematic representation of the photon avalanche upconversion process

2.3. Suitability of the Erbium ion (Er^{3+}) for Upconversion

The Er^{3+} ion was the first ion to show upconversion [149] and is the most studied ion in recent times. Practically, the tripositive erbium ion is ideally suited for upconversion. This is because it possesses a favorable electronic energy level scheme, which allows for many radiative transitions to occur (Figure 2.5). However, more apt for upconversion is that the excited states of the Er^{3+} ion posses long lifetimes and thus can be conveniently populated by the absorption of photons in the near infrared (NIR) region (see Figure 2.5). The advent of efficient and inexpensive semiconductor laser diodes in the 1980's and tunable Ti-Sapphire lasers in the 800 – 1100 nm range, has spawned renewed interest in the upconversion properties of Er^{3+} doped materials. In fact, the Er^{3+} ion has been shown to undergo all the different upconversion schemes (ESA, ETU, and PA) depending on which host material the ion has been doped into [137].

There are diverse applications for the upconversion of Er^{3+} doped materials. For example, there are remarkable advances are being made in upconversion lasers. In 1986, the first continuous wave (cw) upconversion laser operating at cryogenic temperatures was demonstrated in $YAlO_3:Er^{3+}$ crystals, producing green laser output [150]. Approximately five years later, Er^{3+} was again the ion of choice for the first demonstration of a room temperature upconversion laser using $BaYb_2F_8:Er^{3+}$ crystals [151], which generated red laser emission. Today, research on upconversion lasers has focused on tunable UV solid-state lasers, following NIR pumping, since current UV lasers are not tunable [152]. Other notable applications include using upconverting materials for low intensity infrared imaging [153], photoluminescent screens for optically

written displays [154], enhancing the response of near-infrared silicon solar cells [155], three color 3D solid-state displays [156] and biological applications [157].

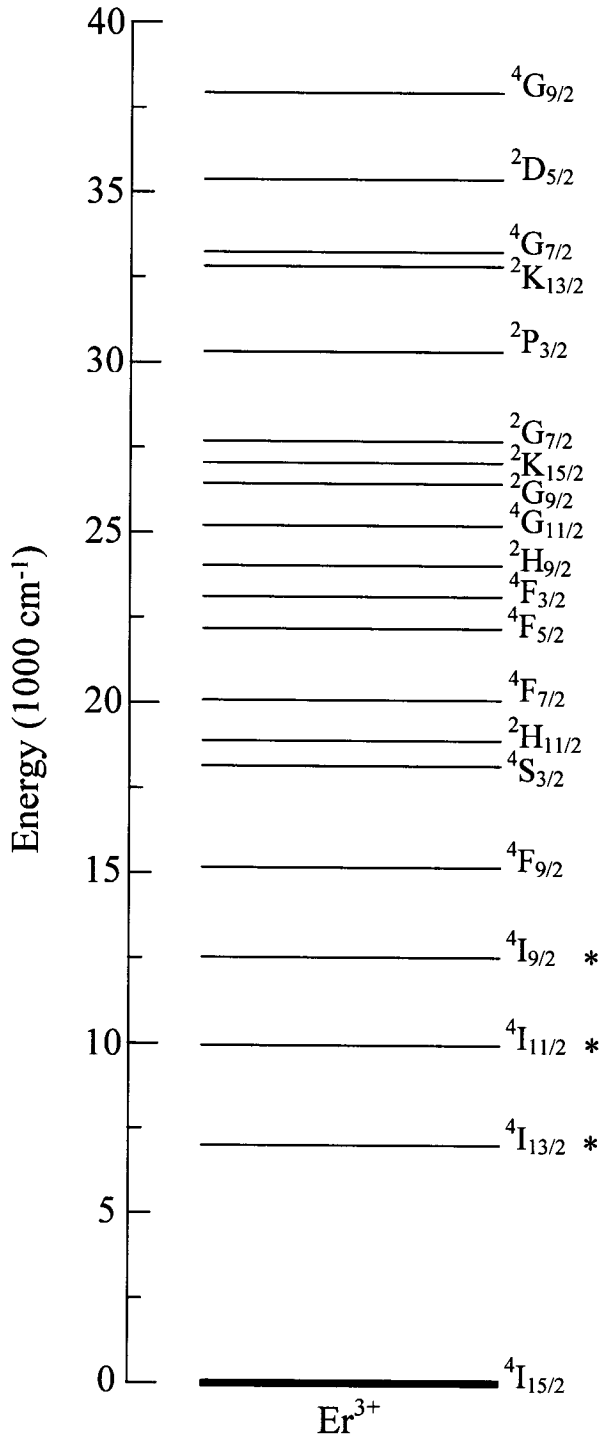

Figure 2.5: Energy level diagram of the tripositive erbium ion. Asterisks (*) point out the NIR excited states, which can act as intermediate states (population reservoirs) in the various upconversion processes

2.4. Upconverting Nanoparticles for Upconversion Based FRET Assays

The medical field has kept a keen eye on the development of nanocrystals as they are ideal for use as luminescent probes in immunoassays. Binding assays (e.g. immunoassays) are currently employed in a wide variety of applications such as medical diagnosis, combinatorial screening for drug-discovery and testing for controlled drugs [158]. Extremely sensitive detection combined with low cost and ease of use is critical for these applications. Normally, these assays are commonly based on well known fluorescence technology. Fluorescent labels are of ultimate importance as they can be detected with very high sensitivity.

The most common method of detecting a binding interaction is to sense the proximity between appropriately labeled binding constituents and a very common method is based on **fluorescence resonance energy transfer** (FRET). In a conventional FRET assay a molecule labeled with a fluorescent dye, which has been excited with high energy blue or UV light, is brought into close proximity with another molecule labeled with a species that absorbs in the wavelength region where the fluorescent dye emits (Figure 2.6). If the fluorescent "donor" and the absorbing "acceptor" are sufficiently close, the emission of the fluorophore is wholly or partially quenched by a radiationless transfer of energy to the absorber. If the absorber is also fluorescent, then its emission is sensitized by the transfer process. The distance over which FRET can operate is very limited, and in practical assays labels must be within a few nanometers for efficient transfer of energy [159].

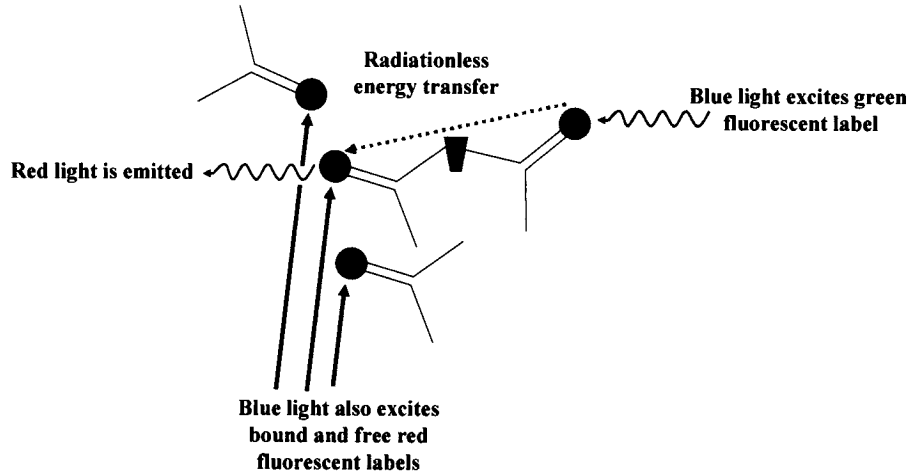

Figure 2.6: Schematic representation of the conventional FRET process.

In the most common assay format a fluorescent FRET acceptor is used and the level of sensitized fluorescence from this is measured when the donor species is selectively excited. Normally, organic dyes are used as the donor and acceptor luminescent species and one of the most common donor – acceptor pair is Fluorescein – Rhodamine [160, 161]. The use of conventional fluorescent labels for FRET-based assays is widespread, but there are significant difficulties that limit the usefulness of this approach. Ideally the donor-acceptor pair used for a FRET-based assay should have the following properties:

(i) The donor should be able to be excited uniquely by radiation that does not excite the acceptor species.

(ii) The donor should not have any long wavelength emission that overlaps the spectral region where the acceptor emission will be detected.

(iii) Neither the donor nor the acceptor species should be readily "quenched" by likely contaminants in the assay medium.

(iv) The donor species should be excited at a wavelength that does not excite any other likely fluorescent contaminants in the assay medium.

It is generally accepted that there are three problems with using dyes as the donor – acceptor pair and thus, the requirements for an ideal FRET pair are not met in most cases. First, the light used to excite the donor often excites fluorescence from other constituents of the sample, giving a background signal. Secondly, donor emission usually will have a weak tail that overlaps the emission region of the acceptor, and hence is detected as if it were acceptor emission. Finally, light that excites the donor usually also excites the acceptor directly, at least to some extent. These problems mean that a small amount of sensitized luminescence (i.e. a low level of bound complex) is difficult to detect against the background signals from bound and unbound material. Taken together these factors seriously limit the dynamic range and sensitivity of FRET-based assays.

Lately, there has been a significant push towards utilizing semiconducting quantum dots (QD) as energy donors in FRET assays [159, 162]. QDs offer several advantages over dye donor species. For instance, they show size dependent and therefore tunable absorption and emission properties due to quantum confinement. The emission from quantum dots is narrow thus will not overlap with the spectral region where the acceptor emission will be detected [159]. However, high energy light would still be required to excite the QD donor leading to high autofluorescence in the assay.

The use of an upconverting donor species for a FRET assay in conjunction with a conventionally luminescent acceptor has the potential to overcome these limitations. It is proposed that nanoparticles of upconverting phosphors be used as donor species for

FRET and thus the limited dynamic range of FRET assays can in principle be overcome by the use of upconverting energy donors (Figure 2.7). Specifically:

(i) An upconverting donor nanoparticle can be excited by NIR radiation that will give no detectable excitation of the conventional acceptor fluorophore.

(ii) The emission spectrum of typical rare earth-doped upconverting phosphors has relatively narrow peaks and thus it is easy to measure sensitized acceptor fluorescence in a spectral region where the upconverting label has no emission.

(iii) If the donor species is an upconverting inorganic nanoparticle it is well protected from quenching by agents such as oxygen and dissolved species in the assay medium. The conventional acceptor is still subject to quenching but this can be minimized by the use of a label with very short fluorescence lifetime.

(iv) NIR radiation will not excite any fluorescence from contaminants in the sample, even if they are present in relatively high concentration. The only source of background is due to reabsorption of emitted donor fluorescence by contaminants, and in practice this is an insignificant effect.

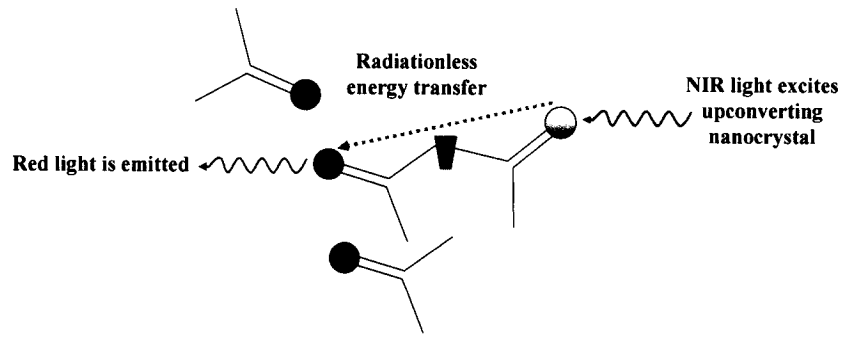

Figure 2.7: Schematic representation of the upconversion FRET process.

The potential advantages of an upconverting donor are clear, but to achieve these it is essential that the label is present as a nanoparticle where all or most of the upconverting label is within a few nanometers of the surface because of the very short range of the FRET process. Surface states can quench emission by other mechanisms, so careful control of interfacial properties is necessary to optimize the luminescence from labels without compromising FRET to bound acceptors.

The erbium ion is ideal for use in an upconverting nanoparticle since it upconverts rather efficiently in a number of hosts lattices, especially when co-doped with Yb^{3+} ions. More importantly, it has an emission spectrum that is extremely well suited for use as a FRET donor (Figure 2.8). The most common acceptor label, Rhodamine, emits in the region of 600 nm, where the Er^{3+} ion has a total absence of emission.

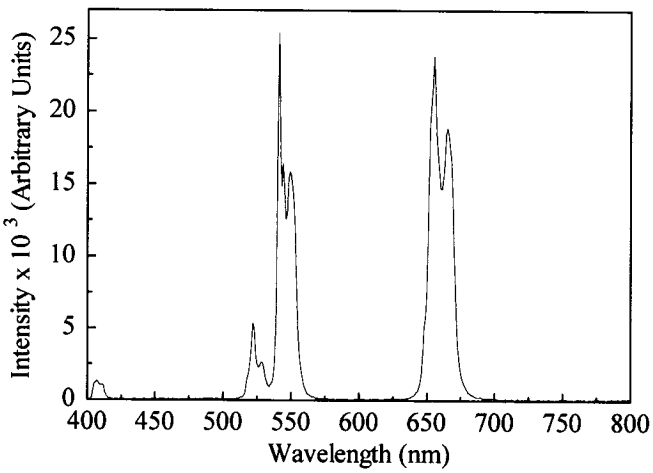

Figure 2.8: Emission spectrum of a typical Er^{3+} doped inorganic material. Note the total absence of emission in the region centered around 600 nm.

Upconverting labels offer a unique set of advantages for the implementation of bioassays based on FRET which is well suited to a variety of commercially important measurement formats. FRET-based assays have the great advantage in that they can

potentially be used in a "mix and measure" (so-called 'homogeneous') assay format, which is well suited to high-throughput measurements. Pharmaceutical companies assay enormous numbers of compounds for potential biological activity based on their ability to bind to target sites such as key receptors, enzymes, etc. FRET-based assays are appropriate to the detection of binding interactions and therefore adapt well to such measurements. So-called "high throughput screening" is a major activity for all large pharmaceutical organizations worldwide. These measurements require extreme sensitivity to keep down the costs of reagents and to allow very small samples to be used and must be robust and easy to implement. In particular, assays must be free of significant interferences from contaminants such as fluorescent components of the sample. Homogeneous assays must be able to operate without the need for extensive washing and separation, so any technology that can operate reliably in the presence of contaminants is likely to be very valuable. Upconverting materials are potentially useful here as they can be excited by infrared light without stimulating the background, so the requirements for purification are minimized. In addition the spectroscopic properties of the labels give rise to extremely low background signals as emission from the upconverting is concentrated into a narrow spectral band which can be detected very efficiently.

2.5. Statement of the Problem

The spectroscopic properties of luminescent rare earth doped nanocrystals have been investigated since the mid-1990's. In the early pioneering works on insulating RE^{3+}-doped nanocrystals, the ion of choice was undoubtedly Eu^{3+}, stemming from its widespread use in the lighting and display industries. The nanomaterial of choice at that time was Y_2O_3 but since then, studies on more complex nanocrystalline oxides, vanadates, titanates, fluorides, tungstates and more have appeared in the literature.

It took more than five years before the first reports on Er^{3+}-doped nanocrystals appeared in the literature. The Er^{3+} dopant ion is ideal for a number of technologically and medically relevant applications due to its versatile luminescent behavior, being able to emit photons with wavelengths ranging from the UV to the NIR. Perhaps its most interesting attribute is its ability to convert NIR photons to the visible, a process known as upconversion. Upconverting Er^{3+}-doped nanocrystals are poised to make a significant breakthrough as labels for binding assays, for example immunoassays, to take the place of currently used organic dyes, which have intrinsic shortcomings that drastically limit their usefulness, but more importantly lower their detection limits.

The phenomenon of upconversion is not a new one and has been studied in macroscopic materials since the middle of the previous century and is fairly well understood. However, in nanometer sized upconverting materials, the spectroscopic properties differ markedly from those of the bulk materials. The upconversion properties of these nanomaterials are dependent on a number of properties such as dopant concentration, particle size, host composition, and sample preparation. Before any commercialization of this or any new technology utilizing upconverting nanoparticles is

possible, it is imperative that we fully comprehend and elucidate the properties of upconversion at the nanoscale.

The research presented in this thesis will permit us to illuminate some of the key fundamental traits of the luminescence behavior in erbium doped nanocrystals, with a heavy slant on the upconversion properties. In particular, we investigate how changing various parameters such as dopant concentration(s), host material, and preparation techniques will affect the mechanisms responsible for populating the emitting states in the upconversion of Er^{3+}-doped nanocrystals.

CHAPTER 3

3. Theory

The subject of this chapter has been comprehensively dealt with by Brian G. Wybourne [163], Stefan Hüfner [164], and Baldassare Di Bartolo [165], amongst others. However, in this chapter, we will endeavor to provide the reader with only the basic theoretical aspects pertinent to this thesis so that it may be read without continual reference to the key textbooks in the field of optical spectroscopy.

3.1. Hamiltonian of the Free Ion

The trivalent rare earth ions in solids have the $4f^{N-1}5s^25p^6$ electronic configuration, where N ranges across the rare earth series from 1 for Ce^{3+} to 14 (closed shell) for Lu^{3+}. The optical transitions take place within the unfilled $4f$ shell, which is essentially shielded from the crystal field by the outer, though less energetic $5s$ and $5p$ shells, whose radial extension is several times that of the $4f$ and thus, the $4f$ electrons are only weakly perturbed by the surrounding ligands. The resulting optical spectra are composed of a series of sharp lines closely resembling the free ion spectra with the relative positions of the $4f$ energy levels for RE^{3+}-doped materials being virtually unchanged from those of the free ion. The shift in the spectra following doping into a crystal is typically less than one percent. This justifies the weak crystal field approximation where the electrostatic interaction between the positively charged rare earth ion and the negatively charged ligands is treated as a perturbation to the free ion Hamiltonian. In the framework of the perturbation theory, one obtains approximate solutions from strong interactions to weaker ones, in consecutive order. Each subsequent interaction is treated as a perturbation superposed on the preceding stronger interaction.

Thus, the different atomic interactions are arranged in the order of transitions from higher to lower energy.

All the electronic shells, except the $4f$ shell, are spherically symmetric and therefore do not contribute significantly to the relative positions of the $4f$ energy levels. Let us consider the Hamiltonian for the $4f$ electrons in the free ion, H_F:

$$H_F = H_0 + H_{ee} + H_{SL} \qquad 3.1.1$$

H_0 represents the substantial part of the interactions and is expressed as:

$$H_0 = -\sum_{i=1}^{N} \frac{h^2 \nabla_i^2}{8\pi^2 m} - \sum_{i=1}^{N} \frac{Ze^2}{r_i} \qquad 3.1.2$$

where the first term describes the electron kinetics motion, and the second illustrates the potential energy determined by Coulomb (electrostatic) interaction between the i^{th} electron and the nucleus while r_i is the distance between the electron and the nucleus. Furthermore, N is the number of $4f$ electrons, m is the mass of the electron, $h^2\nabla^2$ is the square of the momentum operator for the i^{th} electron, and Ze^2 is the screened charge of the nucleus.

H_{ee} is the Coulomb interaction between electrons and is given by:

$$H_{ee} = \sum_{i<j}^{N} \frac{e^2}{r_{ij}} \qquad 3.1.3$$

where the interaction takes place between the i^{th} and j^{th} electrons and r_{ij} is the distance between these electrons. This interaction leads to term formation.

H_{SL} is the spin-orbit interaction, the interaction between the orbital and spin momentum. The subscripts S and L represent the total spin quantum number and the

whole atom orbital quantum number, respectively. This interaction corresponds to the multiplet level formation:

$$H_{SL} = \sum_{i=1}^{N} \zeta(r_i) \cdot s_i l_i \qquad 3.1.4$$

where s_i and l_i are the spin and orbital angular momentum, respectively, of the i^{th} electron and $\zeta(r_i)$ is the spin-orbit coupling function given by:

$$\zeta(r_i) = \frac{\hbar^2}{2m^2c^2r_i} \frac{dU(r_i)}{dr_i} \qquad 3.1.5$$

where $U(r_i)$ is the potential in which the electron I is moving.

In atomic theory, there are two limiting cases for the relative size of these two interactions. In the *Russell-Saunders coupling scheme* ($H_{ee} >> H_{SL}$), the spin-orbit interaction is only a small perturbation on the energy level structure, which has been determined from H_{ee}. This holds true for the light elements and for a long time, was also assumed to hold true for the rare earths. In the second limiting case, the Coulomb interaction is small compared to the spin-orbit interaction ($H_{ee} << H_{SL}$). This case is referred to as the *j-j coupling scheme*. Both limiting cases are relatively easy to deal with theoretically and can be solved by perturbation theory. However in the rare earths, both limiting cases are of approximately equal magnitude and the energy level calculations are more mathematically involved resulting in a situation called the *intermediate coupling scheme*.

3.1.1. Electrostatic (Coulomb) Interaction

As we stated earlier, the largest contributor to the free ion Hamiltonian is the electrostatic interaction. This interaction splits the energy level of the $4f$ configuration into different LS terms. The resultant wavefunctions are characterized by the quantum numbers L, S, M_L, and M_S. The electrostatic interaction matrix elements of the $4f$ configuration have the form:

$$\left\langle f^N SLM_S M_L \left| H_{ee} \right| f^N S'L'M'_S M'_L \right\rangle \qquad 3.1.6$$

or

$$\left\langle f^N SLM_S M_L \left| e^2/r_{ij} \right| f^N S'L'M'_S M'_L \right\rangle \qquad 3.1.7$$

The operator e^2/r_{ij} can be developed in Legendre polynomials as:

$$\frac{1}{r_{ij}} = \sum_k \left(\frac{r_<^k}{r_>^{k+1}} \right) P_k(\cos\omega_{ij}) \qquad 3.1.8$$

where $r_<$ and $r_>$ are the smaller and larger of the radii of the two electrons (i and j), and

$$P_k(\cos\omega_{ij}) = \frac{4\pi}{2k+1} \sum Y_{kq}^*(\vartheta i, \varphi_i) Y_{kq}(\vartheta_j, \varphi_j) \qquad 3.1.9$$

where Y_{kq} are the spherical harmonics. The tensor operator, C_{kq} can be defined as:

$$C_{kq} = \left(\frac{4\pi}{2k+1} \right)^{1/2} Y_{kq} \qquad 3.1.10$$

$$P_k(\cos\omega_{ij}) = \sum_q (-i)^q \left(C_{k-q}(i) \cdot C_{kq}(j) \right) = C_k(i) \bullet C_k(j) \qquad 3.1.11$$

The electrostatic interaction is an electric interaction and therefore does not act on the spin. As a result, S' and M'_S can be displaced by S and M, respectively. The Coulomb matrix element is:

$$\left\langle f^N SLM_S M_L \left| e^2/r_{ij} \right| f^N SL'M_S M'_L \right\rangle = \sum_k f_k(r) \left\langle f^N SLM_S M_L \left| C_k(i) \bullet C_k(j) \right| f^N SL'M_S M'_L \right\rangle \quad 3.1.12$$

In principle, the energy levels of the intra-4*f* transitions due to the Coulomb interaction can be expressed in terms of Slater radial integrals, F^k:

$$f_k(r) = F^k = e^2 \int_0^\infty \frac{r_<^k}{r_>^{k+1}} R_{4f}^2(r_i) R_{4f}^2(r_j) dr_i dr_j \quad 3.1.13$$

$$\frac{r_<}{r_>} = \frac{r_i}{r_j} \text{ if } r_i < r_j \text{ and } \frac{r_j}{r_i} \text{ if } r_i > r_j \quad 3.1.14$$

For the $4f^N$ configuration, only F^0, F^2, F^4, and F^6 appear in the calculation and the F^0 term contributes equally to all *LS* states of the same $4f^N$ configuration and so can be ignored. The matrix elements of the Coulomb interaction are given in terms of F^k while the same interaction for the f^N series is given in terms of a new parameter, E^k, the Racah parameter [166]. Nielson and Koster give for the matrix elements of the Coulomb interaction [166]:

$$\langle \alpha' L'S' | H_{ee} | \alpha LS \rangle = \delta_{LL'} \delta_{SS'} \sum_k g_k(\alpha', \alpha, L, S) E^k \quad 3.1.15$$

and the coefficients $g_k(\alpha', \alpha, L, S)$ are given for each of the f^N states. The relation of E^k to F^k has been detailed in a number of works (see for example [167]).

Instead of writing the Coulombic matrix elements in terms of the parameters F_k (or F^k), Racah found it more convenient to define new parameters. Thus, when the matrix elements of Racah are used to calculate the matrix elements of electrostatic interaction, operators are constructed such that they have simple transformation properties with

respect to the symmetry groups used to classify states. In this case, the Coulomb energy becomes:

$$E = \sum_{k=0}^{3} e_k E^k \qquad 3.1.16$$

where the e_k's represent the angular parts of the new operators and the E_k's are the linear combination of the F_k's.

3.1.2. Spin-Orbit Interaction

The second interaction of reasonable magnitude in the free ion is the spin-orbit coupling and in the rare earth series, this interaction is quite strong. As a result, it is convenient to perform the calculation in a set of basis functions in which the Coulomb and spin-orbit Hamiltonian are diagonal. The set of functions that achieves this is the total angular momentum function $|JM_J>$. The total angular momentum operator is given by:

$$\vec{J} = \vec{L} + \vec{S} \qquad 3.1.17$$

Since both the spin-orbit and Coulomb interaction commute with the total angular momentum, the wavefunctions may be characterized by the eigenvalues of $\vec{J}^2$ and J_Z. As a result, one can write Ψ_{JM} or $|JM>$ for the wavefunctions with:

$$\vec{J}^2 |JM\rangle = J(J+1)|JM\rangle \qquad 3.1.18$$

and

$$J_Z |JM\rangle = M|JM\rangle \qquad 3.1.19$$

The values of J are restricted to:

$$|L-S| \le J \le |L+S| \qquad 3.1.20$$

Thus, the matrix elements may be obtained using the following

$$\langle J', M', L', S' | H_{ee} + H_{SL} | J, M, L, S \rangle = \delta_{JJ'} \delta_{MM'} \qquad 3.1.21$$

The matrix elements of the spin-orbit interaction may also be evaluated using tensor formalism. The matrix elements of the spin-orbit coupling are responsible for the mixing of states with identical J but different L and S. The diagonal matrix elements are obtained using the formula:

$$\left(f^N \ldots | H_{SL} | f^N \ldots\right) = \zeta\left(\frac{\lambda}{2}\right)\left[J(J+1) - L(L+1) - S(S+1)\right] \qquad 3.1.22$$

where the value of the spin-orbit coupling parameter, ζ, is normally determined by comparison with measurement.

3.2. The Crystal Field Effect

When the rare earth ions are doped into a crystalline material, the effect of the crystal field, the interaction between the rare earth ion and the surroundings in the crystalline structure, must be taken into account. The behavior of ions in crystals will obviously be different from the free ion and this difference can be taken into account by introducing an additional Hamiltonian (H_{CF}), which describes the interaction of the ion with the crystal field. Thus, the Hamiltonian of the rare earth in a crystal can be written as:

$$H = H_F + H_{CF} \tag{3.2.1}$$

$$H_{CF} = -\sum \int \frac{e_i \rho(R)}{|R - r_i|} d\tau \tag{3.2.2}$$

where ρ(R) is the charge density function. The relative magnitude of the crystal field splitting (H_{CF}) compared to the Coulomb interaction (H_{ee}) and the spin-orbit interaction (H_{SL}) determines the type of ion behavior. There are three types of ion behavior in crystal fields: weak, medium, and strong crystal field. For the rare earths ($4f$) ions, the weak crystal field applies. For this type of behavior, the order of increasing splitting is $H_{ee} > H_{SL} > H_{CF}$ (see Figure 3.1).

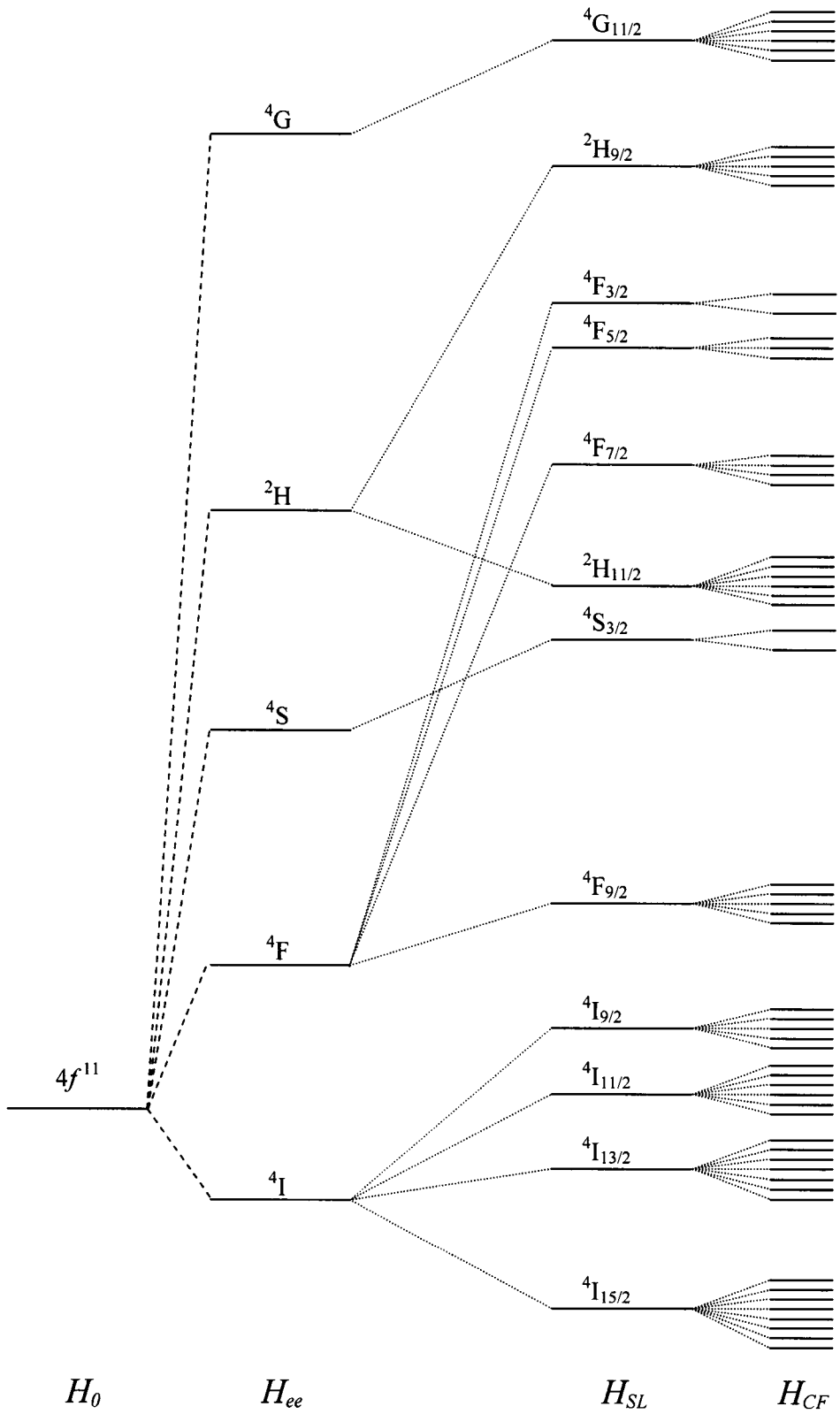

Figure 3.1: Effect of inclusion of successive terms in the atomic Hamiltonian for the $4f^{11}$ configuration (Er^{3+}).

3.3. Selection Rules

In this section, we evaluate the mechanisms responsible for a particular transition between two crystal field levels when the rare earth ion is doped in a crystalline lattice. The perturbation responsible for optical transitions in an RE^{3+} ion is the interaction between the electrons in the $4f$ shell and the electromagnetic field. Generally speaking, two radiative processes are possible when these electrons interact with electromagnetic radiation. The first is absorption, where the ground state electronic distribution is rearranged to a higher energy state. The second radiative process is emission, where an ion in a higher energy state emits a photon to return to a lower energy state. The presence of the electromagnetic field is essential in order to produce a coupling between the various stationary states that can result in transitions from one state to another. The interaction Hamiltonian between the electron(s) in the system and the radiation field contains two terms. One is responsible for the electric dipole interaction while the other is responsible for the magnetic dipole interaction.

Electric dipole transitions require a change in parity between the initial and final states. As a result, they are forbidden between $4f^N$ states of the rare earths. However, if the ion resides in a non-centrosymmetric static or dynamic crystal field, the odd harmonics in the expansion of the crystalline potential can introduce a small admixture of the odd parity states from a higher configuration, such as $4f^{N-1}5d$, into the original $4f^N$ states and as a result, the electric dipole transitions become allowed.

Whether or not a transition between states a and b occurs, and its strength, is dependent upon the value of the square of the matrix element $\langle b|\vec{\mu}\cdot\hat{\varepsilon}|a\rangle$ where $\vec{\mu}\cdot\hat{\varepsilon}$ is

the appropriate operator. For electric dipole transitions, the above operator is replaced by $\vec{\mu}_e \cdot \hat{\varepsilon}_E$ where:

$$\vec{\mu}_e = \sum_i e\vec{r}_i \qquad 3.3.1$$

We note that $\hat{\varepsilon}_E$ is the unit electric polarization vector parallel to the **E** field of the electromagnetic radiation and e is the magnitude of the electronic charge.

In the case of the magnetic dipole transitions, the appropriate operator is $\vec{\mu}_m \cdot \hat{\varepsilon}_B$ where:

$$\vec{\mu}_m = \frac{e\hbar}{2mc}(L + 2S) \qquad 3.3.2$$

Again, it should be noted that $\hat{\varepsilon}_B$ are the unit vectors along the direction of the magnetic field **B**, m is the electronic mass, L is the total angular momentum and S is the total spin angular momentum.

Selection rules are determined from group theory considerations where the components of the electric and magnetic field vectors transform according to definite representation of the point group of the local rare earth environment. A particular transition is either allowed or forbidden according to whether the irreducible representation of the final state is or is not contained in the product of the initial state representation and the representation of the appropriate component of **E** or **B**. A set of selection rules can then be written for both electric and magnetic dipole transitions.

For electric dipole transitions, the following rules apply for $4f$ electrons:

$\Delta l = \pm 1$ (Laporte's Rule)
$\Delta S = 0$
$|\Delta L| \leq 2l$, i.e. $|\Delta L| \leq 6$
$|\Delta J| \leq 2l$, i.e. $|\Delta J| \leq 6$

Laporte's selection rule states that the only allowed transitions are those that are accompanied by a change in parity ($\Delta l = \pm 1$). Thus, according to Laporte's selection rule, $f \leftrightarrow f$ transitions must be forbidden since $l = 3$ for both the initial and final states. Consequently, radiative transitions should not be observed in rare earth doped materials.

It was noted by Van Vleck [41] that electric dipole transitions occur because the $4f^N$ states have admixtures of $4f^{N-1}nl$ (where in most cases, nl is $5d$). The $4f^{N-1}nl$ configuration was chosen such that it has opposite parity from $4f^N$ and thus, admixing of the $4f^{N-1}nl$ into the $4f^N$ wavefunctions is accomplished by interactions that have odd parity. The two mechanisms responsible for the admixing are odd parity crystal field components and crystal vibrations of odd symmetry. The admixing of the two wavefunctions allow for electric dipole transitions to occur in the case where the rare earth ion is not located on an inversion center. In a crystalline lattice where an inversion center is present, the odd crystal field components are zero. However, Van Vleck recognized that crystal field fluctuations due to vibrational motion of the lattice producing non-totally symmetric vibrations may induce electric dipole transitions. Transitions of this type are often referred to as forced or induced electric dipole transitions. Also, since S and L are no longer good quantum numbers, only the selection rule on J will remain valid. An additional rule is implemented in this case:

$$\text{when } J_a \text{ or } J_b = 0 \text{ then } |\Delta J| = 2, 4, 6$$

This rule remains valid as long as the crystal field is not strong enough to substantially admix the J-states.

In the case of transitions induced by magnetic dipole interactions, the selection rules are as follows:

$$\Delta l = 0$$
$$\Delta S = 0$$
$$\Delta L = 0$$
$$\Delta J = 0, \pm 1 \quad \text{with } 0 \leftrightarrow 0 \text{ forbidden}$$

Magnetic dipole transitions with the $4f^N$ configuration, are allowed by Laporte's rule since these transitions occur between states of the same parity.

A final comment on selection rules with regard to the symmetry of the local rare earth environment must be made. For point groups of very low symmetry (such as C_2, C_s, or C_1), all $f \leftrightarrow f$ transitions are allowed. The only consideration will then be the relative magnitude of the contribution from each dipole process.

3.4. Intensity Calculation and the Judd-Ofelt Theory

The nature of rare earth transitions by order of magnitude estimations was elucidated by Van Vleck in the early 1900's [41]. He proposed that only the electric dipole, magnetic dipole, and electric-quadrupole transitions were strong enough to account for the measured oscillator strengths. Sometime later, Broer et al. [168] found a minute error in the values of Van Vleck's calculations and determined that electric-quadrupole transitions would be too small to play any significant role in rare earth spectra. Since that time, only the electric and magnetic dipole transitions were considered. In 1962, the next major development in the spectroscopy of the rare earth ions was achieved, the development of the Judd-Ofelt theory of the intensities of transitions. The solution to what Van Vleck referred to as the "rare earth puzzle" was supplied simultaneously and entirely independently by Brian R. Judd [169] and George S. Ofelt [170]. The results of both studies were published in August of 1962 with neither author aware of the results of the other. Judd's starting point was the intensities of the absorption lines while Ofelt, explained the intensity of the emission lines. However different their methodology, the end results were the same.

In this section, we give a brief explanation of the major relationships obtained by Judd and Ofelt. However, the Judd-Ofelt theory makes use of formalism of tensor operators, *n-j* symbols, and reduced matrix elements. We refer the reader to the original papers by Racah [42, 171-173] and books by Edmonds [174], Judd [167], and Wybourne [163] for a more detailed account of these subjects.

The spontaneous transition probability (per unit time, s^{-1}) due to dipole radiation may be expressed as:

$$A(i,j) = \frac{64\pi^4\sigma^3}{3h}\left|\langle i|D|j\rangle\right|^2 \qquad 3.4.1$$

where i and j denote the initial and final states, respectively, σ (cm^{-1}) is the energy difference between the initial and final states and D is the dipole operator.

Broer et al. [168] defined the oscillator strength as:

$$f_{ij} = \frac{Amc}{8\pi^2\sigma^2 e^2} \qquad 3.4.2$$

If we substitute equation 3.4.1, the oscillator can further be defined as:

$$f_{ij} = \frac{8\pi^2 m\, c\, \sigma}{3he^2}\left|\langle i|D|j\rangle\right|^2 \qquad 3.4.3$$

The matrix elements of D are summed over all components of the initial state, i, and consequently, the factor $2J+1$ must be added resulting in:

$$f_{calculated} = \frac{8\pi^2 m\, c\, \sigma}{3he^2(2J+1)}\left[\chi_{ed}\overline{F}^2 + \chi_{md}\overline{M}^2\right] \qquad 3.4.4$$

where $\overline{F}^2$ and $\overline{M}^2$ represent the matrix elements of the electric and magnetic dipole operators, respectively and J is the total angular momentum quantum number of the ground state. χ_{ed} and χ_{md} are the electric and magnetic (Lorentz) field corrections for the refractive index, n, of the material and are equal to:

$$\chi_{ed} = \frac{n(n^2+2)^2}{9} \quad \text{and} \quad \chi_{md} = n \qquad 3.4.5$$

For electric and magnetic dipole transitions, the respective dipole operators are given by:

$$\overline{F}^2 = e^2 \sum_{\lambda=2,4,6} \Omega_\lambda \left(\psi J\right\| U^{(\lambda)} \left\|\psi' J'\right)^2 \qquad 3.4.6$$

and

$$\overline{M}^2 = \frac{e^2}{4m^2c^2}\left(\psi J\right\| L + 2S \left\|\psi' J'\right)^2 \qquad 3.4.7$$

3.4.1. Induced Electric Dipole Transitions

Judd showed that the oscillator strength for an induced electric dipole transition from level ψJ to level $\psi' J'$, is related to the reduced matrix elements of unit tensor operators, $U^{(\lambda)}$ ($\lambda = 2, 4, 6$), as:

$$f_{ed} = \sum_{\lambda=2,4,6} T_\lambda \nu \left(\psi J \| U^{(\lambda)} \| \psi' J'\right)^2 \qquad 3.4.8$$

where ν is mean frequency of the transition $\psi J \rightarrow \psi' J'$, $U^{(\lambda)}$ is a unit tensor operator of rank λ, and T_λ are three parameters that can be calculated from experimental data. These parameters (T_2, T_4, T_6) contain the radial part of the $4f^N$ wavefunctions, the wavefunctions of perturbing configurations such as $4f^{N-1}5d$ and the interaction between the central ion and the local environment.

Judd gives the equation for T_λ as:

$$T_\lambda = \frac{8\pi^2 m}{3h(2J+1)}\left[\frac{(n^2+2)^2}{9n}\right](2\lambda+1)\sum_t (2t+1) B_t I^2(t,\lambda) \qquad 3.4.9$$

Defining: $\Omega_\lambda = (2\lambda+1)\sum_t (2t+1) B_t I^2(t,\lambda)$, which denotes the Judd-Ofelt parameters.

$$T_\lambda = \frac{8\pi^2 m}{3h(2J+1)}\left[\frac{(n^2+2)^2}{9n}\right]\Omega_\lambda \qquad 3.4.10$$

Therefore, we obtain:

$$f_{ed} = \frac{8\pi^2 m \nu}{3h(2J+1)}\left[\frac{(n^2+2)^2}{9n}\right]\sum_{\lambda=2,4,6}\Omega_\lambda \left(\psi J \| U^{(\lambda)} \| \psi' J'\right)^2 \qquad 3.4.11$$

Substitution of $\nu = c\sigma$ into the above equation yields:

$$f_{ed} = \frac{8\pi^2 m c \sigma}{3h(2J+1)}\left[\frac{(n^2+2)^2}{9n}\right]\sum_{\lambda=2,4,6}\Omega_\lambda \left(\psi J \| U^{(\lambda)} \| \psi' J'\right)^2 \qquad 3.4.12$$

In the *SL* basis, the dependence of the matrix elements on equation 3.4.12 can be separated out using the relationship:

$$\left\langle f^N \alpha SLJ \middle\| U^{(\lambda)} \middle\| f^N \alpha' S'L'J' \right\rangle = \delta(S,S')(-1)^{S+L'+J+\lambda} \times \left\{(2J+1)(2J'+1)\right\}^{1/2} \begin{Bmatrix} J & J' & \lambda \\ L' & L & S \end{Bmatrix} \left\langle f^N \alpha SLJ \middle\| U^{(\lambda)} \middle\| f^N \alpha' SL'J' \right\rangle \quad 3.4.13$$

The reduced matrix elements $\left\langle f^N \alpha SLJ \middle\| U^{(\lambda)} \middle\| f^N \alpha' SL'J' \right\rangle$ have been tabulated by Nielson and Koster [166]. The matrix elements of $U^{(\lambda)}$ have been computed for various transitions of the rare earth ions in aqueous solution and are reported by Carnall and co-workers [175-178]. It is possible to use these matrix elements since they are virtually independent of the host.

3.4.2. Magnetic Dipole Transitions

The oscillator strength for a magnetic dipole transition from level ψJ to level $\psi' J'$ is given by Broer et al. as. [168]:

$$f_{md} = \frac{8\pi^2 m c \sigma}{3he^2(2J+1)} n S(\psi J, \psi' J') \quad 3.4.14$$

where S is the line strength whose square root is defined as:

$$S^{1/2}(\psi J, \psi' J') = \frac{-e}{2mc} \left\langle \psi J \middle\| L + 2S \middle\| \psi' J' \right\rangle \quad 3.4.15$$

For magnetic dipole transitions, the only non-vanishing matrix elements are those for which $\Delta J = 0, \pm 1$, and which are diagonal in α, S, and L. The three cases, which are permitted by the selection rules were evaluated by using the relationships:

(i) $J = J'$

$$\left\langle \alpha SLJ \| \, L + 2S \| \alpha SLJ' \right\rangle = g\hbar\{J(J+1)(2J+1)\}^{1/2} \qquad 3.4.16$$

$$\text{where } g = 1 + \frac{J(J+1)+S(S+1)-L(L+1)}{2J(J+1)} \qquad 3.4.17$$

(ii) $J' = J$ -1

$$\left\langle \alpha SLJ \| \, L + 2S \| \alpha SLJ - 1 \right\rangle = \hbar\left\{\frac{(S+L+J+1)(S+L+1-J)(J+S-L)(J+L-S)}{4J}\right\}^{1/2} \qquad 3.4.18$$

(iii) $J' = J+1$

$$\left\langle \alpha SLJ \| \, L + 2S \| \alpha SLJ + 1 \right\rangle = \hbar\left\{\frac{(S+L+J+2)(S+J+1-L)(L+J+1-S)(S+L-J)}{4(J+1)}\right\}^{1/2} \qquad 3.4.19$$

The line strength (or oscillator strength) may be calculated from the measured absorption spectrum:

$$f_{measured} = \left[\frac{9n}{(n^2+2)^2}\right]\frac{4mc\varepsilon_0}{Ne^2}\int \mu(\nu)\, d\nu \qquad 3.4.20$$

where N is the number of ions per unit volume (ions/cm^3) and $\int \mu(\nu)\, d\nu$ is the integrated absorption co-efficient of the transition between J and J'.

The calculation of the Judd-Ofelt parameters is straightforward: Ω_2, Ω_4 and Ω_6 are fitted via equation 3.4.4 to the measured values from equation 3.4.20 and minimizing the rms deviation [179]:

$$\delta_{rms} = \sqrt{\frac{\sum_{i=1}^{p}(f_{measured} - f_{calculated})^2}{p-3}} \qquad 3.4.21$$

where p is the number of absorption bands used and 3 reflects the number of fitted parameters.

3.4.3. Fluorescence Parameters for RE^{3+} Doped Materials

The Judd-Ofelt parameters as the key results of the absorption measurements are used to predict the radiative emission properties of a given rare earth doped material. The transition probability (A) between the individual components of J and J' for the emission process is given by:

$$A(\psi J, \psi' J') = \frac{64\pi^4 \sigma^3}{3h(2J+1)}\left[\chi_{ed}\overline{F}^2 + \chi_{md}\overline{M}^2\right] \qquad 3.4.22$$

where:

$$\chi_{ed} = \frac{n(n^2+2)^2}{9}; \chi_{md} = n^3 \qquad 3.4.23$$

and σ (cm^{-1}) is the energy gap between the excited state J and ground state J'.

The total radiative relaxation rate is given by:

$$A_T = (\psi J) = \sum_{\psi' J'} A(\psi J, \psi' J') \qquad 3.4.24$$

where the sums runs over all states lower in energy than the emitting state. Two other valuable parameters that can be calculated from the transition probability and the total radiative relaxation are the branching ratio (β_R) and the radiative lifetime (τ_R). The radiative branching ratio is given by the formula:

$$\beta_R(\psi J, \psi' J') = \frac{A(\psi J, \psi' J')}{A(\psi J)} \qquad 3.4.25$$

and the radiative lifetime is:

$$\tau_R(\psi J) = \frac{1}{A_T(\psi J)} \qquad 3.4.26$$

3.5. Energy Transfer

There are two fundamentally different mechanisms of energy transfer. The first is radiative transfer through the emission of the sensitizer and re-absorption by the activator. The second, is non-radiative transfer associated with resonance between the absorber (sensitizer) and emitter (activator). A necessity in energy transfer is a sizeable spectral overlap of the emission region of the sensitizer and the absorption region of the activator as well as an appreciable absorption intensity of the activator.

In a two-atom system, i.e. a donor-acceptor pair situation, is illustrated in Figure 3.2 where each atom is considered hydrogen like. The interaction Hamiltonian (H_{AB}) is paramount in evaluating the energy transfer probability and is given by:

$$\begin{aligned} H_{AB} &= \frac{z_a z_b e^2}{R} + \frac{e^2}{r_{12}} - \frac{z_a e^2}{r_{a2}} - \frac{z_b e^2}{r_{b1}} \\ &= \frac{z_a z_b e^2}{R} + \frac{e^2}{r_{12}} - \frac{z_a e^2}{\left|\vec{R} + \vec{r}_{b2}\right|} - \frac{z_b e^2}{\left|-\vec{R} + \vec{r}_{a1}\right|} \end{aligned} \qquad 3.5.1$$

Consider a transition from an initial state $|a'b\rangle$ to a final state $|ab'\rangle$ of the two-atom system. The matrix element is expressed as $\langle a'b|H_{AB}|ab'\rangle$ and is simplified as:

$$\langle a'b|H_{AB}|ab'\rangle = \left\langle a'(1)b(2)\left|\frac{e^2}{r_{12}}\right|a(1)b'(2)\right\rangle - \left\langle a'(1)b(2)\left|\frac{e^2}{r_{12}}\right|b'(1)a(2)\right\rangle \qquad 3.5.2$$

where $|a\rangle$ and $|a'\rangle$ are the ground state and excited state wavefunctions of atom *A*, respectively, and $|b\rangle$ and $|b'\rangle$ are the ground state and excited state wavefunctions of atom *B*, respectively while the numbers 1 and 2 identify the electron of concern. The first term in equation 3.5.2, $\left\langle a'(1)b(2)\left|\frac{e^2}{r_{12}}\right|a(1)b'(2)\right\rangle$, called the direct term, is used to develop

the multipolar interaction scheme, while the second term, $\left\langle a'(1)b(2)\left|\frac{e^2}{r_{12}}\right|b'(1)a(2)\right\rangle$, is called exchange term and takes into account the overlap of the wavefunctions.

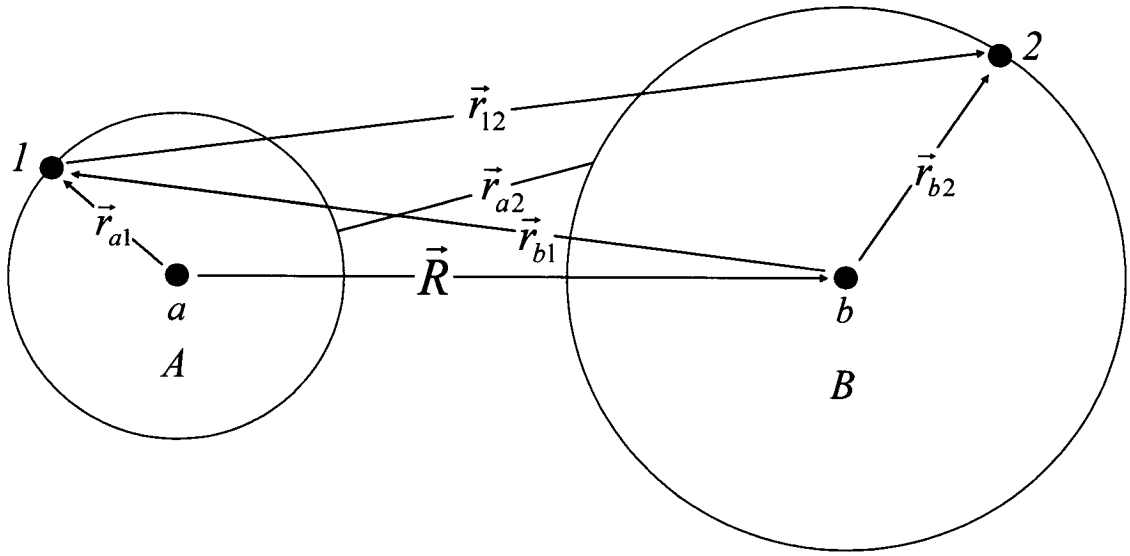

Figure 3.2: Representation of the Coulomb interaction between two atoms (*A* and *B*) in a resonant energy transfer process.

In the case of the interaction between two rare earth atoms in fixed positions in a solid, it is no longer a hydrogen type system, but a many electron system. The relevant energy transfer (or interaction) Hamiltonian for rare earth ions is given by:

$$H_{AB} = \sum_{i,j} \frac{e^2}{r_{ij}} = \frac{e^2}{\left|\vec{R} + \vec{r}_{bj} - \vec{r}_{ai}\right|} \qquad 3.5.3$$

where the sum $\sum_{i,j}$ is over all the electrons of the unfilled $4f$ shells. Detailed calculations of the matrix elements of the Hamiltonian H_{AB} for both the multipolar and exchange interactions are found in the works of Di Bartolo [180, 181].

Dexter [182] considered that energy transfer from a donor (or sensitizer) to an acceptor (or activator) may occur if the energy difference between the ground and excited states of the donor is equal to that of the acceptor and there exists a suitable interaction between both systems. Thus, energy transfer occurs when the resonance condition is satisfied. Of course, non-resonant energy transfer may also take place with the assistance of phonons provided that the energy gap between the ground and excited states is not too large and thus can be mediated by phonons. Dexter derived the energy transfer rate (W_{AB}) between a donor and an acceptor and arrived at:

$$W_{AB} = \frac{2\pi}{\hbar}\left|\langle a'b|H_{AB}|ab'\rangle\right|^2 \int g_A(E)\, g_B(E)\, dE \qquad 3.5.4$$

where atoms A and B are the donor and acceptor atoms, respectively and the factors $g_A(E)$ and $g_B(E)$ represent the normalized shape of the donor emission and acceptor absorption spectra, respectively. Figure 3.3 shows the spectral overlap between the donor emission and the acceptor absorption bands. The matrix elements in equation 3.5.4 can be expressed as a function of the distance between donor and acceptor such that the energy transfer probability depends on the distance between the donor and acceptor. The difference varies with the interaction type. For exchange interaction, it is exponential while for multipolar interactions, it is of the type R^{-n}.

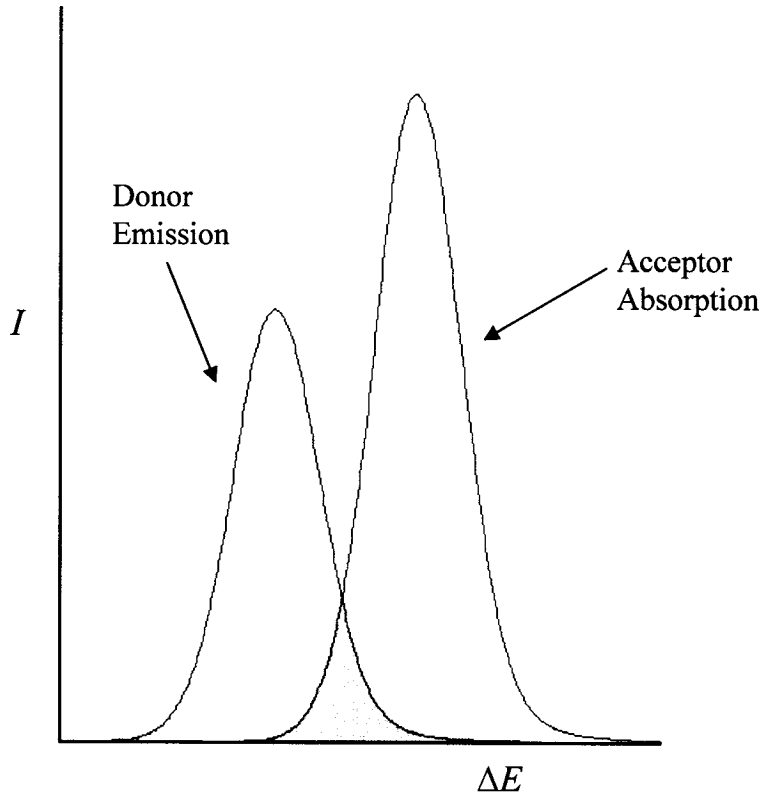

Figure 3.3: Spectral overlap (shaded region) between the Donor emission (in blue) and the acceptor absorption bands (in red).

3.5.1. Multipolar Interaction

The square of the matrix element of the multipolar interaction can be written as:

$$\left|\langle a'b|H_{ab}|ab'\rangle\right|^2 = \frac{c_{dd}}{R^6} + \frac{c_{dq}}{R^8} + \frac{c_{qq}}{R^{10}} \qquad 3.5.5$$

where $\frac{c_{dd}}{R^6}$ is the dipole-dipole interaction term, $\frac{c_{dq}}{R^8}$ is the dipole-quadrupole term and $\frac{c_{qq}}{R^{10}}$ is the quadrupole-quadrupole term. It is clear that there is a dependence between the donor and acceptor distance (R) and the multipolar character. For example, the energy transfer probability based on the dipole-dipole interaction is given by:

$$W_{AB} = \frac{2\pi}{\hbar}\left|\langle a'b|H_{ab}|ab'\rangle^2\right| \int g_A(E) g_B(E) dE \qquad 3.5.6$$

$$= \frac{2\pi}{\hbar}\frac{1}{R^6}\frac{3e^2c^3\hbar^6}{4m}\frac{f_B}{\tau_A}\varepsilon\int\frac{\int g_A(E)g_B(E)}{E^4}dE \qquad 3.5.7$$

where τ_A is the effective lifetime of donor A, f_B is the oscillator strength of the absorption peak of acceptor B, e is electronic charge, m is the electronic mass, c is the speed of light, and ε is the quantum efficiency given by:

$$\varepsilon = \frac{\text{radiative decay rate}}{\text{radiative decay rate} + \text{non - radiative decay rate}} = \frac{1/\tau_{OA}}{1/\tau_A} \qquad 3.5.8$$

where τ_{OA} is the radiative lifetime of donor A. The energy transfer rate, W_{AB}, can be simplified by introducing a new parameter the critical distance, R_0, which is the radius at which the transfer rate is equal to the radiative decay rate:

$$W_{AB} = \frac{1}{\tau_A}\left(\frac{R_0}{R}\right)^6 \qquad 3.5.9$$

where:

$$R_0 = \frac{3e^2c^3\hbar^5\pi}{2m} f_B\varepsilon\int\frac{\int g_A(E)g_B(E)}{E^4}dE \qquad 3.5.10$$

However, Dexter pointed out that this theory must be extended to include higher multipole and exchange interactions [182]. Thus, the energy transfer probability for electric multipolar interactions can be more generally written as:

$$W_{AB} = \frac{1}{\tau_A}\left(\frac{R_0}{R}\right)^S \qquad 3.5.11$$

where S is a positive integer taking the following values:

$S = 6$ for dipole-dipole interactions
$S = 8$ for dipole-quadrupole interactions
$S = 10$ for quadrupole-quadrupole interactions

3.5.2. Exchange Interaction

The exchange interaction term depends strongly on the donor-acceptor distance. In the case of multipolar interaction, the matrix element of the interaction is proportional to the oscillator strength of the donor or acceptor. However, this is not the case for the exchange interaction and thus, the matrix element cannot be related to any spectroscopic characteristic of the donor or acceptor. The exchange term may be written as:

$$\left\langle a'(1)\,b(2)\left|-\frac{e^2}{r_{12}}\right|b'(1)\,a(2)\right\rangle = -\left\langle a'(1)\,b(2)\left|\frac{e^2}{r_{12}}P_{12}\right|b'(1)\,a(2)\right\rangle \qquad 3.5.12$$

where P_{12} is an operator that interchanges the two electron coordinates for a hydrogen type system. In the case of the rare earth ions, a many electron system:

$$\left|\langle a'b|H_{AB}|ab'\rangle\right|^2_{\text{Exchange}} = \left\langle a'b\left|-\sum_{i,j}\frac{e^2}{r_{ij}}P_{ij}\right|ab'\right\rangle \qquad 3.5.13$$

The procedures of operator calculation are quite complex and out of the scope of this chapter and so only the final result is shown below:

$$\left|\langle a'b|H_{AB}|ab'\rangle\right|^2_{\text{Exchange}} = K^2 e^{-(2R/L)} \qquad 3.5.14$$

where K is a constant related to the dimension of energy and L is the effective Bohr radius. Substituting equation 3.5.13 into equation 3.5.4, the energy transfer rate by exchange interaction will be given by:

$$W_{AB} = \frac{2\pi}{\hbar}K^2 e^{-(2R/L)}\int g_A(E)g_B(E)dE \qquad 3.5.15$$

$$\frac{2\pi}{\hbar}K^2\int g_A(E)g_B(E)dE = \frac{e^{2R_0/L}}{\tau_{OA}} \qquad 3.5.16$$

if

$$\frac{2R_0}{L} = \gamma \qquad 3.5.17$$

The final form of the equation is then written as:

$$W_{AB} = \frac{1}{\tau_{OA}} e^{\gamma[1-(R/R_0)]} \qquad 3.5.18$$

The energy transfer rate by exchange interaction is exponentially dependent upon R. For many of the rare earth ions, the effective Bohr radius (L) is smaller than 0.3 Å [183] and as a result, the separation of even the nearest neighbor ions may be large compared to L. Consequently, the exchange interaction has little effect compared with the multipolar interactions in the case of the rare earth ions.

3.5.3. Upconversion by Energy Transfer

Upconversion via energy transfer is simply a generalization of Dexter energy transfer where the activator is in a metastable state rather than it being in its ground state. The requirement is that the interaction between the sensitizer (donor, A) and the acceptor (B), H_{AB}, be smaller than the vibronic transition of A and B in order that both ions be described by single ion levels coupled to the lattice. Furthermore, upconversion requires that the transfer probability for the second step, W_{AB}, be faster than radiative and non-radiative decay from the metastable level. Thus, $W_{AB} > \tau_{obs}^{-1}$ where τ_{obs} is the observed lifetime determined experimentally. W_{AB}, is obtained from:

$$W_{AB} = \frac{2\pi}{\hbar}\left|\left\langle \psi_A^E \psi_B^0 \middle| H_{AB} \middle| \psi_A^0 \psi_B^E \right\rangle\right|^2 \rho(E) \qquad 3.5.19$$

where the wavefunctions are simple products of single ion wavefunctions and $\rho(E)$ describes the dissipative density of states due to the coupling with the lattice.

On the contrary, all cooperative processes including upconversion can be considered as transitions between a pair-level for both ions as whole. A dipolar electric transition would be forbidden for such as two-center transition. Thus, the product wavefunctions must be corrected to first order in order to account for the interaction for electrons of different centers [184].

$$\left|\psi_{pair}\right\rangle = \left|\psi^0(A)\psi^0(B)\right\rangle - \sum_{a''\neq 0}\sum_{b''\neq 0}\frac{\left\langle a''b''\middle|H_{AB}\middle|00\right\rangle}{\delta_{a''}-0+\varepsilon_{b''}-0}\left|\psi_{a''}(A)\psi_{b''}(B)\right\rangle \qquad 3.5.20$$

As given, for instance, for the ground state. In equation where 3.5.19, a'' and b'' denote the intermediate states for A and B, respectively, while $\delta_{a''}$ and $\varepsilon_{b''}$ represent their corresponding energies.

CHAPTER 4

4. Experimental

4.1. Sample Preparation

The nanocrystalline sesquioxide (Y_2O_3, Lu_2O_3, and Sc_2O_3) and garnet ($Gd_3Ga_5O_{12}$) samples prepared via propellant synthesis as well as all bulk samples were prepared at the University of Verona. The $Y_2O_3:Er^{3+}$ nanocrystals prepared via controlled hydrolysis were synthesized at the University of Salerno.

4.1.1. Propellant Synthesis

The solution combustion synthesis technique (propellant synthesis) used to prepare the nanocrystalline sesquioxides and garnets involves the exothermic reaction of an oxidizer and an organic fuel. Typical oxidizers include metal nitrates, ammonium nitrate, or ammonium perchlorate, while typical fuels may include urea (CH_4N_2O), carbohydrazide (CH_6N_4O), or glycine ($C_2H_5NO_2$) [185]. One of the most attractive features of the propellant synthesis is that the nanocrystals are produced at relatively low temperatures with reduced processing time [186]. Thus, a high temperature furnace is not required as the reaction is initiated at temperatures of 500 °C or less. In a typical reaction the precursor mixture of distilled water, oxidizer, and fuel decomposes, dehydrates, and ruptures into a flame after approximately 5 minutes creating a voluminous foamy powder. The combustion reaction is influenced by a number of parameters such as type of fuel, fuel-to-oxidizer ratio, use of excess oxidizer, ignition temperature, and water content of the precursor mixture [94, 187]. This synthesis technique was first employed to prepare rare earth doped yttrium oxide nanocrystals by Tao et al. [188] and later adapted by Bettinelli and co-workers [189-191]. Since, the

combustion process has been used by many to synthesize nanocrystalline yttrium oxide, its derivatives, and many other inorganic nanocrystals [75, 94, 187, 192-202].

In the combustion procedure, the reaction temperature has a great influence on the particle size of the material and by adjusting the glycine-to-metal nitrate molar ratio, the combustion flame temperature can be controlled. The stoichiometric molar ratio of glycine-to-metal nitrate can be calculated using the method of Jain et al. [203] where the ratio is expressed in terms of the elemental stoichiometric coefficient, Φ_e, defined as:

$$\Phi_e = \frac{\sum(\textit{coefficient of oxidizing elements in specific formula})\times(\textit{valcency})}{(-1)\sum(\textit{coefficient of reducing elements in specific formula})\times(\textit{valcency})} \qquad 4.1.1$$

The mixture is stoichiometric when $\Phi_e = 1$, fuel-lean when $\Phi_e > 1$, and fuel-rich when $\Phi_e < 1$. Stoichiometric glycine-to-metal nitrate molar ratios produce the maximum temperature in the combustion process. The following equation can be used to approximate the adiabatic flame temperature, T_f, for a combustion reaction:

$$T_f = T_o + \frac{\Delta H_r - \Delta H_p}{c_p} \qquad 4.1.2$$

where ΔH_r and ΔH_p are the enthalpies of formation of the reactants and products, respectively, and c_p is the heat capacity of the products at constant pressure. The reaction is initiated after the water in the precursor solution boils, thus, T_o is 373 K, the boiling point of water [75].

For RE^{3+}-doped nanocrystal oxides, it was shown that lower temperatures lead to smaller particle sizes. In the case of $Y_{1.80}Eu_{0.20}O_3$ produced by this method, average particle sizes of 8 and 40 nm were obtained for oxidant-rich glycine-to-metal nitrate molar ratios of 1.0:1 (reaction temperature of 1000 °C) and 1.3:1 (reaction temperature of

1320 °C), respectively [188]. For a stoichiometric ($\Phi_e = 1$) glycine-to-metal nitrate molar ratio of 1.7:1 (reaction temperature of 1420 °C) $Y_2O_3:Eu^{3+}$ nanocrystals with an average particle size of 70 nm were produced. In the synthesis of Y_2O_3 nanopowders doped with Ln_2O_3 (Ln = Ce, Pr, Nd, Eu, Gd, Ho, and Er) prepared using the same procedure, a ratio of 1.2:1 was employed yielding nanocrystals with an average particle size of 20 nm with a yield of approximately 80 % [189, 191].

The appearance of nanocrystalline product was shown by Sun et al. [204] to be dependent on the molar ratio of glycine and lanthanide in the precursor solution. When the ratio was less than 1, a light gray product was obtained since the nitroxide was formed instead of the oxide due to the incomplete decomposition of the nitrate. A white, crisp foamy product was obtained when the glycine-to-rare earth ratio was between 1 – 2.5, however, when this ratio was larger than 3, much more glycine in the product made the product yellowish and hygroscopic because of the residual glycine. A study of the propellant synthesis of nanocrystalline yttrium oxide was carried out with yttrium nitrate as the oxidizer but using different fuels [205] (Table 4.1). A difference in particle size with the use of different fuels was observed and was shown to depend on the number of moles of gaseous products released during combustion. As more gas is freed, the agglomerates are disintegrated and more heat is carried from the system thus hindering particle growth [206].

Table 4.1: Different fuels used with stoichiometric amounts of $Y(NO_3)_3 \cdot 6H_2O$ in the combustion reaction from ref [205].

Fuel	Chemical Formula
Oxalodihydrazide (ODH)	$C_2H_6N_4O_2$
Malonodihydrazide (MDH)	$C_3H_8N_4O_2$
Glycine	$C_2H_5NO_2$
Diformylhydrazide (DFH)	$C_2H_4N_2O_2$
Tetraformal trisazine (TFTA)	$C_4H_{16}N_6O_2$
3-methylpyrazol-5-one (3MP5O)	$C_4H_6N_2O$

(i) Sesquioxide Nanocrystals

The sesquioxide nanocrystals prepared by propellant synthesis investigated in this thesis are compiled in Table 4.2. The samples were prepared using an aqueous solution containing appropriate amounts of glycine NH_2CH_2COOH (Sigma, 99 %), metal nitrate $M(NO_3)_3 \cdot H_2O$ (Aldrich, 99.99 %) where M = Y, Lu, or Sc, and the corresponding lanthanide nitrate $Ln(NO_3)_3 \cdot H_2O$ (Aldrich, 99.99+ %) where Ln = Er or Yb. A list of all starting materials used in the combustion synthesis of the sesquioxides is given Table 4.3. The glycine serves as fuel for the propellant reaction, being oxidized by the nitrate ions. The synthesis reaction is:

$$6\ M(NO_3)_3 + 10\ NH_2CH_2COOH + 18\ O_2 \rightarrow 3\ M_2O_3 + 5\ N_2 + 18\ NO_2 + 20\ CO_2 + 25\ H_2O$$

where M = Y, Lu, Sc, Er and/or Yb. A glycine-to-metal nitrate molar ratio of 1.2:1 was employed to prepare the precursor solution.

Table 4.2: List of sesquioxide nanocrystalline samples studied prepared by propellant synthesis.

Sample	Formula	Dopant Concentration
Yttrium Oxide	$Y_2O_3:Er^{3+}$	1 mol%
		2 mol%
		5 mol%
		10 mol%
	$Y_2O_3:Er^{3+}, Yb^{3+}$	0.1 mol% Er^{3+} & 1 mol% Yb^{3+}
		5 mol% Er^{3+} & 1 mol% Yb^{3+}
		1 mol% Er^{3+} & 1 mol% Yb^{3+}
		1 mol% Er^{3+} & 5 mol% Yb^{3+}
		1 mol% Er^{3+} & 10 mol% Yb^{3+}
Lutetium Oxide	$Lu_2O_3:Er^{3+}$	1 mol%
Scandium Oxide	$Sc_2O_3:Er^{3+}$	0.1 mol%
		1 mol%
		10 mol%

After the combustion, the powder was fired for 1 hour at 500 °C in order to decompose the residual nitrate ions. Laser-excited Raman and Fourier transform infrared (FTIR) spectra were measured on all samples confirming the absence of nitrate ions.

All yttria samples were kept in air without any further precaution.

Table 4.3: List of starting materials used in the propellant synthesis of the sesquioxides.

Chemical Name	Chemical Formula
Yttrium Nitrate Hexahydrate	$Y(NO_3)_3 \cdot 6H_2O$
Scandium Nitrate Hydrate	$Sc(NO_3)_3 \cdot xH_2O$
Lutetium Nitrate Hydrate	$Lu(NO_3)_3 \cdot xH_2O$
Erbium Nitrate Pentahydrate	$Er(NO_3)_3 \cdot 5H_2O$
Ytterbium Nitrate Pentahydrate	$Er(NO_3)_3 \cdot 5H_2O$
Glycine	NH_2CH_2COOH

(ii) Garnet Nanocrystals

To synthesize $Gd_3Ga_5O_{12}:Er^{3+}$ nanocrystals, an aqueous solution containing appropriate quantities of carbohydrazide $(NH_2NH)_2CO$ (Aldrich, 98 %), $Gd(NO_3)_3 \cdot 6H_2O$ (Aldrich, 99.99 %), $Ga(NO_3)_3 \cdot xH_2O$ (Aldrich, 99.999 %), $Er(NO_3)_3 \cdot 5H_2O$ (Aldrich, 99.99+ %), and $Yb(NO_3)_3 \cdot 5H_2O$ (Aldrich, 99.99+ %) was prepared having an oxidant-to-reductant molar ratio of 2.5. The precursor solution was heated with a Bunsen flame and after the evaporation of the solvent, the auto combustion process took place with the evolution of brown fumes. The proposed stoichiometric synthesis reaction is:

$$3M(NO_3)_3 + 5Ga(NO_3)_3 + 3(NH_2NH)_2CO \rightarrow M_3Ga_5O_{12} + 24NO_2 + 6N_2 + 3CO_2 + 9H_2O$$

where M = Gd and Er. Once the synthesis reaction was completed, any unreacted carbohydrazide and/or nitrate ions were decomposed by heating the synthesized nanopowders for at 800 °C for 72 hours.

No other actions were taken to prevent the nano sample from coming into contact with the ambient atmosphere.

Table 4.4: List of garnet nanocrystalline samples studied prepared by propellant synthesis.

Sample	Formula	Dopant Concentration
Gadolinium Gallium Garnet	$Gd_3Ga_5O_{12}:Er^{3+}$	1 mol% 5 mol%

4.1.2. Controlled Hydrolysis Procedure

Wet chemical processes are an attractive means of synthesizing nanocrystals since they offer a new level of control over the particle size, crystallinity, and microstructure. A popular technique for the synthesis of yttrium oxide nanocrystals involves a combined method of coprecipitation and hydrothermal processes in the presence of a seed [207]. The coprecipitation method was employed to produce a gel in the presence of a surface modifier followed by the addition of Y_2O_3 seeds to the coprecipitated gel, which was then subjected to a hydrothermal treatment. Synthesis of nanocrystals via wet chemical methods requires control over the thermodynamics of the interfaces due to their tendency to minimize their surface energy by agglomerating or growing large particles [207]. Using a surface modifier in highly alkaline media (pH >10) is one of the approaches used to modify the surface of growing particles. Thus to control the particle size, addition of a surface modifier is necessary as it coats the surface of the particles and provides a barrier-like protection against agglomeration [208].

The nanocrystalline Er^{3+} doped yttria samples studied were obtained using this controlled hydrolysis procedure (wet chemical synthesis) [208-210]. This method calls for the reaction of an alcoholic solution containing $Y(NO_3)_3 \cdot 6H_2O$ (Aldrich, 99.99 %) and $Er(NO_3)_3 \cdot 5H_2O$ (Aldrich, 99.99+ %) with a basic solution of a surface modifier (see Figure 4.1), β-alanine + Tween 80 in 1:1 weight ratio, at pH > 10 (ammonia solution). The two solutions were mixed and the resulting gel was centrifuged for 1 h at 3000 rpm. After removing the aqueous solution, the powder was dried at 70 °C for 24 h and then heat treated in a muffle furnace for 12 h at 500 °C.

Table 4.5: List of nanocrystalline samples studied prepared by the controlled hydrolysis procedure.

Sample	Formula	Dopant Concentration
Yttrium Oxide	$Y_2O_3:Er^{3+}$	0.1 mol% 1 mol% 10 mol%

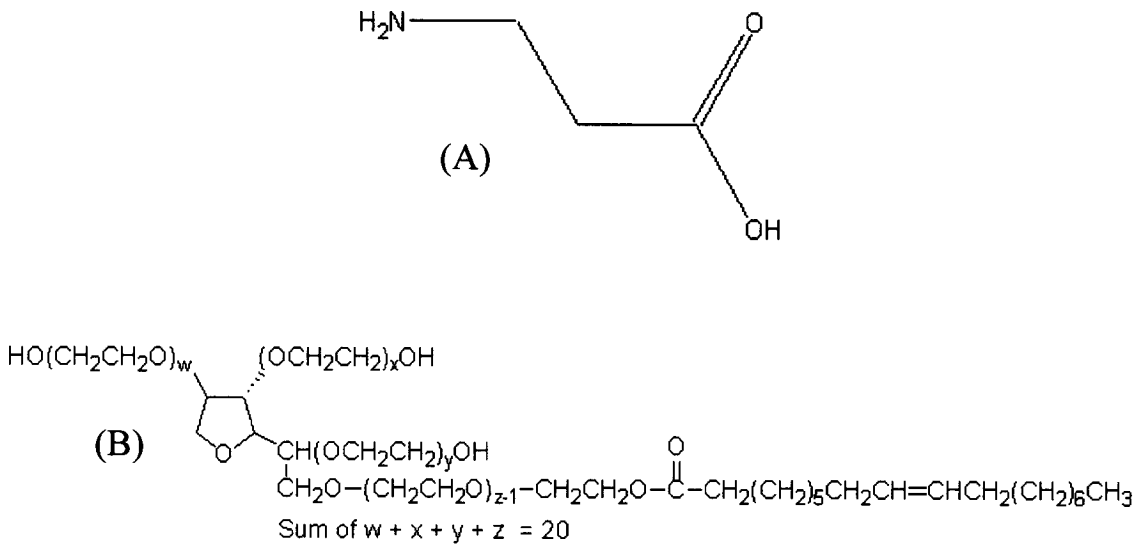

Figure 4.1: Structure of the surface modifiers used in the controlled hydrolysis procedure (A) β-alanine and (B) Tween®80 (polyoxyethylene (20) sorbitan monooleate).

Synthesis of Bulk Sesquioxides

For comparison purposes, microcrystalline (bulk) samples were prepared by conventional solid state synthesis and involved intimately mixing appropriate quantities of M_2O_3 (Aldrich, 99.99 %) where M = Y, Lu, or Sc with Er_2O_3 and/or Yb_2O_3 (Aldrich, 99.99+ %), pressing the powders into a round pellet (approximately 1.3 cm in diameter) under 10 tons of pressure, and firing it in air. Several heat treatments were attempted, but the optimum homogeneity (verified using scanning electron microscopy) was obtained when the sample was fired at 1500 °C for 48 h. The spectroscopic measurements were carried out on the samples, which had undergone this heat treatment. It should be noted that the size of the particles in the bulk sample is at least 10 times larger than the nanocrystalline samples. Table 4.6 lists all bulk samples investigated.

All bulk samples were kept in air without any further precaution.

Table 4.6: List of bulk sesquioxide samples studied.

Sample	Formula	Dopant Concentration
Yttrium Oxide	$Y_2O_3:Er^{3+}$	1 mol%
		2 mol%
		5 mol%
		10 mol%
	$Y_2O_3:Er^{3+}, Yb^{3+}$	1 mol% Er^{3+} & 1 mol% Yb^{3+}
Lutetium Oxide	$Lu_2O_3:Er^{3+}$	1 mol%

4.2. Characterization

The experimental SEM, TEM, and XRD results presented in this thesis were obtained at Università Ca' Foscari, Venezia by Dr. Stefano Polizzi. The XRD patterns shown in Figure 5.13 were obtained in the laboratory of Prof. Georges Denes at Concordia University. All other characterization, including FTIR measurements, was performed at the Università di Verona by Prof. Marco Bettinelli and Dr. Adolfo Speghini.

4.2.1. Scanning Electron Microscopy (SEM)

Scanning electron microscopy (SEM) images were taken with a Jeol JSM 5600 LV electron microscope equipped with an Oxford Instrument 6587 EDS microanalysis detector. Samples were coated with an Au thin film, in order to avoid charging effects. Samples without coating were also measured in the low-vacuum regime and/or low voltage and current, in order to check for possible artifacts.

4.2.2. Transmission Electron Microscopy (TEM)

Transmission electron microscopy (TEM) images were taken with a Jeol 3010 microscope, operating at 300 kV, equipped with a Gatan slow-scan CCD camera (Model 794). The powder was dispersed in an isopropyl alcohol solution by a short sonication and a 5 μm drop was deposited on a copper grid coated with a carbon holey film.

4.2.3. X-ray Diffraction

A Philips X'Pert vertical goniometer with Bragg-Brentano geometry, connected to a highly stabilized generator, was used for X-ray diffraction (XRD) analysis. Cu-K_α (Ni-filtered) radiation, a graphite monochromator on the diffracted beam and a

proportional counter with pulse height discriminator, were used. For the determination of the lattice parameters and Rietveld analysis, measurements on a 14°-140° range in 2θ (Bragg angle) were collected with a step size of 0.05° and 10 s per point for five runs of 10 s per each point and then averaged. The cubic unit cell-edge values were calculated by using the angular peak position of 23 reflections in the 2θ range of 25°-85°. In accordance with Wagner, [211, 212] the cell-edge value was extrapolated by applying a weighted least-square linear fit to the cell-edge values calculated from the position of each single reflection as a function of $cos\theta\ cotg\theta$. The peak positions were obtained using a best-fitting procedure [213, 214], where each peak is described by a couple of constrained pseudo-Voigt functions (K_{α_1} and K_{α_2} profiles) and the background by a polynomial function.

The line-broadening analysis was carried out by the Warren-Averbach method [215, 216] using the two 222/444 and 400/800 pairs of reflections. In accordance with this method, the following equation can be written for the Fourier transform $A(D)$ (D is the variable in direct space) of the fitted peak profile:

$$\ln\left[A\left(D,\frac{1}{d_{hkl}^2}\right)\right]=\ln\left[A^s(D)\right]-\frac{2\pi\left\langle\varepsilon^2(D)\right\rangle}{d_{hkl}^2}D^2 \qquad 4.2.1$$

where hkl are the Miller indices; d_{hkl} is the interplanar spacing; $A^s(D)$ is the Fourier transform of the peak profile corrected for broadening caused by lattice disorder effects and $\langle\varepsilon^2(D)\rangle$ is the mean square microstrain distribution. Thus, by using the Fourier coefficients of two different peaks belonging to the same family of crystallographic planes, the real distribution of crystallite dimensions, $A^s(D)$, and the corresponding distribution of microstrains can be obtained. Both distributions refer to the direction

perpendicular to the (*hkl*) family of crystallographic planes. $A^s(D)$ is suitably averaged, in order to obtain the volume-weighted average crystallite size, $\langle D \rangle_v$. The value of $\langle \varepsilon^2(D) \rangle$ at $\langle D \rangle_v/2$ is taken as a measure of the average microstrain. The instrumental broadening was previously deconvolved by using Stokes' method, adapted to analytically defined profiles.

4.3. Spectroscopy

Unless otherwise indicated, all spectroscopic studies were performed at Concordia University.

4.3.1. Fourier Transform Infrared Spectroscopy (FTIR)

Diffuse reflectance spectra in the medium infrared (MIR) region were measured at room temperature with a Nicolet Magma 760 FTIR spectrometer using an aluminated mirror as a reference.

4.3.2. Reflectance Spectroscopy

Diffuse reflectance spectra in the UV-Visible region were measured in a 0.2 mm quartz cell using a Shimadzu UV-265 spectrophotometer equipped with an integrating sphere and a standard white reflecting plate containing $BaSO_4$ (Eastman Kodak White reference standard). The signal was detected with an R-446U photomultiplier tube.

4.3.3. Luminescence Spectroscopy

A sketch showing the instrumentation found in the laser spectroscopy laboratory is shown on page 90 with a detailed description of each piece of equipment given on pages 91-95.

The visible emission spectra were obtained by exciting the bulk and nanocrystalline material with 488 nm using a Coherent Sabre Innova, 20 W continuous wave (cw) argon ion laser. Upconversion emission spectra were obtained by exciting at either 650 nm using a cw Spectra-Physics 375 dye-laser operating with DCM (Exciton), 800 nm or 980 nm using the Spectra-Physics Model 3900 cw titanium sapphire ($Al_2O_3:Ti^{3+}$) laser. Both the dye and Ti sapphire lasers were pumped by the 514.5 nm

line of the Coherent Sabre Innova Ar^+ laser. Upconversion spectra were also obtained with 1064 nm pulses from a Lumonics HY 400 Q-switched Nd:YAG laser (pulse duration ~10 ns, 400 mJ).

The sample was placed on an Oriel micropositioning stand (adjustable on the X and Y axes). The emissions were focused using a Mamiya/Sekor camera lens (f = 55 mm) and collected at right angle from the incident beam.

The UV emissions were collected with Spex Minimate ¼ meter monochromator equipped with an Oriel 70680 photomultiplier tube.

The visible emissions were collected using a Jarrell-Ash 1 meter Czerny-Turner double monochromator. The visible light exiting the monochromator was detected with a thermoelectrically cooled Hamamatsu R943-02 photomultiplier tube with a background dark count rate of less than 10 counts per second. The photomultiplied signals were processed by a Stanford Research Systems Model SR 440 preamplifier and a gated dual channel photon counter Stanford Research Systems Model SR 400 data acquisition system was utilized as an interface between the computer and the spectroscopic hardware. The signal was recorded under computer control using the Stanford Research Systems SR 465 software data acquisition/analyzer system.

The near-infrared (NIR) emissions were recorded with a Jarrell-Ash ¾ meter Czerny-Turner single monochromator operating in second order. The signal was detected by a North Coast EO-817P liquid nitrogen-cooled germanium detector connected to a computer-controlled Stanford Research Systems Model SR 510 lock-in amplifier. A personal computer using Stanford Research Systems SR 565 software data acquisition/analyzer system was used to record the data.

4.3.4. Lifetime Measurements

Luminescence decay curves were measured at each of the excitation wavelengths (488, 650, 800, or 980 nm) by modulating the laser beam with a Stanford Research Systems SR 540 optical chopper. They were recorded using the same gated photon counter mentioned previously.

The temporal dependence of the upconverted emission was obtained by modulating the excitation beam at 20 Hz with the chopper and the photomultiplier tube output was recorded using a two channel digitizing oscilloscope (Tektronix TDS 520A).

4.3.5. Power Dependence Studies

The upconversion power dependence studies were carried out by varying the upconversion excitation wavelengths (λ_{exc} = 650, 800, or 980 nm) using a New Focus dual neutral density filter wheel Model 5215. The laser power was measured with a Gentec Solo P/E digital power meter.

4.3.6. Low Temperature

All low temperature emission spectra were acquired using a Janis Research ST-VP-4 continuous flow cryostat with the temperature being monitored by a LakeShore Model 330 controller.

4.3.7. Raman Spectra

Raman spectra were recorded using the Jarrell-Ash 1 meter double monochromator. Light scattered at $\pi/2$ from the incident beam was monitored with an RCA C31034-02 photomultiplier operating in the photon counting mode.

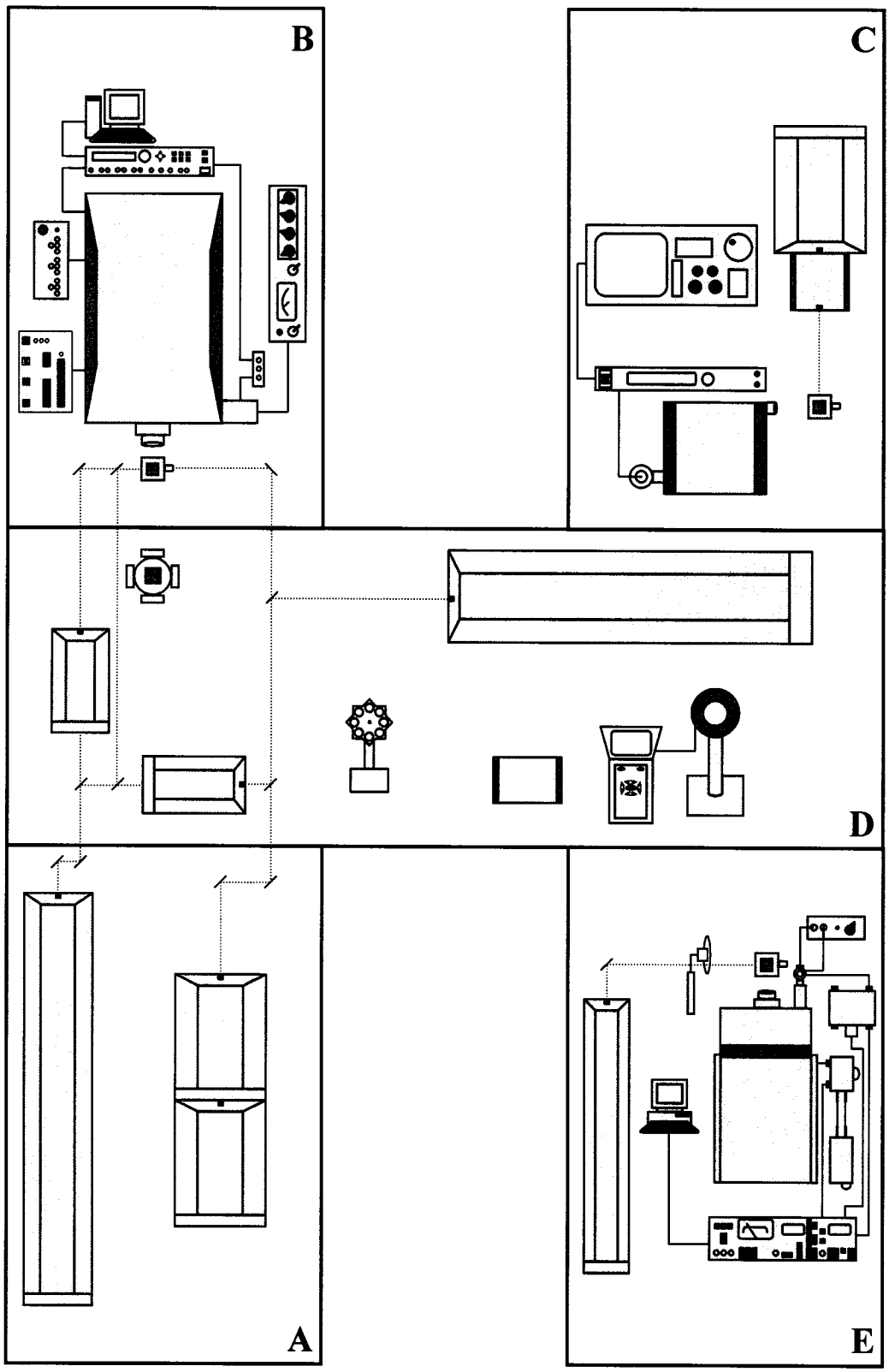

Figure 4.2: Schematic representation of the Lanthanide Research Group laser spectroscopy laboratory. A more specific explanation of each optical table is shown in the subsequent pages.

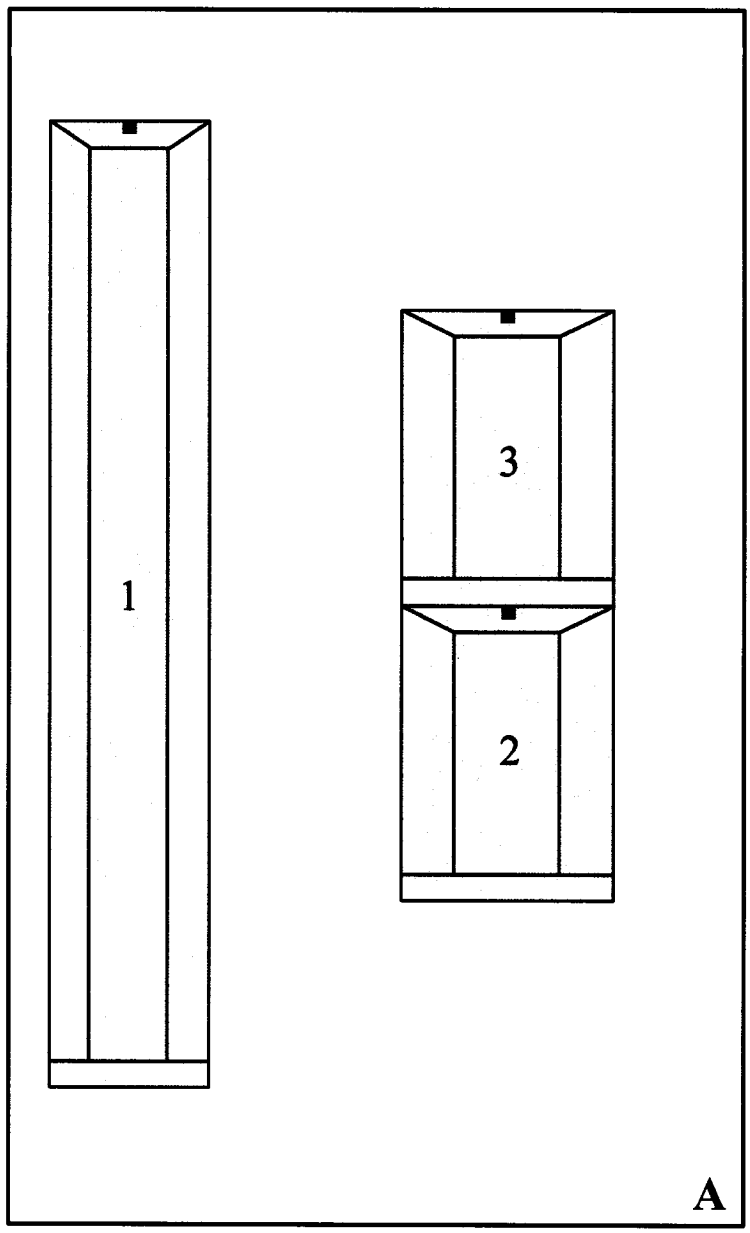

Legend:

A1 – Coherent Sabre Innova 20 watt continuous wave argon ion laser
A2 – Molectron Corp. pulsed nitrogen laser Model UV-12
A3 – Molectron Corp. DL-II tunable dye laser

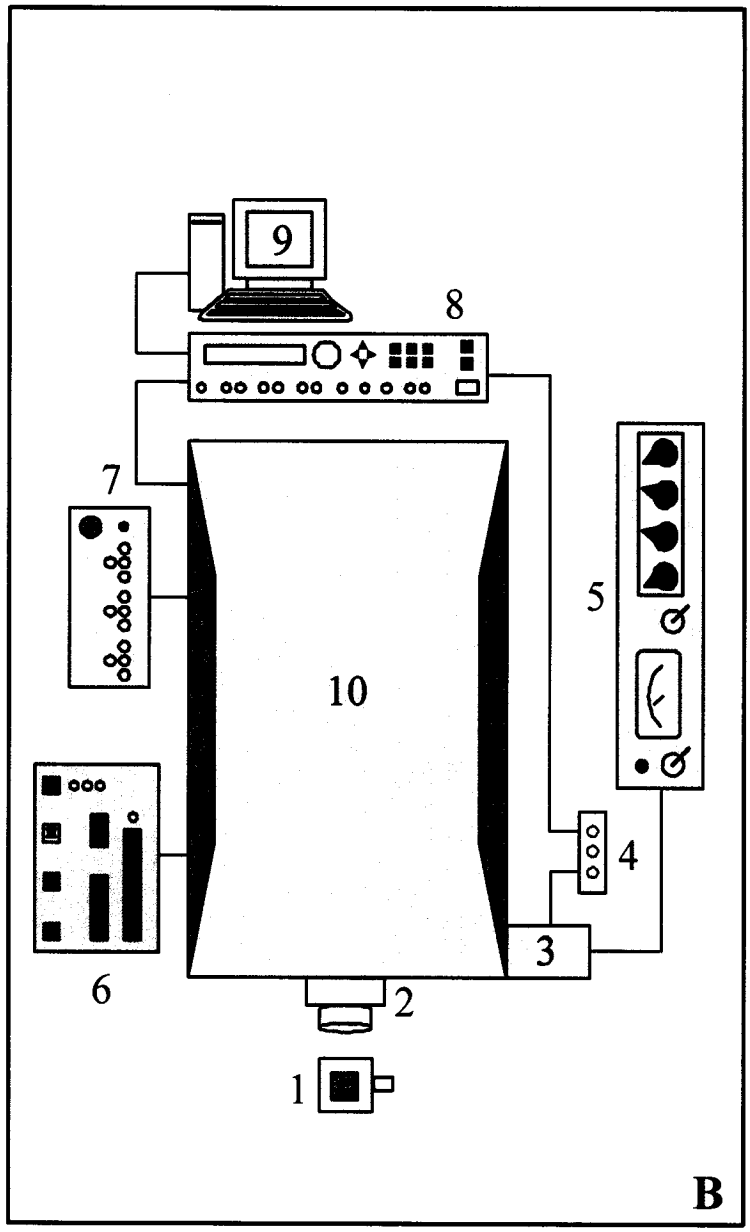

Legend:

B1 – Oriel micropositioner sample holder
B2 – Mamiya/Sekor camera lens (f = 55 mm)
B3 – Thermoelectrically cooled Hamamatsu R943-02 photomultiplier tube
B4 – Pre-amplifier (Stanford Research Systems, Model SR 440)
B5 – High voltage power supply (Science Technical Center, Concordia University)
B6 – Stepper motor controller (Compumotor 2100 Series Indexer)
B7 – Monochromator power supply (Science Technical Center, Concordia University)
B8 – Gated dual-channel photon counter (Stanford Research Systems, Model SR 400)
B9 – Personal computer using Stanford Research Systems SR 465 software data acquisition/analyzer system
B10 – Jarrell-Ash 1 meter Czerny-Turner double monochromator

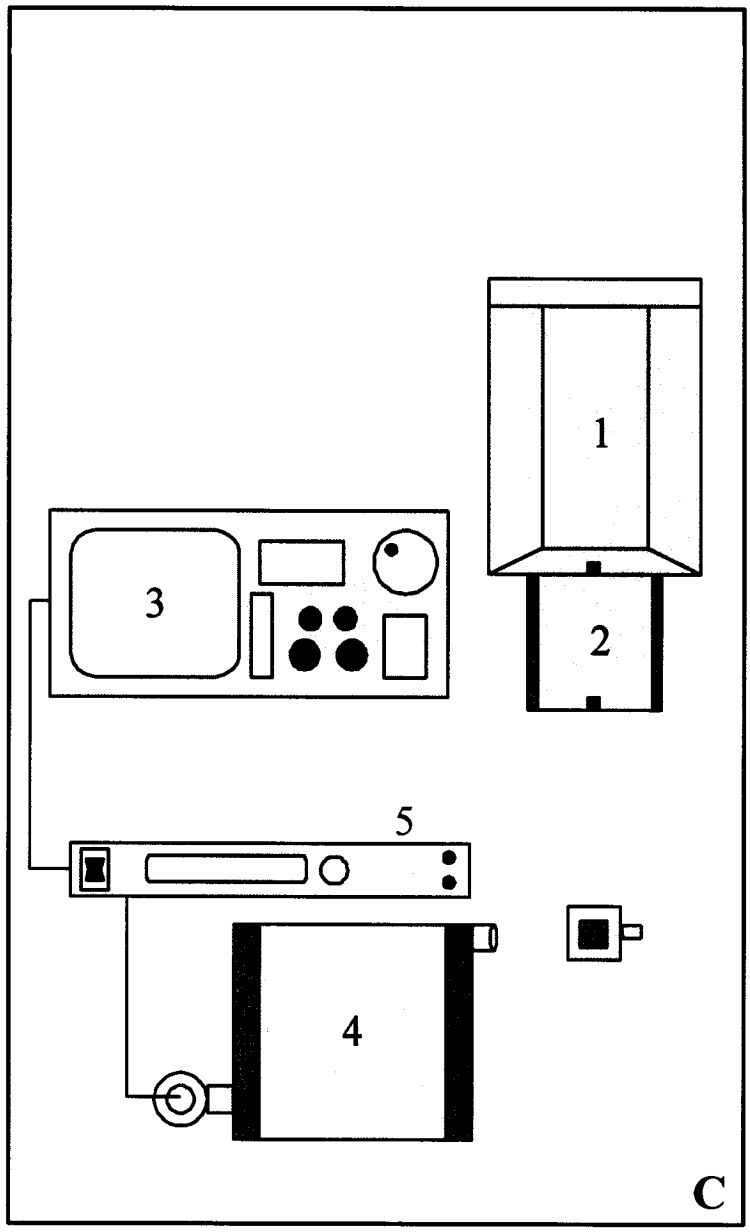

Legend:

C1 – Laser Photonics MegaPlus nitrogen pulsed laser
C2 – Laser Photonics dye laser
C3 – Tektronix TDS 520A two channel digitizing oscilloscope
C4 – Spex Minimate ¼ meter monochromator with Oriel 70680 photomultiplier tube
C5 – Oriel high voltage power supply

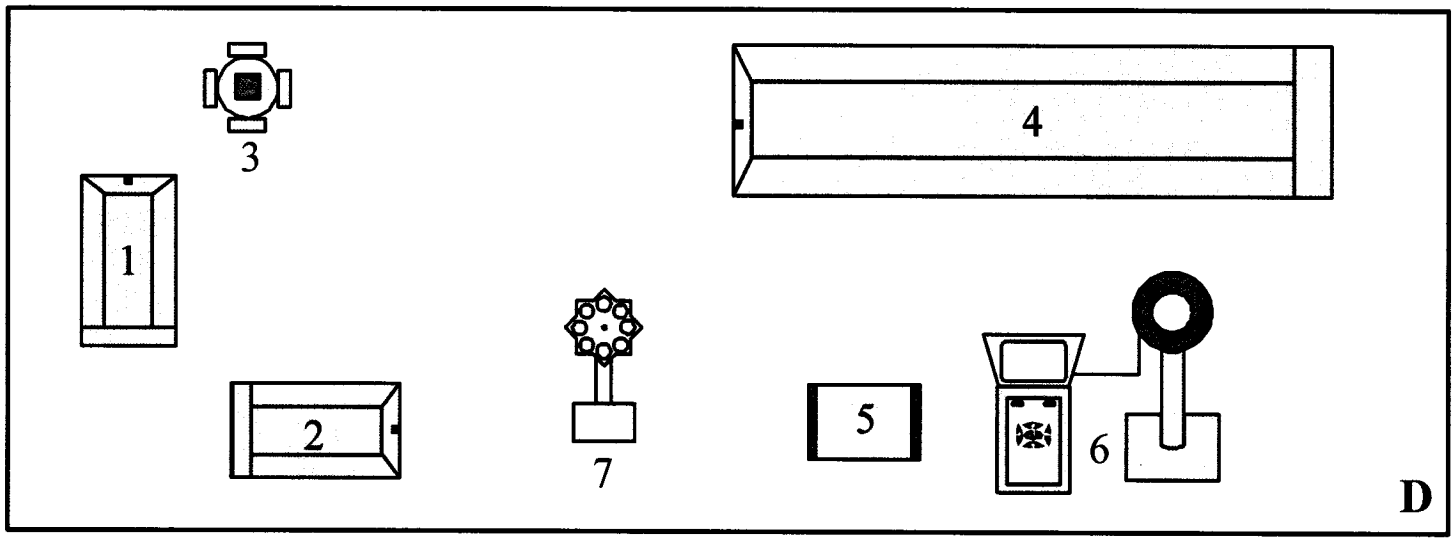

Legend:

D1 – Spectra-Physics Model 3900 continuous wave titanium sapphire ($Al_2O_3:Ti^{3+}$) laser
D2 – Spectra-Physics Model 375 continuous wave dye laser
D3 – Janis Research ST-VP-4 continuous flow cryostat with LakeShore Model 330 temperature controller
D4 – Lumonics HY 400 Q-switched Nd:YAG pulsed laser
D5 – Coherent Model 440 Ultraviolet Generator
D6 – Gentec Solo P/E power meter
D7 – New Focus dual neutral density filter wheel Model 5215

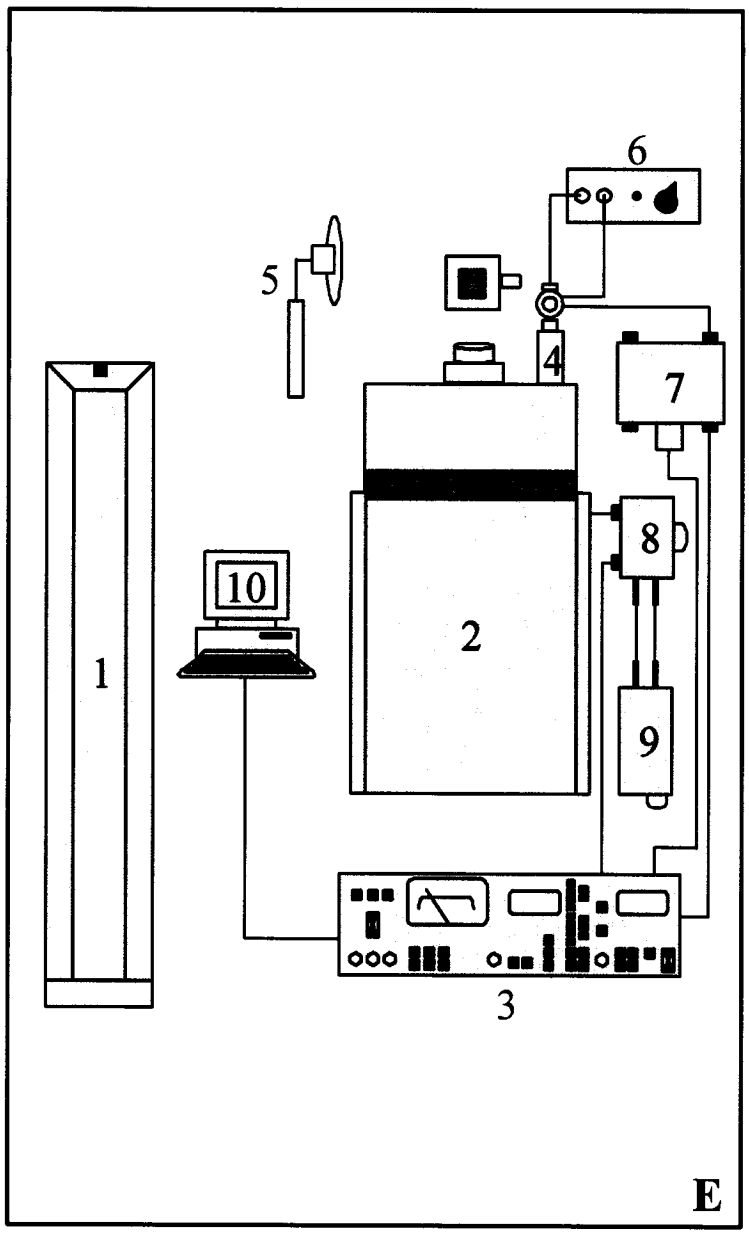

Legend:

E1 – Spectra-Physics Stabilite 2016 5 watt argon ion laser
E2 – Jarrell-Ash ¾ meter Czerny-Turner single monochromator operating in second order
E3 – Lock-in amplifier (Stanford Research Systems, Model SR 510)
E4 – North Coast EO-817P germanium detector
E5 – Optical chopper (Stanford Research Systems, Model SR 540)
E6 – North Coast power supply for Ge detector
E7 – Pre-amplifier (Stanford Research Systems, Model SR 550)
E8 – Lock-in trigger (Science Technical Center, Concordia University)
E9 – Lock-in trigger power supply (Science Technical Center, Concordia University)
E10 – Personal computer using Stanford Research Systems SR 565 software data acquisition/analyzer system

CHAPTER 5

5. Morphology and Structure

5.1. Transmission Electron Microscopy (TEM) and Scanning Electron Microscopy (SEM)

TEM and SEM are useful techniques for examining the physical characteristics of nanomaterials. SEM is capable of examining the morphology of the microstructure of nanoscale powders while TEM allows for the probing of materials on the nanometer scale and confirmation of the particle size determination [217, 218].

5.1.1. Sesquioxide and Garnet Nanocrystals Prepared Via Propellant Synthesis

Figures 5.1 – 5.3 show typical SEM images of the sesquioxide nanocrystals. The morphology is characteristic of samples prepared by propellant synthesis showing a microscopic open, sponge-like appearance [191]. The fact that the same morphology is observed over different scales (see also the TEM images), clearly suggests a fractal behavior. Similarly, the morphology of the garnet nanocrystals is practically the same (Figure 5.4). At the sub-micrometer level, the morphology of the material exhibits the typically porous and sponge-like properties observed in nanocrystals prepared by the solution combustion process.

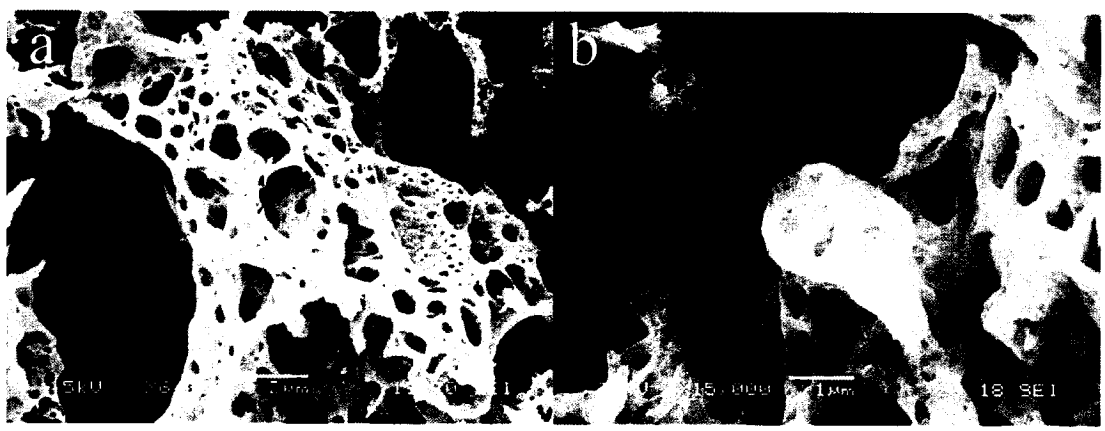

Figure 5.1: SEM micrographs of Y_2O_3 nanocrystals prepared via propellant synthesis.

The porosity is maintained at the nanometer level, again suggesting a fractal organization [219].

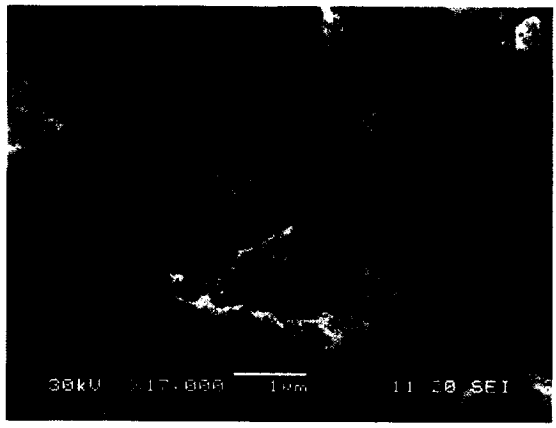

Figure 5.2: SEM micrograph of Lu_2O_3 nanocrystals prepared via propellant synthesis.

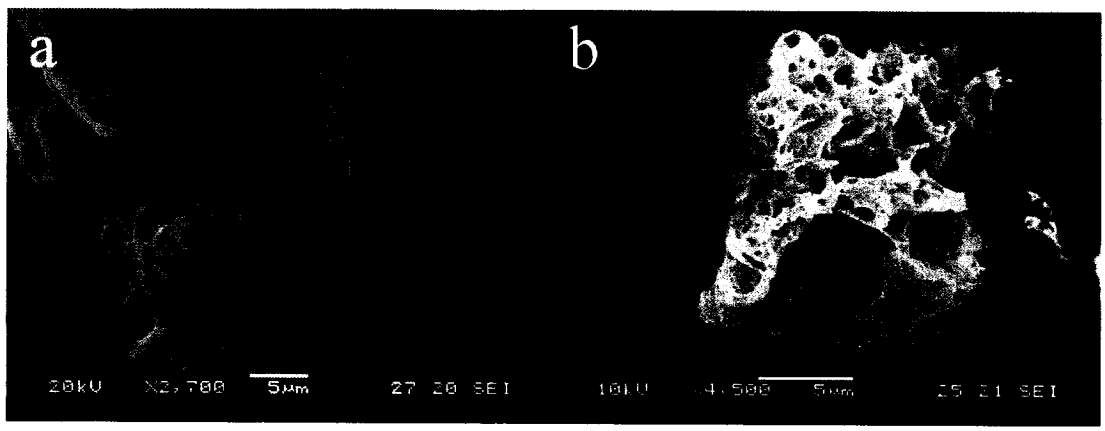

Figure 5.3: SEM micrographs of Sc_2O_3 nanocrystals prepared via propellant synthesis.

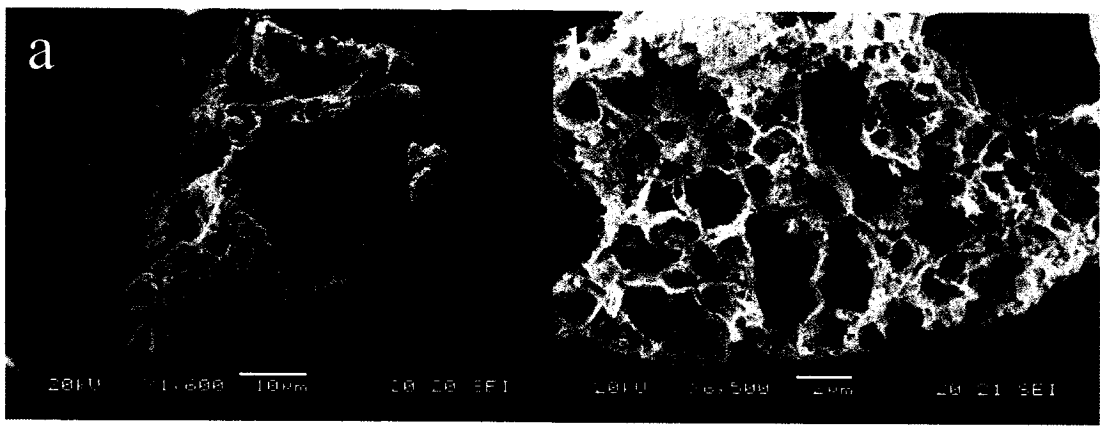

Figure 5.4: SEM micrographs of $Gd_3Ga_5O_{12}$ nanocrystals prepared via propellant synthesis.

TEM micrographs of the sesquioxide nanocrystal samples are shown at different magnifications in Figures 5.5 – 5.7. The samples are composed of interconnected crystalline particles with irregular, sharp-edged shapes and dimensions [220]. High resolution TEM (HRTEM) images (Figures 5.5c, 5.6c, and 5.7c) show that these particles, which are the building units of the porous structure, are single crystallites [221]. Some small voids are visible, which are most likely generated by gas bubbles during the very rapid combustion process.

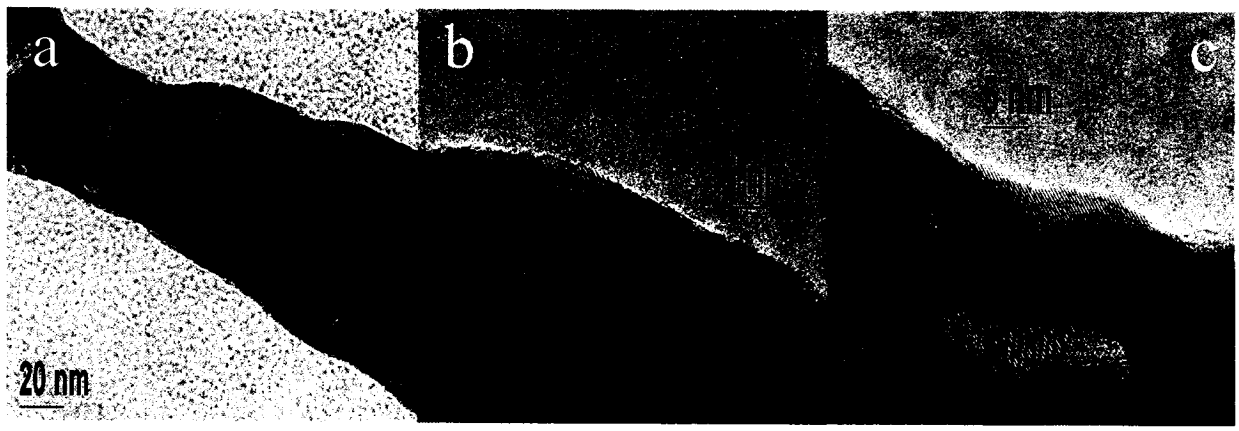

Figure 5.5: TEM micrographs of Y_2O_3 nanocrystals prepared via propellant synthesis.

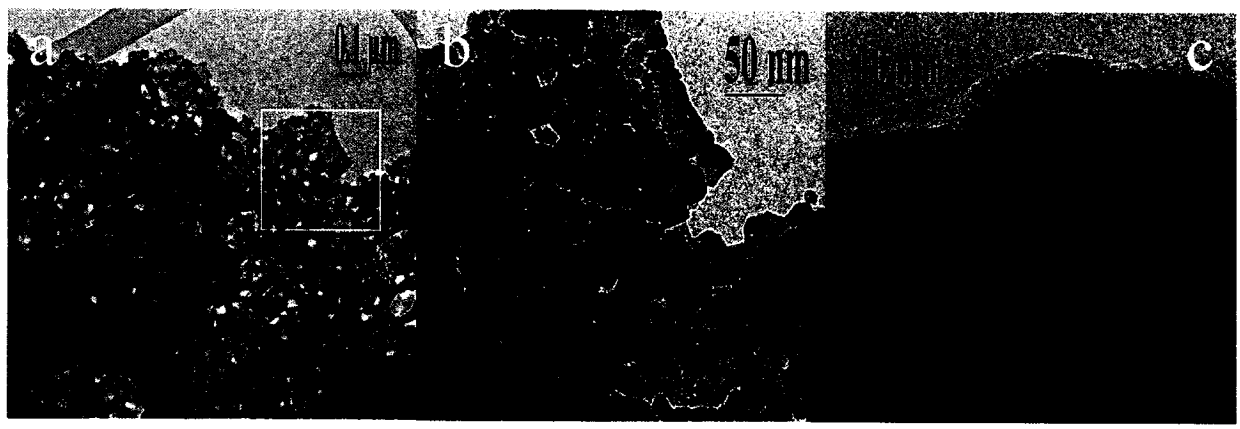

Figure 5.6: TEM micrographs of Sc_2O_3 nanocrystals prepared via propellant synthesis.

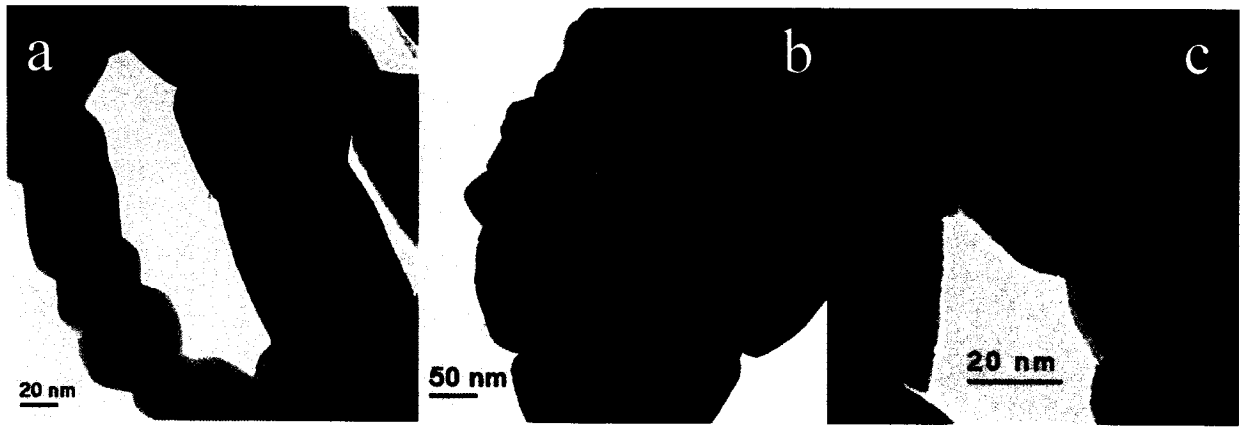

Figure 5.7: TEM micrographs of Lu_2O_3 nanocrystals prepared via propellant synthesis.

Similarly for the $Gd_3Ga_5O_{12}$ nanocrystals, HRTEM images (Figure 5.8) show the repeating crystal planes of the $Gd_3Ga_5O_{12}$ nanocrystalline lattice. The TEM images show that the crystallites have a broad distribution of sizes ranging from a few nanometers to several tens of nanometers.

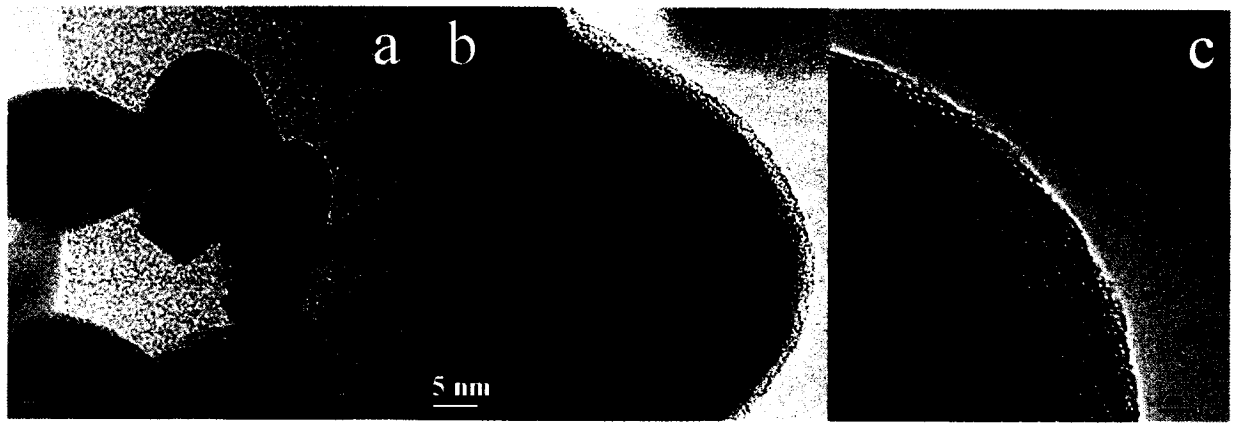

Figure 5.8: TEM micrographs of $Gd_3Ga_5O_{12}$ nanocrystals prepared via propellant synthesis.

5.1.2. Sesquioxide Nanocrystals Prepared Via Wet Chemical Synthesis

SEM images of Y_2O_3 nanocrystals prepared via the controlled hydrolysis procedure show a completely different underlying morphology (Figure 5.9). The samples prepared by combustion synthesis have a similar morphology over a wide range of magnifications due to their fractal structure. In contrast, the nanocrystalline material prepared via wet chemical synthesis has a much more compact structure [210]. At the sub-micrometer scale, the compact structure is an aggregate of platelets about 200 nm large and 10 nm thick, arranged with some degree of orientation. Many of the platelets have irregular shapes, but there seems to be a roughly rounded basic unit that can merge together to give rise to larger particles [210].

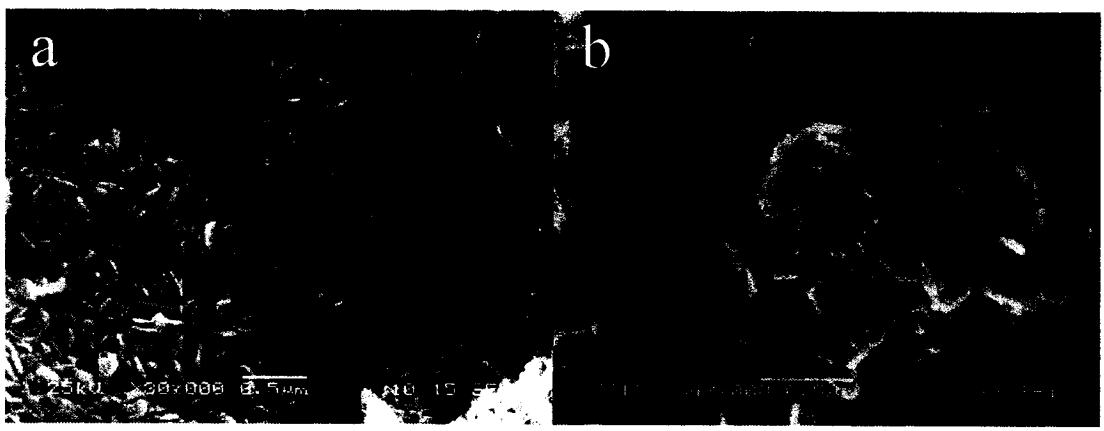

Figure 5.9: SEM micrographs of Y_2O_3 nanocrystals synthesized via a controlled hydrolysis procedure.

TEM micrographs show that the platelets have a non-uniform density as well as an inner structure, which is clear at higher magnifications. At the nanometer level, the platelets have a porous structure, with pores 2 – 4 nm randomly distributed inside the platelets (Figure 5.10a) [210]. At higher magnifications, fringes separated by 0.19 nm

become visible over the whole area of the image. The fringes are due to the (440) crystal planes of cubic yttrium oxide (Figure 5.10b) [210].

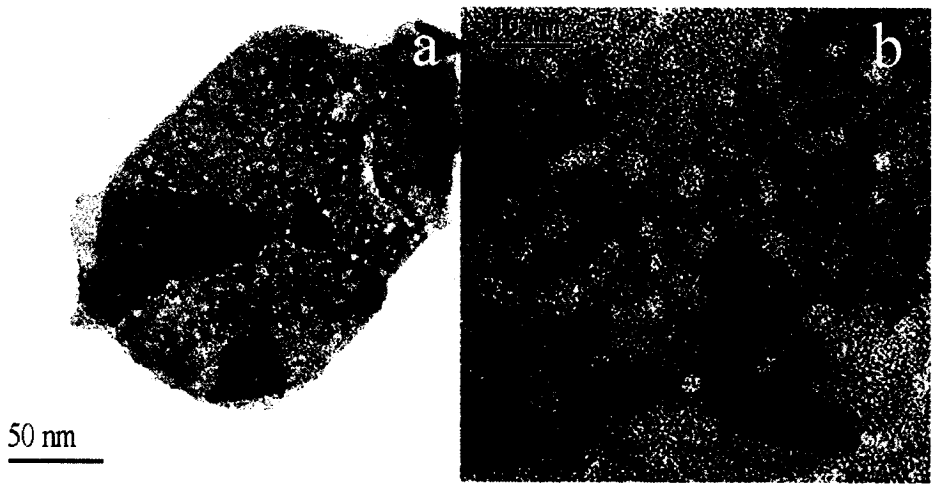

Figure 5.10: TEM micrographs of Y_2O_3 nanocrystals synthesized via a controlled hydrolysis procedure.

5.2. X-ray Diffraction

5.2.1. Sesquioxides

Cubic M_2O_3 (M = Y, Lu, or Sc) crystallizes in the *C* bixbyite structure, with space group *Ia3* (T_h^7) [222]. The M^{3+} ions occupy 24 sites in the unit cell with point symmetry C_2 and 8 sites with point symmetry C_{3i} (see Figure 5.11). The RE^{3+} ions replace the M^{3+} ions with no charge compensation and have been found to be statistically distributed in both sites of Y_2O_3 nanocrystals [223]. In either site, each M^{3+} and dopant RE^{3+} ion has around it six closest oxygen atoms. The presence of inversion symmetry in the C_{3i} site is important as it affects the luminescence spectra of the nanocrystals. The $f \rightarrow f$ electric dipole transitions are forbidden in the C_{3i} site according to the selection rules and as a result, the electric dipole transitions occur only by weak vibronic coupling. Thus, the luminescence spectra of the sesquioxides are ascribed to emissions from the ions residing in the C_2 symmetry sites (electric dipole allowed) and to the magnetic dipole allowed transitions from both the C_2 and C_{3i} sites.

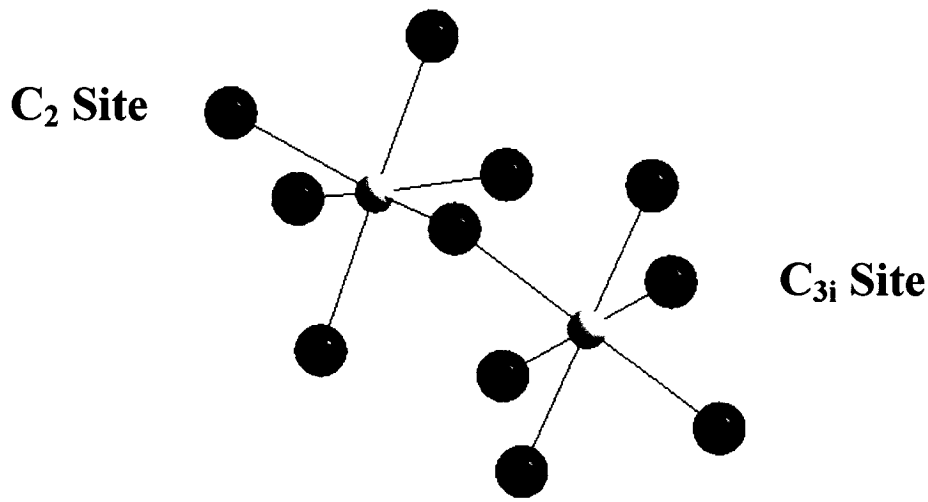

Figure 5.11: Pictorial representation of the C_2 and C_{3i} cation sites of the cubic Y_2O_3 lattice.

For the sesquioxides (prepared by both combustion and wet chemical synthesis), XRD patterns indicate that in all samples, the crystalline domains preserve the crystallographic structure of pure yttria, lutetia, and scandia, respectively (M_2O_3 where M = Y, Lu, or Sc, cubic system; space group *Ia*3). No other segregated phases are present, within the sensitivity of X-ray diffraction (Figure 5.13 – 5.14). Despite the very different morphology and nanostructure, the diffractograms of the Y_2O_3 nanocrystalline samples prepared by the two different techniques are almost identical. Furthermore, it is obvious that the Er^{3+} doped Y_2O_3 samples prepared by either propellant or wet chemical synthesis give rise to broader peaks, corresponding to nanocrystallites, while the XRD pattern of commercial Y_2O_3 gives rise to narrower peaks, corresponding to larger domains. Slight peak shifts are observed for the doped nanocrystal samples relative to the undoped material. The unit-cell edge value, *a*, in Y_2O_3:RE^{3+} nanocrystals, synthesized via both methods, was determined to undergo systematic variations in relation to the dopant and a good linear correlation was found between the unit-cell edge and the rare earth ionic radius [191]. Peak shifts are also observed for the 10 mol% Er^{3+} doped Sc_2O_3 sample [221] (see inset of Figure 5.14) and RE^{3+} doped Lu_2O_3 [220]. The unit-cell edge value, *a*, obtained for the undoped scandia sample (9.8378(7) Å) is smaller than the one reported in the literature [224] (9.8450(4) Å), whereas a larger value is obtained for the 10 mol% Er^{3+} doped sample (9.9056(5) Å), as expected from the larger value of the Er^{3+} ionic radius with respect to that of the Sc^{3+} ion [225]. Similarly for nanocrystalline Lu_2O_3:RE^{3+}, the unit-cell edge value, *a*, obtained for the undoped lutetia sample was exactly the one reported in the literature [226], whereas a roughly linear increase with the rare earth ionic radius [225] was observed with doping.

A quantitative line-broadening analysis of the diffraction peaks was performed to determine the average crystallite dimension (see Table 5.1) for all samples studied. No significant amorphous fraction was present in the material.

Table 5.1: Average crystallite dimensions, $\langle D \rangle_v$, obtained from two pairs of reflections (222/444 and 400/800) for all sesquioxide nanocrystals under investigation.

Sample	Synthesis Technique	$\langle D \rangle_v$ (nm)
$Y_2O_3:Er^{3+}$	Combustion	16
$Y_2O_3:Er^{3+}$, Yb^{3+}		
$Y_2O_3:Er^{3+}$	Wet Chemical	12
$Lu_2O_3:Er^{3+}$	Combustion	37
$Sc_2O_3:Er^{3+}$	Combustion	25

It should be noted that the bulk material, the microcrystalline sample prepared via conventional solid state synthesis, had particle sizes at least ten times larger than the corresponding nanocrystalline samples.

5.2.2. Garnets

The overall crystal structure of the garnets is cubic and belongs to the O^{10}_h (*Ia*3*d*) space group with eight equivalent gadolinium sites per elementary unit cell and having a lattice parameter of approximately 12 Å [227]. Their molecular formula can be expressed as $A_3B_2C_3O_{12}$, where B and C may be the same atoms ($Gd_3Ga_2Ga_3O_{12}$). The garnet lattice possesses three crystallographically distinct cation sites (c, a, and d, see Figure 5.12) available for dopant ion substitution [228]. In the c-site which has D_2 symmetry, the A ions are surrounded by a distorted dodecahedron of eight O^{2-} ions while

the B ions in the a-site of C_{3i} symmetry are surrounded by a trigonally distorted octahedron of O^{2-} ions. Finally in the d-site, which has S_4 site symmetry, the C ions are surrounded by an O^{2-} tetrahedron. Due to ionic size considerations in the GGG lattice, the RE^{3+} ions will predominantly enter the dodecahedral c-sites by replacing the Gd^{3+} and therefore possess D_2 symmetry. On the other hand, the transition metal ions will substitute the ions in the octahedral and/or tetrahedral sites of the garnet lattice [229].

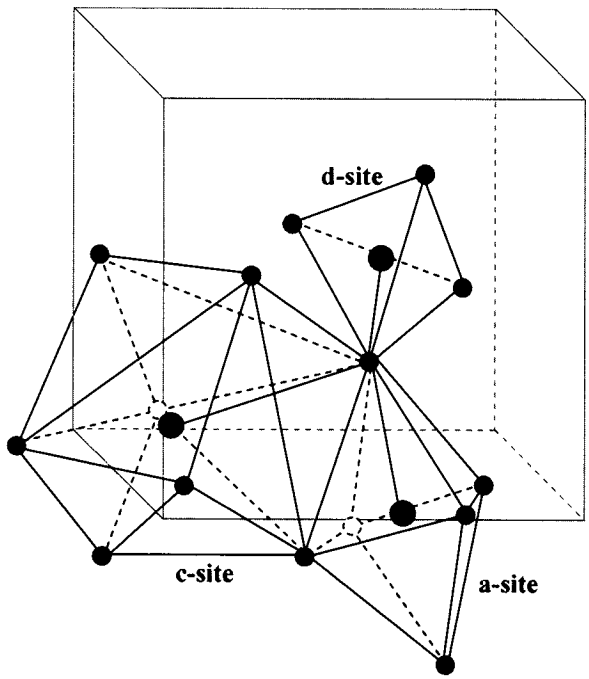

Figure 5.12: Pictorial representation of the polyhedra of the garnet structure showing: one dodecahedron (• A ions), one octahedron (• B ions), and one tetrahedron (• C ions).

For the $Gd_3Ga_5O_{12}$ nanocrystals, wide angle powder X-ray diffraction has confirmed that the samples under investigation contain GGG and that no important contamination from other phases is present. The broadening of the diffraction peaks indicates that the particle sizes are in the 10 nm range.

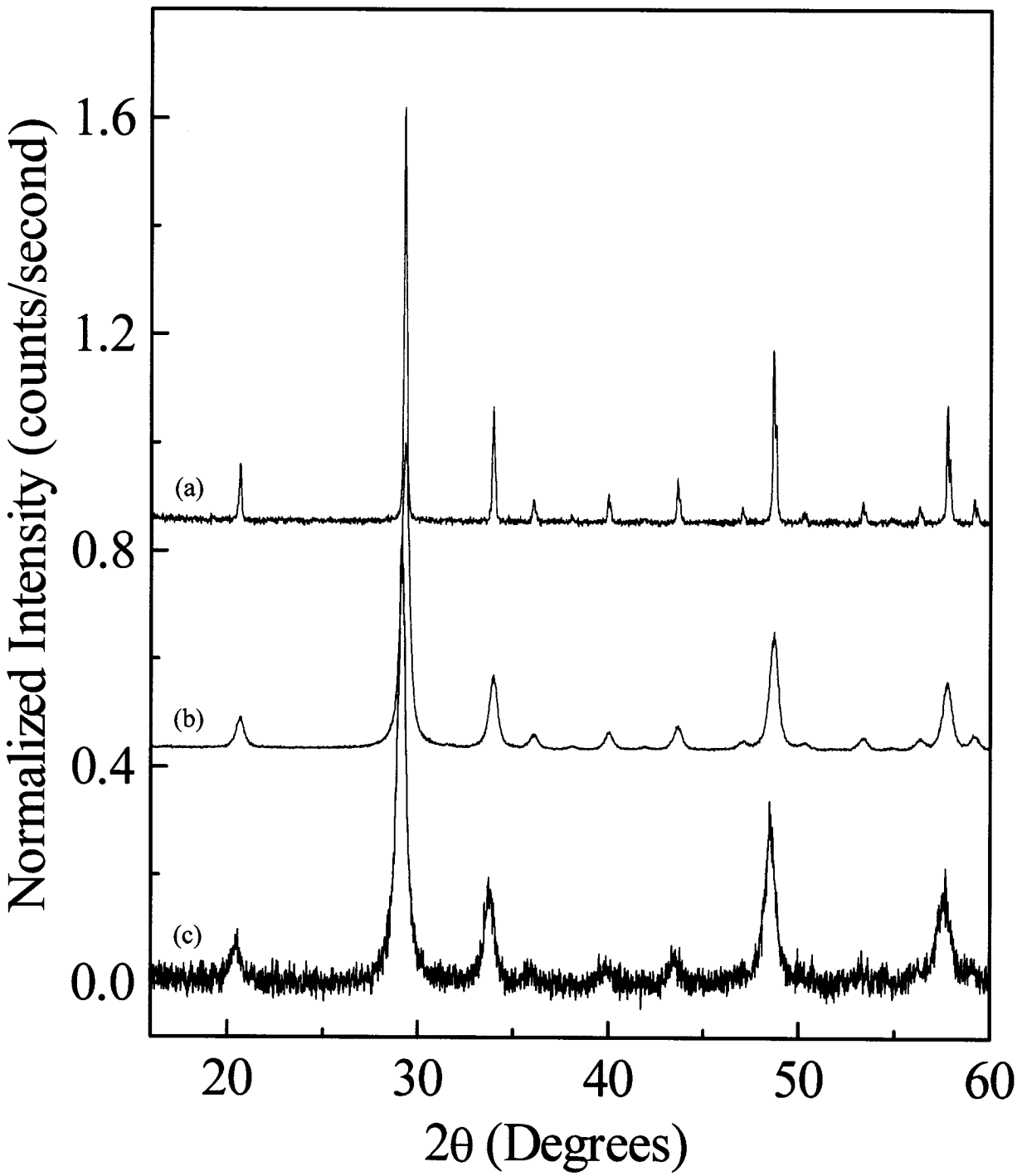

Figure 5.13: XRD patterns of the different Y_2O_3 samples. (a) Commercial Y_2O_3 (Aldrich, 99.99 %) (b) $Y_2O_3:Er^{3+}$ synthesized via combustion synthesis and (c) $Y_2O_3:Er^{3+}$ synthesized via the controlled hydrolysis procedure. All peaks normalized to the 222 reflection.

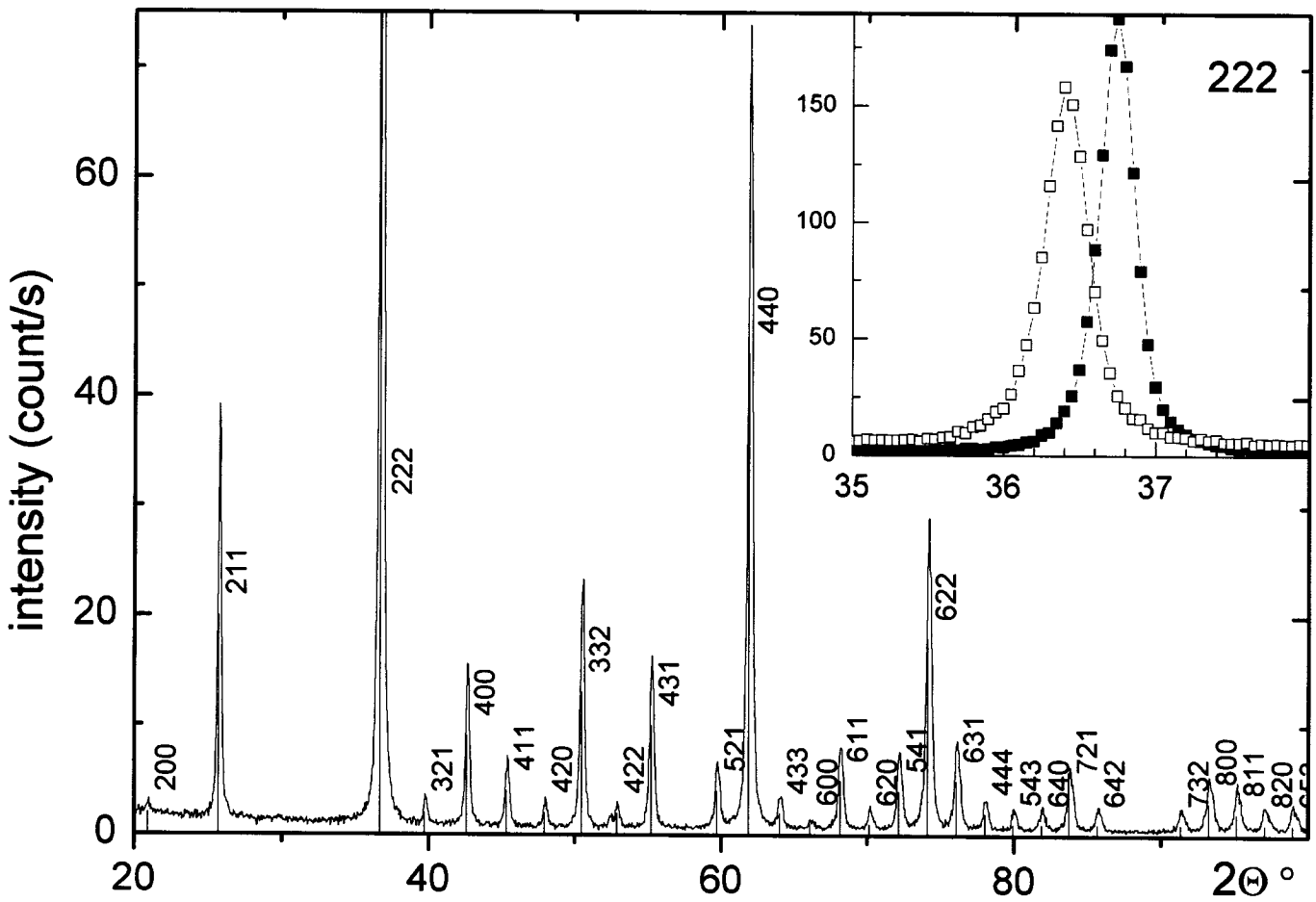

Figure 5.14: XRD pattern of the nanocrystalline Sc_2O_3 sample obtained by propellant synthesis. Inset: (222) peaks for the 10 mol% Er^{3+} doped (□) and undoped (■) nanocrystalline Sc_2O_3 showing the peak shifts and the different profile width. The (222) peak is not shown entirely in the full spectrum (see inset).

CHAPTER 6

6. Results and Discussion of the Spectroscopic Investigation

When this thesis was originally initiated, it was necessary to establish a baseline from which to extrapolate. This was deemed essential since the spectroscopy of Er^{3+} doped inorganic nanocrystals had never before been investigated. In this chapter, we present the results of the spectroscopic investigation of various Er^{3+} doped nanocrystalline materials and consequently, this chapter is divided into six main sections. In the first section, we investigated the spectroscopic properties of $Y_2O_3:Er^{3+}$ and $Y_2O_3:Er^{3+}$, Yb^{3+} nanocrystals prepared via solution combustion synthesis. This was our baseline study where we investigated a well known inorganic host material, a laser crystal and phosphor (Y_2O_3), but at the nanoscale and compared these results to the microcrystalline (bulk) material. In the subsequent section, we studied the same materials but synthesized via a different method, the controlled hydrolysis procedure, in order to determine whether the method of preparation had any effect on the spectroscopic behavior. In sections three and four, we explored nanocrystalline $Lu_2O_3:Er^{3+}$ and $Sc_2O_3:Er^{3+}$, respectively, also prepared via propellant synthesis. In that study, we attempted to ascertain whether changing the cation in the sesquioxide host material would significantly affect the spectroscopy. In the penultimate section, we moved away from the binary oxides and examined the more complex ternary nanocrystal $Gd_3Ga_5O_{12}:Er^{3+}$ and $Gd_3Ga_5O_{12}:Er^{3+}$, Yb^{3+} oxides again prepared via solution combustion. In the final section, we investigated the optical properties of Y_2O_3 and Lu_2O_3 nanocrystals (synthesized by combustion) but doped with other rare earth ions to observe if there are spectroscopic changes in these materials at the nanometer level.

6.1. An Investigation of $Y_2O_3:Er^{3+}$ and $Y_2O_3:Er^{3+}$, Yb^{3+} Nanocrystals Prepared Via Propellant Synthesis

6.1.1. Reflectance Spectroscopy

Diffuse reflectance spectra in the visible and UV regions were measured on all the nanocrystalline and bulk $Y_2O_3:Er^{3+}$ samples (1, 2, 5, and 10 mol% Er^{3+}). The reflectance spectrum of the $Y_2O_3:Er^{3+}$ (10 mol%) nanocrystals is shown in Figure 6.1; it is composed of a series of relatively sharp features in the visible region, accompanied by an absorption edge at approximately 350 nm. The sharp bands are assigned to the intraconfigurational $f-f$ transitions from the $^4I_{15/2}$ ground state of the Er^{3+} ion to the $^4F_{9/2}$, $^4S_{3/2}$, $^2H_{11/2}$, $^4F_{7/2}$, $^4F_{5/2}$, $^4F_{3/2}$, $^2H_{9/2}$, $^4G_{11/2}$, and $^2G_{9/2}$ excited states, whilst the edge is assigned to intrinsic absorption of the yttria host. The reflectance spectra of the more diluted nanocrystalline samples are characterized by weaker $f-f$ transitions, whose intensity scales with the Er^{3+} concentration (not shown). The onset of the UV edge of the nanosized samples does not appear to be influenced by the Er^{3+} concentration.

For comparison, the reflectance spectrum of bulk $Y_2O_3:Er^{3+}$ (10 mol%) shown in Figure 6.2 is composed of the same $f-f$ transitions, and an absorption edge extending from at least 400 nm. It is evident that the onset of the intrinsic absorption of the Y_2O_3 host, assigned to band-to-band transitions, is shifted towards the blue for the nanocrystals, compared to the bulk sample. In semiconductor nanocrystals, this phenomenon was attributed by some authors to quantum confinement [82]. However, quantum confinement is unlikely in insulating materials. The work of Konrad et al. disproved the notion that quantum confinement was the rationale for the blue shifted absorption edge in the reflectance spectrum of the Y_2O_3 nanocrystalline insulator [111].

They studied the luminescent properties of undoped nanocrystalline Y_2O_3 synthesized by a chemical vapor technique (10, 20, and 50 nm) and compared the results to an undoped bulk Y_2O_3 sample (10 μm). The authors used a quantum mechanical configurational coordinate diagram to describe the absorption and emission mechanisms caused by a localized exciton or luminescence center. As a consequence of the barrier-free self-trapping exciton in Y_2O_3, the measured emission spectrum was significantly Stoke shifted relative to the absorption spectrum. Thus, the absorption and emission properties within the configurational coordinate diagram were explained by the ground state and a single excited state parabola. The results were in agreement Blasse's results who found similarity between the optical transition behavior of Y_2O_3 and the charge transfer transition between the oxygen $2p$ and the empty d orbitals of the metal ions in oxo complexes [230].

In the range of weak quantum confinement, where the particle radius $R \geq 4a_B$ (a_B = excitonic Bohr radius), the energy upshift ΔE is given by [110, 231, 232]:

$$\Delta E = \frac{\hbar^2 \pi^2}{2\mu} \frac{1}{R^2} \qquad 6.1.1$$

where ΔE is the particle size dependent energy shift of the exciton excitation energy due to quantum confinement and μ is the reduced mass of the exciton, which is equal to $0.634m_e$ (m_e is the mass of the electron) and R is radius of the nanoparticle. The authors showed that their results were not in the possible range of the quantum confinement effect.

It is also very obvious that the bands in the reflectance spectrum of nanocrystalline $Y_2O_3:Er^{3+}$ were broadened compared to the bulk material. The reduced

resolution of the spectral features in the reflectance spectrum of the $Y_2O_3:Er^{3+}$ nanocrystal sample was very evident and believed to be due to inhomogeneous broadening induced by the presence of disorder in the nanomaterial. This phenomenon of spectral broadening in the nanocrystalline material will be discussed in significant detail later.

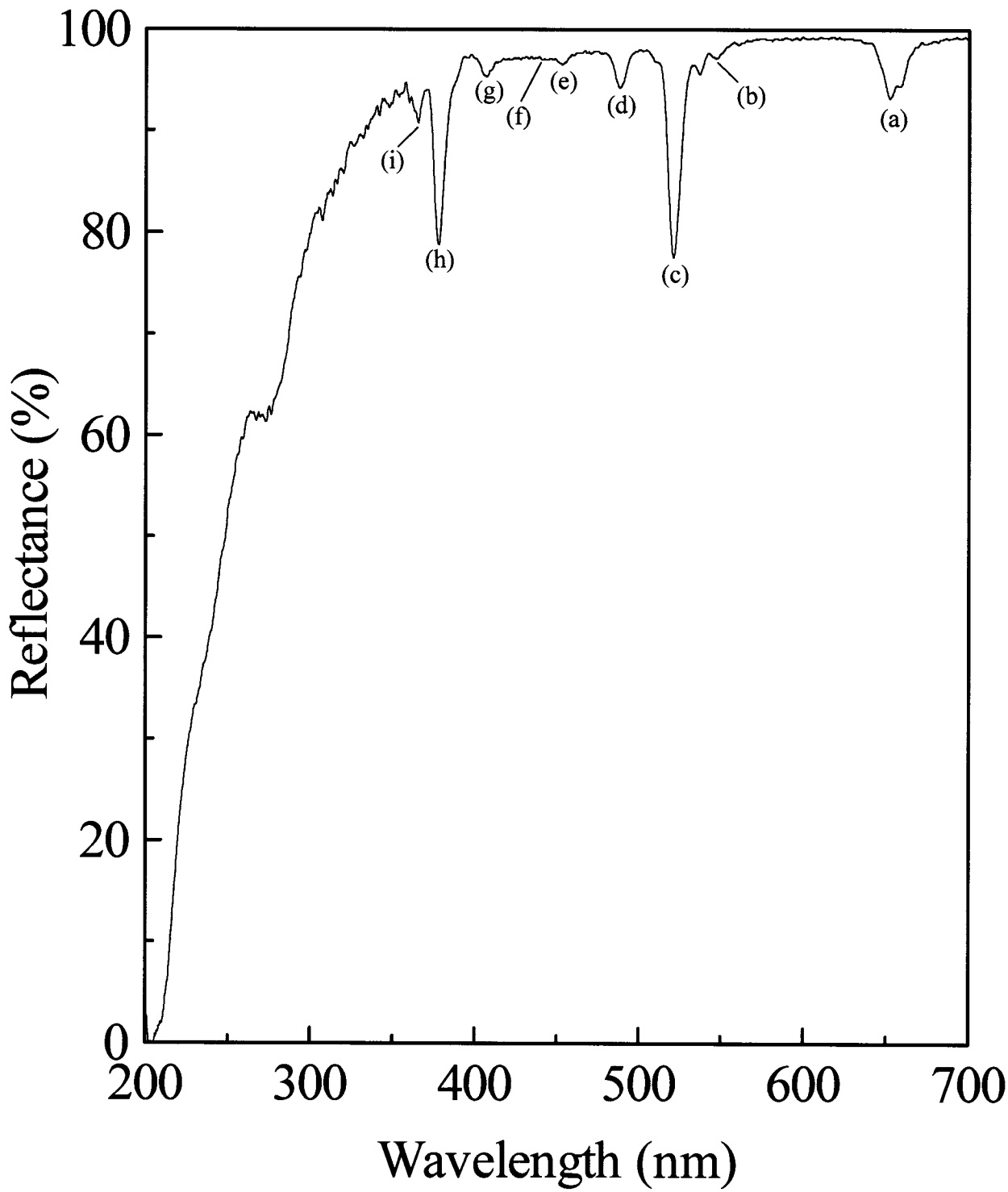

Figure 6.1: Reflectance spectrum of nanocrystalline $Y_2O_3:Er^{3+}$ (10 mol%) showing transitions from the $^4I_{15/2}$ ground state to the various Er^{3+} excited states:
(a) $^4F_{9/2}$, (b) $^4S_{3/2}$, (c) $^2H_{11/2}$, (d) $^4F_{7/2}$, (e) $^4F_{5/2}$, (f) $^4F_{3/2}$, (g) $^2H_{9/2}$, (h) $^4G_{11/2}$, (i) $^2G_{9/2}$.

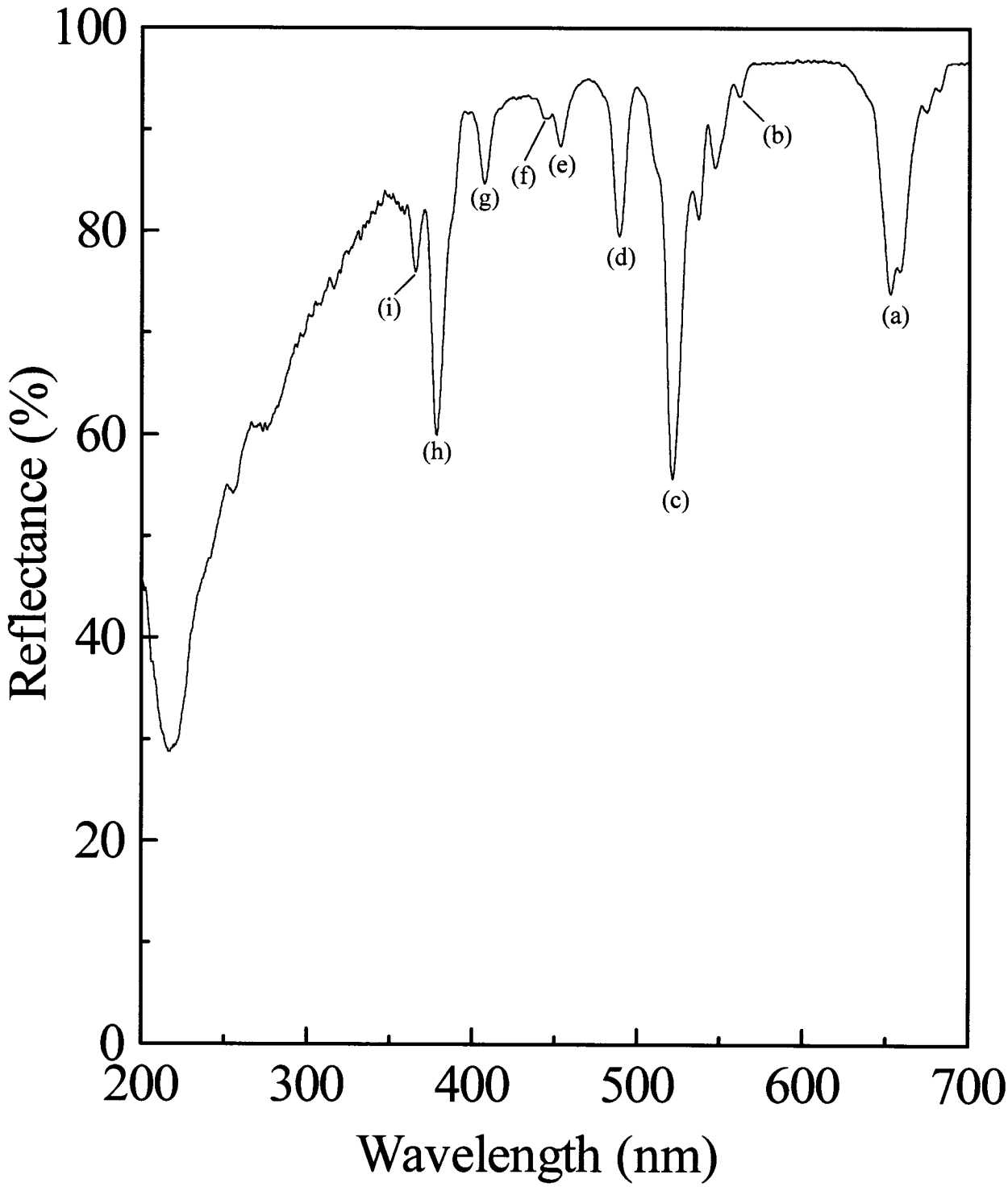

Figure 6.2: Reflectance spectrum of bulk $Y_2O_3:Er^{3+}$ (10 mol%) showing transitions from the $^4I_{15/2}$ ground state to the various Er^{3+} excited states:
(a) $^4F_{9/2}$, (b) $^4S_{3/2}$, (c) $^2H_{11/2}$, (d) $^4F_{7/2}$, (e) $^4F_{5/2}$, (f) $^4F_{3/2}$, (g) $^2H_{9/2}$, (h) $^4G_{11/2}$, (i) $^2G_{9/2}$.

6.1.2. Emission Spectroscopy of $Y_2O_3:Er^{3+}$ Nanocrystals

The room temperature visible luminescence spectra of nanocrystalline and bulk $Y_2O_3:Er^{3+}$ (10 mol%) excited at 488 nm are shown in Figure 6.3 where we observed four transitions in the green, red, and NIR portions of the spectrum [233]. In both bulk and nanocrystalline $Y_2O_3:Er^{3+}$, green emission was observed and attributed to the transition from the thermalized $^2H_{11/2}$ and $^4S_{3/2}$ states to the $^4I_{15/2}$ ground state, centered at 530 and 550 nm, respectively. Red emission was observed centered at 660 nm, attributed to the transition from the $^4F_{9/2}$ level to the ground state. Also, relatively weak NIR emission (Figure 6.3, inset) was observed centered at 810 and 860 nm and ascribed to the $^4I_{9/2} \rightarrow {}^4I_{15/2}$ and $^4S_{3/2} \rightarrow {}^4I_{13/2}$ transitions, respectively. The overall shape of the emission bands for the two samples were similar except for a slight difference in the relative intensity of the peaks at 520 – 540 nm (assigned to emission from the $^2H_{11/2}$ state), which were more intense for the nanocrystals. This was believed to be caused by the hypersensitivity of the $^2H_{11/2} \rightarrow {}^4I_{15/2}$ transition, whose intensity is strongly influenced by small distortions of the sites accommodating the Er^{3+} ions. Thus, the degree of distortion of the C_2 sites, in which the emitting dopant ions were found, was greater in the nanocrystalline material than in the bulk sample. This explanation is quite plausible since the nanocrystals were formed as a result of a violent reaction in the propellant synthesis. Therefore, it is probable that the unit cell may be slightly distorted consequently resulting in a minute distortion of the C_2 and C_{3i} dopant sites. However, it is also quite possible that there exists an alternative explanation for the greater $^2H_{11/2} \rightarrow {}^4I_{15/2}$ relative intensity of the nanocrystalline material. Liu et al. observed an optical thermalization effect in 20 – 40 nm $Y_2O_2S:Er^{3+}$ nanocrystals, which was not present in the 400 nm sized bulk material

[95]. This effect leads to the presence of "hot" bands that normally would not be present. In the case of the $^2H_{11/2}$ and $^4S_{3/2}$ states, a thermal equilibrium exists resulting in the $^4S_{3/2}$ state being responsible for populating the $^2H_{11/2}$ state. At room temperature, this thermalization is very efficient leading to the presence of the $^2H_{11/2} \rightarrow {}^4I_{15/2}$ transition. At elevated temperatures, the thermal process is obviously more efficient leading to an increased $^2H_{11/2} \rightarrow {}^4I_{15/2}$ emission intensity. The experimental conditions were identical for both the bulk and nanocrystalline samples. So, if the intensity of the $^2H_{11/2} \rightarrow {}^4I_{15/2}$ transition is greater in the nanocrystals, then it is logical to assume that they must "feel" a higher temperature than the bulk. The work of Liu et al. [95] revealed that in 20 nm $Y_2O_2S:Er^{3+}$ nanocrystals, the phonon modes with energy less than 200 cm^{-1} were significantly reduced. In fact, there existed no phonon modes below 24 cm^{-1}. This effectively prohibits the nanocrystals from dissipating heat as efficiently as the bulk essentially reducing the ability of the lattice wave to propagate through the nanocrystal. Consequently, this results in an increase in the apparent temperature felt by the nanocrystals and consequently increases the intensity of the $^2H_{11/2}$ hot bands. A more detailed investigation of the thermalization of $^2H_{11/2}$ and $^4S_{3/2}$ states will follow in Section 6.3.

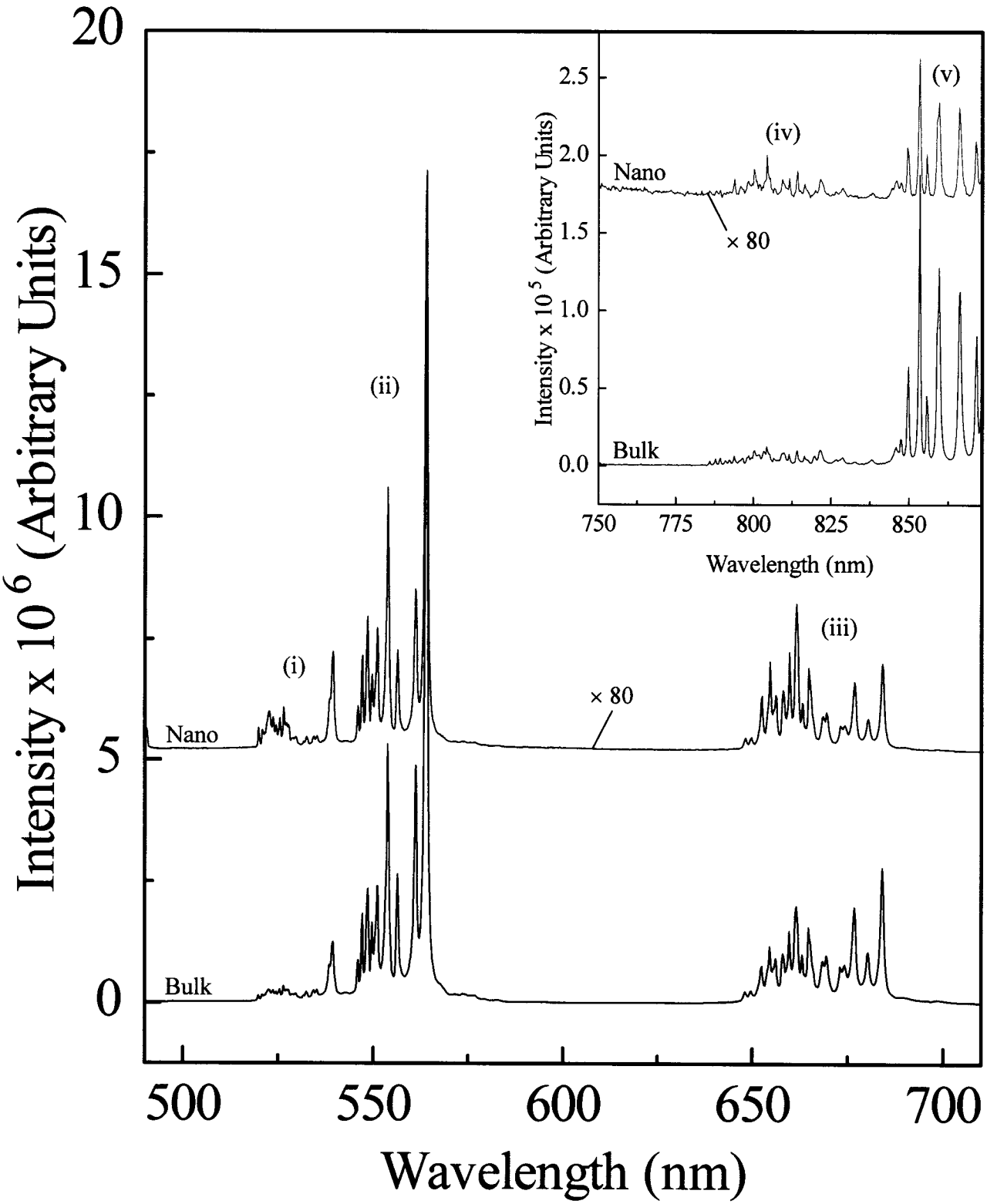

Figure 6.3: Room temperature luminescence of nanocrystalline and bulk $Y_2O_3:Er^{3+}$ (10 mol%) upon excitation at 488 nm. (i) $^2H_{11/2} \rightarrow {}^4I_{15/2}$ (ii) $^4S_{3/2} \rightarrow {}^4I_{15/2}$ (iii) $^4F_{9/2} \rightarrow {}^4I_{15/2}$. Inset: (iv) $^4I_{9/2} \rightarrow {}^4I_{15/2}$ (v) $^4S_{3/2} \rightarrow {}^4I_{13/2}$.

The emission spectra of 10 mol% bulk and nanocrystalline $Y_2O_3:Er^{3+}$ obtained at 77 K showed similar spectral features as the room temperature data. However, these spectra differ in that the $^2H_{11/2} \rightarrow {}^4I_{15/2}$ transition was not observed in the nanocrystalline and bulk samples at 77 K. At low temperatures, the feeding of the $^2H_{11/2}$ state from the $^4S_{3/2}$ state is very low and thus the intensity of the $^4S_{3/2} \rightarrow {}^4I_{15/2}$ transition increases with respect to the $^2H_{11/2} \rightarrow {}^4I_{15/2}$ one. As the temperature is raised, the $^2H_{11/2}$ level is populated thermally at the expense of the $^4S_{3/2}$ level causing the intensity of the $^2H_{11/2} \rightarrow {}^4I_{15/2}$ transition to increase while the intensity of the $^4S_{3/2} \rightarrow {}^4I_{15/2}$ transition decreases proportionally.

6.1.3. Decay Times of Bulk and Nanocrystalline $Y_2O_3:Er^{3+}$ (λ_{exc} = 488 nm)

The decay times, τ, of the green emitting excited states ($^2H_{11/2}$, $^4S_{3/2}$) were obtained from the fit of a single exponential model to the decay curves of the emission following excitation with 488 nm (Table 6.1). The measured τ value of the thermalized $^2H_{11/2}$, $^4S_{3/2}$ states in the $Y_2O_3:Er^{3+}$ (10 mol%) bulk material (56 μs) is comparable to the results obtained from other studies on $Y_2O_3:Er^{3+}$ crystalline materials [105, 234]. The decay times obtained for the identically doped $Y_2O_3:Er^{3+}$ nanocrystalline sample (3.8 μs) is significantly faster than that observed for the bulk material. In fact, the τ value for bulk $Y_2O_3:Er^{3+}$ (10 mol%) is more than one order of magnitude longer than for the nanocrystal sample with the same Er^{3+} concentration. This observation appears to be consistent with the fact that the relative intensity of the $^2H_{11/2}$, $^4S_{3/2} \rightarrow {}^4I_{15/2}$ transition compared to $^4F_{9/2} \rightarrow {}^4I_{15/2}$ is approximately three times weaker in the nanocrystalline sample. The Er^{3+} ion is known to undergo cross-relaxation processes of the type: $^2H_{11/2} + {}^4I_{15/2} \rightarrow {}^4I_{9/2} + {}^4I_{13/2}$.

This process quenches the luminescence and consequently, the decay time. Clearly, simple concentration quenching process cannot account for these remarkable differences, if a random distribution of Er^{3+} in the yttria nanocrystalline particles is present.

It has been suggested [189] that this behavior could indicate that the Er^{3+} tend to form clusters in nanocrystalline Y_2O_3, therefore making cross-relaxation processes more probable than in the corresponding bulk phase. However, an alternative explanation can be proposed. It is well known that yttria powders can adsorb atmospheric carbon dioxide and water, and the IR absorption spectra of Ce^{3+} doped Y_2O_3 powders clearly show the typical lines of the CO_3^{2-} ion [235]. In fact, the FTIR spectra of all the nanocrystalline materials under investigation show the presence of features at about 1500 and 3350 cm^{-1}, which are attributed to the presence of CO_3^{2-} and OH^- ions, respectively. The adsorption of these species is clearly easier in the case of the nanocrystalline materials obtained by the combustion synthesis, as this procedure yields powders characterized by an exceedingly small apparent density and by a large surface area (64 $m^2\ g^{-1}$, measured by the BET method), greater than that observed for other nanocrystalline yttria materials [236]. The presence of surface adsorption of atmospheric molecules is also confirmed by SAXS measurements, showing that doped and undoped Y_2O_3 prepared by combustion synthesis is characterized by fuzzy particle interfaces [190].

The presence of CO_3^{2-} and OH^- ions on the surface yields vibrational quanta of relatively high wavenumbers (1500 and 3350 cm^{-1}, respectively) compared to the intrinsic phonons of yttria (having a cut-off wavenumber of 597 cm^{-1} [237]), which are the only ones available in bulk $Y_2O_3:Er^{3+}$. The energy gap separating $^4S_{3/2}$ from the lower lying $^4F_{9/2}$ manifold is 2795 cm^{-1}. It is clear that for nanocrystalline $Y_2O_3:Er^{3+}$ the

presence of the extra vibrational quanta makes multiphonon relaxation of the $^2H_{11/2}$, $^4S_{3/2}$ excited states much more probable than for the bulk material, where at least 5 phonons are required to bridge the gap. The fact that the $^4F_{9/2}$ state is relatively less quenched in the samples obtained by combustion synthesis than in the bulk material [189] could be explained using the same argument. In fact, in the latter material this state is already efficiently relaxed by multiphonon relaxation, since a lower number of phonons are required (slightly more than 4) to bridge the gap from the $^4I_{9/2}$ state (2516 cm^{-1}). This state appears to be strongly quenched in the nanostructured samples, by the presence of the high wavenumber carbonate stretching vibration, as it appears to be non-luminescent.

Table 6.1: Decay times obtained from an exponential fit of the room temperature decay curves for the $^4S_{3/2} \rightarrow {}^4I_{15/2}$ transition upon 488 nm excitation.

Sample	Concentration (mol%)	Decay Time, τ (μs)
Nanocrystalline $Y_2O_3:Er^{3+}$	1	34
	2	31
	5	12
	10	3.8
Bulk $Y_2O_3:Er^{3+}$	10	56

6.1.4. Consequence of Adsorbed Surface Species

As discussed earlier, in nanocrystalline yttrium oxide, CO_2, and H_2O are produced as byproducts of the propellant synthesis reaction and could be adsorbed immediately after the formation of the nanoparticles. As the preparation is performed in air, CO_2 and H_2O could be adsorbed from air as well. The residual nitrate ions are decomposed after firing the nanocrystals at 500 °C for 1 h as was evidenced by the absence of their characteristic bands in the medium-infrared (MIR) and Raman spectra. However, this heat treatment was not sufficient to remove either the carbonate or hydroxyl ions from the surface of the nanopowders. The MIR spectra obtained after the heat treatment show bands occurring at approximately 1500 and 3350 cm^{-1} and are assigned to vibrations from the carbonate and hydroxyl groups, respectively (see Figure 6.4-a). In order to reduce the amount of CO_3^{2-} and OH^- ions on the surface of the nanoparticles, additional heat treatments on a nanocrystalline $Y_{1.80}Er_{0.20}O_3$ sample were carried out [238]. Initially, the sample was treated at 800 °C for 17 hours and subsequently cooled to room temperature. The same sample was further treated at 1000 °C for 65 hours and then cooled again to room temperature. From the MIR spectra of the doped nanoparticles after the successive heat treatments, bands were still observed at approximately 1500 and 3350 cm^{-1} (Figure 6.4-b). After the second heat treatment, the overall intensities of the bands at 1500 and 3350 cm^{-1} indicate that the heat treatments did reduce the overall surface contamination but, in the present experimental conditions, the contaminants were not completely removed. On the other hand, a longer heat treatment at higher temperatures could induce an aggregation of the nanoparticles, a process in which they combine to form larger particles. In this case, as the spectroscopy of the nanocrystalline material is particle size

dependent, a comparison between the luminescence of the heat-treated and non-heat treated nanocrystalline materials could be difficult to make. We further undertook another thermal treatment on a nanocrystalline $Y_{1.98}Er_{0.02}O_3$ sample in which the nanocrystals were heated under an N_2 flow (2 liters/minute) for 2 hours at 700 °C (Figure 6.4, inset) [239]. The nanocrystals were then cooled to 200 °C under the N_2 flux after which the sample was sealed in a vacuum box. Once the sample had cooled to room temperature, the MIR spectrum was immediately measured. Bands attributed to CO_2 and H_2O are still evidenced. In Figure 6.4-c, a bulk sample is also shown for comparison and shows no bands at either 1500 or 3350 cm^{-1} indicating the lack of adsorption of CO_2 and H_2O. Therefore it is important to note that when studying the optical properties of nanocrystalline $Y_2O_3:Er^{3+}$ or related materials obtained by the same synthesis technique, the surface contaminants must be taken into account.

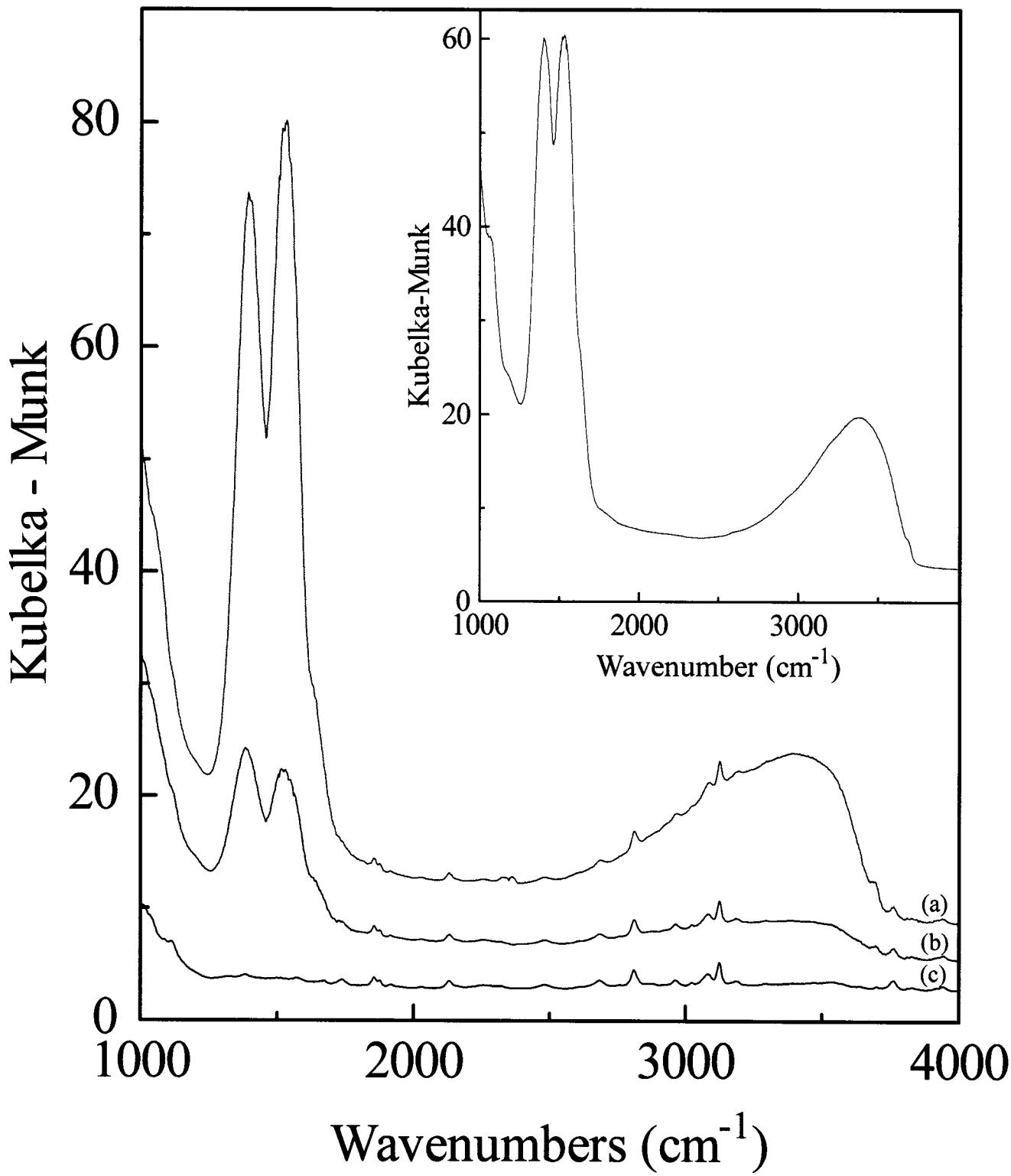

Figure 6.4: Diffuse reflectance spectra of nanocrystalline $Y_2O_3:Er^{3+}$ (10 mol%) following sequential heat treatment: (a) 800 °C for 17 h (b) 1000 °C for 65 h (c) bulk $Y_2O_3:Er^{3+}$ (10 mol%) sample shown for comparison. Inset: Diffuse reflectance spectrum of nanocrystalline $Y_2O_3:Er^{3+}$ (1 mol%) following heat treatment under an N_2 flow (2 liters/minute) for 2 hours at 700 °C.

6.1.5. Concentration Dependence of the Luminescence Properties in $Y_2O_3:Er^{3+}$

In sections 6.1.2 – 6.1.3, we discussed the basic optical properties of $Y_2O_3:Er^{3+}$, both bulk and nanocrystalline. Specifically, the emission spectra of the 10 mol% bulk and nanocrystalline cubic $Y_2O_3:Er^{3+}$ samples as well as the decay time of the $^4S_{3/2} \rightarrow {}^4I_{15/2}$ transition following excitation with 488 nm. In this section, we extend the spectroscopic investigation by studying the effects of Er^{3+} concentration (1, 2, 5, and 10 mol%) on the visible luminescence properties of bulk and nanocrystalline cubic Y_2O_3 [238]. The visible luminescence spectra of bulk and nanocrystalline $Y_2O_3:Er^{3+}$ (1, 2, 5, and 10 mol%) are shown in Figures 6.5 and 6.6, respectively. Bands are observed in the 550 and 675 nm region of the spectra and are assigned to the transitions from the thermalized ($^2H_{11/2}$, $^4S_{3/2}$) and $^4F_{9/2}$ excited states, respectively, to the $^4I_{15/2}$ ground state of Er^{3+} ions in the C_2 and C_{3i} sites. This is in good agreement with previous experimental [240] and theoretical [29] studies. Furthermore, the similarity in the emission spectra indicates that the crystal field is not significantly altered with the addition of Er^{3+} up to 10 mol%.

Table 6.1 clearly shows that the decay times of the $^4S_{3/2}$ excited state in the nanosized materials increase significantly when the Er^{3+} concentration decreases. This is the result of the reduced efficiency of the previously discussed $^2H_{11/2} + {}^4I_{15/2} \rightarrow {}^4I_{9/2} + {}^4I_{13/2}$ cross-relaxation pathway. At lower concentrations, the dopant ions are further apart resulting in a lower probability of interaction thus leading to a longer observed decay time. For the most diluted nanocrystalline $Y_2O_3:Er^{3+}$ sample (1 mol%), the observed decay time is one order of magnitude longer than its 10 mol% counterpart and almost approaches the value obtained for the 10 mol% bulk material.

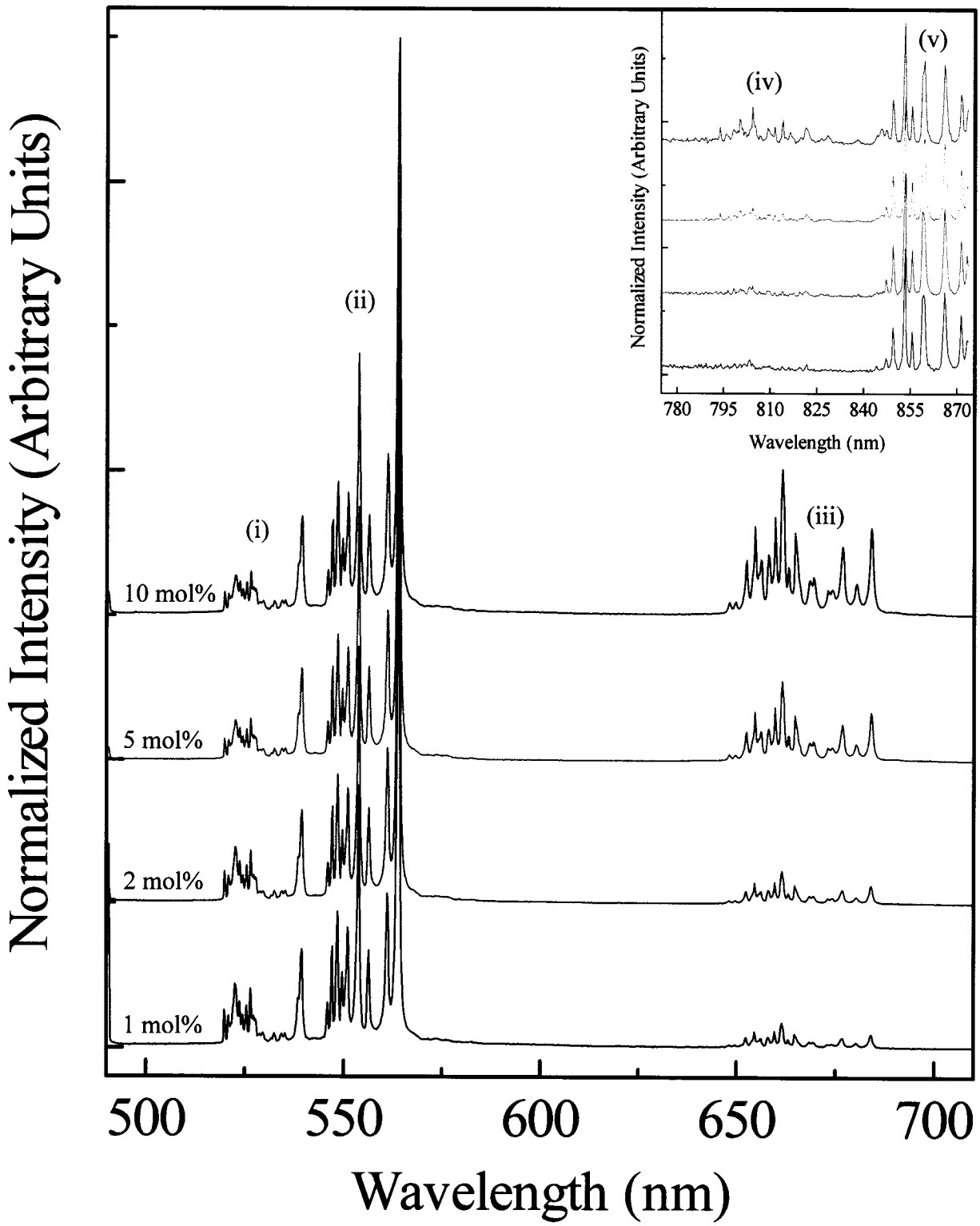

Figure 6.5: Room temperature luminescence of nanocrystalline $Y_2O_3:Er^{3+}$ (1, 2, 5, and 10 mol%) upon excitation at 488 nm. (i) $^2H_{11/2} \rightarrow {}^4I_{15/2}$ (ii) $^4S_{3/2} \rightarrow {}^4I_{15/2}$ (iii) $^4F_{9/2} \rightarrow {}^4I_{15/2}$. Inset: (iv) $^4I_{9/2} \rightarrow {}^4I_{15/2}$ (v) $^4S_{3/2} \rightarrow {}^4I_{13/2}$.

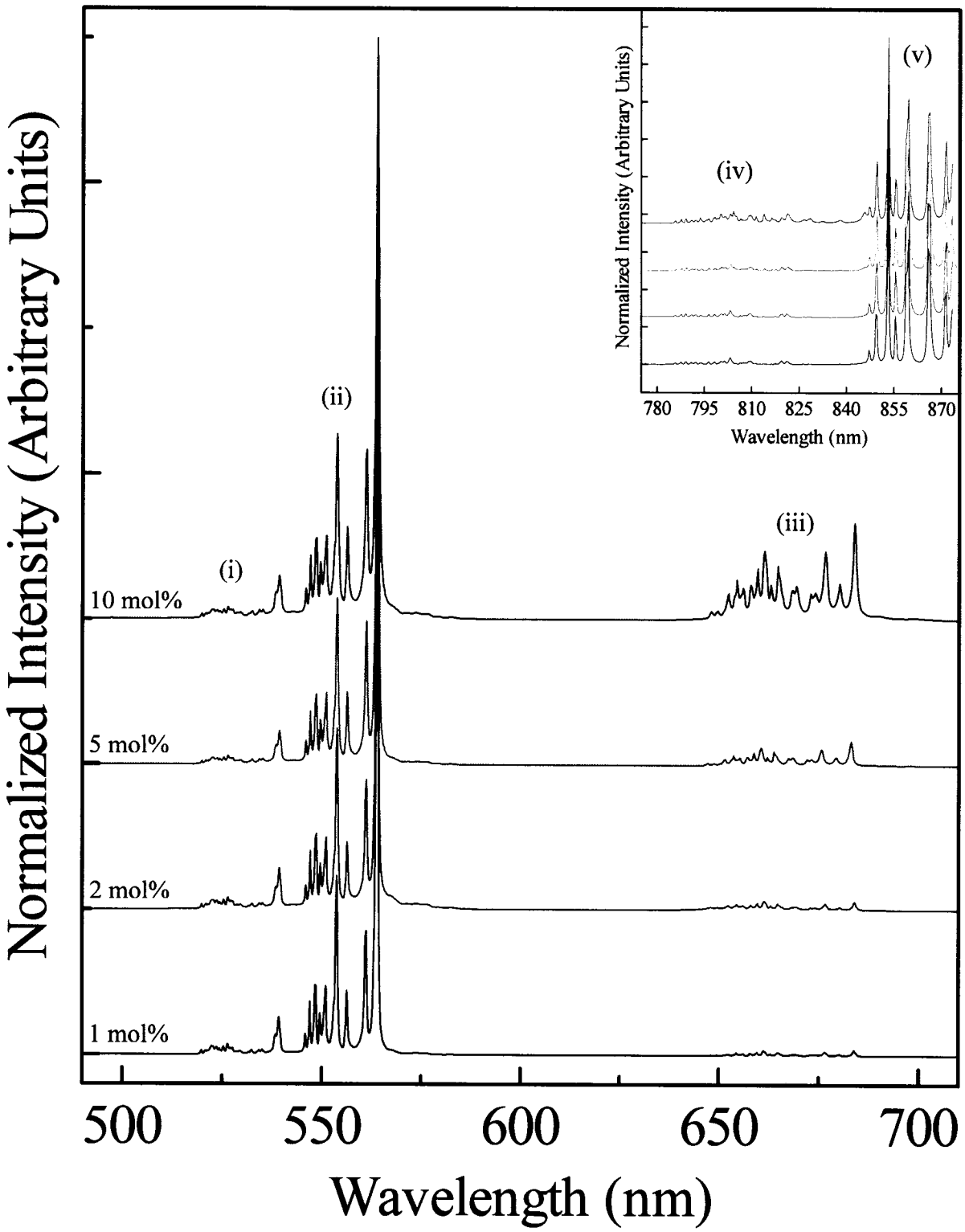

Figure 6.6: Room temperature luminescence of bulk $Y_2O_3:Er^{3+}$ (1, 2, 5, and 10 mol%) upon excitation at 488 nm. (i) $^2H_{11/2} \rightarrow {}^4I_{15/2}$ (ii) $^4S_{3/2} \rightarrow {}^4I_{15/2}$ (iii) $^4F_{9/2} \rightarrow {}^4I_{15/2}$. Inset: (iv) $^4I_{9/2} \rightarrow {}^4I_{15/2}$ (v) $^4S_{3/2} \rightarrow {}^4I_{13/2}$.

6.1.6. Anti-Stokes (Upconversion) Luminescence Spectroscopy Following Excitation into the $^4I_{9/2}$ Level (λ_{exc} = 815 nm)

Continuous wave excitation with NIR radiation (815 nm) into the $^4I_{9/2} \leftarrow {}^4I_{15/2}$ transition of the bulk and nanocrystalline samples produced intense luminescence peaks in the visible region (Figures 6.7 and 6.8) [238]. The peaks were assigned to the following transitions; green emission in the 520-570 nm region assigned to the ($^2H_{11/2}$, $^4S_{3/2}$) $\rightarrow$ $^4I_{15/2}$ transition and red emission in the 650-700 nm region assigned to the $^4F_{9/2}$ $\rightarrow$ $^4I_{15/2}$ transition for Er^{3+} ions in the C_2 and C_{3i} sites of Y_2O_3. Also, it should be noted that a relatively weak blue emission was observed in bulk Y_2O_3:Er^{3+} (Figure 6.9). The peaks were assigned to the $^4F_{5/2} \rightarrow {}^4I_{15/2}$ and $^4F_{7/2} \rightarrow {}^4I_{15/2}$ transitions in the 450-465 nm and 485-505 nm regions, respectively. We have also observed a manifold in the 468-480 nm region and have assigned it to the intraconfigurational $^2P_{3/2} \rightarrow {}^4I_{11/2}$ transition. Interestingly, no blue emission was observed in the nanocrystalline samples.

After irradiating the nanocrystalline material with 815 nm, we notice primarily that the absolute intensities of the ($^2H_{11/2}$, $^4S_{3/2}$) $\rightarrow$ $^4I_{15/2}$ and $^4F_{9/2} \rightarrow {}^4I_{15/2}$ transitions are very weak in the 1 mol% sample when compared to the sample with 10 mol% dopant concentration. However, as the Er^{3+} dopant concentration is increased, the upconversion luminescence becomes more intense. At this point, we should note that the bulk samples do not follow the same general trend as its nanocrystalline counterpart. In the bulk material, the absolute intensities of the ($^2H_{11/2}$, $^4S_{3/2}$) $\rightarrow$ $^4I_{15/2}$ and $^4F_{9/2} \rightarrow {}^4I_{15/2}$ transitions increase up to 5 mol% and then decrease in absolute intensity for the 10 mol% sample.

Furthermore, we have observed an enhancement of red emission upon 815 nm excitation. The intensity of the red ($^4F_{9/2} \rightarrow {}^4I_{15/2}$) emission increases at a more rapid rate

than the green [($^2H_{11/2}$, $^4S_{3/2}$) → $^4I_{15/2}$] emission. In fact, the enhancement of the red emission is clearly evident upon comparing the calculated relative intensities of the ($^2H_{11/2}$, $^4S_{3/2}$ → $^4I_{15/2}$) and ($^4F_{9/2}$ → $^4I_{15/2}$) transitions. In the nanocrystalline material, the 1 mol% sample has a relative (Green:Red) intensity ratio of 3.5:1. As the dopant concentration is increased, the red component becomes more prominent which affects the relative intensity ratio. For example, in the 10 mol% sample the ratio becomes 1:2.7. In the bulk material, the enhancement is slightly less prominent. In the 1 mol% sample, we obtain a ratio of 3:1 while in the 10 mol% sample, the ratio is approximately 1:1. From this observation, we postulate that the channel populating the red upconversion is more concentration dependant in the nanocrystalline material than for its bulk counterpart.

While the relative enhancement of the red emission ($^4F_{9/2}$ → $^4I_{15/2}$) is observed in the upconverted luminescence, it was also observed in the direct luminescence spectra (λ_{exc} = 488 nm). However, the effect of the $^4F_{9/2}$ enhancement is clearly much more pronounced when exciting at 815 nm. This is demonstrated in Figures 6.10 and 6.11 which show a graph of the ratio of the integrated intensity of the green emission [($^2H_{11/2}$, $^4S_{3/2}$) → $^4I_{15/2}$] over that of the red emission [$^4F_{9/2}$ → $^4I_{15/2}$], versus Er^{3+} concentration, for the bulk and nanocrystalline samples at both (488 and 815 nm) wavelengths. We observe that for both the bulk and nanocrystalline samples, as the dopant concentration is increased, the difference in ratios becomes less significant.

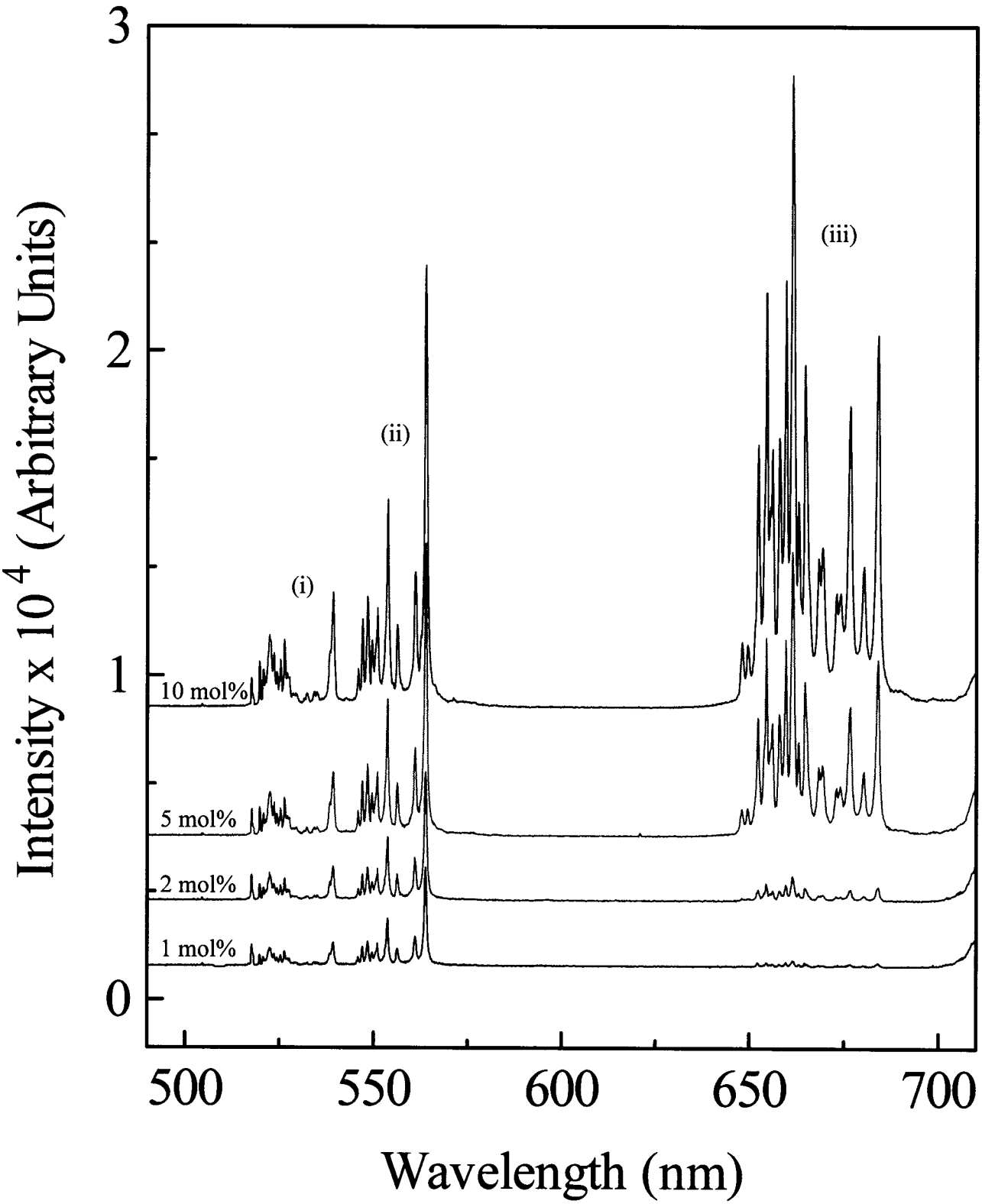

Figure 6.7: Upconverted emission of Er^{3+} doped Y_2O_3 nanocrystals (1, 2, 5, and 10 mol%) at room temperature, showing (i) $^2H_{11/2} \rightarrow {}^4I_{15/2}$ (ii) $^4S_{3/2} \rightarrow {}^4I_{15/2}$ (iii) $^4F_{9/2} \rightarrow {}^4I_{15/2}$, λ_{exc} = 815 nm.

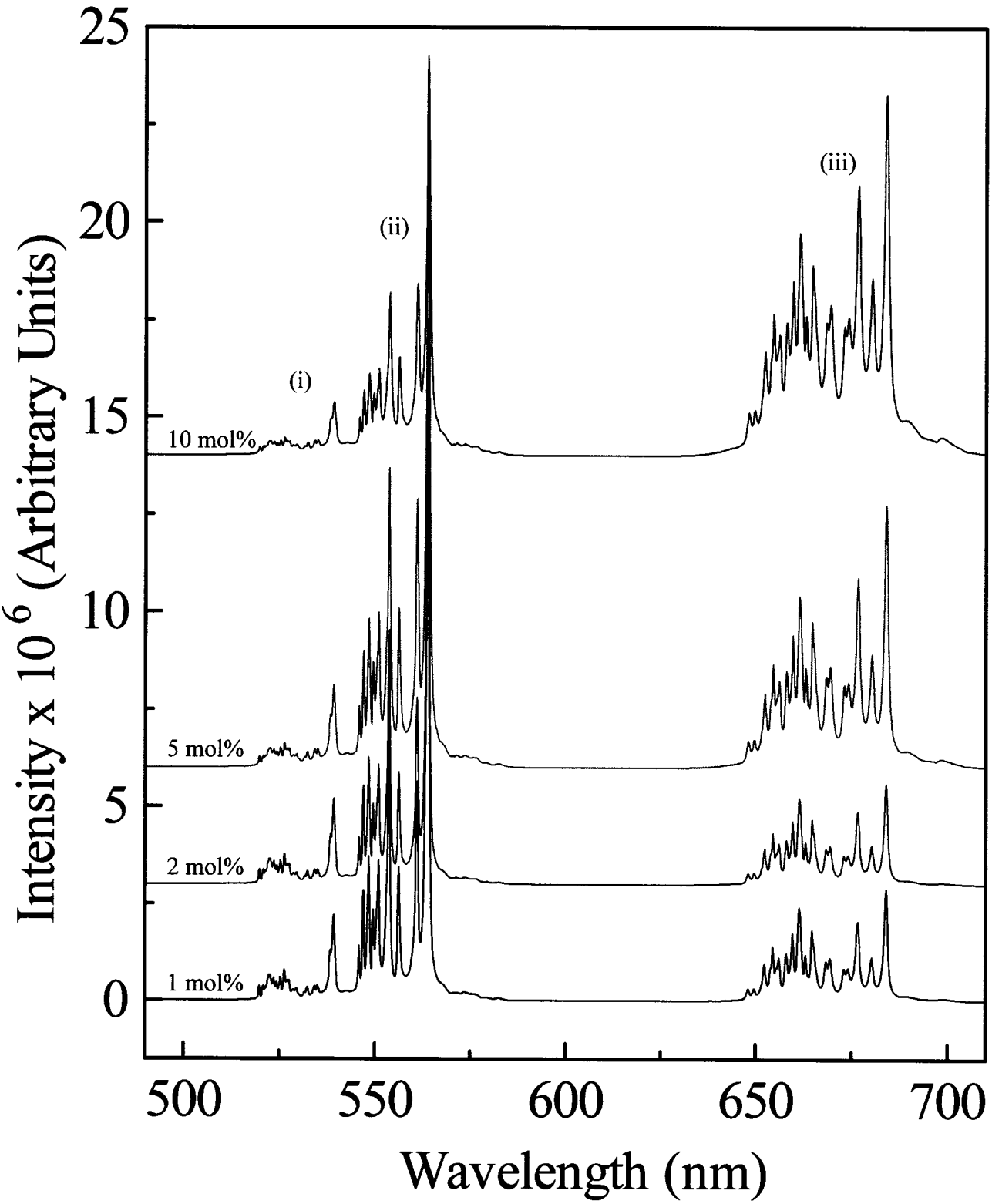

Figure 6.8: Upconverted emission of bulk Er^{3+} doped Y_2O_3 (1, 2, 5, and 10 mol%) at room temperature, showing (i) $^2H_{11/2} \rightarrow {}^4I_{15/2}$ (ii) $^4S_{3/2} \rightarrow {}^4I_{15/2}$ (iii) $^4F_{9/2} \rightarrow {}^4I_{15/2}$, $\lambda_{exc} = 815$ nm.

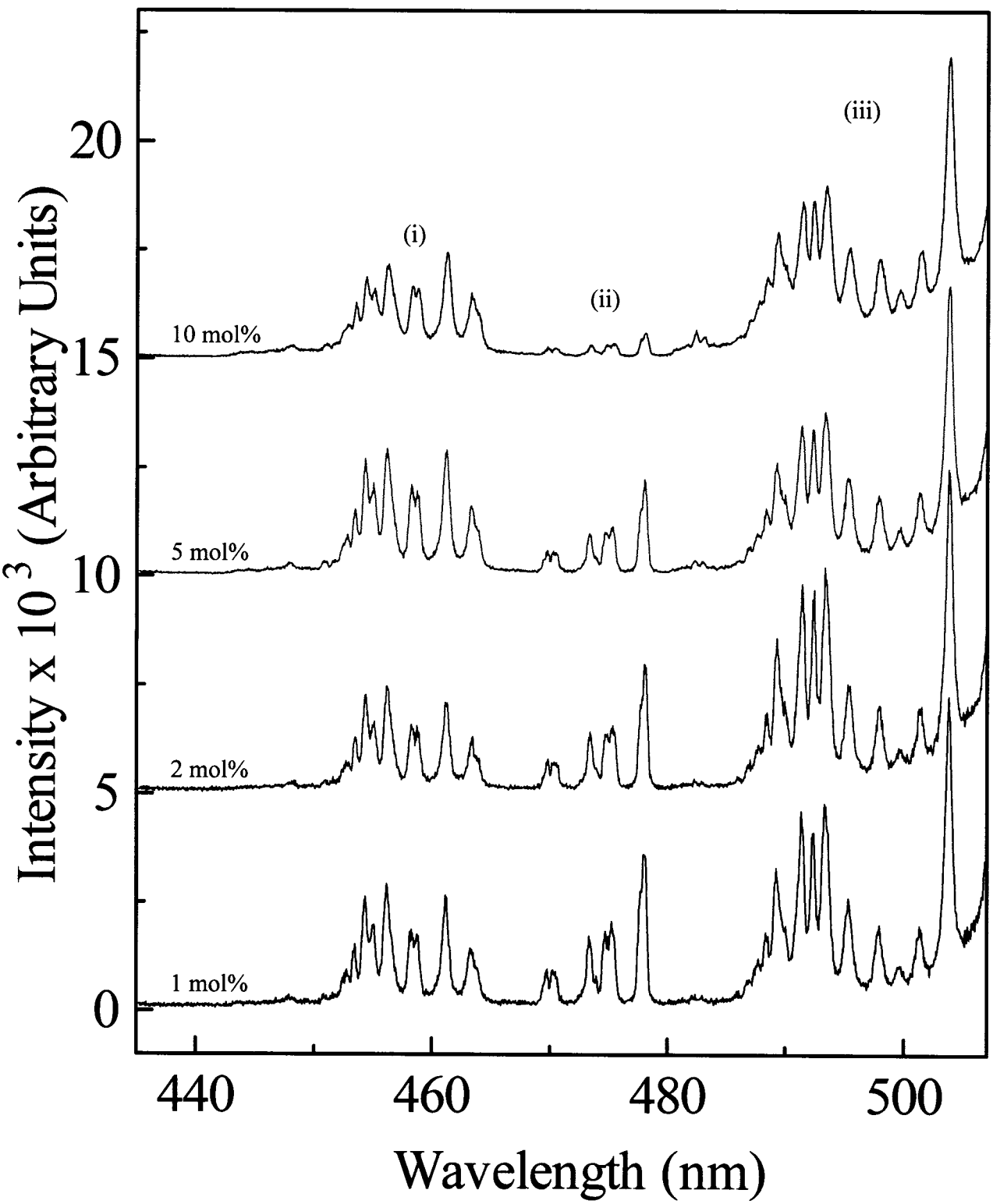

Figure 6.9: Upconverted emission of bulk $Y_2O_3:Er^{3+}$ (1, 2, 5, and 10 mol%) at room temperature, showing (i) $^4F_{5/2} \rightarrow {}^4I_{15/2}$ (ii) $^2P_{3/2} \rightarrow {}^4I_{11/2}$ (iii) $^4F_{7/2} \rightarrow {}^4I_{15/2}$, λ_{exc} = 815 nm.

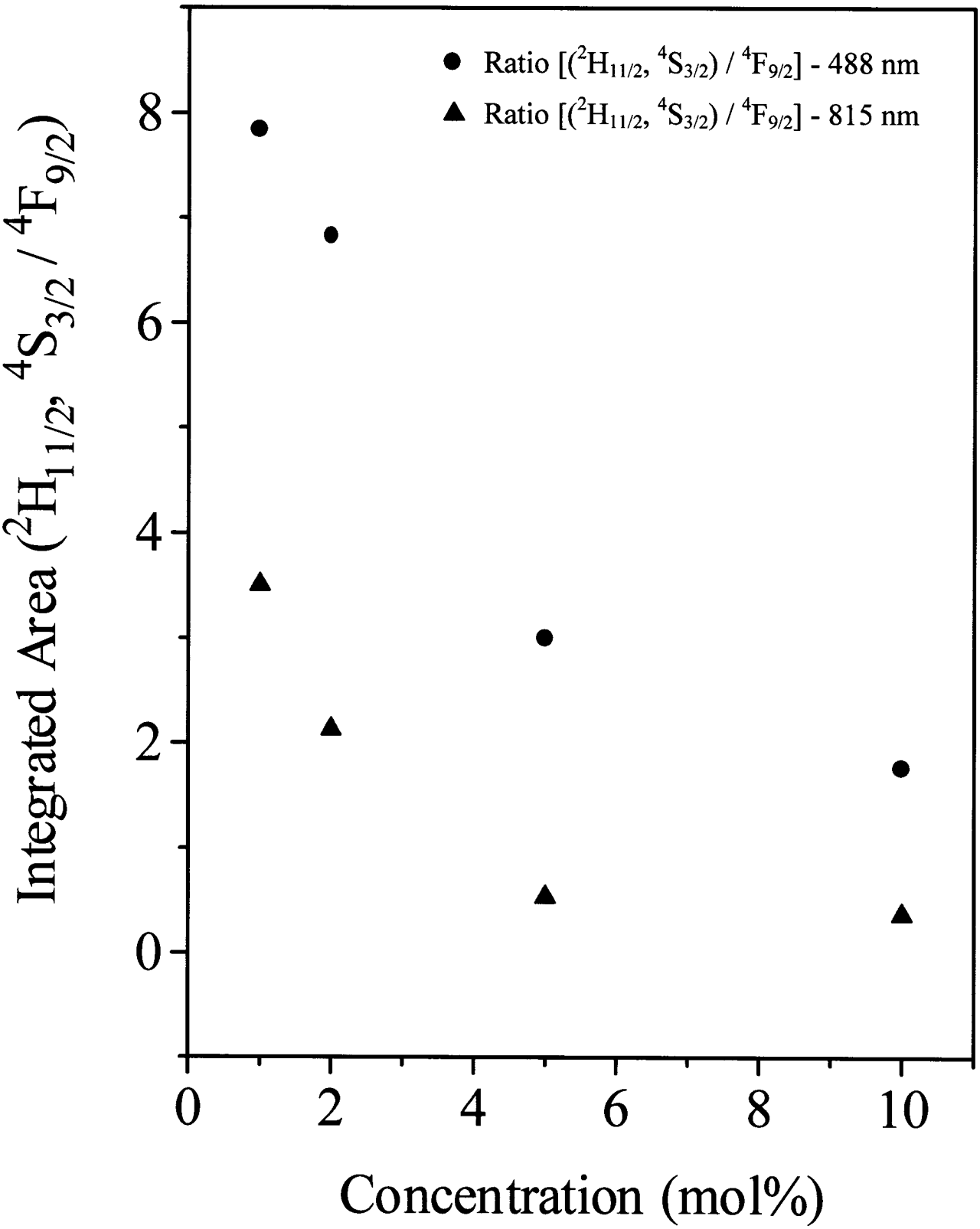

Figure 6.10: Graph of the ratio of the integrated areas of the ($^2H_{11/2}$, $^4S_{3/2}$) → $^4I_{15/2}$ and $^4F_{9/2}$ → $^4I_{15/2}$ bands [($^2H_{11/2}$, $^4S_{3/2}$) / $^4F_{9/2}$] versus Er^{3+} concentration for the nanocrystalline material

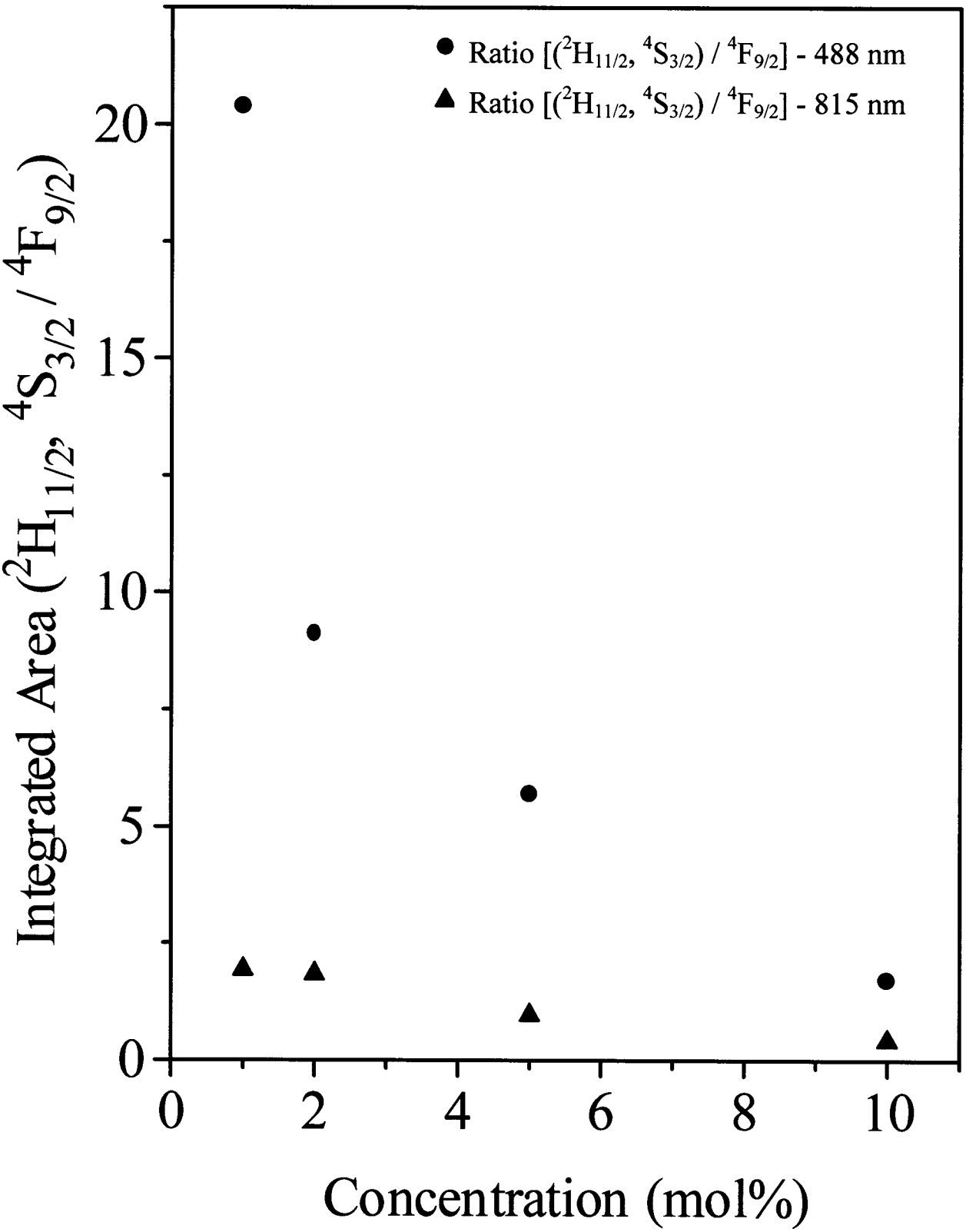

Figure 6.11: Graph of the ratio of the integrated areas of the ($^2H_{11/2}$, $^4S_{3/2}$) → $^4I_{15/2}$ and $^4F_{9/2}$ → $^4I_{15/2}$ bands [($^2H_{11/2}$, $^4S_{3/2}$) / $^4F_{9/2}$] versus Er^{3+} concentration for the bulk material

6.1.7. Comparison of the Stokes (λ_{exc} = 488 nm) and Upconversion (λ_{exc} = 815 nm) Spectra

Comparison of the $^2H_{11/2}$, $^4S_{3/2}$, and $^4F_{9/2}$ emission peak shapes in both the upconversion and downconversion spectra for all nanocrystalline samples under investigation showed no dissimilarities. The same is also observed for the bulk samples. That is, the peak shape is insensitive to dopant concentration or pump wavelength. While the overall peak shape is the same, the relative intensities of several peaks are significantly different. In particular, the peaks at λ = 670 nm are clearly more intense for the bulk material. This difference in the relative intensities within the manifolds may be attributed to the vibronic transitions associated with the C_{3i} sites, which may be stronger in the bulk sample due to more favorable electron-phonon coupling [233].

Although the spectra are identical and unaffected by the pump wavelength, 488 or 815 nm, there is a notable reduction in the overall luminescence when pumping with 815 nm. We have discussed how yttria nanoparticles prepared by the propellant synthesis adsorb CO_2 and H_2O. The presence of these groups on the surface yields vibrational quanta of relatively high wavenumbers compared to the phonons of pure yttria (phonon cutoff $\approx$600 cm^{-1}), which are the only ones available in the bulk material. The rate of multiphonon relaxation is dependent upon the energy gap separating the emitting state and the next lower lying state as well as the highest phonon energy in the material [241]. The rate of the multiphonon relaxation can be expressed as [106]:

$$W_{MPR} = C \exp^{-\alpha \Delta E} \qquad 6.1.2$$

where ΔE is the energy gap to the next lower level and the parameters C and α are constants that can be derived from the measurements of the luminescence decay times and the calculation of the radiative transition rates. It follows that in the nanocrystalline

material, the presence of vibrational quanta of about 1500 and 3350 cm^{-1} makes multiphonon relaxation much more probable than in the bulk material. Therefore, in the nanocrystalline material, the ions relax through the emission of phonons rather than the emission of photons.

As we have shown in Figures 6.7 and 6.8, the upconverted luminescence intensity increases as a function of the Er^{3+} concentration. It is quite clear that the upconversion process is concentration dependent. The mechanism can take place through either an energy transfer upconversion (ETU) process or via excited state absorption (ESA) since, it is well known that both processes are dependent upon dopant concentration. The concentration dependence can be readily discerned as in the more dilute samples, the Er^{3+} - Er^{3+} distances are far to large for any effective ion-ion interactions to take place. Since there are more Er^{3+} ions available at higher concentrations, one may postulate substantial energy transfer can occur, since the energy transfer rate is strongly dependent on the distance between the ions involved. However, since upconversion does occur in the dilute samples, we must assume that both energy transfer upconversion (ETU) and the excited state absorption (ESA) occur concomitantly.

In order to obtain a better understanding of the mechanism(s) of upconversion, a power dependence study of the luminescence intensity versus pump power was performed (Figure 6.12). For any upconversion mechanism, it has been shown [242] that the intensity of the upconverted UV or visible luminescence, I_o, is proportional to some power n of the near-infrared excitation intensity I_i, i.e., $I_o \propto I_i^n$ where n = 2, 3... For the interpretation of the upconverted luminescence, it is often assumed that n is the order of the upconversion process. More specifically, n is, under normal circumstances, [243] the

number of pump photons required to populate the emitting state and is determined from the slope of the line of the graph, $\ln(I_o)$ versus $\ln(I_i)$ or, ln(Intensity) versus ln(Power). The fitting of the data yields a straight line with a slope of approximately 2 for the ($^2H_{11/2}$, $^4S_{3/2}$) $\rightarrow$ $^4I_{15/2}$, and $^4F_{9/2} \rightarrow {}^4I_{15/2}$ transitions in all the samples under investigation. It was therefore determined that the upconversion occurs via a two-photon process. No inflection was observed in the power study and therefore, photon avalanche was ruled out as a possible mechanism for upconversion [148].

The population of the higher energy levels after NIR pumping is relatively well known and usually occurs by two independent processes, ETU and ESA. The mechanism for red and green upconversion is as follows: The laser light brings the Er^{3+} ion to the $^4I_{9/2}$ level, which then non-radiatively decays into the $^4I_{11/2}$ level. After this non-radiative relaxation, either a sequential absorption of a second photon or an energy transfer from a neighboring Er^{3+} ion in the $^4I_{9/2}$ state brings the ion to the $^4F_{3/2}$ level [244] (Figure 6.13). Alternatively, after the initial excitation, the Er^{3+} ion can non-radiatively decay down to the $^4I_{13/2}$ level. Again, either an energy transfer process from another Er^{3+} ion in the $^4I_{9/2}$ state or a second photon from the incident laser beam populates the $^2H_{11/2}$ level. Emission from the green ($^2H_{11/2}$, $^4S_{3/2} \rightarrow {}^4I_{15/2}$) and red ($^4F_{9/2} \rightarrow {}^4I_{15/2}$) transitions can then be observed.

If upconversion occurs only via the above proposed ESA and ETU mechanisms, we would then expect upconversion spectra with identical relative intensities as in the direct luminescence spectra (λ_{exc} = 488 nm). This is clearly not the case as we observe an enhancement of the red emission for the $^4F_{9/2}$ state with increasing Er^{3+} concentration. Chen et al. [244] have also observed an enhancement of the red emission for the

upconversion of Er^{3+} in Gadolinium Gallium Garnet (GGG) single crystals. They observed that when GGG:Er^{3+} single crystals were pumped with 790 nm from a diode laser, both the green and red upconverted emission became much more intense with increasing concentration of erbium ions. However, they also observed that the red emission ($^4F_{9/2} \rightarrow {}^4I_{15/2}$) became stronger by a greater factor than the green emission ($^2H_{11/2}$, $^4S_{3/2} \rightarrow {}^4I_{15/2}$). It was postulated that an additional mechanism was responsible for populating the $^4F_{9/2}$ level only (Figure 6.14). The laser light (815 nm) excites the two neighboring Er^{3+} ions to the $^4I_{9/2}$ state. This is followed by an immediate non-radiative decay of one of the Er^{3+} ions to the $^4I_{11/2}$ state. The two excited Er^{3+} ions, one in the $^4I_{9/2}$ state and one in the $^4I_{11/2}$ state, undergo an ion pair process of the type; ($^4I_{9/2}$, $^4I_{11/2}$) $\rightarrow$ ($^4I_{13/2}$, $^4F_{9/2}$) resulting in the direct population of the $^4F_{9/2}$ state. This behavior can occur because the ESA/ETU mechanisms and this mechanism could be of different multipolar nature and therefore do not depend in the same way on the dopant concentration. As a result, this latter mechanism would be more effective as the Er^{3+} concentration is increased [244].

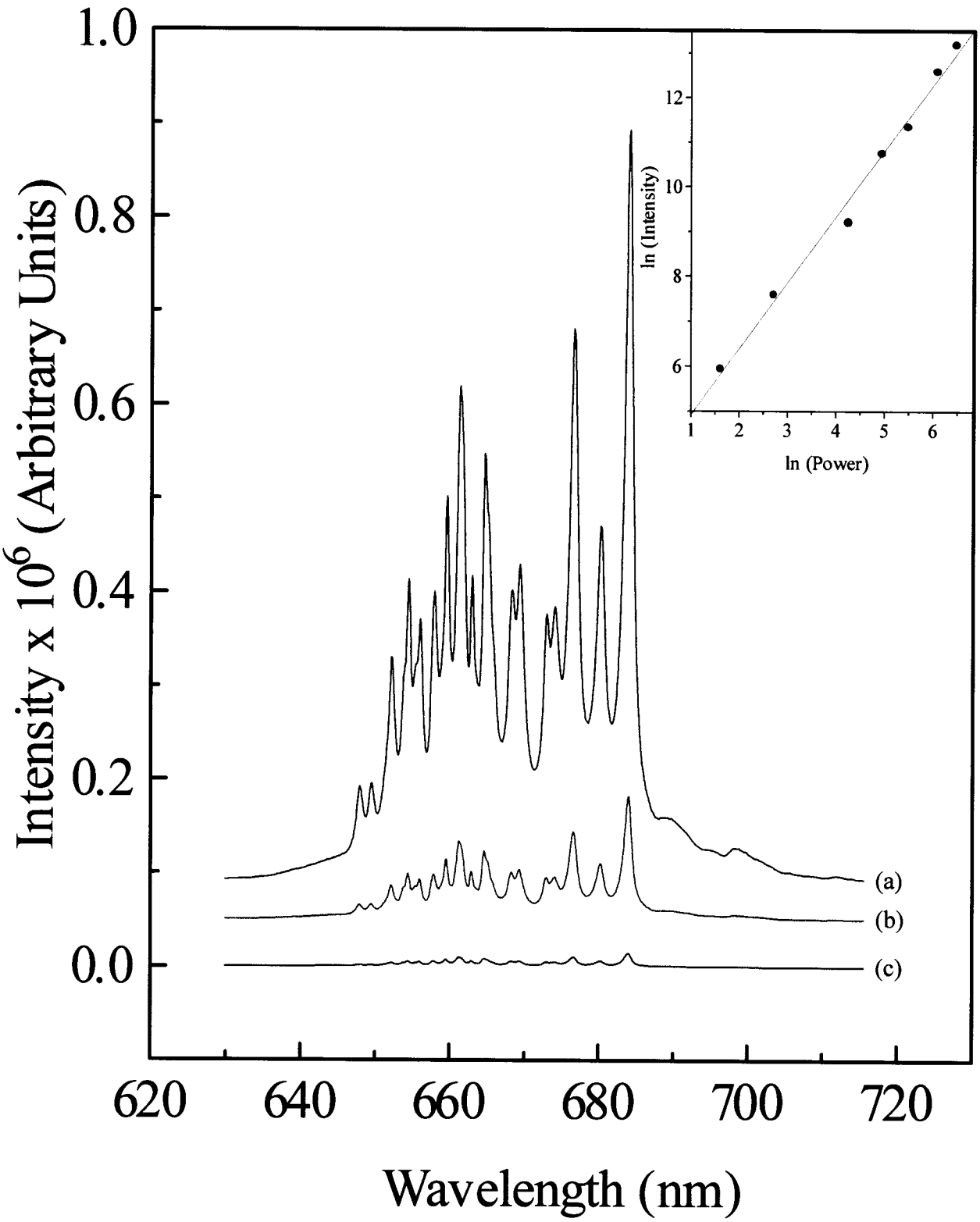

Figure 6.12: Power study of the $^4F_{9/2} \rightarrow {}^4I_{15/2}$ transition in 10 mol% bulk $Y_2O_3:Er^{3+}$ (λ_{exc} = 815 nm). Inset: Power dependence of the upconversion luminescence intensity observed with 815 nm excitation.
(a) 650 mW (b) 240 mW (c) 70 mW

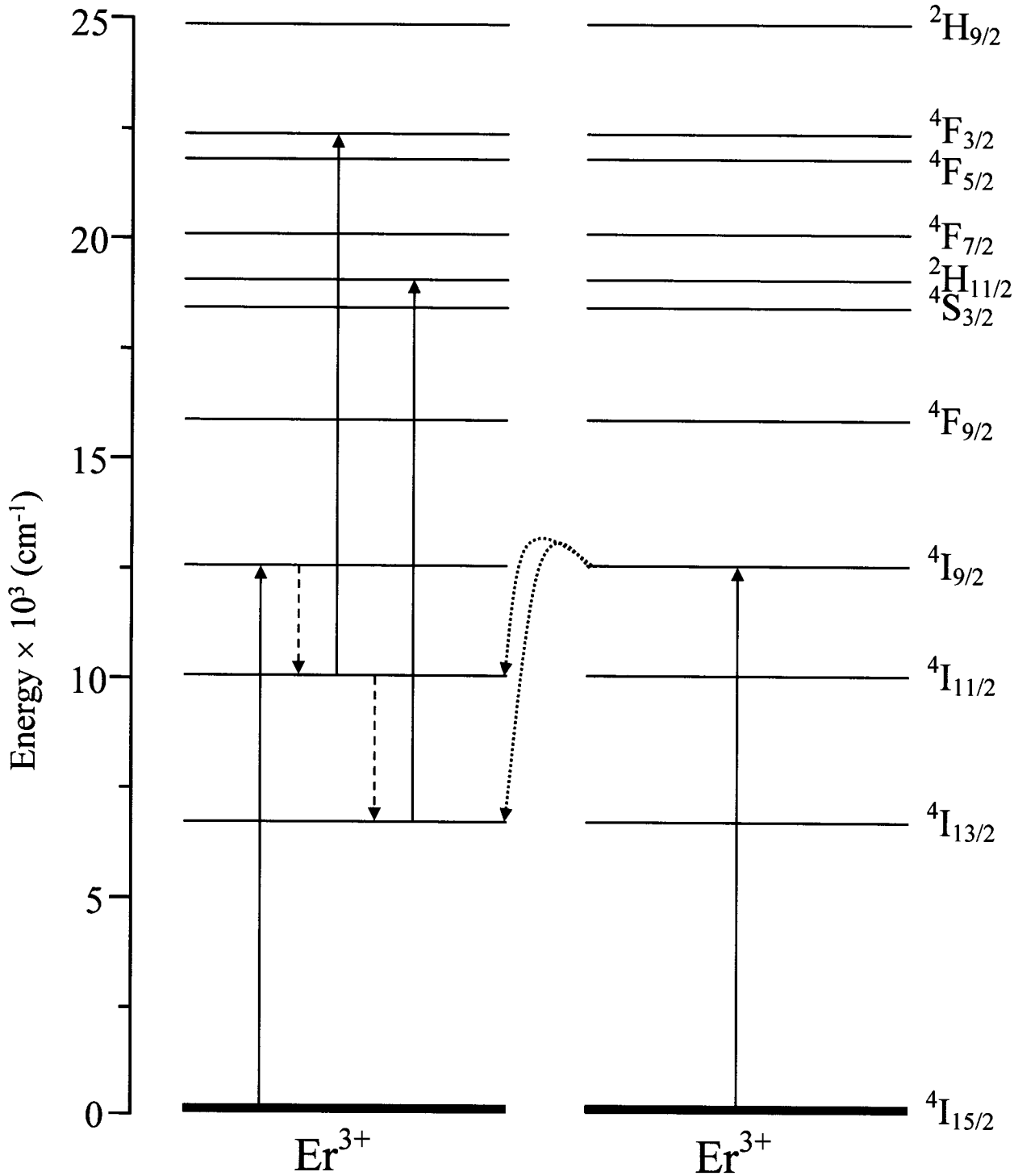

Figure 6.13: Energy level diagram of Er^{3+} ions in Y_2O_3 showing the ($^4I_{9/2}$, $^4I_{11/2} \rightarrow {}^4I_{13/2}$, $^4F_{9/2}$) ion-pair process responsible for directly populating the $^4F_{9/2}$ level (λ_{exc} = 815 nm).

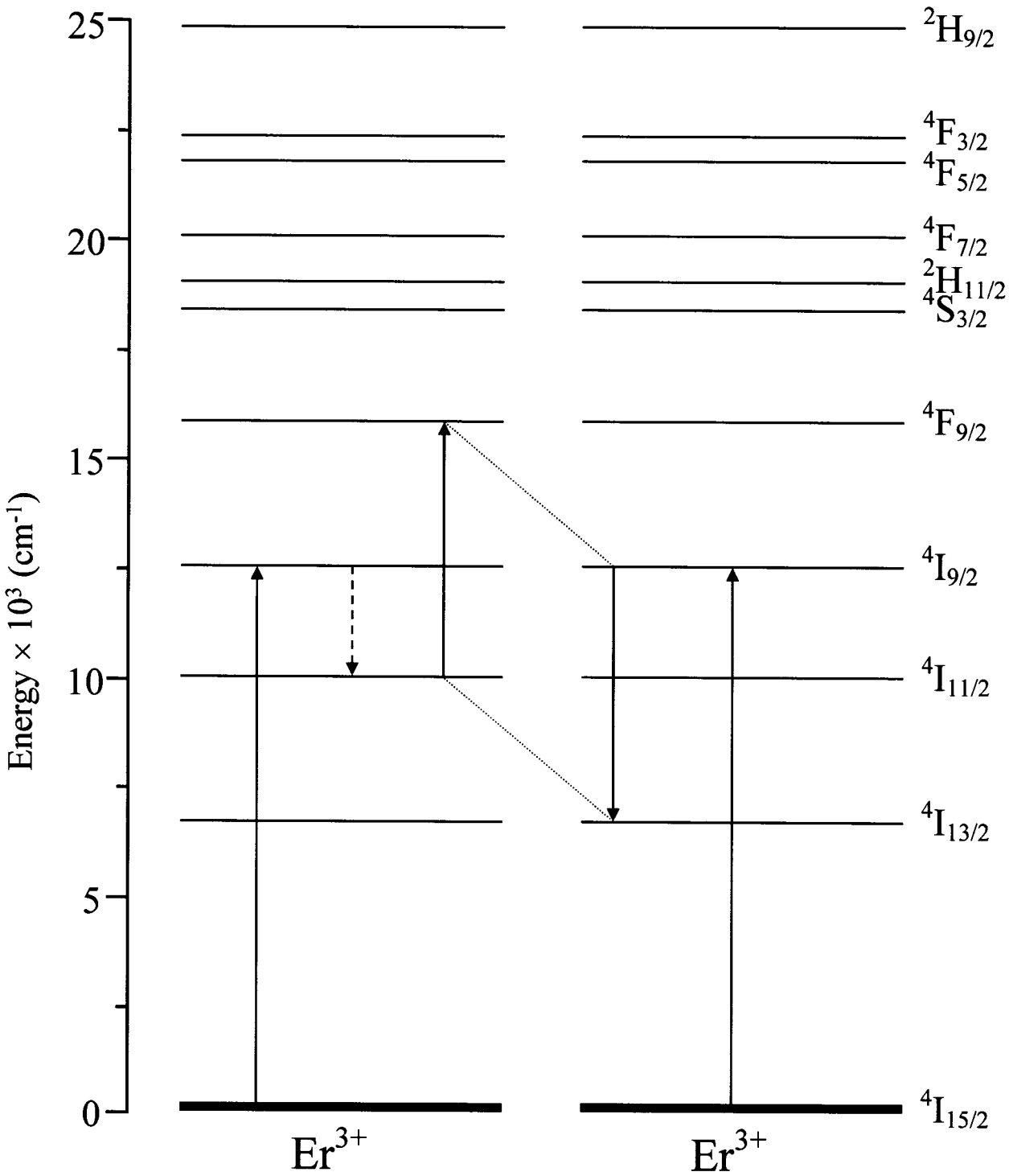

Figure 6.14: Energy level diagram of Er^{3+} ions in Y_2O_3 showing the ($^4I_{9/2}$, $^4I_{11/2} \rightarrow {}^4I_{13/2}$, $^4F_{9/2}$) ion-pair process responsible for directly populating the $^4F_{9/2}$ level (λ_{exc} = 815 nm).

In bulk and nanocrystalline cubic $Y_2O_3:Er^{3+}$, we have shown that the mechanism resulting in green ($^2H_{11/2}$, $^4S_{3/2}$) and red ($^4F_{9/2}$) upconversion occurs via two distinct processes acting simultaneously; an energy transfer upconversion (ETU) process and an excited state absorption (ESA) process. However, we cannot readily exclude the possibility of even more upconversion mechanisms occurring to populate the higher energy levels. We observe emission from the $^2P_{3/2}$ level, which is much higher in energy than the either the $^4F_{3/2}$ or $^2H_{11/2}$ states that are populated by the mechanisms previously described. Therefore, it follows from this that another mechanism must be operative to populate the high-energy $^2P_{3/2}$ level. This hypothesis was elucidated by the power study of the blue intraconfigurational $^2P_{3/2} \rightarrow {}^4I_{11/2}$ transition. While the power dependence study of the $^4F_{5/2,\ 7/2} \rightarrow {}^4I_{11/2}$ transitions revealed a quadratic dependence on the pump power, the power study of the $^2P_{3/2} \rightarrow {}^4I_{11/2}$ transition revealed a cubic dependence. That is, a three-photon mechanism is responsible for populating the $^2P_{3/2}$ upper state.

The $^2P_{3/2}$ state is populated via another ESA process and occurs by the following mechanism. First, the 815 nm light excites the Er^{3+} ion to the $^4I_{9/2}$ multiplet, after which, the Er^{3+} ion relaxes to the $^4I_{11/2}$ level by a non-radiative process. Second and third photons excite the Er^{3+} ion to the $^4G_{7/2}$ level. Again, non-radiative decay results in the population of the $^2P_{3/2}$ level and of course the ($^2H_{11/2}$, $^4S_{3/2}$) and $^4F_{9/2}$ levels.

From the upconversion spectra, it was revealed that ETU and ESA are simultaneously occurring to populate the red and green upper states. From the upconversion spectra of the bulk material in the blue region, we observed that the relative intensity of the $^2P_{3/2} \rightarrow {}^4I_{11/2}$ and the $^4F_{5/2,\ 7/2} \rightarrow {}^4I_{15/2}$ transitions is approximately 1:1:1 in the 1 mol% sample. However, as the concentration of Er^{3+} dopant is increased, the

intensities of the $^4F_{5/2} \rightarrow {}^4I_{15/2}$ and $^4F_{7/2} \rightarrow {}^4I_{15/2}$ transitions increase while the intensity of the $^2P_{3/2} \rightarrow {}^4I_{11/2}$ remains unchanged. We believe that the $^4F_{5/2}$ and $^4F_{7/2}$ levels are populated by non-radiative relaxation from the $^4F_{3/2}$ state via the two photon ETU/ESA processes described earlier while the $^2P_{3/2}$ level is populated by a three photon ESA process. As a result of this hypothesis, we postulate that at low Er^{3+}concentrations, the dominant mechanism is ESA process populating the $^2P_{3/2}$ level as the Er^{3+} ions are too far apart for any substantial energy transfer to take place. However, as the concentration of the dopant is increased, there are more Er^{3+} ions available and in closer proximity. Thus, substantial energy transfer can then take place. So, we believe that at high dopant concentrations, the ETU process "takes over" and becomes the dominant upconversion mechanism.

6.1.8. Anti-Stokes (Upconversion) Luminescence Spectroscopy Following Excitation into the $^4I_{11/2}$ Level (λ_{exc} = 980 nm)

Excitation of nanocrystalline and bulk $Y_2O_3:Er^{3+}$ with NIR radiation into the $^4I_{11/2} \leftarrow {}^4I_{15/2}$ absorption band (λ_{exc} = 980 nm) produced upconversion luminescence (Figures 6.15 – 6.16) [239]. Blue upconversion was observed with bands centered at 460, 475 and 495 nm, which are assigned to the $^4F_{5/2} \rightarrow {}^4I_{15/2}$, $^2P_{3/2} \rightarrow {}^4I_{11/2}$ and $^4F_{7/2} \rightarrow {}^4I_{15/2}$ transitions, respectively (Figure 6.17). The observed bands in the green region centered at 525 nm and 550 nm are assigned to the $^2H_{11/2} \rightarrow {}^4I_{15/2}$ and $^4S_{3/2} \rightarrow {}^4I_{15/2}$ transitions, respectively. Bands in the red region, centered at 660 nm, are assigned to the $^4F_{9/2} \rightarrow {}^4I_{15/2}$ transition. As with 815 nm excitation, no blue upconversion was observed in the nanocrystalline samples.

The spectral band shapes and position are very similar to those obtained upon 488 nm excitation (see Figures 6.5 and 6.6). However, we observe a marked decrease in the overall luminescence intensity for the nanocrystalline material compared to its bulk counterpart. Clearly, the presence of the CO_3^{2-} and OH^- contaminants adsorbed on the nanocrystal surface yields vibrational quanta, which makes multiphonon relaxation in the nanocrystalline material much more efficient.

Table 6.2 shows the decay times of the green ($^4S_{3/2}$) and red ($^4F_{9/2}$) excited states in nanocrystalline $Y_2O_3:Er^{3+}$ following excitation with 980 nm. The upconverted decay curves for all samples under investigation deviated slightly from single exponentiality. The same behavior was observed in $Y_2O_3:Ho^{3+}$ nanocrystals [245] and was explained as being due to a distribution of dopant ions within the individual nanocrystals that were coupled in various degrees to the adsorbed surface molecules. The dopant ions located close to the particle surface would have a faster decay than those ions located inside the nanocrystals. In the nanocrystal material, a significant portion of the rare earth ions are located on the particle surface due to their small size and therefore leads to a non-exponential decay curve. Moreover, the presence of the adsorbed surface molecules on the nanocrystals were also responsible for the drastic difference between the decay times of the bulk and nanocrystal materials [233]. Furthermore, energy transfer processes could also contribute in making the decay curves non-exponential. The emission decay time constants, τ_m, of nanocrystalline $Y_2O_3:Er^{3+}$ were determined using the Nakazawa model [246]:

$$\tau_m = \frac{\int_0^\infty t\phi(t)dt}{\int_0^\infty \phi(t)dt} \qquad 6.1.3$$

where: $\phi(t)$ is the intensity at time t. As seen from Table 6.2, the decay times for the more heavily doped samples are considerably shorter in comparison to those that are more weakly doped and is caused by an increase in the interaction between Er^{3+} dopant ions.

Table 6.2: Room temperature decay time constants (τ_m) for nanocrystalline Y_2O_3:Er^{3+} following excitation with 980 nm.

Transition	Decay Times (μs)			
	1 mol%	2 mol%	5 mol%	10 mol%
$^4S_{3/2} \rightarrow {}^4I_{15/2}$	177	156	115	80
$^4F_{9/2} \rightarrow {}^4I_{15/2}$	280	262	215	163

The risetime of the temporal evolution of the green upconverted luminescence (not shown), due to the ($^2H_{11/2}$, $^4S_{3/2} \rightarrow {}^4I_{15/2}$) transition, is in excellent agreement with the lifetime of the $^4I_{11/2}$ level. From this behavior it is clearly evident that the $^4I_{11/2}$ level is the intermediate state in the upconversion process and thus, acts as a population reservoir. The observed rate of depopulation (W) of the $^4I_{11/2}$ excited state is expressed as the sum of the radiative transition probability (W_R) and the non-radiative or multiphonon transition probability (W_{MPR}) [106]. The radiative decay rates for the Er^{3+} ions in the bulk and nanocrystalline samples should reasonably be of the same order of magnitude, thus the higher multiphonon transition probability in the nanopowders lead to the lower upconversion luminescence intensity. The gap between the $^4I_{11/2}$ state and the next lower level, $^4I_{13/2}$, is approximately 3600 cm^{-1}. Moreover, the energy gap between the thermalized ($^2H_{11/2}$, $^4S_{3/2}$) emitting levels and the next lower level, $^4F_{9/2}$, is approximately

3100 cm^{-1} while the gap between the $^4F_{9/2}$ emitting level and the next lower level, $^4I_{9/2}$, is in the region of 2800 cm^{-1}. Therefore, the presence of the adsorbents on the nanocrystalline surface leads to a more efficient depopulation not only of the intermediate $^4I_{11/2}$ level, but also of the emitting levels with respect to the bulk material. Consequently, lower upconversion luminescence intensity in the nanocrystalline material is expected, in agreement with the experimental results. From these considerations, it is no surprise that blue upconversion is not observed for the nanocrystalline samples but only for the bulk ones (see below).

As described in section 6.1.4, $Y_2O_3:Er^{3+}$ (10 mol%) nanocrystals were heated at 800 °C for 17 hours and subsequently at 1000 °C for 65 hours. Once cooled to room temperature, the nanocrystalline sample was immediately sealed in a glass capillary and the upconversion luminescence (λ_{exc} = 980 nm) was measured. The upconversion spectrum of the heat-treated nanocrystalline sample, which was obtained under identical experimental conditions as the non-heat treated sample, showed a small improvement in the luminescence intensity, but was still of much weaker intensity than the bulk sample. As we discussed earlier, the heat treatments did not entirely remove the adsorbed H_2O and CO_2 from the surface of the nanocrystals. Therefore, the multiphonon relaxation rate is still greater than in the bulk sample having identical Er^{3+} concentration and resulted in the observed weaker upconversion intensity.

A pronounced concentration dependence of the upconverted emission signal was observed for both the nanocrystalline and bulk material. In the 1 mol% $Y_2O_3:Er^{3+}$ samples, the green ($^2H_{11/2}$, $^4S_{3/2} \rightarrow {}^4I_{15/2}$) emission dominates the spectrum following excitation at 980 nm. However, as the concentration of Er^{3+} is increased, we observe an

enhancement of the red ($^4F_{9/2} \rightarrow {}^4I_{15/2}$) emission, which increases at a more rapid rate than the green emission. This effect is most striking in the nanocrystalline material where in the 10 mol% sample, the red emission dominates over the green emission. A marked concentration dependence of the blue upconversion was also evidenced in bulk $Y_2O_3:Er^{3+}$. In the 1 mol% sample, the $^2P_{3/2} \rightarrow {}^4I_{11/2}$ transition dominates the spectrum in the 440-510 nm range. However, as the Er^{3+} ion concentration is increased, the intensity of the $^4F_{5/2} \rightarrow {}^4I_{15/2}$ transition increases while the intensities of the $^2P_{3/2} \rightarrow {}^4I_{11/2}$ and $^4F_{7/2} \rightarrow {}^4I_{15/2}$ transitions decrease, for the bulk samples.

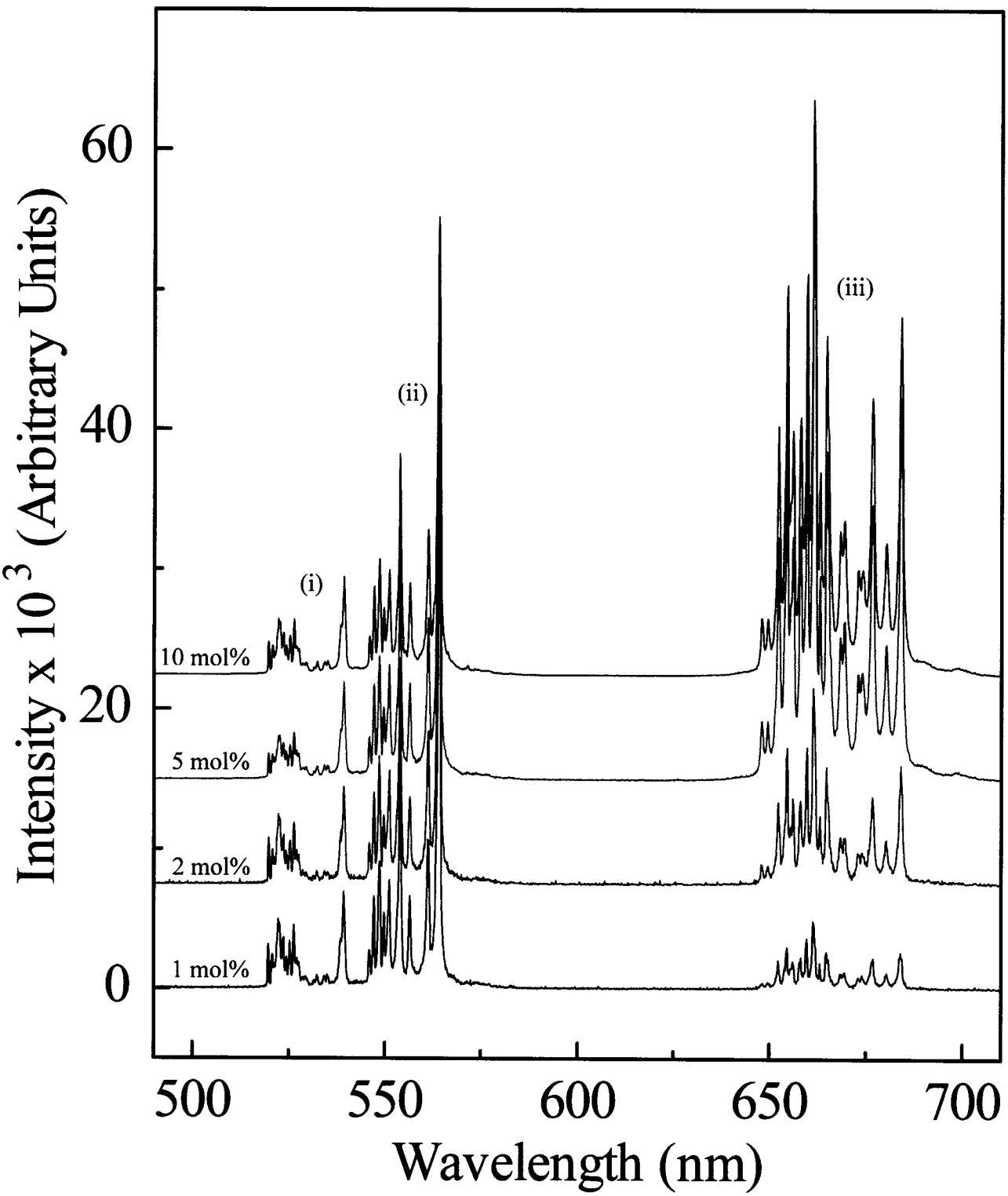

Figure 6.15: Room temperature luminescence of nanocrystalline $Y_2O_3:Er^{3+}$ upon excitation at 980 nm. (i) $^2H_{11/2} \rightarrow {}^4I_{15/2}$ (ii) $^4S_{3/2} \rightarrow {}^4I_{15/2}$ (iii) $^4F_{9/2} \rightarrow {}^4I_{15/2}$.

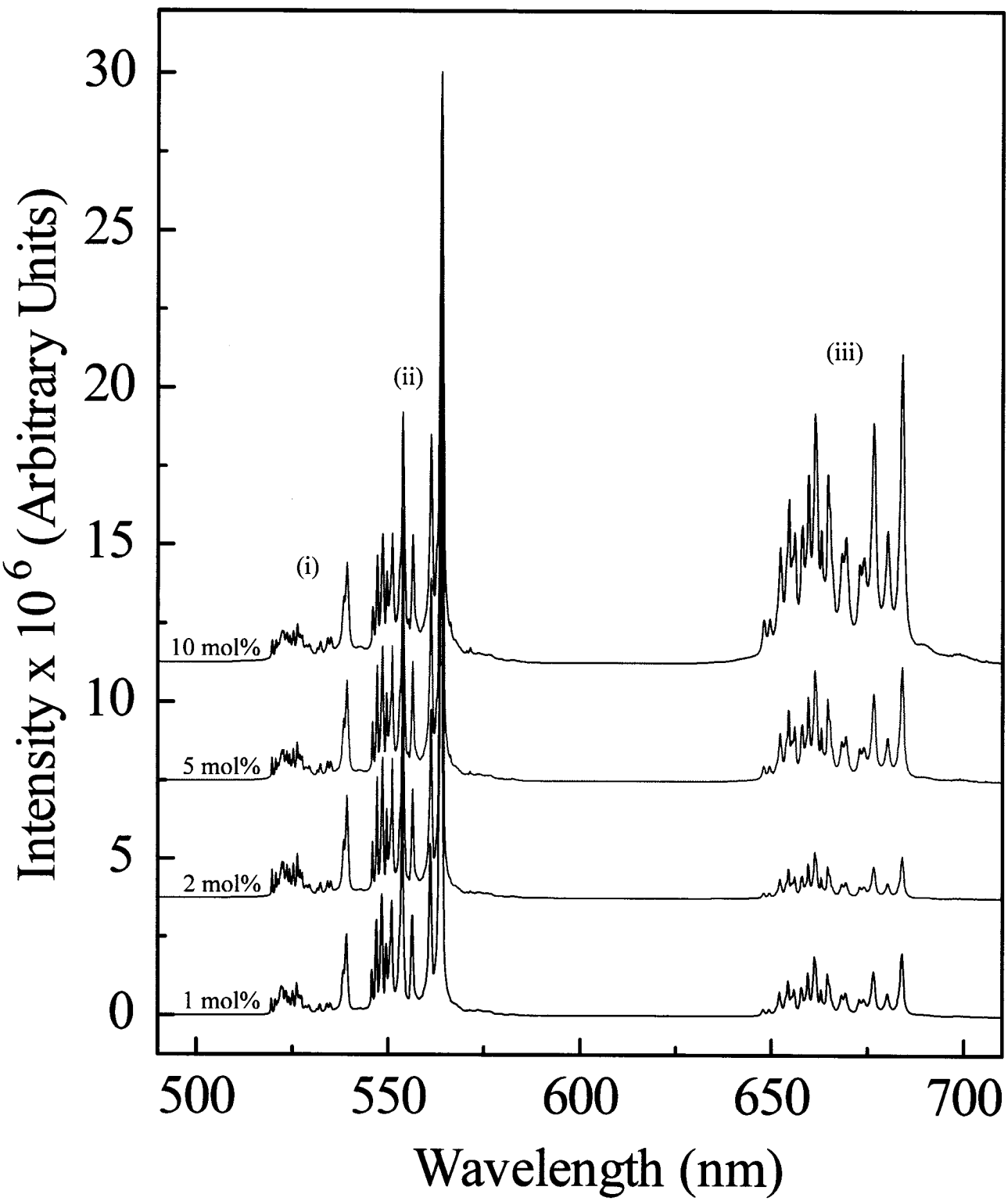

Figure 6.16: Room temperature luminescence of bulk $Y_2O_3:Er^{3+}$ upon excitation at 980 nm. (i) $^2H_{11/2} \rightarrow {}^4I_{15/2}$ (ii) $^4S_{3/2} \rightarrow {}^4I_{15/2}$ (iii) $^4F_{9/2} \rightarrow {}^4I_{15/2}$.

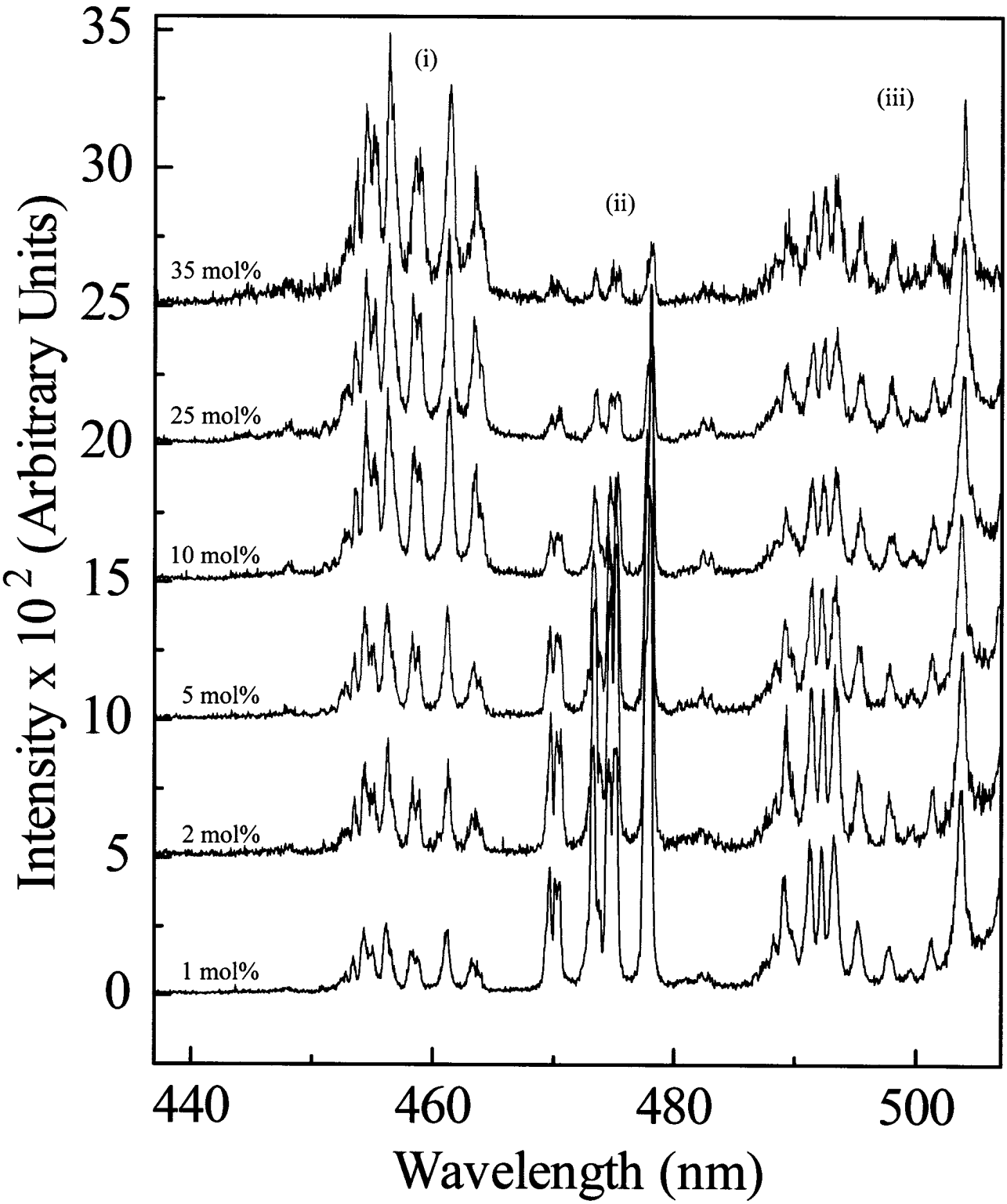

Figure 6.17: Upconverted blue emission of bulk $Y_2O_3:Er^{3+}$ at room temperature, showing (i) $^4F_{5/2} \rightarrow {}^4I_{15/2}$ (ii) $^2P_{3/2} \rightarrow {}^4I_{11/2}$ (iii) $^4F_{7/2} \rightarrow {}^4I_{15/2}$ (λ_{exc} = 980 nm).

To better comprehend the mechanism(s), which populate the ($^2H_{11/2}$, $^4S_{3/2}$) green and ($^4F_{9/2}$) red emitting levels, the upconversion luminescence intensity was measured as a function of the pump power. The slope of the curve of ln (Intensity) versus ln (Power) is approximately 2 for both the green and red manifolds and for all samples under investigation. We can immediately rule out PA as a mechanism of upconversion in Y_2O_3:Er^{3+} as no inflection point was observed in the power study [247]. So, upconversion can occur either via ESA or ETU (Figure 6.18). The mechanism for ESA is quite simple, as there exists an energy level, which can be populated by absorption of a second 980 nm wavelength photon from the intermediate $^4I_{11/2}$ state and so, the ion is excited to the $^4I_{11/2}$ intermediate state via a photon from the pump beam. Another photon in turn excites the same ion to the $^4F_{7/2}$ state. Non-radiative multiphonon decay is then responsible for populating the $^2H_{11/2}$, $^4S_{3/2}$ and $^4F_{9/2}$ states. Similarly, ETU can also populate the $^2H_{11/2}$, $^4S_{3/2}$ and $^4F_{9/2}$ states. In this mechanism, two Er^{3+} ions in close proximity are each excited to the $^4I_{11/2}$ state. One ion in turn transfers its energy to the other and non-radiatively decays back to the ground state. Consequently, the other ion is promoted to the $^4F_{7/2}$ state. ESA would be the most likely mechanism in samples with low dopant concentration as the dopant ions are too far apart to interact with each other. However, as the dopant concentration is increased the probability of ETU occurring also increases. Evidence of ETU is provided by the upconverted decay times (λ_{exc} = 980 nm), which are lengthened compared to those obtained following direct excitation of the $^4F_{7/2}$ excited state with 488 nm (see Tables 6.1 and 6.2). Lengthening of the upconverted decay times alludes to the presence of energy transfer in the upconversion process.

If the above mechanisms were solely responsible for the upconversion, we would then expect upconversion spectra (λ_{exc} = 980 nm) that have identical relative intensities of the green and red transitions as the direct excitation (λ_{exc} = 488 nm) spectra. This clearly is not the case as we observe an enhancement of the red emission as the Er^{3+} concentration is increased. Thus, we propose that another mechanism is responsible for populating the $^4F_{9/2}$ state only. A mechanism for the direct two photon population of the $^4F_{9/2}$ state is ruled out as no resonance is present, therefore there must exist some process that allows for the bypassing of the $^2H_{11/2}$ and $^4S_{3/2}$ levels and transferring the pump energy to the $^4F_{9/2}$ state. We propose that a cross-relaxation process is responsible for populating the $^4F_{9/2}$ level and occurs via two resonant transitions (Figure 6.18): $^4F_{7/2} \rightarrow {}^4F_{9/2}$ and $^4F_{9/2} \leftarrow {}^4I_{11/2}$ [248]. In fact, the efficiency of the cross-relaxation process would increase on decreasing the average distance between the dopant ions and therefore with increasing the Er^{3+} concentration, giving rise to the enhancement of the red emission, in agreement with the obtained experimental data (see Figures 6.15 – 6.16).

We have discussed the mechanisms responsible for populating the $^2H_{11/2}$, $^4S_{3/2}$ and $^4F_{9/2}$ states. However, we cannot rule out the presence of even more upconversion mechanisms. We observe emission from the $^2P_{3/2}$ and $^4F_{5/2}$ states for the bulk yttria samples (see Figure 6.17) which are higher in energy than $^4F_{7/2}$ state that is populated by the ESA and ETU mechanisms. Therefore, it follows that other mechanism(s) may be operative beyond those previously discussed. This hypothesis was elucidated by the power study of the three manifolds in the blue region of the spectrum. This study revealed that the intensities of the $^4F_{5/2} \rightarrow {}^4I_{15/2}$ and $^4F_{7/2} \rightarrow {}^4I_{15/2}$ transitions obey a quadratic dependence whilst the intensity of the $^2P_{3/2} \rightarrow {}^4I_{11/2}$ transition obeys a cubic

dependence on the pump power. That is, the $^4F_{5/2}$ and $^4F_{7/2}$ levels are populated via a 2 photon upconversion process while 3 photon upconversion populates the $^2P_{3/2}$ state.

Again, as the relative intensities of the $^4F_{5/2} \rightarrow {}^4I_{15/2}$, $^2P_{3/2} \rightarrow {}^4I_{11/2}$ and $^4F_{7/2} \rightarrow {}^4I_{15/2}$ transitions change with the dopant concentration, we can presume that a concentration dependent upconversion process is active. The mechanism to populate the $^4F_{7/2}$ state is described above. However, the $^4F_{5/2}$ level lies approximately 1400 cm^{-1} higher in energy with respect to the $^4F_{7/2}$ level and thus two 980 nm wavelength photons do not have the necessary energy to populate the $^4F_{5/2}$ level. Therefore, it is conceivable that 2-3 intrinsic phonons of yttria can bridge the gap and allow for the population of the state via a phonon-assisted energy transfer process (PET). The population of the $^2P_{3/2}$ level involves 3 photons however; the Er^{3+} energy level diagram reveals that there is no energy level, which could be populated by a sequential absorption of three pump photons. In fact, even if the $^4F_{7/2}$ level is populated by ESA or ETU, and non-radiatively decays to lower lying levels, again there is no energy level that could be populated by the absorption of another 980 nm wavelength pump photon. Similarly, if the ion in the ground state is excited by one photon to the $^4I_{11/2}$ level and then non-radiatively decays to the lower $^4I_{13/2}$ level, there is no higher energy state, which is resonant with the $^4I_{13/2}$ state. Therefore, we propose that another PET mechanism populates the $^2P_{3/2}$ level (Figure 6.19), in which 1-2 phonons are requested to compensate the mismatch in energy (approximately 690 cm^{-1}).

A possible explanation for the change in the relative intensities of the blue upconversion is the following. As shown in Figure 6.17, the intensity of the $^4F_{5/2} \rightarrow {}^4I_{15/2}$ transition increases significantly with increasing the Er^{3+} concentration and this behavior

is most probably due to the increasing number of emitting ions. On the other hand, the intensities of the $^2P_{3/2} \rightarrow {}^4I_{11/2}$ and $^4F_{7/2} \rightarrow {}^4I_{15/2}$ transitions decrease as the concentration of Er^{3+} in the material increases. In particular, the $^2P_{3/2} \rightarrow {}^4I_{11/2}$ emission intensity almost disappears at the higher Er^{3+} concentration, indicating a dramatic decrease in the population of the $^2P_{3/2}$ state. An explanation for these behaviors could be invoked by considering that the efficiency of the ($^4F_{7/2}$, $^4I_{11/2} \rightarrow {}^4F_{9/2}$,$^4F_{9/2}$) cross-relaxation process, which depopulates the $^4F_{7/2}$ state, increases with increasing the dopant concentration. Correspondingly, the intensity of the $^4F_{7/2} \rightarrow {}^4I_{15/2}$ emission would decrease, in agreement with the experimental data. Moreover, since the $^2P_{3/2}$ level is populated starting from the $^4F_{7/2}$ level, a decrease in the population of the $^4F_{7/2}$ state would also translate into a decrease of the population of the $^2P_{3/2}$ state and therefore in a decrease of the intensity of the $^2P_{3/2} \rightarrow {}^4I_{11/2}$ emission, in agreement with our experimental findings.

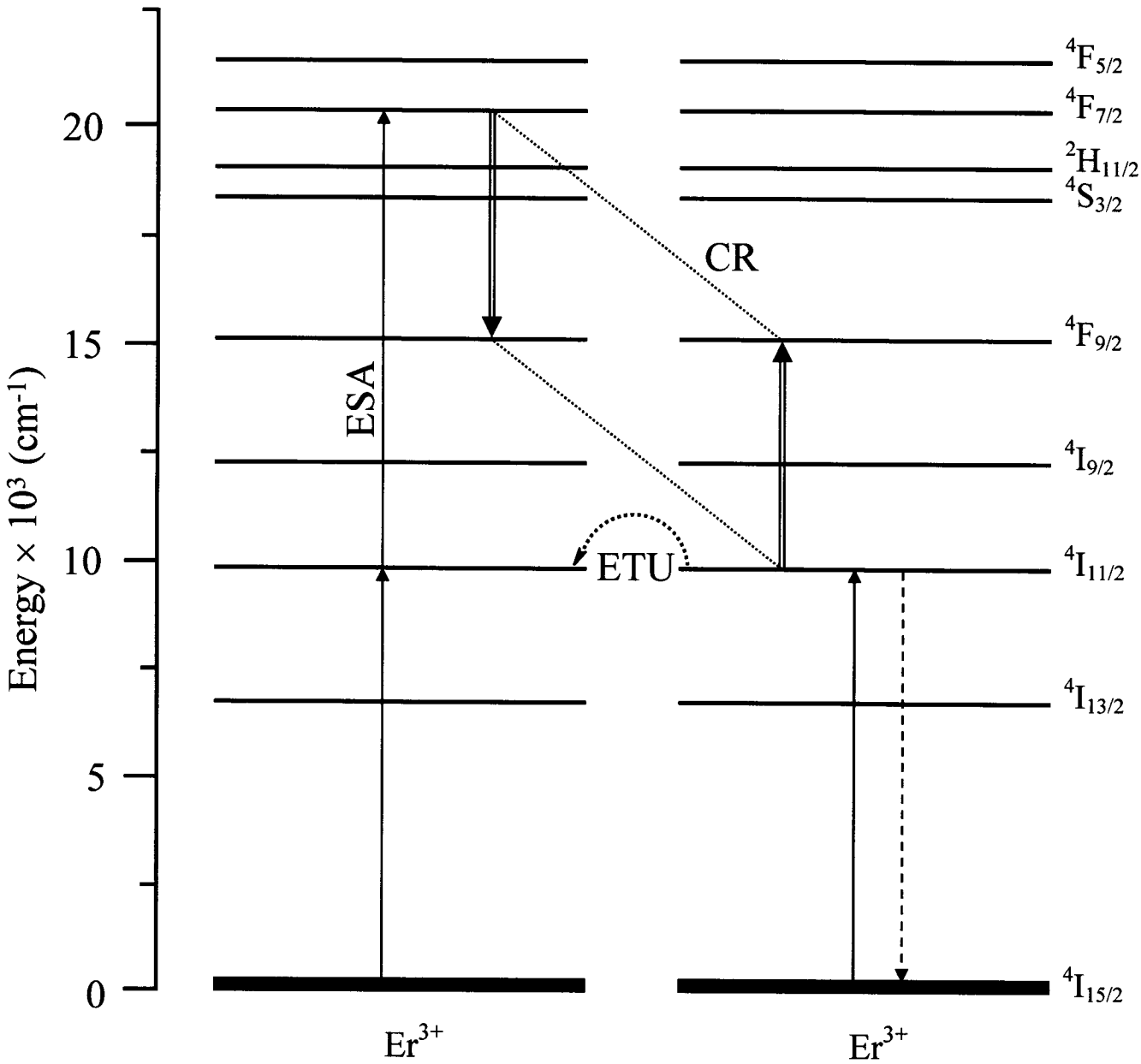

Figure 6.18: Schematic representation of the excited state absorption (ESA) and energy transfer upconversion (ETU) mechanisms. The $^4F_{7/2} \rightarrow {}^4F_{9/2}$ and $^4F_{9/2} \leftarrow {}^4I_{11/2}$ cross-relaxation (CR) process responsible for populating the $^4F_{9/2}$ state is also shown.

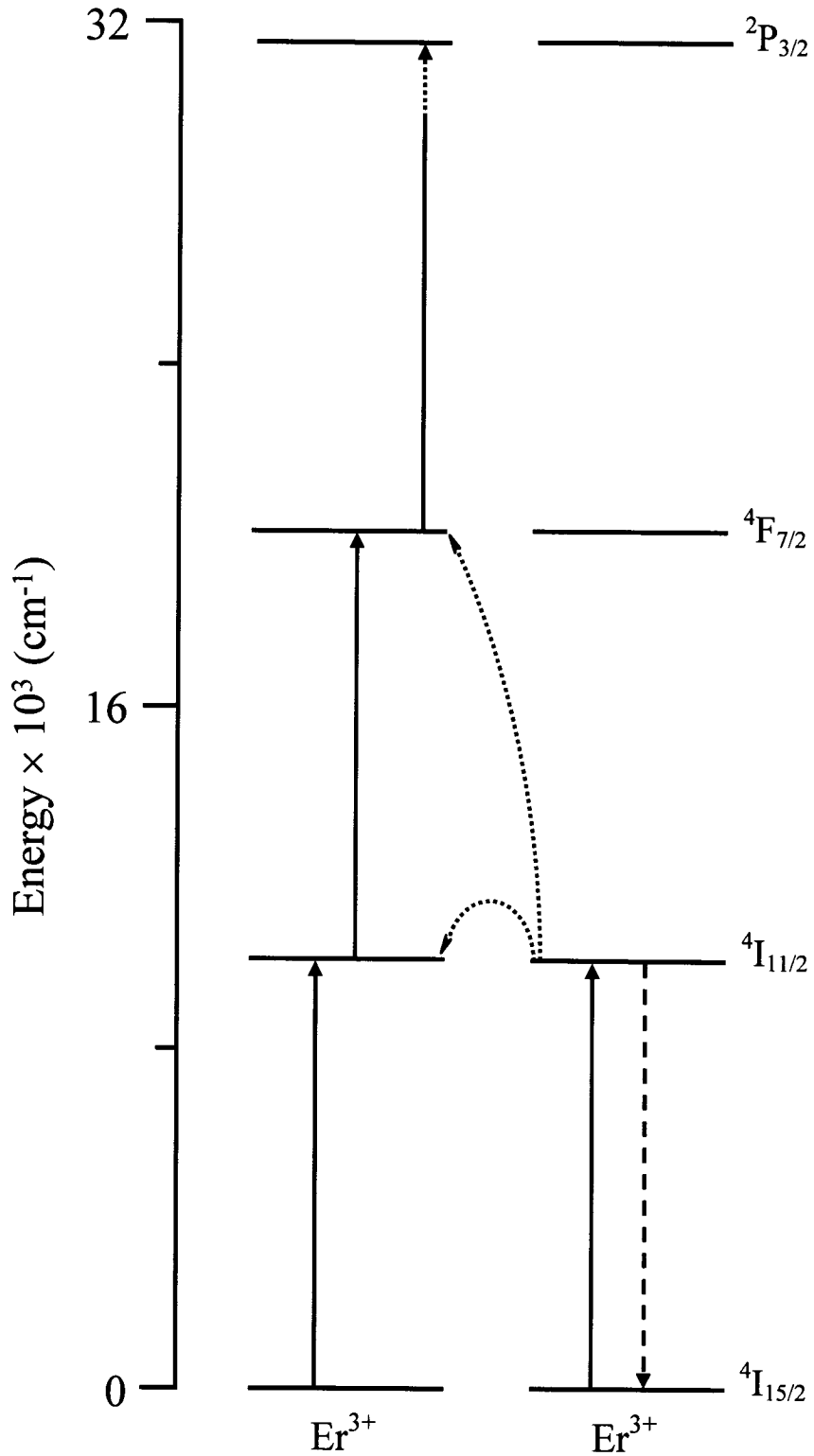

Figure 6.19: Schematic representation of the 3 step phonon-assisted energy transfer (PET) upconversion process responsible for populating the $^2P_{3/2}$ state.
Note: Only the relevant energy levels of the Er^{3+} ions are shown for simplicity.

6.1.9. Effect of Yb^{3+} Co-doping on the Upconversion Emission in Nanocrystalline $Y_2O_3:Er^{3+}$

The room temperature emission spectrum for the nanocrystalline $Y_2O_3:Er^{3+}$, Yb^{3+} sample (1 mol% each of Er^{3+} and Yb^{3+}) produced by the propellant synthesis technique in the 500-870 nm region and following 488 nm excitation, is shown in Figure 6.20. The spectrum exhibits four distinct emission bands corresponding to the radiative decay from some excited states of the erbium ion [249]. Similar to the singly doped $Y_2O_3:Er^{3+}$ nanocrystal samples, green emission was observed between 500-580 nm corresponding to the thermalized $^2H_{11/2}$, $^4S_{3/2} \rightarrow {}^4I_{15/2}$ transition and red emission was observed between 640-690 nm corresponding to the $^4F_{9/2} \rightarrow {}^4I_{15/2}$ transition. NIR emission was observed between 785-825 nm corresponding to the $^4I_{9/2} \rightarrow {}^4I_{15/2}$ transition and between 840-870 nm corresponding to the $^4S_{3/2} \rightarrow {}^4I_{13/2}$ transition.

Figure 6.20 (inset) presents the emission spectrum for bulk $Y_2O_3:Er^{3+}$, Yb^{3+} with identical doping levels as the nanocrystals. Similar to the nanomaterial, emission from the $^2H_{11/2}$, $^4S_{3/2} \rightarrow {}^4I_{15/2}$ transition was observed between 500-580 nm. Red emission was observed between 640-690 nm corresponding to the $^4F_{9/2} \rightarrow {}^4I_{15/2}$ transition. NIR emission was observed between 785-825 nm corresponding to the $^4I_{9/2} \rightarrow {}^4I_{15/2}$ transition and between 840-870 nm corresponding to the $^4S_{3/2} \rightarrow {}^4I_{13/2}$ transition.

The emission spectra of the co-doped bulk sample as well as the nanocrystalline sample following excitation with 488 nm are similar in both intensity and peak shape to their respective singly doped erbium Y_2O_3 spectra. Figure 6.21 presents the NIR emission spectrum of the bulk $Y_2O_3:Er^{3+}$, Yb^{3+} sample and provides evidence that there exists an energy transfer process from the excited Er^{3+} ions to the Yb^{3+} ions in the ground state. Following irradiation of the co-doped bulk sample with 488 nm, only the Er^{3+} ions

should be excited as Yb^{3+} has only one excited state in the NIR (circa 10 600 cm^{-1}) and therefore no emission from the Yb^{3+} ions should be observed. However, we observe peaks attributed to Yb^{3+} emission in the NIR emission spectrum (marked with $*$) and thus, it is reasonable to assume that an energy transfer between the Er^{3+} and Yb^{3+} ions is operative. The Er^{3+} ion is initially excited to its $^4F_{7/2}$ state with the 488 nm pump photons. A cross-relaxation process of the form $(^4F_{7/2}, {}^2F_{7/2}) \rightarrow (^4I_{11/2}, {}^2F_{5/2})$ occurs following the initial excitation [250]. After the Yb^{3+} ion is excited to its $^2F_{5/2}$ state, it can emit radiatively, as evidenced by the NIR emission spectrum, or it can transfer its energy back to the Er^{3+} ion exciting it to the $^4F_{7/2}$ state once again. It is apparent from the intensity of the $^4S_{3/2} \rightarrow {}^4I_{15/2}$ transition compared to that of the $^4I_{11/2} \rightarrow {}^4I_{15/2}$ and $^2F_{5/2} \rightarrow {}^2F_{7/2}$ transitions, that the back transfer from Yb^{3+} to Er^{3+} is favored over the radiative $^2F_{5/2} \rightarrow {}^2F_{7/2}$ emission from the Yb^{3+} ion. We should note however that the peaks attributed to Yb^{3+} emission are very weak and barely detected in the nanocrystalline co-doped samples.

The next logical question that must be posed is why the Er^{3+} to Yb^{3+} energy transfer does not occur as efficiently in the nanocrystalline material. We believe that this is simply due to the high phonon energies inherent in this type of material and is evidenced by the luminescence intensity difference between the bulk and the nanocrystalline samples, which had significantly lower overall intensities compared to the bulk material. These high-energy CO_3^{2-} and OH^- vibrations reduce many of the radiative processes allowing the ion to decay primarily via the emission of phonons. In the nanocrystalline material the energy transfer from Er^{3+} to Yb^{3+} is severely limited due to the very efficient multiphonon relaxation from the $^4I_{11/2}$ to the $^4I_{13/2}$ excited state. The

high phonon energies significantly reduce the population reservoir in the $^4I_{11/2}$ state and since this mechanism involves this state, the process becomes highly inefficient.

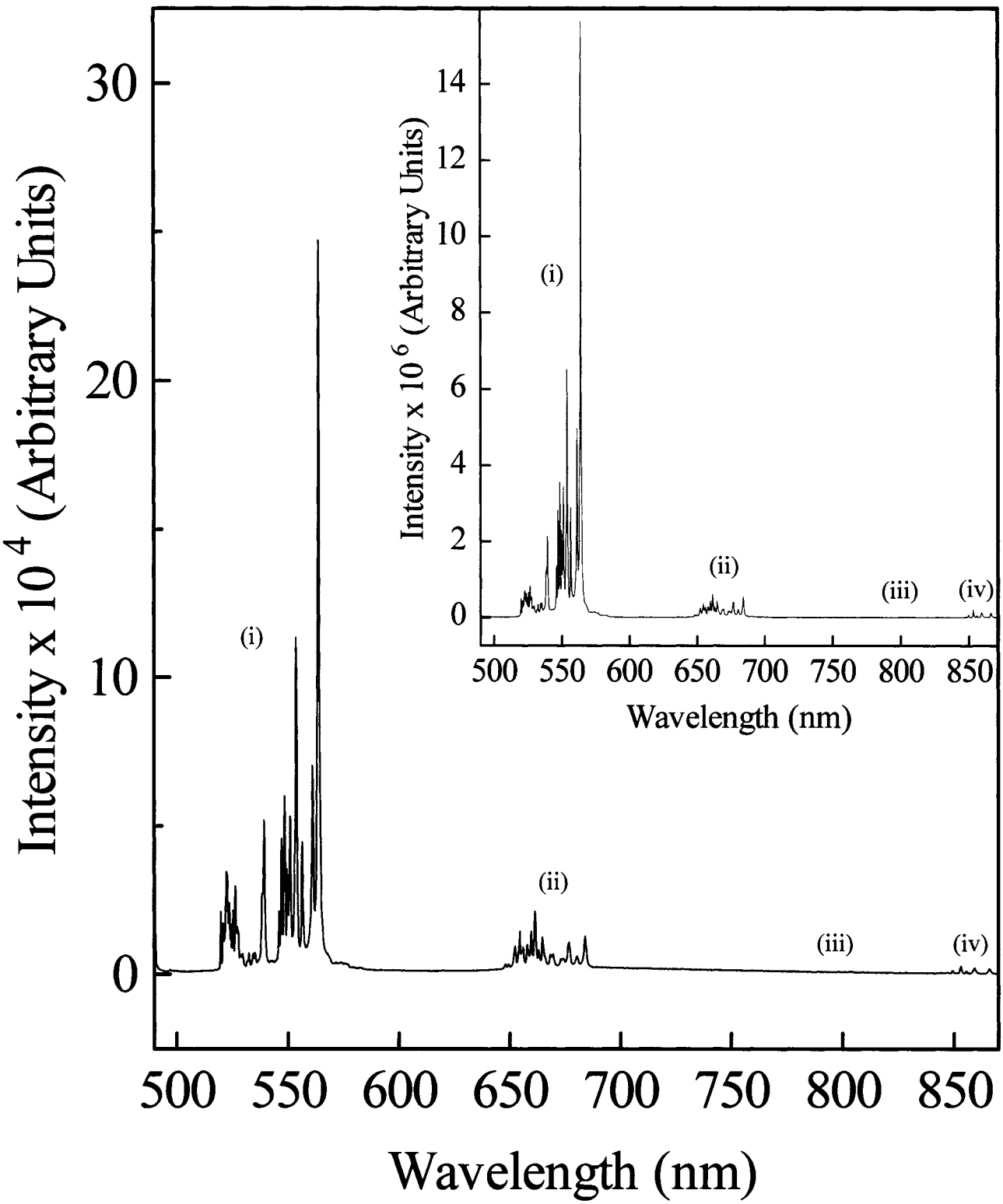

Figure 6.20: Room temperature Stokes luminescence of nanocrystalline $Y_2O_3:Er^{3+}$, Yb^{3+} (1 mol% Er^{3+} and 1 mol% Yb^{3+}) prepared via propellant synthesis following excitation with 488 nm. Inset: Room temperature Stokes luminescence of bulk $Y_2O_3:Er^{3+}$, Yb^{3+} (1 mol% Er^{3+} and 1 mol% Yb^{3+})
(i) $^2H_{11/2}$, $^4S_{3/2} \rightarrow {}^4I_{15/2}$ (ii) $^4F_{9/2} \rightarrow {}^4I_{15/2}$ (iii) $^4I_{9/2} \rightarrow {}^4I_{15/2}$ (iv) $^4S_{3/2} \rightarrow {}^4I_{13/2}$.

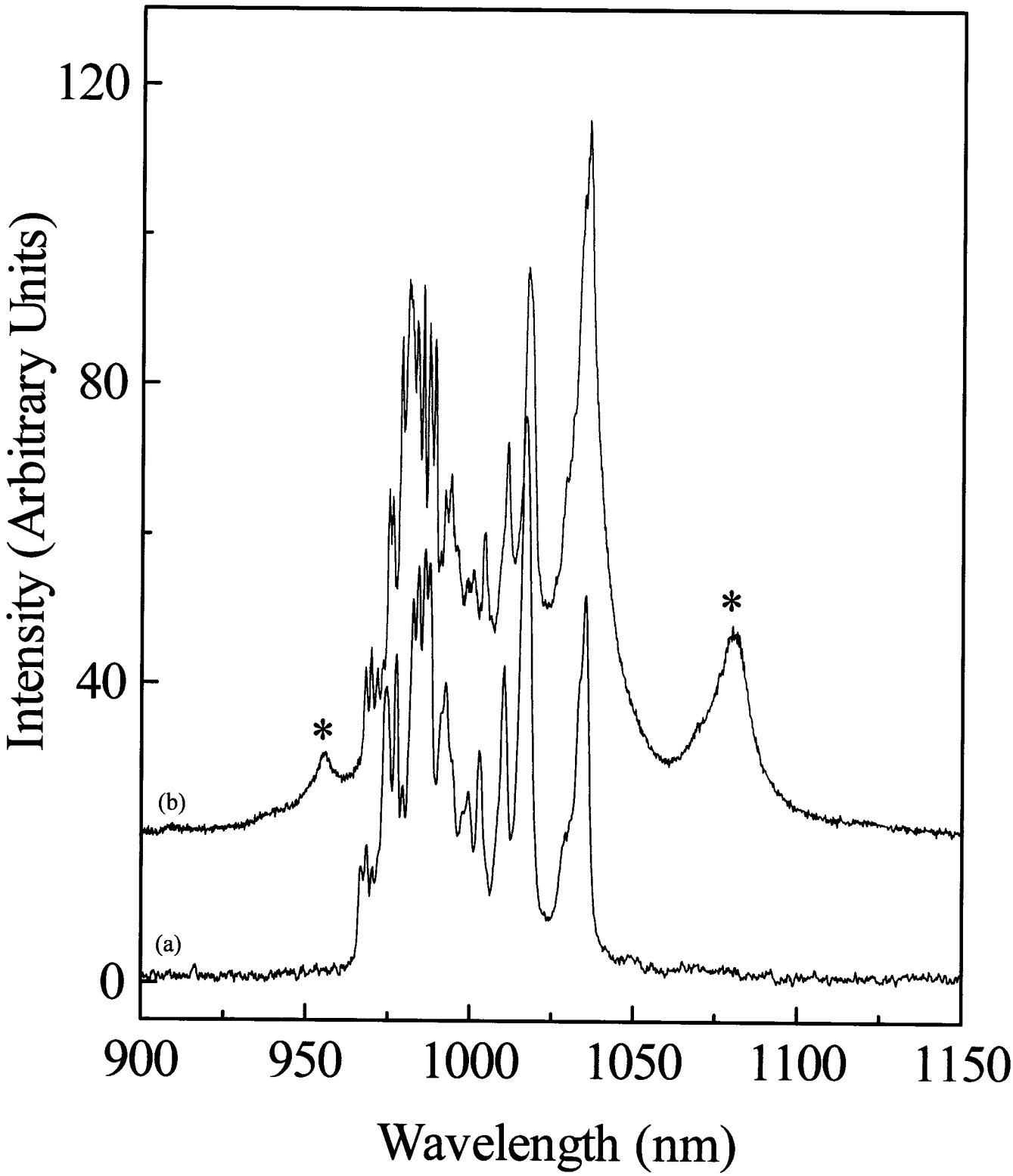

Figure 6.21: Near-infrared Stokes luminescence of the $^4I_{11/2} \rightarrow {}^4I_{15/2}$ transition in bulk (a) $Y_2O_3:Er^{3+}$ (1 mol% Er^{3+}) and (b) $Y_2O_3:Er^{3+}$, Yb^{3+} (1 mol% Er^{3+} and 1 mol% Yb^{3+}) following excitation with 488 nm. Emission from the $^2F_{5/2} \rightarrow {}^2F_{7/2}$ transition denoted with an asterisk (*).

Figures 6.22 and 6.23 present the upconversion (anti-Stokes) spectra of nanocrystalline and bulk $Y_2O_3:Er^{3+}$, Yb^{3+} following excitation with 978 nm radiation. The spectra exhibit three distinct emission bands centered at approximately 530, 560, and 670 nm and correspond to green emission from the $^2H_{11/2}$, $^4S_{3/2}$ and red emission from the $^4F_{9/2}$ excited states to the $^4I_{15/2}$ ground state of the erbium ions, respectively.

To better understand the mechanism by which the $^2H_{11/2}$, $^4S_{3/2}$ and $^4F_{9/2}$ excited states are populated following NIR irradiation, the upconverted luminescence intensity of the green ($^2H_{11/2}$, $^4S_{3/2} \rightarrow {}^4I_{15/2}$) and red ($^4F_{9/2} \rightarrow {}^4I_{15/2}$) emissions were measured as a function of the excitation power (Figure 6.24). The graph of ln(Intensity) versus ln(Power) yields a slope of n equal to approximately 2 for all samples under investigation (Figure 6.24, inset). Thus, we can propose that two photons are involved in the upconversion mechanism responsible for populating the green and red levels. Following 978 nm irradiation of Y_2O_3, the Er^{3+} ion is excited to the $^4F_{7/2}$ state via two successive energy transfers from the Yb^{3+} ions in the $^2F_{5/2}$ state [145, 251]. Thus, one Yb^{3+} ion will transfer its energy to an Er^{3+} ion in the ground state, thereby exciting it to the $^4I_{11/2}$ state. This process is followed by a transfer of energy from another Yb^{3+} ion also in its excited state resulting in the population of the $^4F_{7/2}$ state of the erbium ion. The lower emitting levels are then populated via multiphonon relaxation and green and red is emission is then observed. Of course, interactions between two Er^{3+} ions cannot necessarily be ignored. An NIR photon from the pump beam will also excite an Er^{3+} ion to its $^4I_{11/2}$ state. Another Er^{3+} ion also in the $^4I_{11/2}$ state and in close proximity will transfer its energy to the initial ion thereby exciting it to the $^4F_{7/2}$ state. However, following the addition of Yb^{3+} ions, this process is greatly diminished due to the large absorption cross-

section of the ytterbium ions. Thus, the simultaneous transfer of energy from Yb^{3+}, which populates the $^4F_{7/2}$ state is dominant.

Having described the upconversion pumping mechanisms responsible for populating the $^4F_{7/2}$ state of Er^{3+}, we would expect the green emission to dominate the spectrum, as was the case when directly exciting the $^4F_{7/2}$ state with 488 nm radiation. In the bulk material the green emission still dominates however, there is a clear difference in the relative green-to-red emission intensity in the upconversion spectrum. In the nanocrystalline material, we observe that this effect is much more pronounced and the red emission in fact dominates the spectrum. This is rather unexpected as the $^4F_{9/2}$ state is populated via non-radiative decay from the $^4S_{3/2}$ state involving the emission of several phonons to bridge the 3000 cm^{-1} energy gap between the $^4S_{3/2}$ and $^4F_{9/2}$ states. Thus, we would expect the population in the $^4F_{9/2}$ state to be lower than the $^4S_{3/2}$ state as in the bulk material. Therefore, a process must be operative that allows for the bypassing of the $^2H_{11/2}$ and $^4S_{3/2}$ levels while transferring the pump energy to the $^4F_{9/2}$ state.

It is known that microcrystalline $Y_2O_3:Er^{3+}$, Yb^{3+} shows predominantly red emission following infrared excitation with 980 nm [248] into the $^2F_{5/2}$ state of the Yb^{3+} ion in contrast with the direct excitation of the $^4F_{7/2}$ state of Er^{3+} (with 488 nm), which shows predominantly green emission. The enhancement of the population in the red ($^4F_{9/2}$) emitting level was observed to occur through an ion-pair process and is achieved via two resonant transitions: ($^4F_{7/2}$, $^4I_{11/2}$) → ($^4F_{9/2}$, $^4F_{9/2}$) (Figure 6.25). An enhancement of the red emission occurs in both the bulk and the nanocrystalline samples albeit to different extents, however as the above process occurs via two energy transfer processes, it should in principle occur with equal probability in both the bulk and the nanocrystalline

samples having the same dopant concentration. Thus, this process does not account for such a drastic difference in the magnitude of the red enhancement between the bulk and nanocrystalline samples.

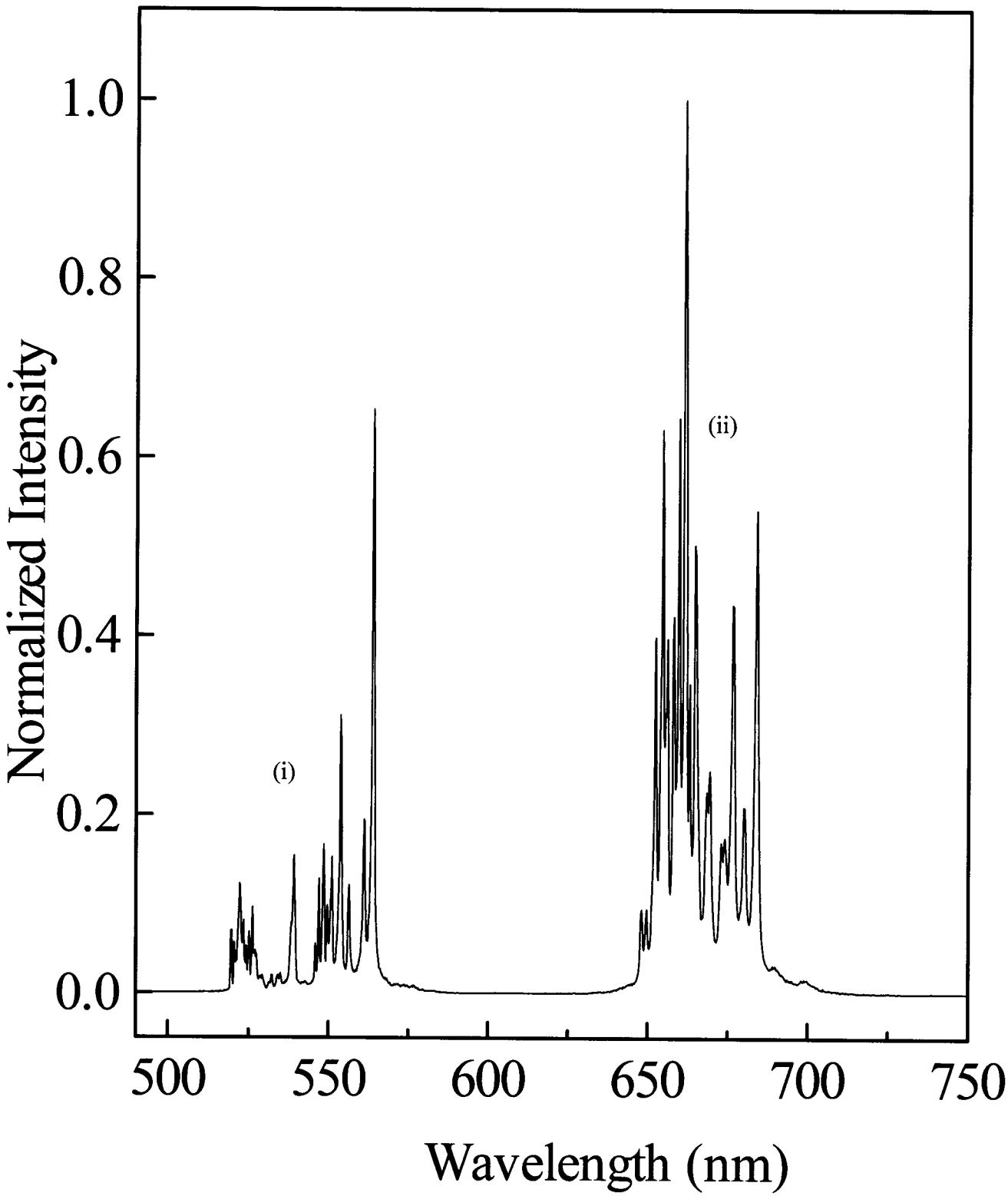

Figure 6.22: Room temperature upconversion (anti-Stokes) luminescence of nanocrystalline $Y_2O_3:Er^{3+}$, Yb^{3+} (1 mol% Er^{3+} and 1 mol% Yb^{3+}) prepared via propellant synthesis following excitation with 978 nm.
(i) $^2H_{11/2}$, $^4S_{3/2} \rightarrow {}^4I_{15/2}$ (ii) $^4F_{9/2} \rightarrow {}^4I_{15/2}$.

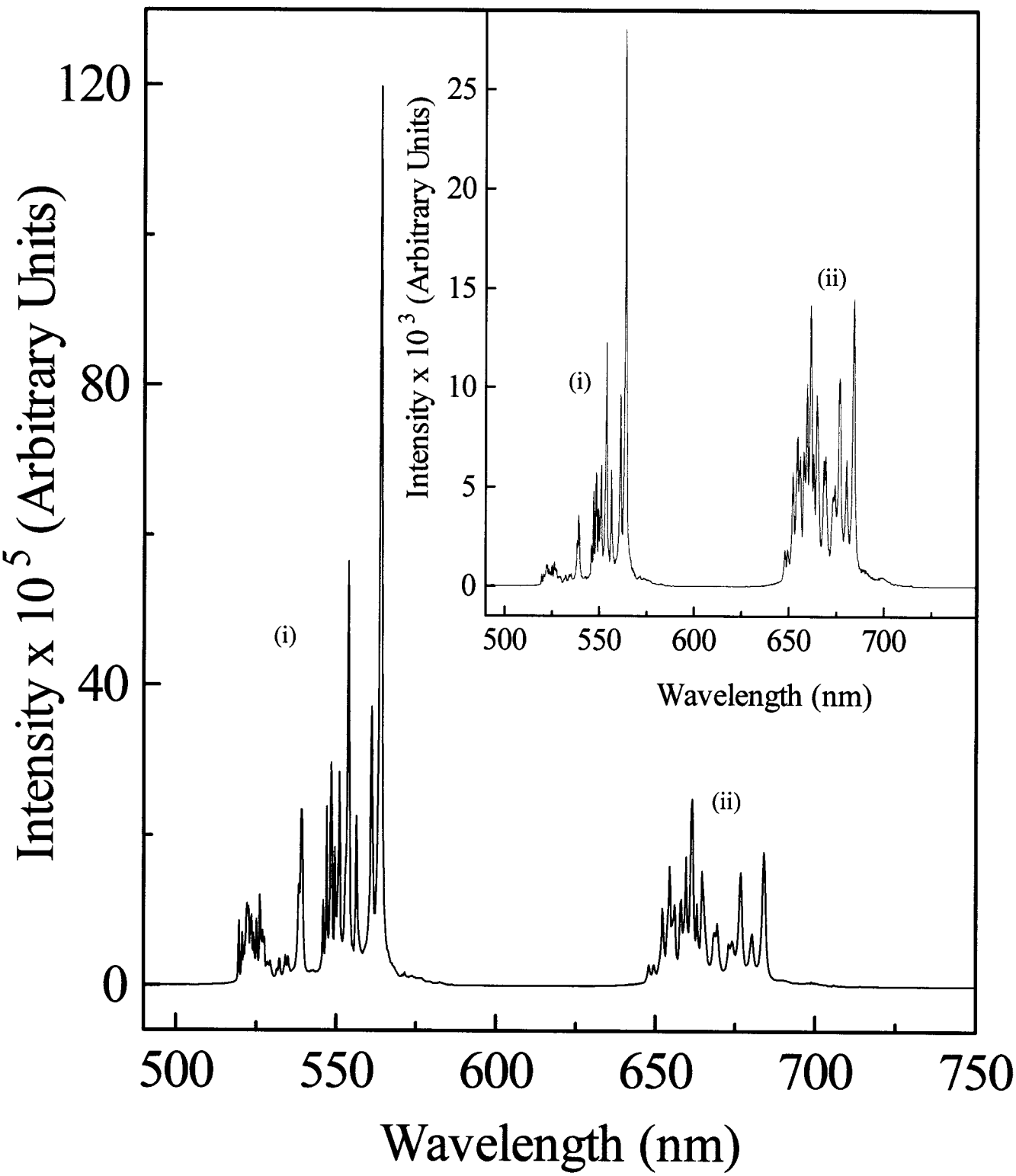

Figure 6.23: Room temperature anti-Stokes luminescence of bulk $Y_2O_3:Er^{3+}$, Yb^{3+} (1 mol% Er^{3+} and 1 mol% Yb^{3+}) following excitation with 978 nm. Inset: Room temperature anti-Stokes luminescence of bulk $Y_2O_3:Er^{3+}$, Yb^{3+} following excitation with 1064 nm. (i) $^2H_{11/2}$, $^4S_{3/2} \rightarrow {}^4I_{15/2}$ (ii) $^4F_{9/2} \rightarrow {}^4I_{15/2}$.

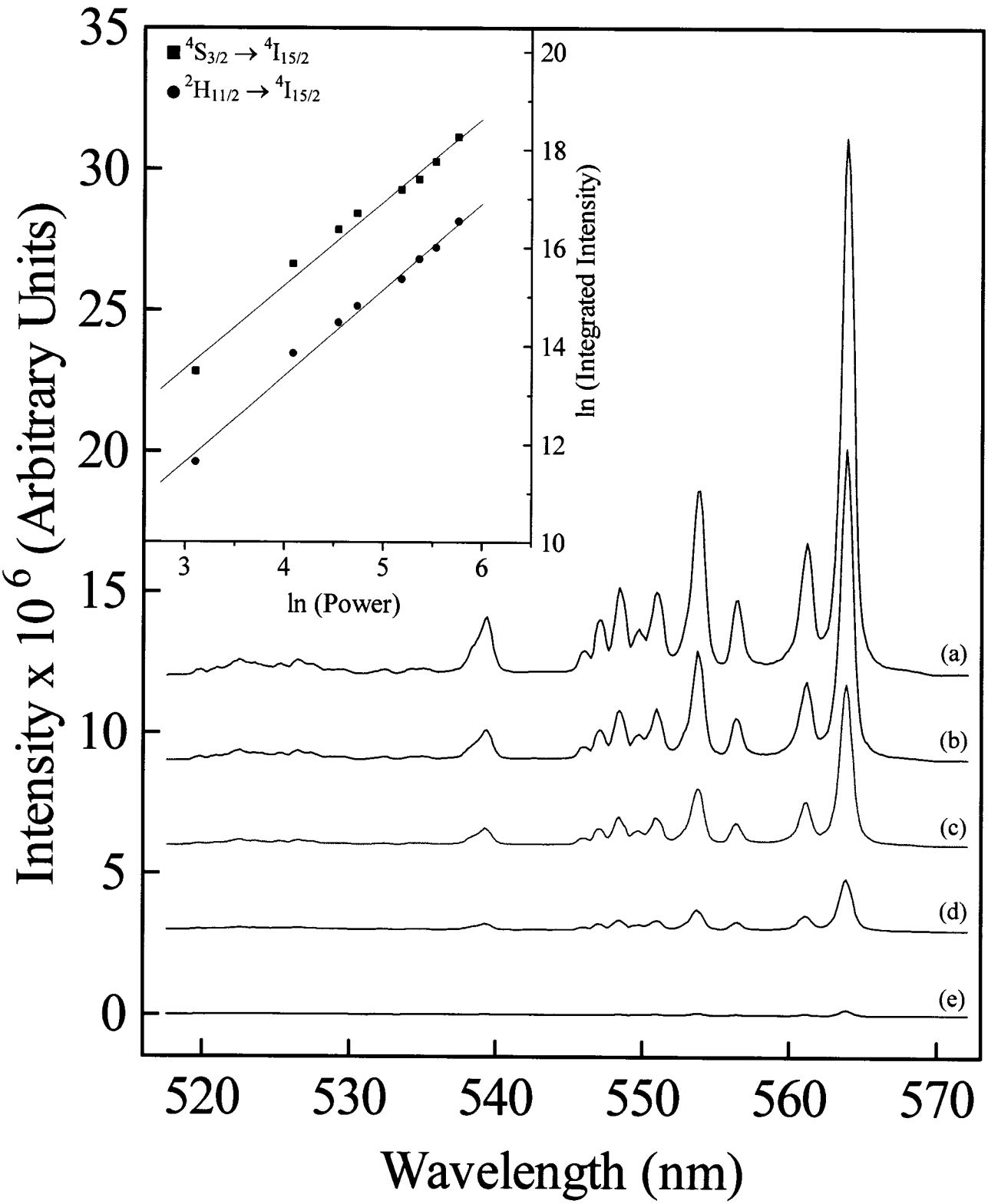

Figure 6.24: Study of the upconversion luminescence of the $^2H_{11/2}$, $^4S_{3/2} \rightarrow {}^4I_{15/2}$ transitions in bulk $Y_2O_3:Er^{3+}$, Yb^{3+} following excitation with 978 nm as a function of pump power; (a) 320 mW (b) 215 mW (c) 115 mW (d) 60 mW (e) 25 mW.
Inset: Power dependence of the $^2H_{11/2}$, $^4S_{3/2} \rightarrow {}^4I_{15/2}$ anti-Stokes luminescence intensity of bulk $Y_2O_3:Er^{3+}$, Yb^{3+} observed following 978 nm excitation

In order to effectively understand why this phenomenon occurs in the nanocrystalline material and not in the bulk, the structural properties of the samples under investigation must certainly be discussed. As previously discussed, the nanocrystals contain CO_3^{2-} and OH^- impurities on their surface and thus have available large vibrational quanta to efficiently depopulate the excited states non-radiatively. Thus, this is the distinguishing factor between the bulk and nanocrystalline samples as the bulk lattice does not posses any high-energy phonons and must solely rely on the intrinsic phonons of yttria. Therefore, a mechanism must be operative which utilizes these high-energy phonons.

In the nanocrystalline material, the Er^{3+} ion will decay non-radiatively from the $^4I_{11/2}$ state to the $^4I_{13/2}$ state following the initial energy transfer from the Yb^{3+} ion by very efficient multiphonon relaxation. Essentially, the rate of multiphonon relaxation is dependent upon the energy gap separating the emitting level and the next lower level as well as the highest phonon energy in the material [106]. As the nanocrystalline material possesses relatively high phonon energies, the rate of multiphonon relaxation is rather large. The gap between the $^4I_{11/2}$ and $^4I_{13/2}$ states is approximately $3600cm^{-1}$ and few high-energy phonons can easily bridge the gap. In contrast, the bulk material utilizing only the intrinsic yttria phonons to bridge the same gap requires many more phonons. Following the multiphonon relaxation to the $^4I_{13/2}$ state, another energy transfer from the Yb^{3+} ion in the $^2F_{5/2}$ state will excite the Er^{3+} ion to the $^4F_{9/2}$ state [252, 253]. However, an excess energy of approximately 1600 cm^{-1} is present and must be dissipated by the lattice to conserve energy (Figure 6.25). Again, the high phonon energies in the nanocrystalline material can easily accommodate the extra energy.

Further proof for this mechanism is provided from the anti-Stokes emission spectrum of bulk $Y_2O_3:Er^{3+}$, Yb^{3+} following excitation with 1064 nm (Figure 6.23, inset). The red ($^4F_{9/2} \rightarrow {}^4I_{15/2}$) emission was observed to be more intense relative to the green ($^2H_{11/2}$, $^4S_{3/2} \rightarrow {}^4I_{15/2}$) emission when compared to the spectrum obtained following excitation with 978 nm. The enhancement in the bulk occurs because the $^4F_{9/2} \leftarrow {}^4I_{13/2}$ transition is nearly resonant with the 1064 nm line of the Nd:YAG laser [253]. The excess energy in this transition is on the order of about 800 cm^{-1} and thus the probability of the process occurring in the bulk material is much greater resulting in an enhancement of the $^4F_{9/2}$ population. Yamada [107] showed from experimental evidence that the phonon of ~400 cm^{-1} and not the maximum phonon energy contributes dominantly to the energy transfer processes and therefore is more coupled to the electronic transitions. Thus, the bulk sample would require only two yttria phonons to conserve energy in the process.

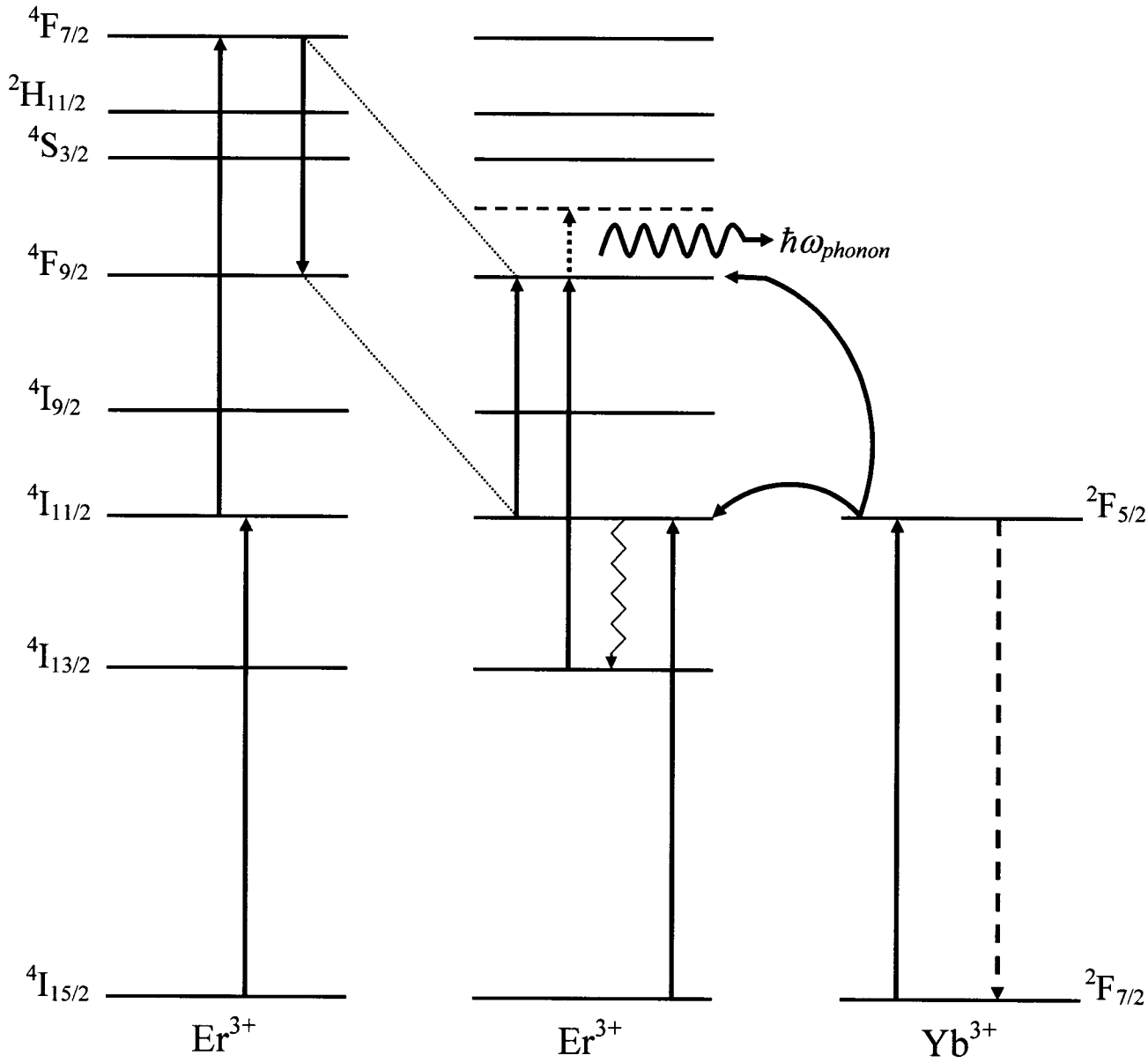

Figure 6.25: Schematic representation of the Yb^{3+} to Er^{3+} energy transfers responsible for population of the $^4F_{7/2}$ state as well as the $(^4F_{7/2}, {}^4I_{11/2}) \rightarrow (^4F_{9/2}, {}^4F_{9/2})$ ion-pair process and the phonon-assisted energy transfer process responsible for directly populating the $^4F_{9/2}$ state in $Y_2O_3:Er^{3+}$, Yb^{3+} following 978 nm excitation.

6.1.10. Significance of Yb^{3+} Concentration on the Upconversion Mechanisms in Co-doped $Y_2O_3:Er^{3+}$, Yb^{3+} Nanocrystals

In this section, we will be examining how the concentration of Yb^{3+} alters the upconversion pathway in co-doped $Y_2O_3:Er^{3+}$, Yb^{3+} nanocrystals. We investigate 6 different co-doped $Y_2O_3:Er^{3+}$, Yb^{3+} samples. Five nanocrystalline samples and one bulk used for comparison. A list of all samples studied in this section is given in Table 6.3 and for simplicity, we will refer to the samples by their assigned names shown below.

Table 6.3: List of the bulk and nanocrystalline $Y_2O_3:Er^{3+}$, Yb^{3+} samples investigated.

Sample Name	Er^{3+} Concentration (mol%)	Yb^{3+} Concentration (mol%)
Nanocrystalline $Y_2O_3:Er^{3+}$		
Er1Yb1	1	1
Er1Yb5	1	5
Er1Yb10	1	10
Er01Yb1	0.1	1
Er5Yb1	5	1
Bulk $Y_2O_3:Er^{3+}$		
BErYb	1	1

The visible emission spectra of nanocrystalline $Y_2O_3:Er^{3+}$, Yb^{3+} for all samples under investigation are presented in Figure 6.26. Green emission was observed centered at approximately 535 nm and was attributed to the thermalized $^2H_{11/2}$, $^4S_{3/2} \rightarrow {}^4I_{15/2}$ transition [254]. Furthermore, red emission was observed from the $^4F_{9/2} \rightarrow {}^4I_{15/2}$ transition centered at approximately 670 nm. It is clear from the visible emission spectra that the relative intensities of the green and red emission bands change with concentration. For example, in the samples with constant Er^{3+} concentration (Er1Yb1,

Er1Yb5, and Er1Yb10) the red ($^4F_{9/2} \rightarrow {}^4I_{15/2}$) emission increases relative to the green with increasing concentration of Yb^{3+}. Similarly, in the samples with constant Yb^{3+} concentration (Er01Yb1 and Er5Yb1), the red emission becomes stronger as the concentration of the Er^{3+} ions is increased. Previously, in singly doped Y_2O_3:Er^{3+} nanocrystals we have demonstrated that a resonant cross-relaxation mechanism of the type: $^4F_{7/2} \rightarrow {}^4F_{9/2}$ and $^4F_{9/2} \leftarrow {}^4I_{11/2}$ could directly populate the red emitting $^4F_{9/2}$ state when resonantly exciting the $^4I_{11/2}$ state with 980 nm [239]. It is also possible for this cross-relaxation mechanism to occur following 488 nm excitation where one Er^{3+} ion directly excited to the $^4F_{7/2}$ state interacts with another Er^{3+} ion that has non-radiatively decayed to the $^4I_{11/2}$ state. This cross-relaxation mechanism is concentration dependent and thus increasing the number of Er^{3+} ions would undoubtedly increase the efficiency of the mechanism. However, in the case of samples Er1Yb1, Er1Yb5, and Er1Yb10, the Er^{3+} concentration is constant and 488 nm should not excite the ytterbium ions since Yb^{3+} has only one excited state ($^2F_{5/2}$) with energies between 900 and 1000 nm [255]. Thus, we should not see the emission from the $^4F_{9/2} \rightarrow {}^4I_{15/2}$ transition grow with increasing Yb^{3+} concentration. Clearly, this is not the case and increasing the concentration of Yb^{3+} ions also increases the intensity of the $^4F_{9/2} \rightarrow {}^4I_{15/2}$ transition. In Y_2O_3:Er^{3+}, Yb^{3+} we have earlier observed that exciting the $^4F_{7/2}$ state of Er^{3+} with 488 nm also excites the Yb^{3+} ions via an Er^{3+} to Yb^{3+} energy transfer where neighboring Er^{3+} and Yb^{3+} ions interact via the $^4F_{7/2} \rightarrow {}^4I_{11/2}$ and $^2F_{5/2} \leftarrow {}^2F_{7/2}$ cross-relaxation mechanism [249]. This process populates the $^4I_{11/2}$ state of the Er^{3+} ion, which in turn can interact with another Er^{3+} ion in the $^4F_{7/2}$ state and undergo the $^4F_{7/2} \rightarrow {}^4F_{9/2}$ and $^4F_{9/2} \leftarrow {}^4I_{11/2}$ mechanism to directly populate the $^4F_{9/2}$ level thus causing the red enhancement (see Figure 6.27).

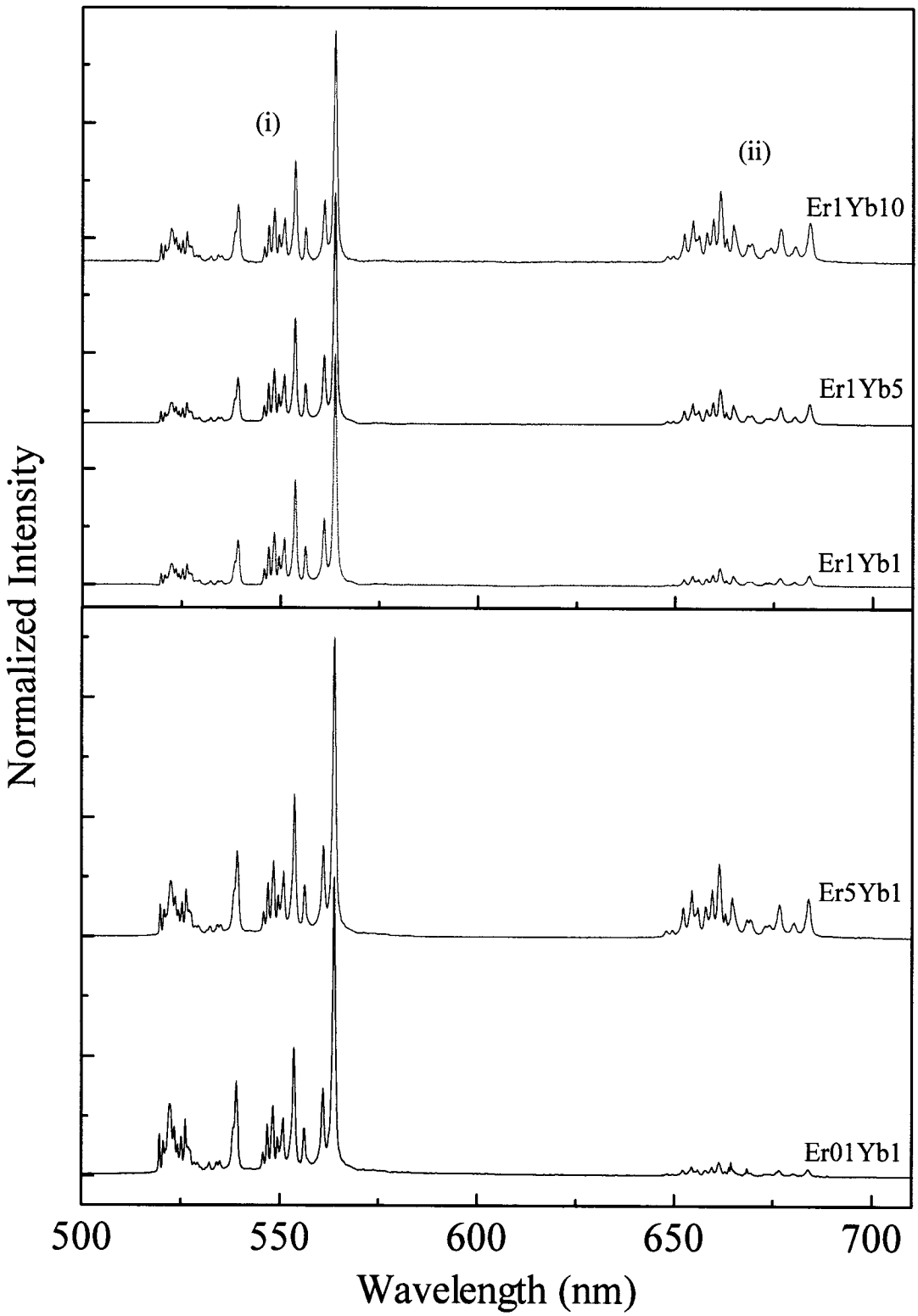

Figure 6.26: Visible emission spectra of nanocrystalline $Y_2O_3:Er^{3+}$, Yb^{3+} (λ_{exc} = 488 nm) showing the (i) $^2H_{11/2}$, $^4S_{3/2} \rightarrow {}^4I_{15/2}$ and (ii) $^4F_{9/2} \rightarrow {}^4I_{15/2}$ transitions.

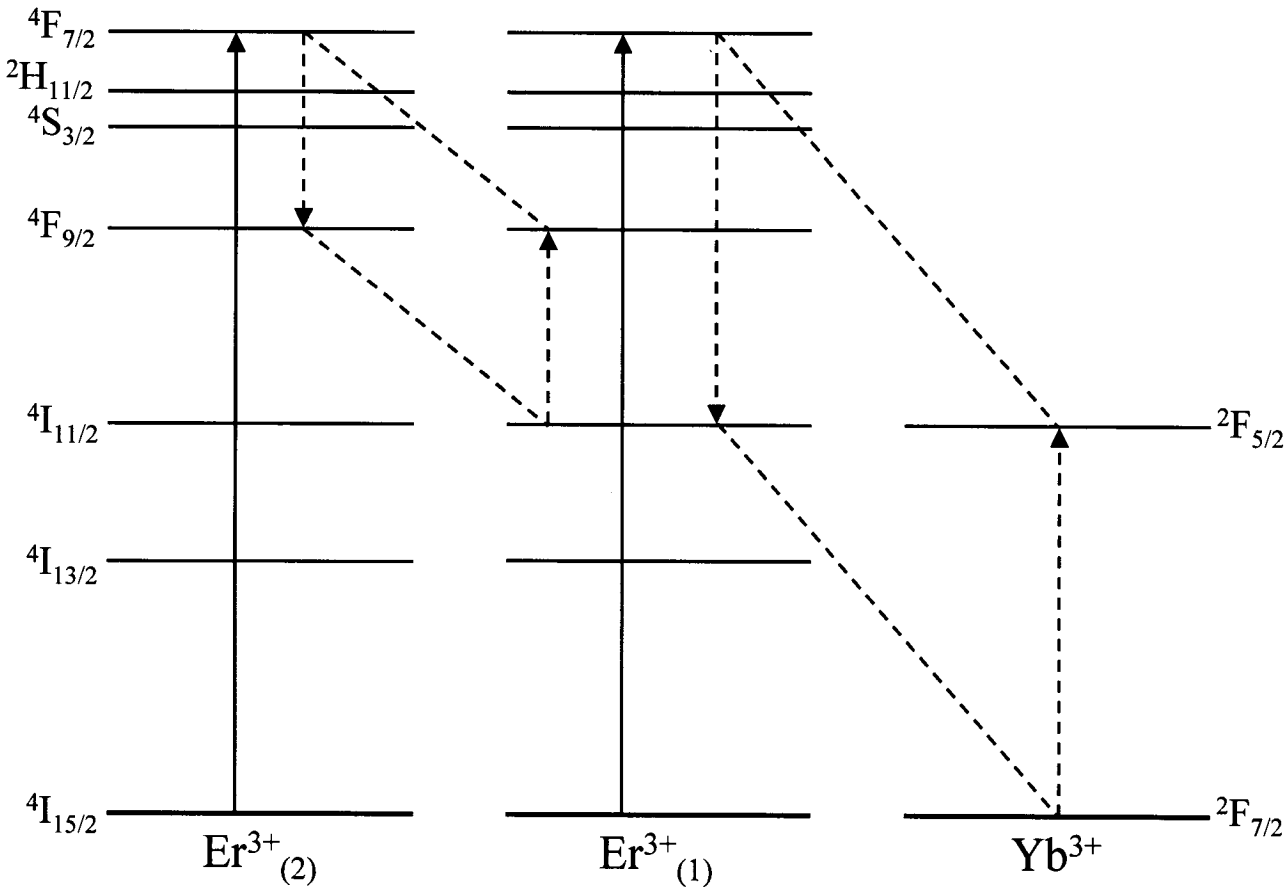

Figure 6.27: Schematic representation of the process responsible for the red enhancement following excitation of nanocrystalline $Y_2O_3:Er^{3+}$, Yb^{3+} with 488 nm.

The visible emission spectrum of the bulk $Y_2O_3:Er^{3+}$, Yb^{3+} material (BErYb) also shows green and red emission from the $^2H_{11/2}$, $^4S_{3/2} \rightarrow {}^4I_{15/2}$ and $^4F_{9/2} \rightarrow {}^4I_{15/2}$ transitions, respectively [249]. The energies of these two transitions in the bulk are identical to the nanocrystalline material indicating that the crystal field surrounding the Er^{3+} and Yb^{3+} ions is reasonably similar and not affected by the small size of the particle. However, we note that the intensity of the emission is much greater in the bulk material. Again, the reduction in emission intensity in the nanocrystalline material is caused by the adsorption of atmospheric CO_2 and H_2O on the surface of the particles.

The decay times of the nanocrystalline $Y_2O_3:Er^{3+}$, Yb^{3+} samples were acquired following excitation with 488 nm and are presented in Table 6.4. The decay curves obtained deviated from exponential behavior as is expected when energy transfer is involved and thus could not be fit with a single exponential model. We therefore determined the emission decay time constant, τ_m, using the model proposed by Nakazawa (eqn 6.1.3) [246]. Table 6.4 clearly demonstrates that increasing the concentration of Yb^{3+} results in a reduction of the decay times of the $^4S_{3/2}$ and $^4F_{9/2}$ excited states. It is possible that at increased doping levels, the pairing or aggregation of donor Yb^{3+} ions may turn some of those ions into quenchers and thus induces a quenching effect following an $Er^{3+} \rightarrow Yb^{3+}$ back transfer [256]. This is evident in the pre-normalized visible emission spectra of the nanocrystalline material where the overall luminescence intensity is lowest for the sample with 10 mol% Yb^{3+} (Er1Yb10). Thus, at higher concentrations of Yb^{3+}, the Yb^{3+} ions may act as trapping centers and dissipate the energy non-radiatively. Moreover, increasing the concentration of Er^{3+} similarly results in a drastic reduction of the decay time constant. This self quenching is the result of cross-

relaxation mechanisms such as $^2H_{11/2} + {}^4I_{15/2} \rightarrow {}^4I_{9/2} + {}^4I_{13/2}$ where it has been shown that at higher concentrations of Er^{3+}, this process causes significant depopulation of the upper excited states [257].

Table 6.4: Decay time constants, τ_m, of nanocrystalline $Y_2O_3:Er^{3+}$, Yb^{3+} following excitation with 488 nm into the $^4F_{7/2}$ state of Er^{3+}.

Sample Name	Decay Time Constants (μs)	
Nanocrystalline $Y_2O_3:Er^{3+}$	$^4S_{3/2} \rightarrow {}^4I_{15/2}$	$^4F_{9/2} \rightarrow {}^4I_{15/2}$
Er1Yb1	25	25
Er1Yb5	20	21
Er1Yb10	13	14
Er01Yb1	56	41
Er5Yb1	9	18
Bulk $Y_2O_3:Er^{3+}$		
BErYb	190	176

Following excitation of the nanocrystalline $Y_2O_3:Er^{3+}$, Yb^{3+} material with NIR radiation (λ_{exc} = 978 nm), green and red luminescence was observed centered at approximately 535 and 670 nm ascribed to the $^2H_{11/2}$, $^4S_{3/2} \rightarrow {}^4I_{15/2}$ and $^4F_{9/2} \rightarrow {}^4I_{15/2}$ transitions of the Er^{3+} ions, respectively (Figure 6.28).

The upconversion mechanism in Er^{3+} and Yb^{3+} co-doped systems is very well known and occurs via two successive transfers of energy from the Yb^{3+} ion to the Er^{3+} ion (Figure 6.29) [248]. This is supported by the study of the power dependence on the upconverted luminescence as well as the decay times in the samples under investigation (Figure 6.30). A slope equal to approximately 2 was obtained for the $^2H_{11/2} \rightarrow {}^4I_{15/2}$, $^4S_{3/2} \rightarrow {}^4I_{15/2}$, and $^4F_{9/2} \rightarrow {}^4I_{15/2}$ upconverted transitions in the graph of $\ln(I_{vis})$ versus $\ln(I_{NIR})$

for the Er1Yb1 sample indicating that the upconversion occurs via a two photon process (Figure 6.30, inset). Thus, the Yb^{3+} ion is excited to the $^2F_{5/2}$ state via the 978 nm photons and transfers its energy to an Er^{3+} ion in the ground state, thereby exciting it to the $^4I_{11/2}$ intermediate excited state. Immediately following this process, a subsequent transfer of energy from another Yb^{3+} ion also in its excited state results in the population of the $^4F_{7/2}$ state of the Er^{3+} ion. This process is particularly dominant in the co-doped samples with higher concentrations of Yb^{3+} due to the larger absorption cross-section of the Yb^{3+} $^2F_{5/2}$ excited state compared to the $^4I_{11/2}$ excited state of Er^{3+}. However, in the Er5Yb1 sample for example, where there are 5× more Er^{3+} ions than Yb^{3+} ions, we cannot exclude the possibility that the upconversion occurs principally via the Er^{3+} ions, either via an excited state absorption (ESA) process or by way of two Er^{3+} ions interacting in energy transfer upconversion (ETU) (Figure 6.29). In ESA upconversion, ground state absorption (GSA) of an Er^{3+} ion to the $^4I_{11/2}$ state via the 978 nm photons is followed by the excited state absorption of a second pump photon to populate the $^4F_{7/2}$ state. In the ETU process, two ions in close proximity interact in order to populate the $^4F_{7/2}$ state. Thus, two neighboring Er^{3+} ions are excited via ground state absorption to the $^4I_{11/2}$ level. One ion immediately transfers its energy to the other and returns to the $^4I_{15/2}$ ground state, while the second ion is excited to the $^4F_{7/2}$ level.

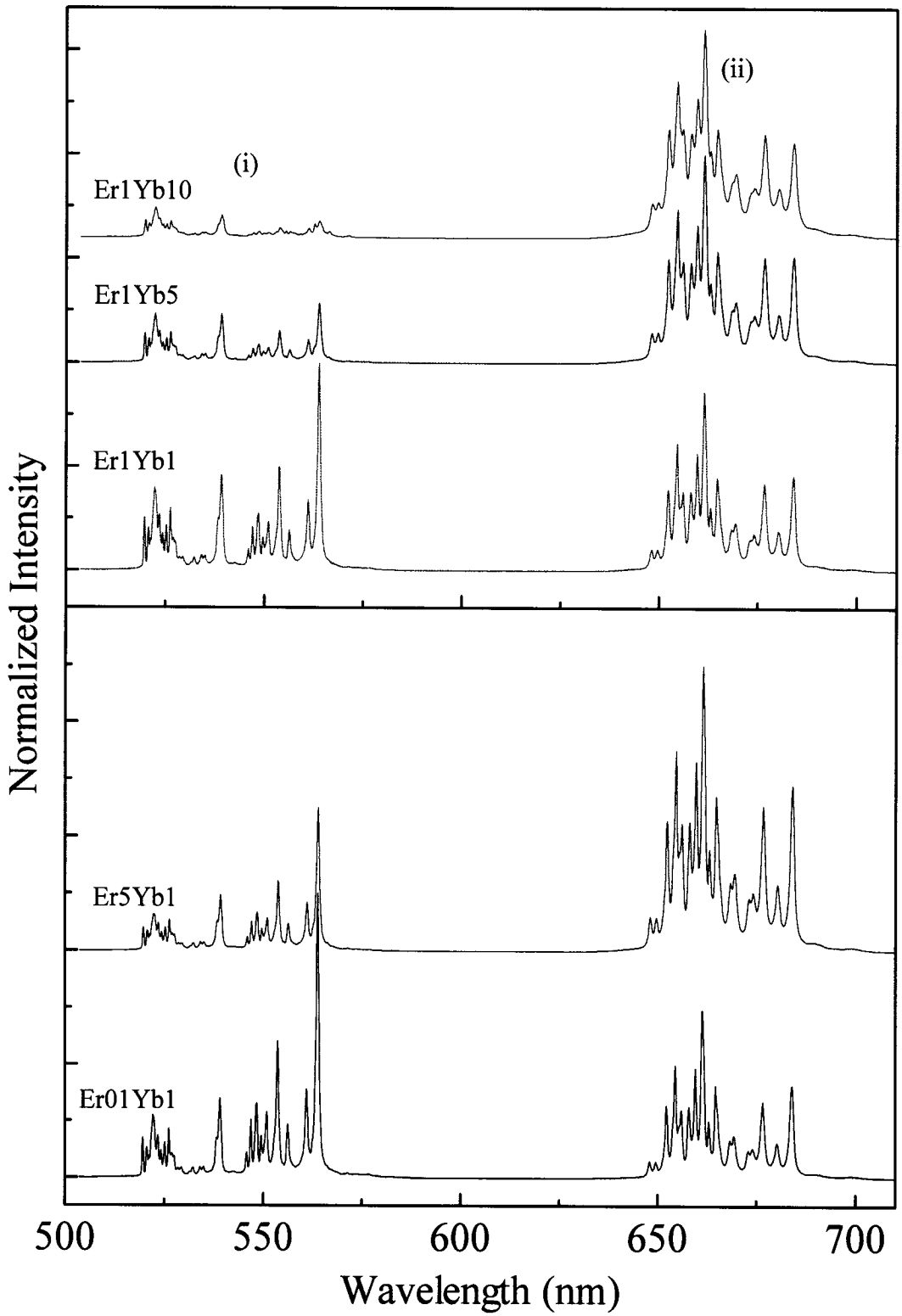

Figure 6.28: Upconversion spectra of nanocrystalline $Y_2O_3:Er^{3+}$, Yb^{3+} (λ_{exc} = 978 nm) showing the (i) $^2H_{11/2}$, $^4S_{3/2} \rightarrow {}^4I_{15/2}$ and (ii) $^4F_{9/2} \rightarrow {}^4I_{15/2}$ transitions.

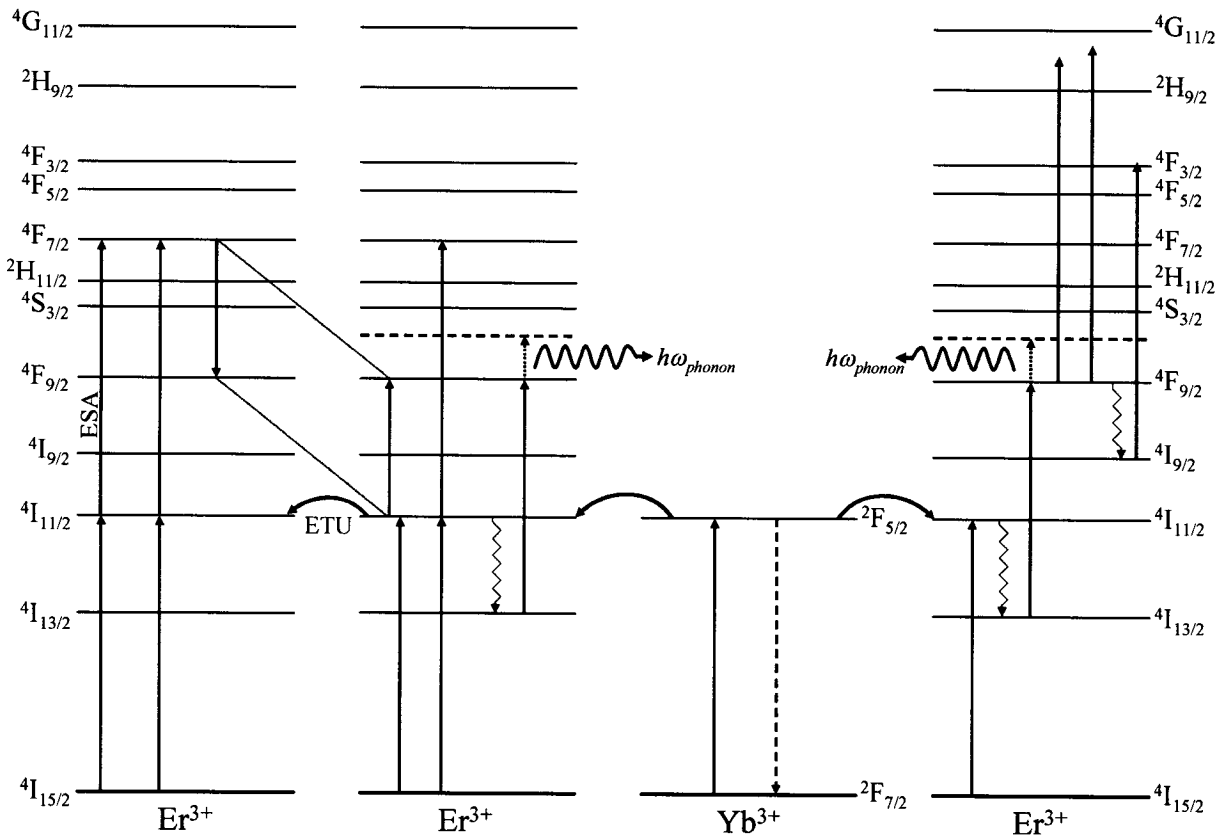

Figure 6.29: Schematic representation of the various upconversion mechanisms in nanocrystalline Y_2O_3:Er^{3+}, Yb^{3+} following excitation with 978 nm.

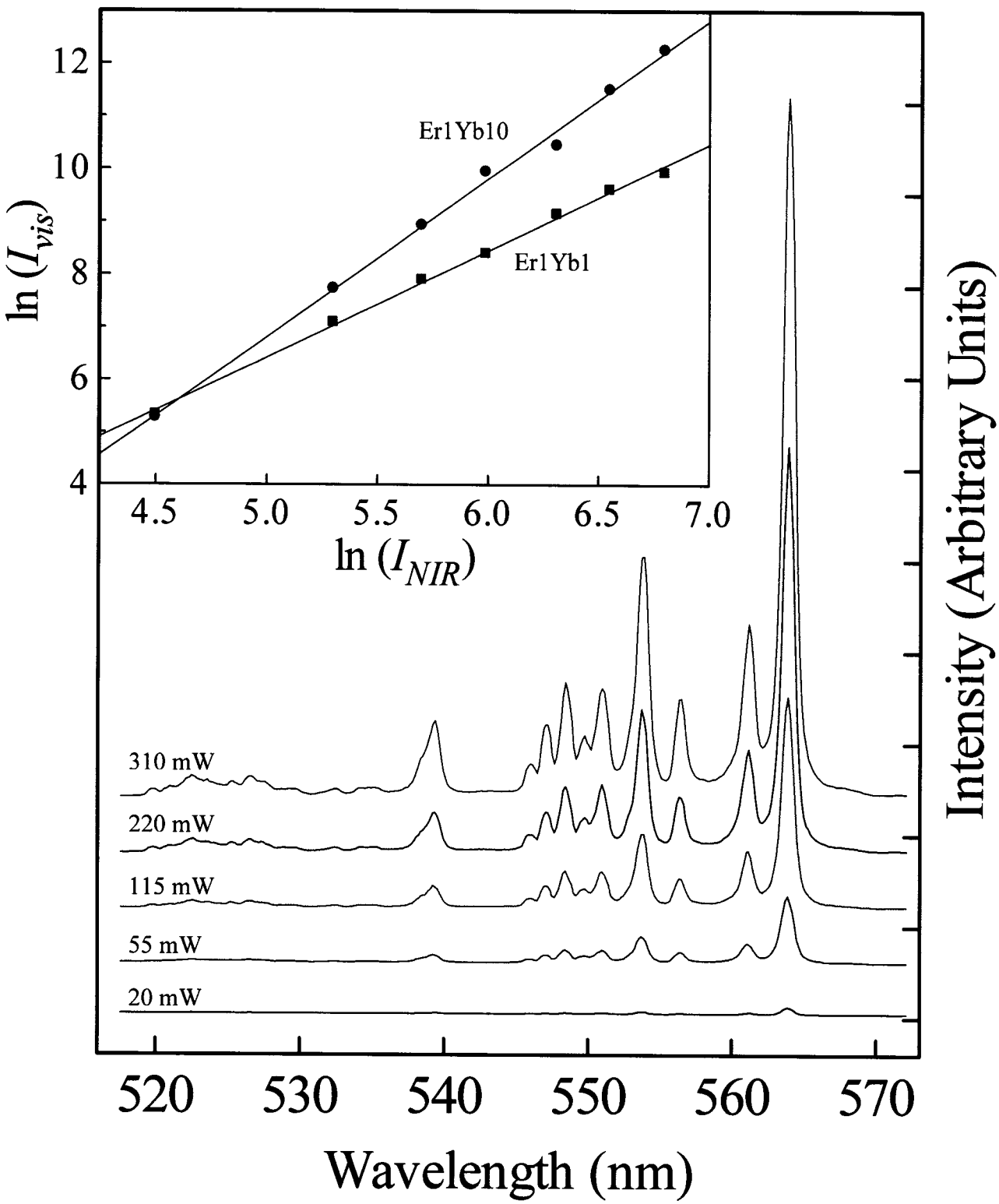

Figure 6.30: Power dependence of the green ($^4S_{3/2} \rightarrow {}^4I_{15/2}$) upconverted luminescence in nanocrystalline Y_2O_3:Er^{3+}, Yb^{3+} (Er1Yb1) following excitation with 978 nm. Inset: Graph of ln(I_{vis}) versus ln(I_{NIR}) for the Er1Yb1 and Er1Yb10 samples for the $^4S_{3/2} \rightarrow {}^4I_{15/2}$ transition.

The upconverted decay time constants follow the same general trend as those obtained with 488 nm pumping (Table 6.5). Again, energy migration amongst donor ions may carry the energy to a distant killer or a quenching center resulting in the shorter observed decay time constant. However, of variance with the decay times obtained with 488 nm, a lengthening of the upconverted decay times is observed and represents clear confirmation that energy transfer is the dominant mechanism of upconversion.

Table 6.5: Decay time constants, τ_m, of nanocrystalline $Y_2O_3:Er^{3+}$, Yb^{3+} following excitation with 978 nm into the $^2F_{5/2}$ state of Yb^{3+}.

Sample Name	Decay Time Constants (μs)	
Nanocrystalline $Y_2O_3:Er^{3+}$	$^4S_{3/2} \rightarrow {}^4I_{15/2}$	$^4F_{9/2} \rightarrow {}^4I_{15/2}$
Er1Yb1	142	153
Er1Yb5	65	73
Er1Yb10	11	21
Er01Yb1	174	198
Er5Yb1	88	120
Bulk $Y_2O_3:Er^{3+}$		
BErYb	246	279

We have observed in the spectra obtained with direct excitation of the $^4F_{7/2}$ state using 488 nm, that the red emission is enhanced with the addition of both Yb^{3+} and Er^{3+}. However, the upconversion spectra (λ_{exc} = 978 nm) clearly reveal an even greater augmentation of the red ($^4F_{9/2} \rightarrow {}^4I_{15/2}$) emission intensity. In the most extreme case, the Er1Yb10 had almost entirely red emission and its luminescence appeared yellow to the naked eye following NIR excitation. This is ideal as it allows for tailoring of the upconversion emission properties of the material simply by varying the Yb^{3+} and Er^{3+}

concentrations. The most likely cause of this increased enhancement is an increase in the efficiency of the $^4F_{7/2} + {}^4I_{11/2} \rightarrow {}^4F_{9/2} + {}^4F_{9/2}$ cross-relaxation mechanism, which is responsible for the direct population of the $^4F_{9/2}$ level (Figure 6.29).

Moreover, if we compare the upconversion spectrum of identically doped bulk and nanocrystalline $Y_2O_3:Er^{3+}$, Yb^{3+} (1 mol%, each) we observe a drastic difference in the relative red-to-green ratios where the red enhancement is much more pronounced in the nanocrystalline material (Figure 6.31). In the $Y_2O_3:Er^{3+}$, Yb^{3+} nanocrystals the red ($^4F_{9/2} \rightarrow {}^4I_{15/2}$) emission is of higher intensity than the green while in the bulk material, the emission from the green $^2H_{11/2}$, $^4S_{3/2} \rightarrow {}^4I_{15/2}$ transition is much more intense relative to the red. In the case of multipolar interactions, the cross-relaxation probability depends on the product of the probabilities of two radiative transitions [180]. Therefore, in similarly doped bulk and nanocrystals, the magnitude of the red enhancement should be equivalent as the probability of the two transitions occurring is identical. Clearly, an additional mechanism not present in the bulk material is operative beyond the previously discussed cross-relaxation mechanism. Ground state absorption of 978 nm photons from Yb^{3+} will bring the ion to the $^2F_{7/2}$ state, which in turn donates its energy to an Er^{3+} ion in close proximity and exciting it to the $^4I_{11/2}$ level. In the nanocrystalline material a rapid non-radiative decay from this state will populate the $^4I_{13/2}$ level. The energy gap separating the $^4I_{11/2}$ and $^4I_{13/2}$ states of Er^{3+} is approximately 3600 cm^{-1} so the high energy phonons in nanocrystalline yttria could bridge the gap with relative ease. On the other hand, the bulk material would require approximately 6 intrinsic yttria phonons, which makes this multiphonon relaxation much less likely. It has been shown that in Er^{3+}/Yb^{3+} co-doped systems, the $^4F_{9/2}$ state could be populated via the non-resonant $^4F_{9/2} \leftarrow {}^4I_{13/2}$

transition following excitation with 1064 nm where the small excess energy is easily dissipated by most lattices. However, with 978 nm excitation of $Y_2O_3:Er^{3+}$, Yb^{3+} the excess energy would be approximately 1600 cm^{-1}. This energy could easily be accommodated by the yttrium oxide nanocrystals although it would be more difficult in the bulk material with only the intrinsic yttria phonons. Thus as we previously saw, in nanocrystals of $Y_2O_3:Er^{3+}$, Yb^{3+} another mechanism is operative, which proceeds as follows. Ground state absorption of 978 nm photons from Yb^{3+} will bring the ion to the $^2F_{5/2}$ state, which in turn will donate its energy to an Er^{3+} ion in close proximity thereby exciting it to the $^4I_{11/2}$ level. As discussed, a rapid non-radiative decay from this state will populate the $^4I_{13/2}$ level. A subsequent energy transfer from another Yb^{3+} ion in its excited state will directly populate the $^4F_{9/2}$ level with the excess energy being dissipated by the nanocrystal lattice and resulting in the red enhancement (Figure 6.29). Clearly, this is a concentration dependent process since increasing the concentration of the Yb^{3+} ions results in a corresponding increase of the red enhancement. It should also be noted that the Yb^{3+} to Er^{3+} ratio is not key to the red emission enhancement. By comparing the Er1Yb10 and Er01Yb1 nanocrystalline samples both with 10:1 Yb:Er ratio, we notice that the Er1Yb10 has a much greater red emission than the Er01Yb1 sample. Clearly, this is the result of a higher efficiency of both previously discussed mechanisms, which are responsible for populating the $^4F_{9/2}$.

This mechanism is supported by the power study of the Er1Yb10 sample where the results indicate that the $^4S_{3/2}$ state is populated via a 3 photon process (Figure 6.30, inset). This is in contrast to the power study of the Er1Yb1 sample where 2 photons were responsible for populating the state. At high Yb^{3+} concentrations the $^4F_{9/2} \leftarrow {}^4I_{13/2}$

upconversion mechanism is very efficient and results in the bypassing of the green $^4S_{3/2}$ state altogether. The upconversion emission spectrum (Figure 6.32) in the UV/blue region (370 – 430 nm) reveals emission from the $^4G_{11/2} \rightarrow {}^4I_{15/2}$ and $^2H_{9/2} \rightarrow {}^4I_{15/2}$ transitions between 375 – 395 and 400 – 425 nm, respectively. It should be noted that the transitions from the $^4F_{9/2}$ state to either the $^4G_{11/2}$ or $^2H_{9/2}$ states are non-resonant and thus must be mediated by phonons. The mechanism involving the $^4G_{11/2} \leftarrow {}^4F_{9/2}$ transition (λ_{exc} = 978 nm) would require at least 430 cm^{-1} of energy from the lattice to bridge the gap whereas the one involving the $^2H_{9/2} \leftarrow {}^4F_{9/2}$ transition would require approximately 735 cm^{-1} of energy to be dissipated. However, the UV/blue upconversion spectrum reveals that the relative emission intensity of the $^4G_{11/2} \rightarrow {}^4I_{15/2}$ and $^2H_{9/2} \rightarrow {}^4I_{15/2}$ transitions is approximately 1:8 suggesting that the transition from $^4F_{9/2}$ to $^2H_{9/2}$ is preferred and is reasonable since this process requires phonon emission. So, the preferential 3 photon mechanism occurs as follows; a Yb^{3+} ion is excited to the $^2F_{5/2}$ following ground state absorption of 978 nm photons. This is followed by a transfer of energy to a neighboring Er^{3+} ion thus promoting it to the $^4I_{11/2}$ state, which subsequently decays to the $^4I_{13/2}$ level. Following another energy transfer from a Yb^{3+} ion, the Er^{3+} ion is further excited to the $^4F_{9/2}$ state. The Er^{3+} ion accepts energy once again from a Yb^{3+} ion finally promoting it to the $^2H_{9/2}$ state with the excess energy being dissipated by the lattice (Figure 6.29). Of course, the $^4S_{3/2}$ level is populated via non-radiative decay from the upper states and thus explaining the slope of 3 in the graph of $\ln(I_{vis})$ versus $\ln(I_{NIR})$ of the Er1Yb10 sample. Furthermore, it is conceivable that following the excitation of the Er^{3+} ion to the $^4F_{9/2}$ state, the ion non-radiatively decays to the $^4I_{9/2}$ state. Another

Yb^{3+} transfer of energy excites the ion to the $^4F_{3/2}$ level where only 60 cm^{-1} is required to bridge the gap (Figure 6.29).

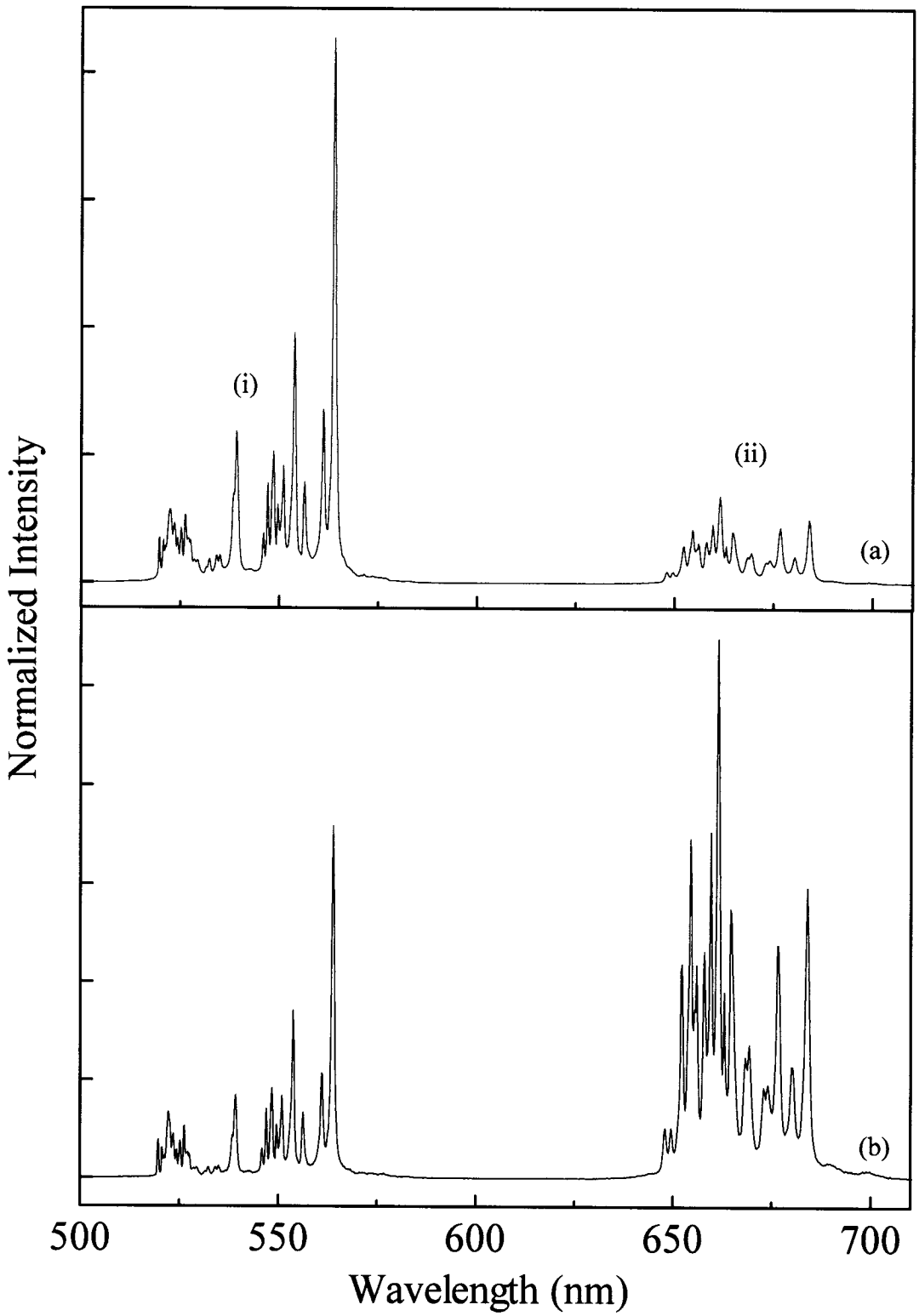

Figure 6.31: Comparison of the upconversion spectra of (a) bulk $Y_2O_3:Er^{3+}$, Yb^{3+} (BErYb), and (b) nanocrystalline $Y_2O_3:Er^{3+}$, Yb^{3+} (Er1Yb1) showing the (i) $^2H_{11/2}$, $^4S_{3/2} \rightarrow {}^4I_{15/2}$ and (ii) $^4F_{9/2} \rightarrow {}^4I_{15/2}$ transitions (λ_{exc} = 978 nm).

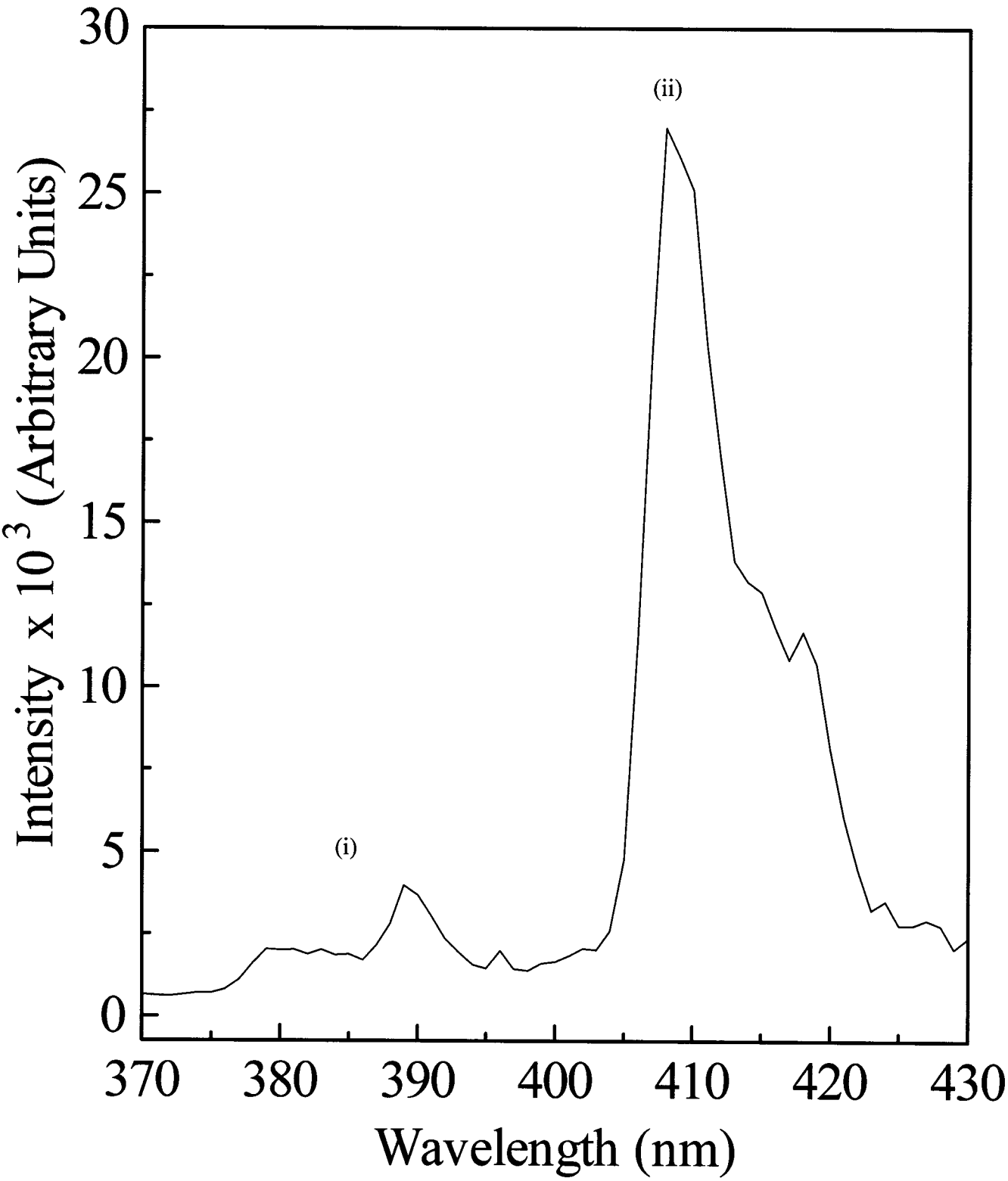

Figure 6.32: Upconversion spectrum of nanocrystalline $Y_2O_3:Er^{3+}$, Yb^{3+} (1 mol% Er^{3+} and 10 mol% Yb^{3+}) showing the (i) $^4G_{11/2} \rightarrow {}^4I_{15/2}$ and (ii) $^2H_{9/2} \rightarrow {}^4I_{15/2}$ transitions following excitation with 978 nm.

6.2. Luminescence Properties of Erbium Doped Nanocrystalline Yttrium Oxide Prepared Via The Controlled Hydrolysis Procedure

6.2.1. Reflectance and Emission Spectroscopy

The diffuse reflectance spectra of nanocrystalline $Y_2O_3:Er^{3+}$ (10 mol%) prepared via wet chemical synthesis obtained between 200 and 700 nm is presented in Figure 6.33. The spectrum is composed of a series of relatively sharp bands assigned to the intraconfigurational $f-f$ transitions from the $^4I_{15/2}$ ground state to the $^4F_{9/2}$, $^4S_{3/2}$, $^2H_{11/2}$, $^4F_{7/2}$, $^4F_{5/2}$, $^4F_{3/2}$, $^2H_{9/2}$, $^4G_{11/2}$, and $^2G_{9/2}$ excited states of the Er^{3+} ions. An absorption edge is observed at approximately 300 nm, which is assigned to the intrinsic absorption of the yttrium oxide host. The reflectance spectrum of the nanocrystalline material was compared to that of the bulk (microcrystalline) material (Figure 6.2) and two key observations were made. First, the spectrum of the bulk sample was composed of the same $f-f$ transitions albeit more resolved. The reduced resolution of the spectral features in the reflectance spectrum of the nanocrystalline material was attributed to the inhomogeneous broadening induced by the presence of disorder. Due to the nanoparticles' small size, a greater fraction of Er^{3+} ions will lie on the surface of the particle with respect to the bulk sample and thus will be affected by a different crystal field. Second, the intrinsic absorption of the Y_2O_3 host, assigned to band-to-band transitions, was blue shifted in the nanocrystalline material. This particle size dependent behavior of the reflectance spectrum has also been observed by other authors. [111, 258] and discussed in detail earlier.

The disorder caused by the small size of the nanocrystals is also evidenced in the 77 K luminescence spectrum (λ_{exc} = 488 nm) of 10 mol% $Y_2O_3:Er^{3+}$ [259]. As can be seen from the $^4S_{3/2} \rightarrow {}^4I_{15/2}$ transition in Figure 6.34, the 77 K spectrum of the

nanocrystalline material is significantly broadened compared to the spectrum of the corresponding bulk sample. In nanocrystalline materials, the influence of defects in the host lattice and/or contamination of their surface cannot be ignored and induces inhomogeneous broadening not unlike what occurs in rare earth doped glasses. The size restrictions associated with the nanocrystalline material will force a greater fraction of the rare earth ions to lie on the surface compared to the bulk sample. The ions on the surface of the nanoparticle will have a more disordered environment in comparison to the ions situated in the particle centre (in the C_2 and C_{3i} sites). Thus, the ions on the particle surface would give rise to inhomogeneously broadened emission bands and the luminescence spectrum of the doped nanoparticles will consist of broader emission bands compared to the Er^{3+} doped bulk material. Thus, the observed spectrum is a superposition of emission from both types of Er^{3+} ions, those buried within the nanoparticle and those found on the surface. This behavior is in agreement with the luminescence results for the same nanocrystalline host doped with Eu^{3+} ions [210]. In fact, all the bands of the Eu^{3+} doped yttria sample were determined to be broader with respect to an identically doped bulk Y_2O_3:Eu^{3+} sample, denoting a higher disorder of the crystalline environment of the Eu^{3+} ions in the nanoparticles. Moreover, the higher value of the asymmetry ratio (which is the ratio of the integrated intensities of the $^5D_0 \rightarrow {}^7F_2$ to the $^5D_0 \rightarrow {}^7F_1$ Eu^{3+} emission bands of the luminescence spectrum) obtained for the nanoparticles (6.5 ± 0.1) with respect to that of the bulk sample (5.3 ± 0.1) suggested that on the average the local environment of the Eu^{3+} ions was more distorted for the nanocrystals.

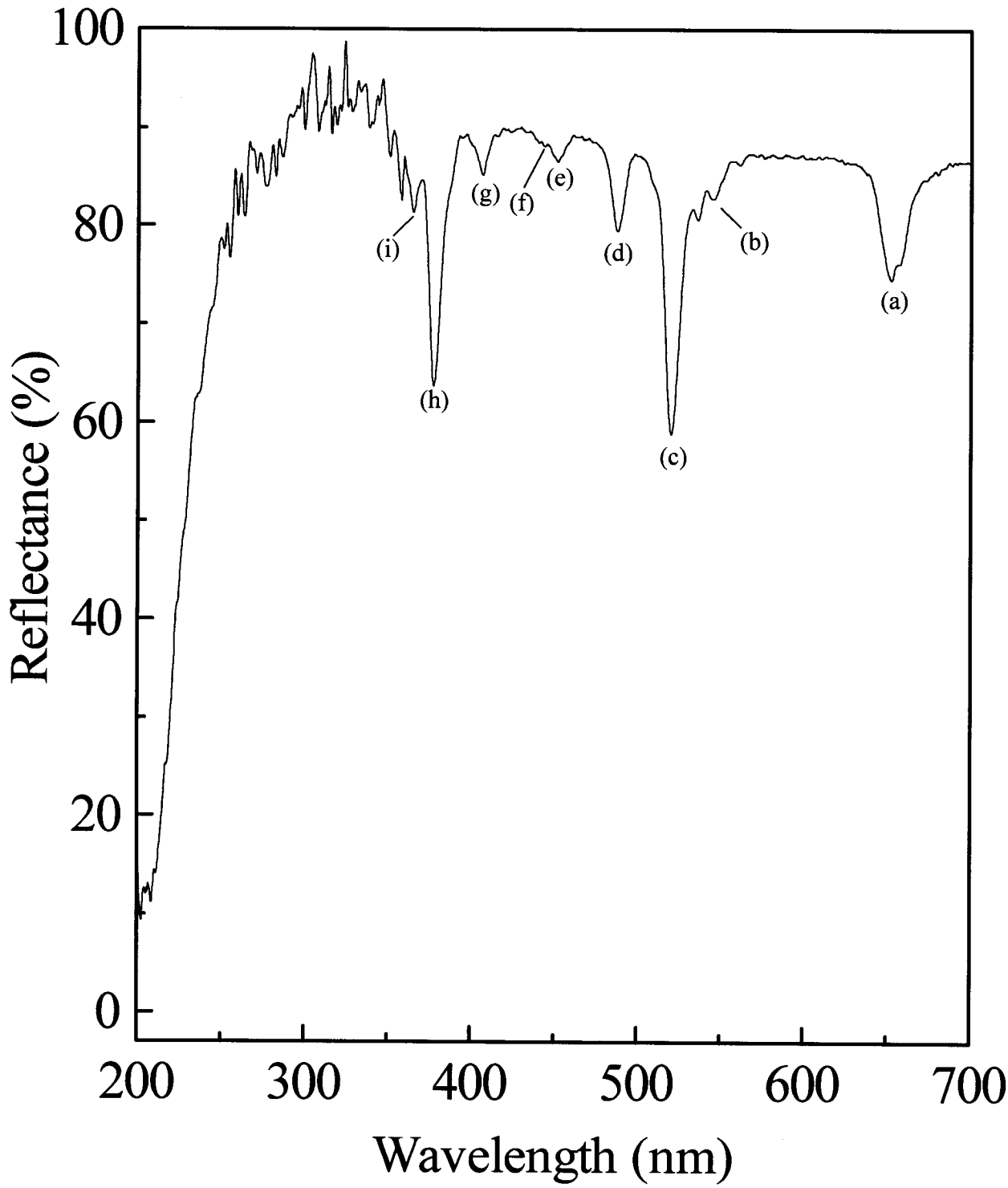

Figure 6.33: Reflectance spectrum of nanocrystalline $Y_2O_3:Er^{3+}$ (10 mol%) prepared via the controlled hydrolysis procedure showing transitions from the $^4I_{15/2}$ ground state to the various Er^{3+} excited states:
(a) $^4F_{9/2}$, (b) $^4S_{3/2}$, (c) $^2H_{11/2}$, (d) $^4F_{7/2}$, (e) $^4F_{5/2}$, (f) $^4F_{3/2}$, (g) $^2H_{9/2}$, (h) $^4G_{11/2}$, (i) $^2G_{9/2}$.

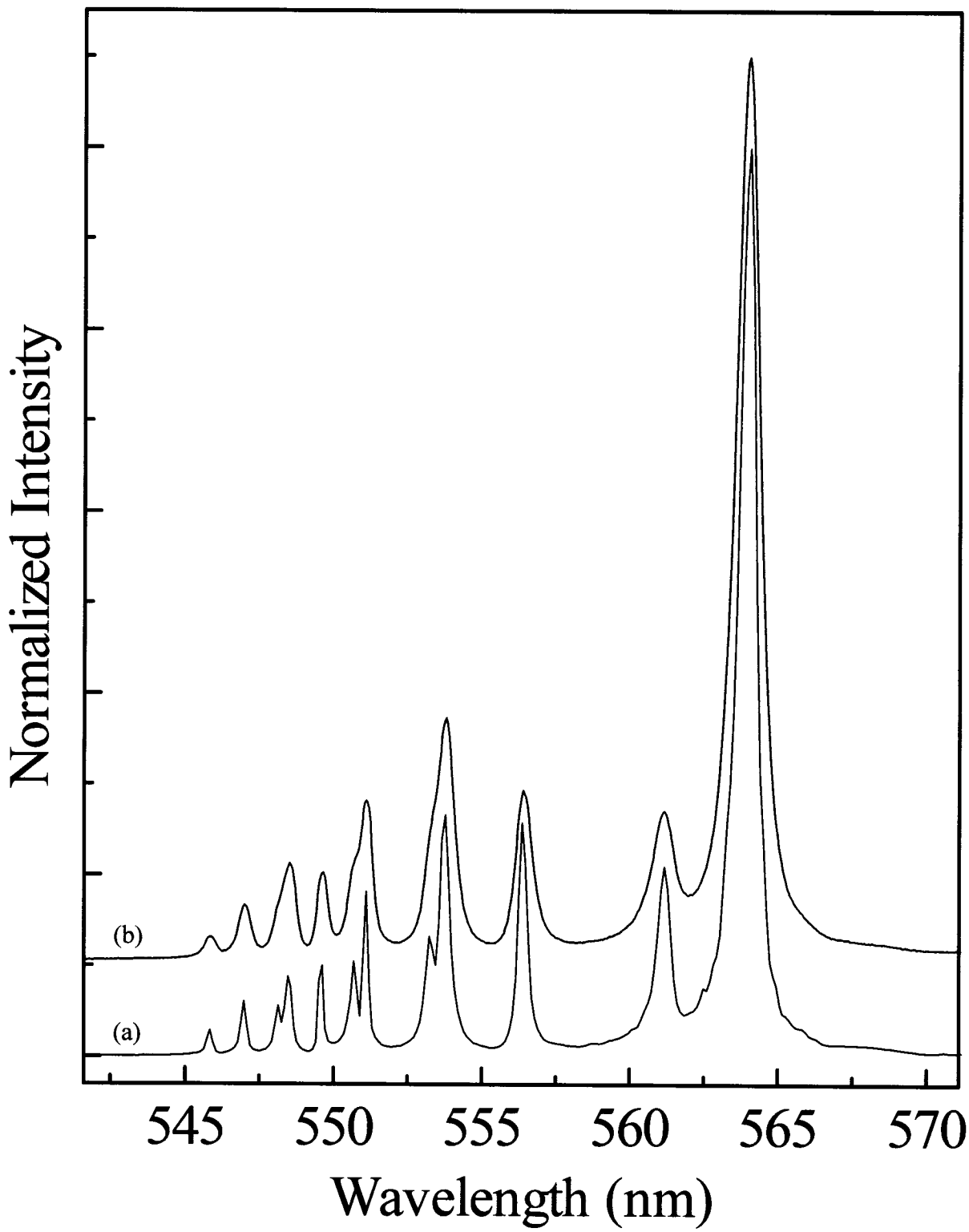

Figure 6.34: 77 K luminescence spectra showing the $^4S_{3/2} \rightarrow {}^4I_{15/2}$ transition in (a) bulk and (b) nanocrystalline 10 mol% $Y_2O_3:Er^{3+}$ ($\lambda_{exc} = 488$ nm).

Figure 6.35 shows the room temperature luminescence spectra of bulk (10 mol%) and nanocrystalline (1 and 10 mol%) $Y_2O_3:Er^{3+}$ following excitation with 488 nm into the $^4F_{7/2}$ state. The luminescence spectrum, which is normalized to the green $^4S_{3/2} \rightarrow {}^4I_{15/2}$ transition, has a predominantly green emission from the thermalized $^2H_{11/2}$, $^4S_{3/2} \rightarrow {}^4I_{15/2}$ transition in the region of approximately 525 – 575 nm. A red emission ascribed to the transition from the $^4F_{9/2}$ excited state to the $^4I_{15/2}$ ground state is also observed in the region of 640 – 690 nm. Furthermore, a much weaker NIR emission is observed (not shown) between 785 – 825 nm and between 840 – 870 nm corresponding to the $^4I_{9/2} \rightarrow {}^4I_{15/2}$ and $^4S_{3/2} \rightarrow {}^4I_{13/2}$ transitions, respectively. The normalized spectrum clearly illustrates that the red emission from the $^4F_{9/2} \rightarrow {}^4I_{15/2}$ transition is more intense in the bulk material compared to the nanocrystalline sample. It is conceivable that a cross-relaxation process is responsible by populating the $^4F_{9/2}$ level via two resonant transitions: $^4F_{7/2} \rightarrow {}^4F_{9/2}$ and $^4F_{9/2} \leftarrow {}^4I_{11/2}$. This phenomenon was observed to a much greater extent in nanocrystalline $Y_2O_3:Er^{3+}$ (prepared via propellant synthesis) following direct population of the $^4I_{11/2}$ state with 980 nm photons [239]. The spectrum of the $Y_2O_3:Er^{3+}$ nanocrystals prepared via the wet chemical synthesis reveals that this cross-relaxation mechanism is much less efficient in the nanocrystalline material, which can be explained by the presence of the high vibrational energies associated with this type of material. In fact, the MIR spectrum (Figure 6.36) of the $Y_2O_3:Er^{3+}$ nanocrystals synthesized via the present method also displays the characteristic stretching of the CO_3^{2-} and OH^- groups (1500 and 3350 cm^{-1}, respectively) attributed to the adsorption of atmospheric CO_2 and H_2O on the particle surface. The large energies associated with the stretching vibrations of these two species increase the rate of multiphonon relaxation. Thus, since the energy

gap between $^4F_{7/2}$ and the next lower lying level ($^2H_{11/2}$) is approximately 1535 cm^{-1}, one high energy CO_3^{2-} phonon can easily bridge the gap. Conversely the bulk material, which has no contamination of carbonate and hydroxyl groups, would need more than two intrinsic yttria phonons (600 cm^{-1}) [107] rendering the multiphonon relaxation less probable. As a result, there is a larger population of Er^{3+} ions in the $^4F_{7/2}$ state making the cross-relaxation mechanism more efficient.

Similarly, the adsorbed species on the surface of the nanocrystalline material also affects the decay of the emitting state. The decay curves for all investigated samples showed a deviation from single exponential behavior (Figure 6.37, for example). However, the degree of non-exponentiality was dependent upon the concentration of the Er^{3+} dopant as evidenced in Figure 6.38. The decay curves of the $^4S_{3/2} \rightarrow {}^4I_{15/2}$ transition in the 10 mol% sample shows a much greater deviation from exponential behavior compared to the decay curves of the 1 mol% nanocrystal sample. Multi-exponential decay curves were similarly observed in $Y_2O_3:Er^{3+}$ and $Y_2O_3:Ho^{3+}$ nanocrystals synthesized via the combustion method, and this was due to a distribution of dopant ions within the individual nanocrystals that were coupled in various degrees to the adsorbed surface CO_3^{2-} and OH^- anions. In the nanocrystal material, a significant portion of the rare earth ions are located on the particle surface due to their small size and therefore leads to the observed non-exponential decay curve. The dopant ions located close to the particle surface would have a faster decay than those ions located inside the nanocrystals. Furthermore, energy transfer processes also contribute in making the decay curves non-exponential. For these reasons, the effective decay time constants, τ_m, of nanocrystalline $Y_2O_3:Er^{3+}$ were determined [246]. The effective decay time constant of the $^4S_{3/2}$ state,

following excitation with 488 nm, was determined to be 5.1 μs for the Y_2O_3 nanocrystal samples doped with 10 mol% Er^{3+}. However, the bulk sample with identical doping level has a decay time constant of 56 μs, one order of magnitude greater. The rate of depopulation of an excited state, W, is equal to the sum of the radiative decay rate, W_R, and the multiphonon relaxation rate, W_{MPR} [260]. Hence:

$$W = W_R + W_{MPR} \qquad 6.2.1$$

where: $W = 1 / \tau_m$ (τ_m is the effective decay time)

An increase in the rate of multiphonon relaxation will increase the overall rate of depopulation of the excited state, thus decreasing the observed decay time (Table 6.6). Once again, in the nanocrystalline material, the adsorbed species (CO_3^{2-} and OH^-) play a pivotal role in multiphonon relaxation. For example, the maximum energy gap between the $^4S_{3/2}$ state and the level beneath it ($^4F_{9/2}$) is approximately 3120 cm^{-1}. Multiphonon relaxation is thus very efficient as either two carbonate phonons or one hydroxyl phonon can bridge the energy gap. On the other hand, the bulk sample would require 5 intrinsic yttria phonons to bridge the same gap.

Table 6.6: Effective decay time constants, τ_m, of the $^4S_{3/2}$ state in $Y_2O_3:Er^{3+}$ nanocrystals prepared via the controlled hydrolysis procedure (0.1, 1, and 10 mol% Er^{3+}) following excitation with 488, 650, or 800 nm.

Er^{3+} Concentration (mol%)	τ_m (μs)		
	λ_{exc} = 488 nm	λ_{exc} = 650 nm	λ_{exc} = 800 nm
0.1	58	60	62
1	20	29	32
10	5.1	19	22

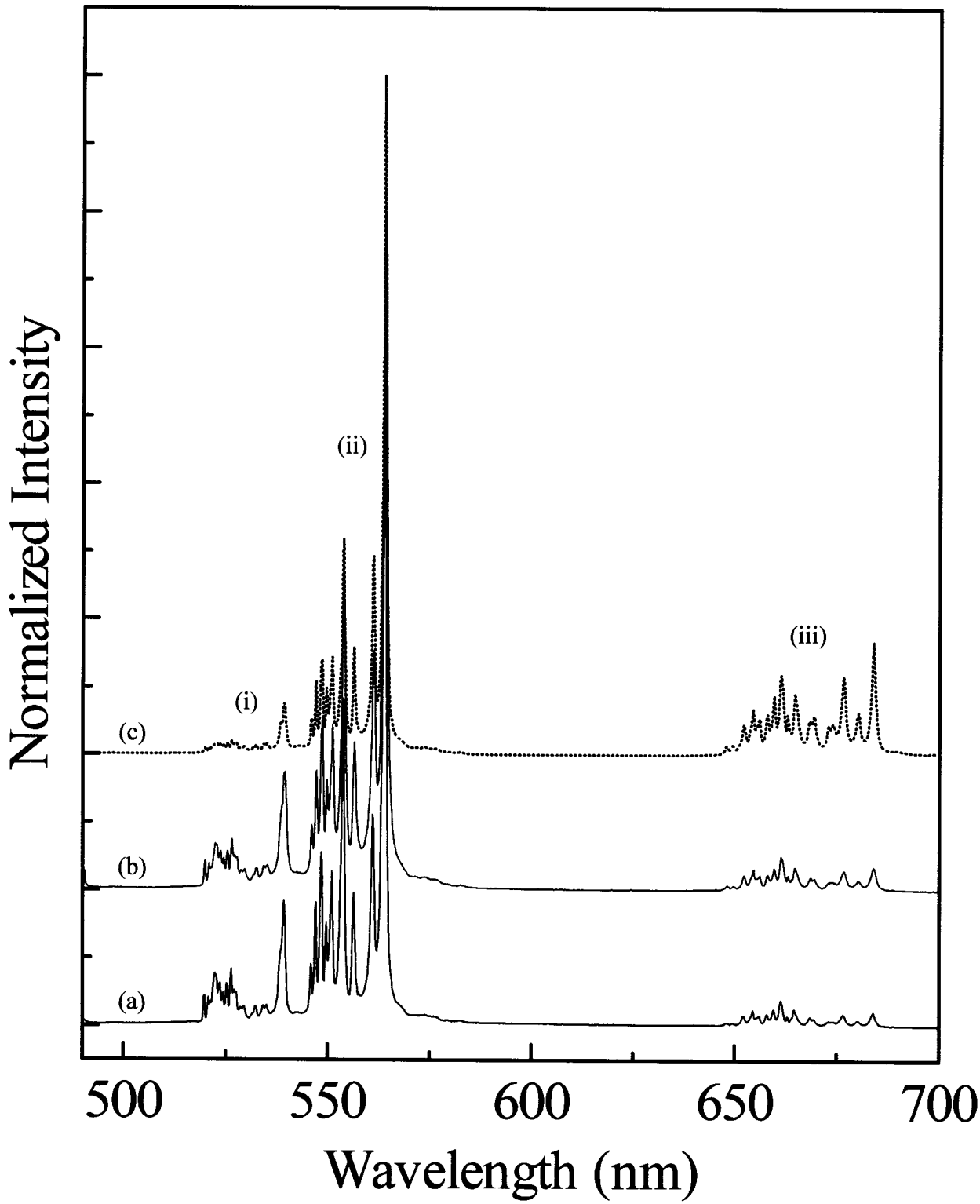

Figure 6.35: Room temperature luminescence spectrum of nanocrystalline $Y_2O_3:Er^{3+}$ (a) 1 mol% and (b) 10 mol% as well as (c) 10 mol% bulk $Y_2O_3:Er^{3+}$ shown for comparison (λ_{exc} = 488 nm).
(i) $^2H_{11/2} \rightarrow {}^4I_{15/2}$ (ii) $^4S_{3/2} \rightarrow {}^4I_{15/2}$ (iii) $^4F_{9/2} \rightarrow {}^4I_{15/2}$.

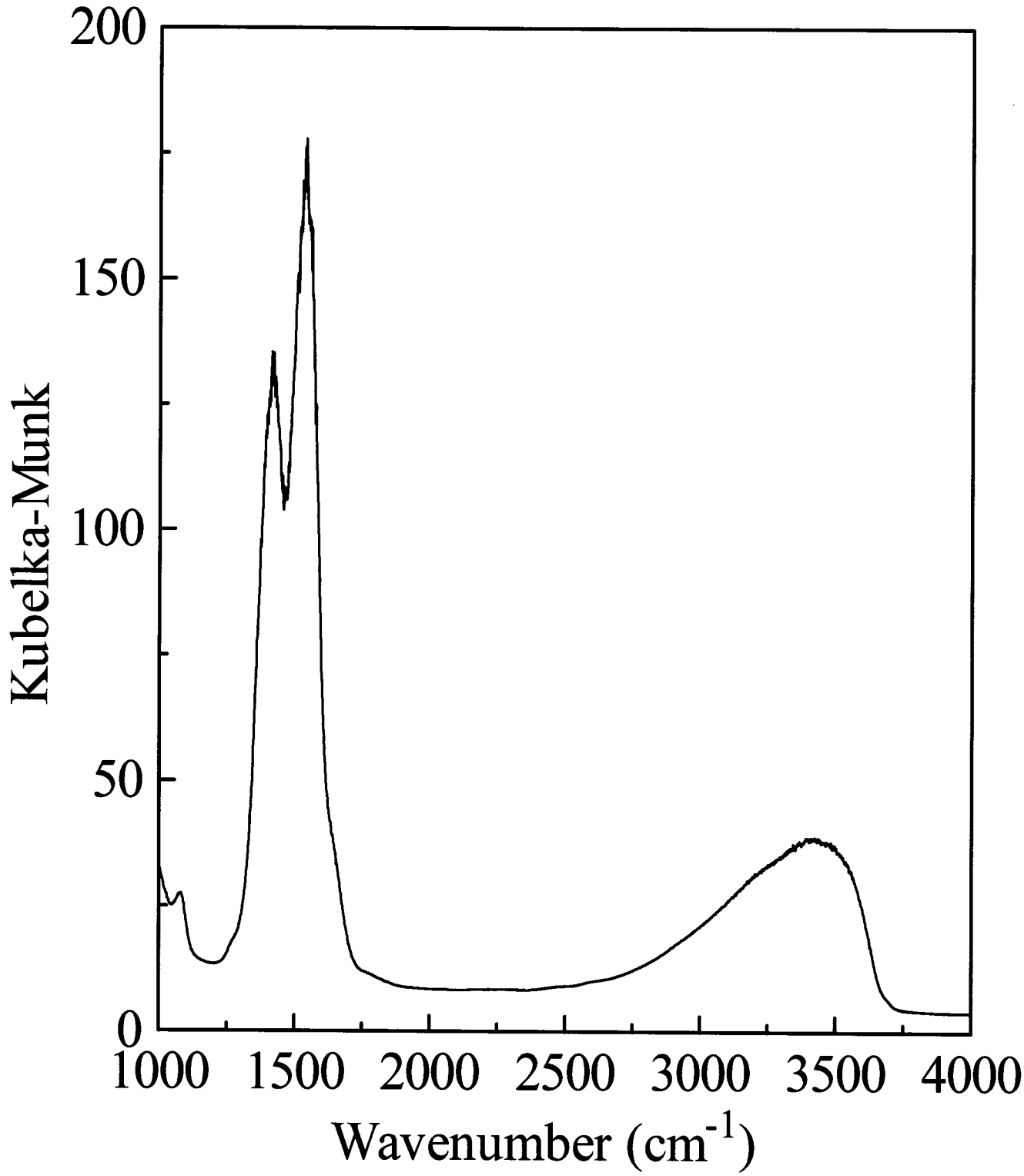

Figure 6.36: Diffuse reflectance spectrum of $Y_2O_3:Er^{3+}$ nanocrystals (10 mol%) prepared via wet chemical synthesis.

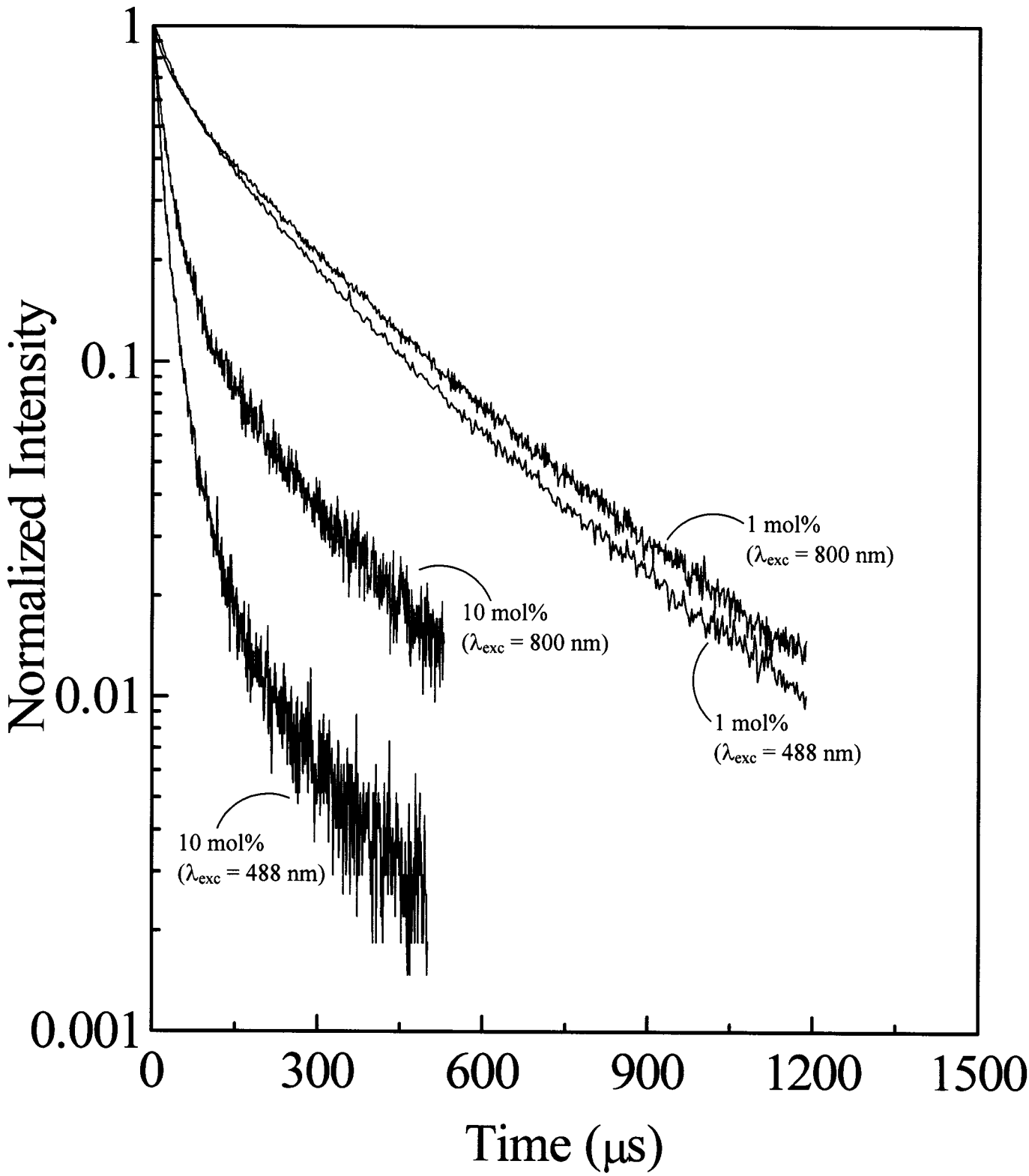

Figure 6.37: Decay curves of the $^4S_{3/2} \rightarrow {}^4I_{15/2}$ transition in 1 and 10 mol% $Y_2O_3:Er^{3+}$ nanocrystals following excitation with 488 or 800 nm.

6.2.2. Upconversion Luminescence Spectroscopy Following Excitation into the $^4F_{9/2}$ State (λ_{exc} = 650 nm)

Following excitation with 650 nm into the $^4F_{9/2} \leftarrow {}^4I_{15/2}$ absorption band, green upconversion was observed from the $^2H_{11/2}$, $^4S_{3/2} \rightarrow {}^4I_{15/2}$ transition in the region of approximately 525 – 575 nm (Figure 6.38). The plot of $\ln(I_o)$ versus $\ln(I_i)$ yields slopes of approximately 2 for all samples under investigation (see Figure 6.39) indicating that two photons (n = 2) participate in the upconversion process. The ln-ln plots show no inflection point and thus, we can rule out PA as the mechanism, which populates the upper emitting states. This leaves the ESA and ETU mechanisms, which can easily be distinguished from decay experiments. If ESA is the principle mechanism of upconversion, the upconverted decay time will be identical to the decay time obtained when pumping the upper state directly (Table 6.6). A lengthening of the decay time is a clear indication of the presence of ETU [261].

From Table 6.6, it is obvious that the upconversion occurs principally via ETU as the upconverted decay times are lengthened compared to those obtained with 488 nm radiation. However, ESA is ever present and cannot be discounted. In preliminary studies performed on Y_2O_3:Er^{3+} nanocrystals with 0.1 mol% dopant level prepared via the same technique, upconversion was observed and can only occur via ESA as the Er^{3+}–Er^{3+} distances are far to large for any effective interaction to occur. A schematic representation of the mechanisms responsible for upconversion luminescence is presented in Figure 6.40. Ground state absorption of a 650 nm photon raises the Er^{3+} ion to the $^4F_{9/2}$ state. A second pump photon or energy transfer from another Er^{3+} ion also in the $^4F_{9/2}$ state, will populate the $^2P_{3/2}$ state. However, the ion can non-radiatively decay to the $^4I_{9/2}$ state following absorption of the pump photon. Another pump photon or energy transfer

from a neighboring ion in the $^4F_{9/2}$ state will excite the initial Er^{3+} ion to the $^2K_{15/2}$ state. Furthermore, multiphonon relaxation will also populate the $^4I_{11/2}$ and $^4I_{13/2}$ states and again, resonant absorption of another pump photon or energy transfer will populate the $^4G_{11/2}$ and $^4F_{5/2}$ states, respectively. Green emission from the $^2H_{11/2}$, $^4S_{3/2} \rightarrow {}^4I_{15/2}$ transition is subsequently observed.

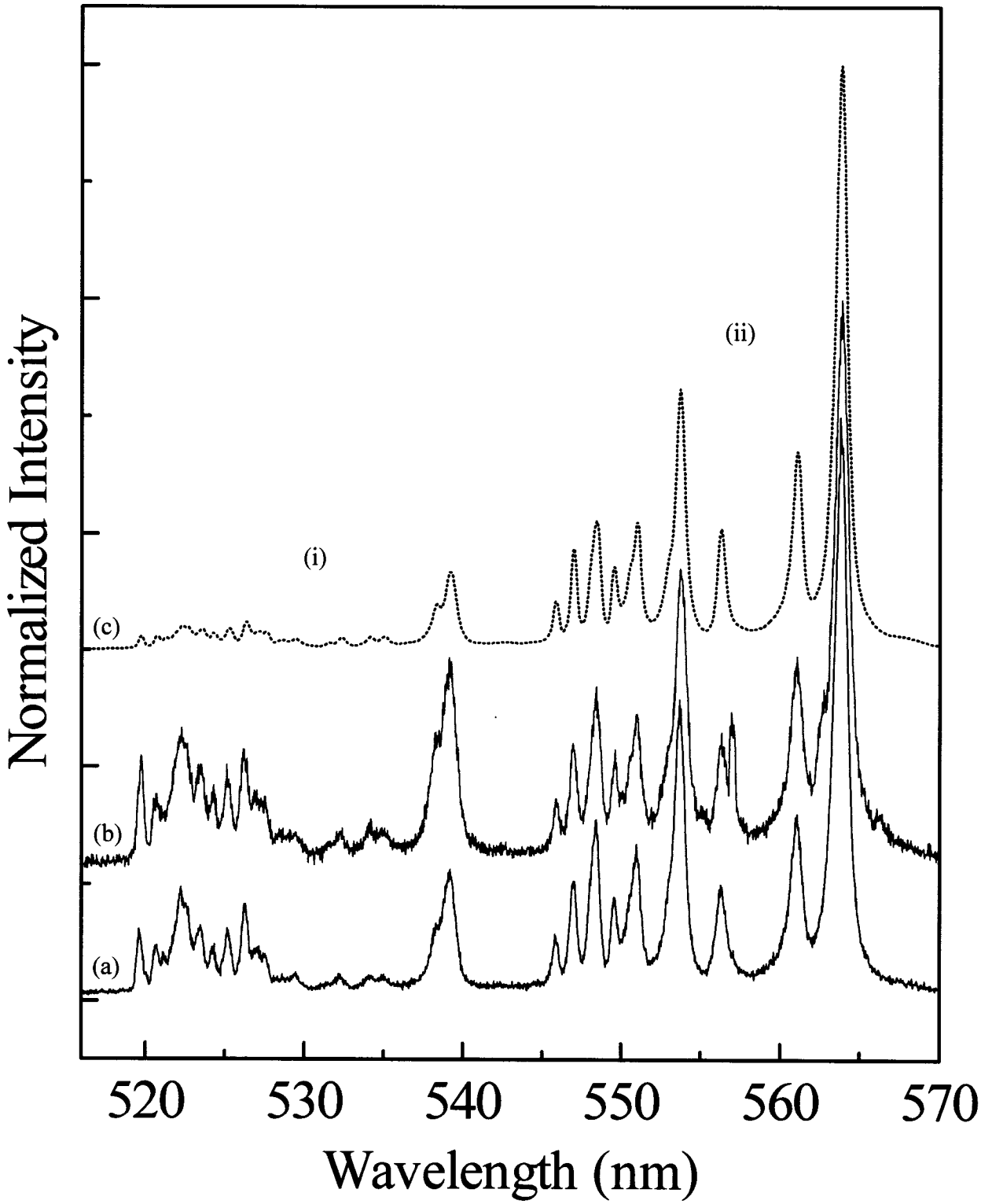

Figure 6.38: Upconversion luminescence spectrum of nanocrystalline $Y_2O_3:Er^{3+}$ (a) 1 mol% and (b) 10 mol% as well as (c) 10 mol% bulk $Y_2O_3:Er^{3+}$ shown for comparison ($\lambda_{exc} = 650$ nm). (i) $^2H_{11/2} \rightarrow {}^4I_{15/2}$ (ii) $^4S_{3/2} \rightarrow {}^4I_{15/2}$.

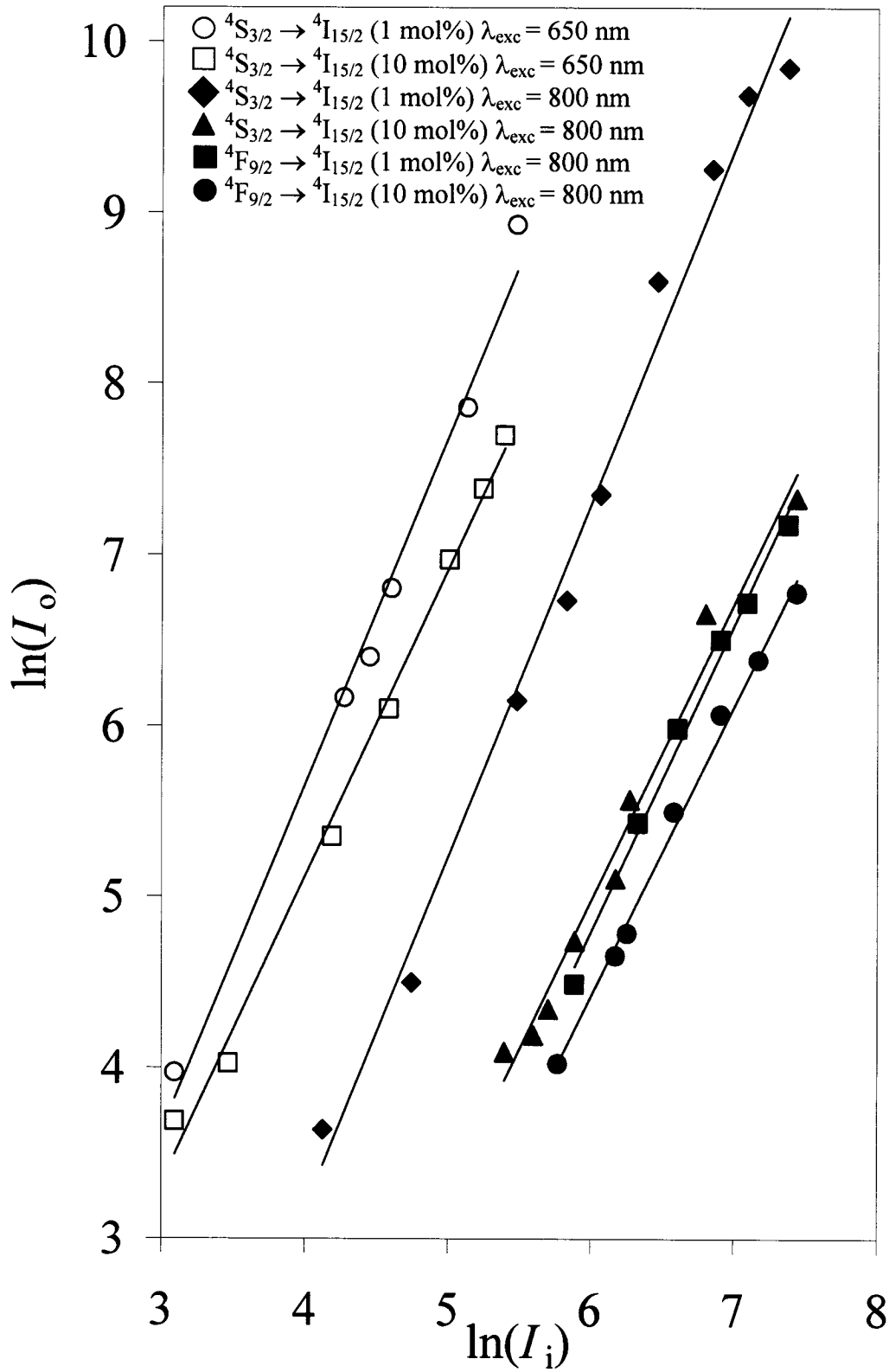

Figure 6.39: Upconversion power studies of 1 and 10 mol% nanocrystalline $Y_2O_3:Er^{3+}$ prepared via wet chemical synthesis.

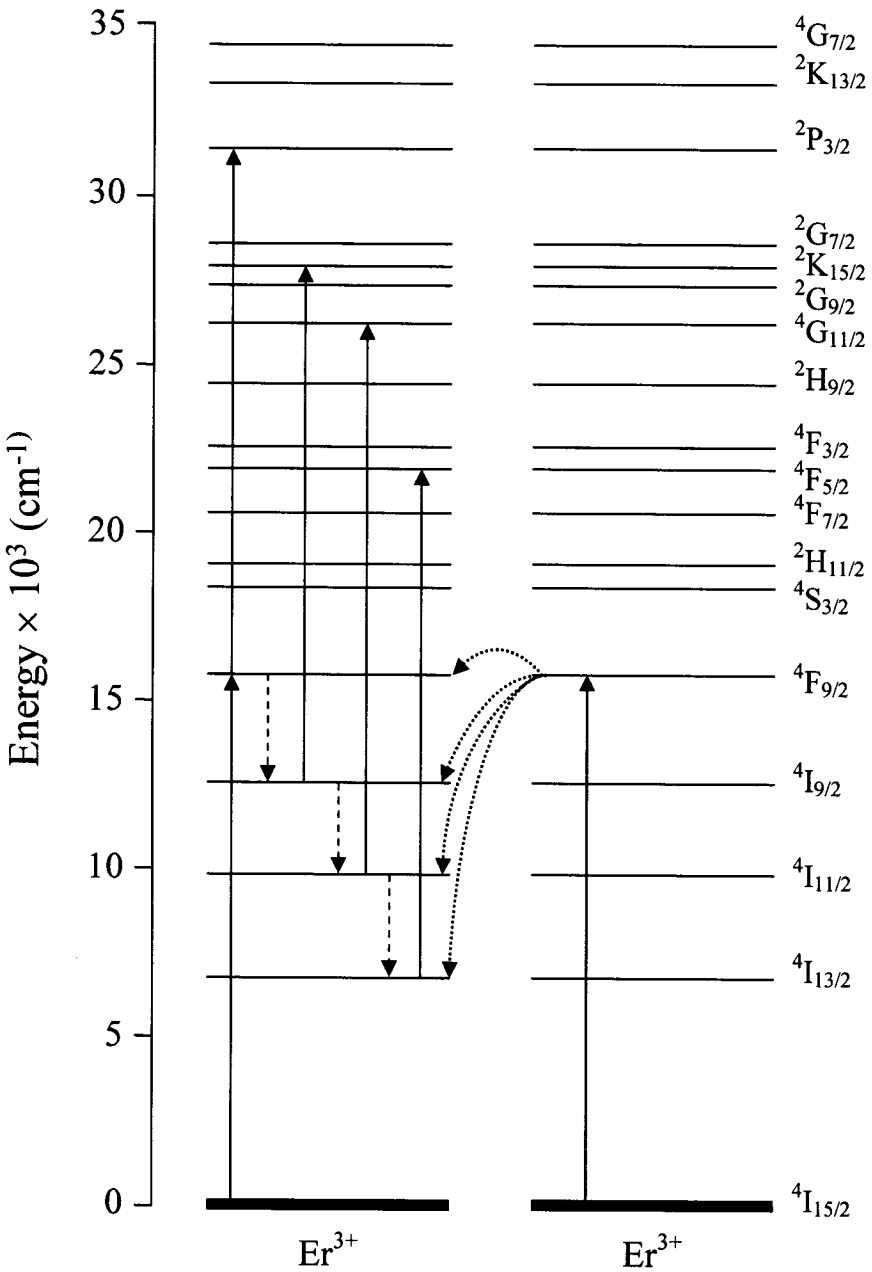

Figure 6.40: Schematic representation of the 650 nm upconversion mechanism(s) in bulk and nanocrystalline $Y_2O_3:Er^{3+}$.

6.2.3. Upconversion Luminescence Spectroscopy Following Excitation into the $^4I_{9/2}$ State (λ_{exc} = 800 nm)

Upconversion luminescence was also observed following excitation with NIR radiation (λ_{exc} = 800 nm) into the $^4I_{9/2} \leftarrow {}^4I_{15/2}$ absorption band. Green and red luminescence was observed from the $^2H_{11/2}$, $^4S_{3/2} \rightarrow {}^4I_{15/2}$ and $^4F_{9/2} \rightarrow {}^4I_{15/2}$ transitions between 525 – 575 nm and 640 – 690 nm, respectively (Figure 6.41). Similar to the upconversion following excitation with 650 nm, the power study revealed that two photons are required to populate the upper states (see Figure 6.39). Also, no bending point was observed in the ln–ln graph effectively ruling out PA as the mechanism by which upconversion occurs. The principle mechanism of upconversion (ESA or ETU) depends primarily on the concentration of the dopant Er^{3+} ion. As can be seen from Figure 6.37, the decay curves of the $^4S_{3/2} \rightarrow {}^4I_{15/2}$ transition in the Y_2O_3:Er^{3+} nanocrystals (10 mol%) are significantly lengthened when pumping with an upconversion wavelength (λ_{exc} = 800 nm). However, in the 1 mol% nanocrystal samples, the decay time lengthening is much less drastic compared to the 10 mol% sample. This undoubtedly suggests that in the nanocrystals doped with 10 mol% Er^{3+}, ETU is the dominant mechanism of upconversion. Conversely, both ESA and ETU mechanisms are operative with reasonably equal efficiency in the 1 mol% sample. So, ground state absorption of 800 nm photons will excite the Er^{3+} ions to the $^4I_{9/2}$ excited state, which in turn rapidly undergoes multiphonon relaxation thus populating the $^4I_{11/2}$ intermediate state (Figure 6.42). Another 800 nm pump photon or energy transfer from another Er^{3+} ion in the $^4I_{9/2}$ state and in close proximity will populate the $^4F_{3/2}$ state. Following the non-radiative decay to the $^4I_{11/2}$ state, the ion can non-radiatively decay further to the $^4I_{13/2}$ state. Again, either an energy transfer process from another Er^{3+} ion in the $^4I_{9/2}$ state or a second pump

photon populates the $^2H_{11/2}$ level. Once the upper states are populated via the two photon upconversion processes, the ion will relax non-radiatively to the lower energy states thereby populating the green ($^2H_{11/2}$, $^4S_{3/2}$) and red ($^4F_{9/2}$) emitting levels.

As the upconversion spectrum following excitation with 800 nm reveals (see Figure 6.41), the case is not as simple as described above. The relative green-to-red intensities are different in the upconversion spectrum compared with the direct excitation spectrum (λ_{exc} = 488 nm). Specifically, the red ($^4F_{9/2} \rightarrow {}^4I_{15/2}$) emission is enhanced relative to the green ($^2H_{11/2}$, $^2S_{3/2} \rightarrow {}^4I_{15/2}$) emission indicating that some other mechanism must be present. The process by which this red enhancement occurs has been well documented [238] in $Y_2O_3:Er^{3+}$ nanocrystals synthesized via the combustion technique and the mechanism is as follows. The laser beam excites two Er^{3+} ions in close proximity to the $^4I_{9/2}$ state and rapid non-radiative decay of one of the excited ions to the $^4I_{11/2}$ state ensues. The energy gaps from the $^4I_{11/2}$ level to the $^4F_{9/2}$ level and from the intermediate $^4I_{9/2}$ state to the $^4I_{13/2}$ state are identical causing the two ions to undergo an ion-pair process of the type; ($^4I_{9/2}$, $^4I_{11/2}$) $\rightarrow$ ($^4I_{13/2}$, $^4F_{9/2}$) [244]. This mechanism is fairly well understood, although what is extremely interesting is that the magnitude of the red enhancement differs between similar materials with identical doping levels but synthesized using different procedures (see Figure 6.7 for comparison). In 10 mol% $Y_2O_3:Er^{3+}$ nanocrystals prepared by combustion, the upconverted red ($^4F_{9/2} \rightarrow {}^4I_{15/2}$) emission is more intense than the green ($^2H_{11/2}$, $^2S_{3/2} \rightarrow {}^4I_{15/2}$) emission. In the same study, the $Y_2O_3:Er^{3+}$ bulk material with a 10 mol% Er^{3+} doping level has a relative green-to-red ratio of approximately 1:1 (Figure 6.8), compared to approximately 2:3 for the nanocrystalline material (Figure 6.7). In 10 mol% $Y_2O_3:Er^{3+}$ nanocrystals prepared by

wet chemical synthesis, the relative green-to-red ratio is nearly 2:1. This difference in the red enhancement points to a reduction in the efficiency of the ion-pair process in the nanocrystalline material prepared by the wet synthesis method. The efficiency of the $(^4I_{9/2}, {}^4I_{11/2}) \rightarrow (^4I_{13/2}, {}^4F_{9/2})$ ion-pair process can be altered if the average distance between Er^{3+} centers is different. This ion-pair process depends on the proximity between Er^{3+} ions and it is therefore conceivable that if the Er^{3+} - Er^{3+} distances are larger, less interaction between Er^{3+} ions will occur causing the mechanism to be less efficient. This is entirely possible as the nanocrystals prepared by combustion and wet chemical synthesis have very different basic morphologies. The nanocrystals prepared by the wet synthesis give rise to compact nanosized materials with no fractal dimensions. The powders are built up of crystalline platelets with a porous structure at the nanometer scale, which forms large partially ordered aggregates at the micrometer scale [210]. In contrast, the nanocrystals prepared by combustion give rise to very porous nanosized materials with a sponge-like microstructure directly suggesting a fractal behavior. The building units of this porous structure are composed of crystallites with different orientations and dimensions. These samples show a similar morphology over a large range of magnifications (SEM), which is due to their fractal structure [191].

Furthermore, an increase in the multiphonon relaxation probability in the nanocrystalline material prepared by wet chemical synthesis will also result in a corresponding decrease in the ion-pair process efficiency. It is possible that the multiphonon relaxation due to the high energy CO_3^{2-} and OH^- stretching vibrations is more efficient in the nanocrystal material prepared by wet chemical synthesis. This will similarly result in a reduction of the efficiency of the mechanism, which populates the

$^4F_{9/2}$ state. Once the ions are excited to the $^4I_{9/2}$ state with 800 nm photons, they can quickly non-radiatively decay to the ground state resulting in a lower population of Er^{3+} ions in the $^4I_{9/2}$ and $^4I_{11/2}$ states.

Evidence for the latter hypothesis is given by examining the upconversion spectrum of $Y_2O_3:Er^{3+}$, Yb^{3+} nanocrystals (synthesized via wet chemical route) obtained following excitation with 978 nm (Figure 6.43) [249]. As was discussed in section 6.1.9, the enhancement of the red ($^4F_{9/2} \rightarrow {}^4I_{15/2}$) emission in $Y_2O_3:Er^{3+}$, Yb^{3+} nanocrystals, prepared via propellant synthesis, was caused by the efficient $^4F_{9/2} \leftarrow {}^4I_{13/2}$ transition. The efficiency of this mechanism was greatly improved in the nanocrystalline material (compared to the bulk), which underwent efficient multiphonon relaxation from $^4I_{11/2}$ to $^4I_{13/2}$ following energy transfer from the Yb^{3+} ion in the $^2F_{5/2}$ excited state. In the case of the $Y_2O_3:Er^{3+}$ nanocrystalline materials prepared via wet chemical synthesis, an increase in the multiphonon relaxation probability was believed to be the cause for a lower enhancement of the red emission following excitation with 800 nm since the cross-relaxation mechanism involved both the $^4I_{9/2}$ and $^4I_{11/2}$ excited states. Thus, this increase in non-radiative decay due the large stretching vibrations would obviously correspond to a decreased population in those states and an increase in the population of the $^4I_{13/2}$ state. The enhancement of the red emission in the upconversion spectrum of $Y_2O_3:Er^{3+}$, Yb^{3+} nanocrystals prepared via the controlled hydrolysis procedure is greater than in identically doped nanocrystals prepared via the combustion synthesis (Figure 6.22). This points to an increase in the $^4F_{9/2} \leftarrow {}^4I_{13/2}$ transition efficiency due to a larger multiphonon relaxation probability and agrees with what was observed in the upconversion spectrum (λ_{exc} = 800 nm) of $Y_2O_3:Er^{3+}$ nanocrystals prepared via the controlled hydrolysis

procedure where an increase in the non-radiative decay decreases the red enhancement compared to the nanomaterials prepared by combustion.

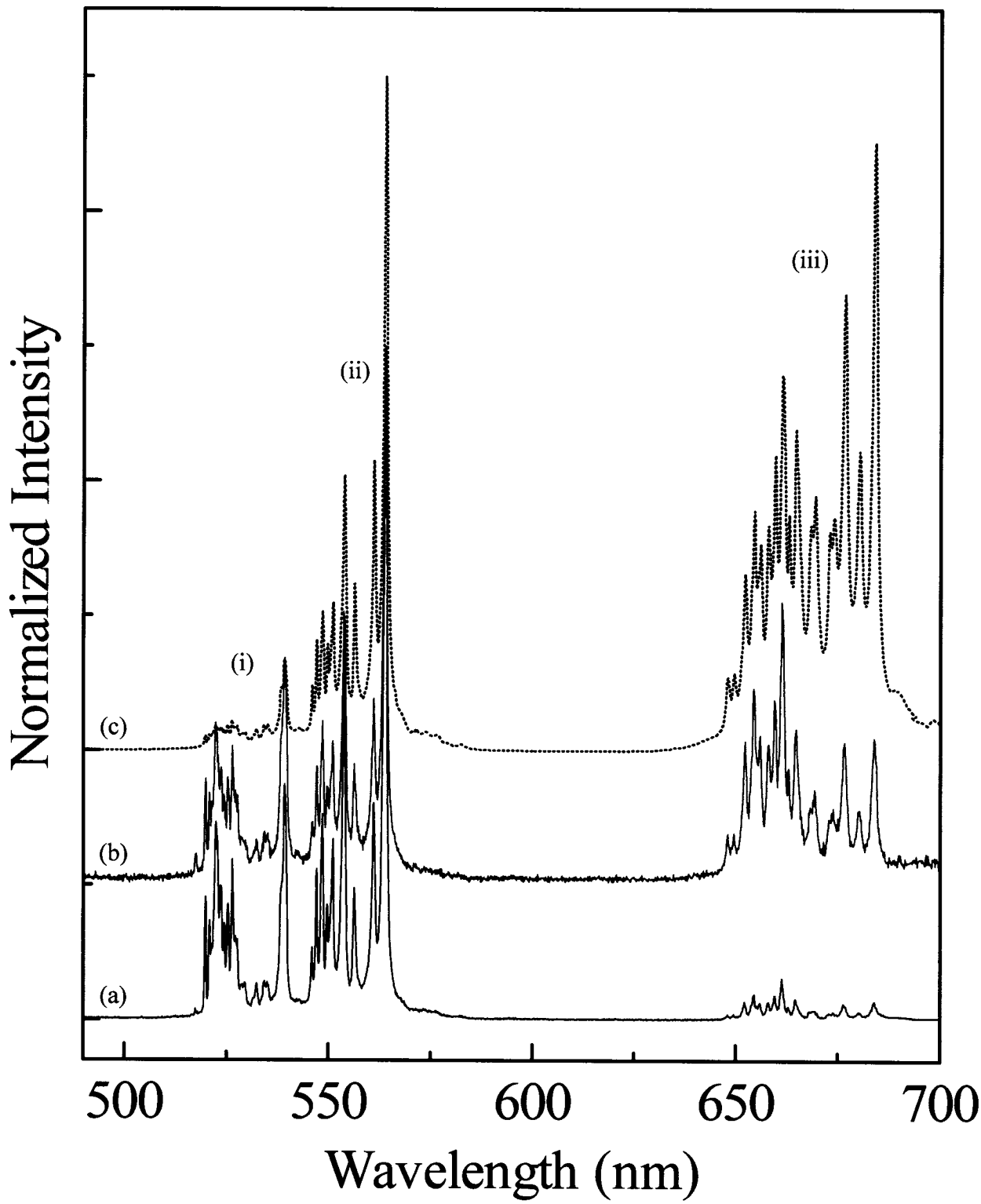

Figure 6.41: Upconversion luminescence spectrum of nanocrystalline $Y_2O_3:Er^{3+}$ (a) 1 mol% and (b) 10 mol% as well as (c) 10 mol% bulk $Y_2O_3:Er^{3+}$ shown for comparison (λ_{exc} = 800 nm).
(i) $^2H_{11/2} \rightarrow {}^4I_{15/2}$ (ii) $^4S_{3/2} \rightarrow {}^4I_{15/2}$ (iii) $^4F_{9/2} \rightarrow {}^4I_{15/2}$.

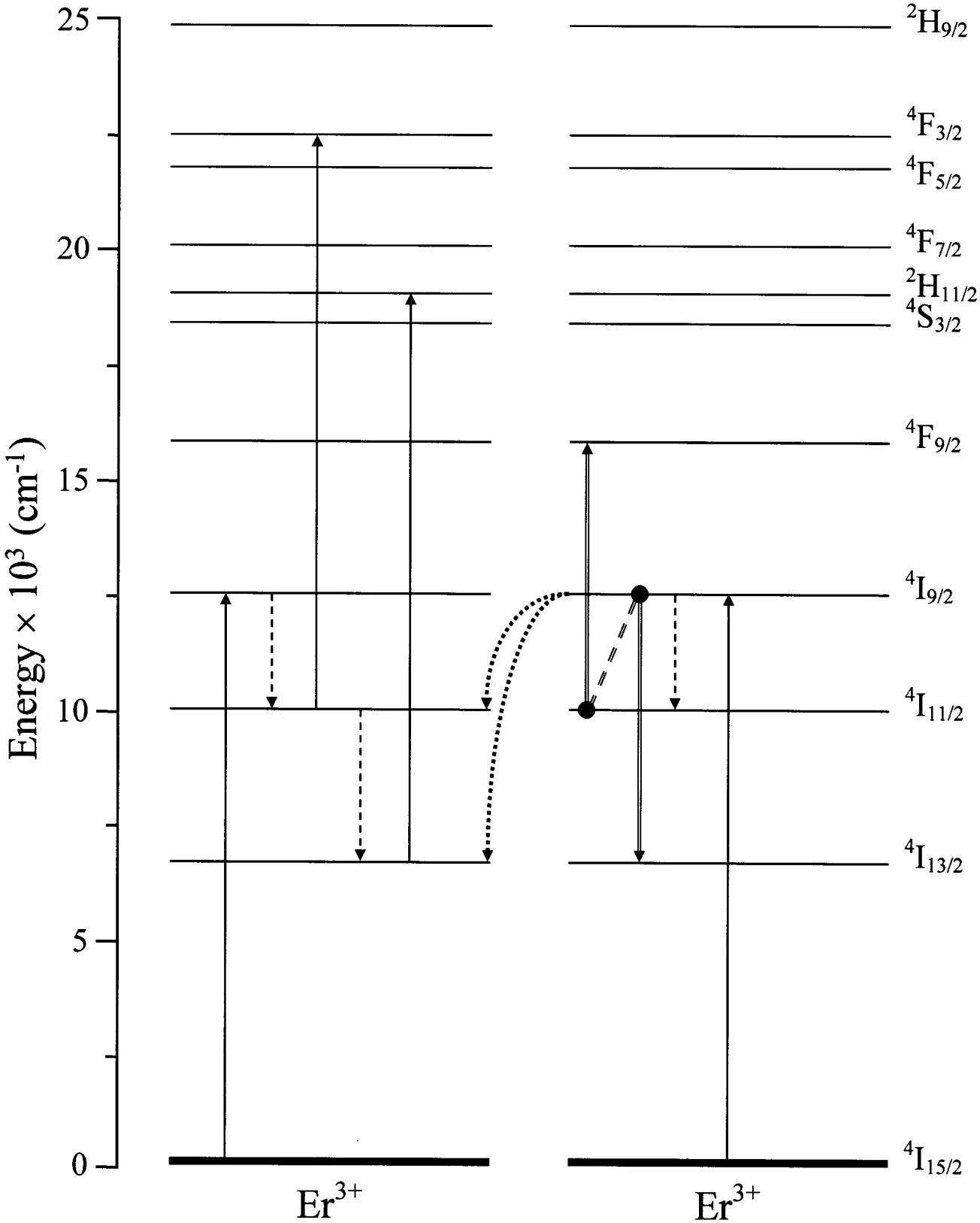

Figure 6.42: Schematic representation of the 800 nm upconversion mechanism(s) in bulk and nanocrystalline $Y_2O_3:Er^{3+}$.

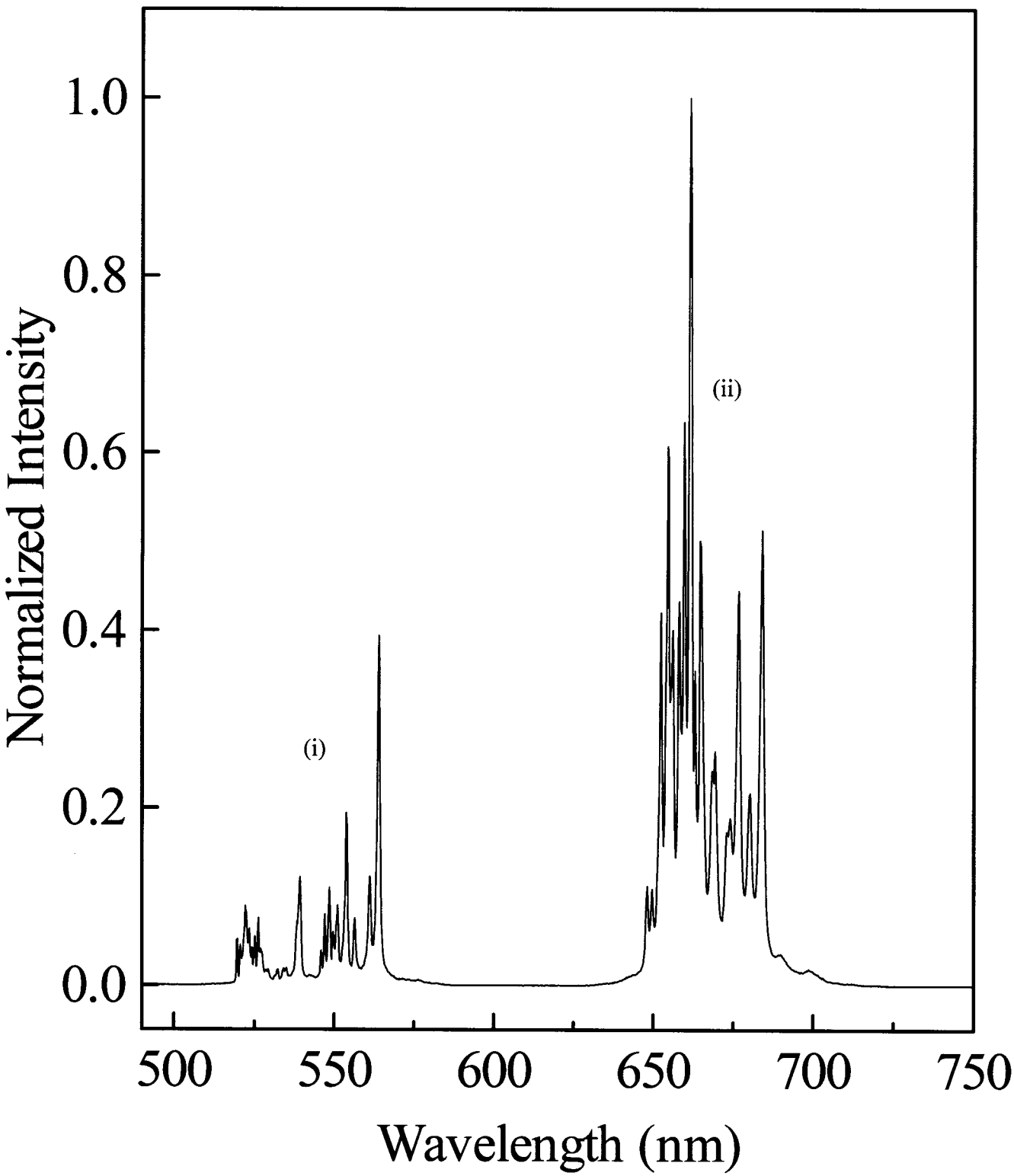

Figure 6.43: Room temperature upconversion (anti-Stokes) luminescence of nanocrystalline $Y_2O_3:Er^{3+}$, Yb^{3+} (1 mol% Er^{3+} and 1 mol% Yb^{3+}) prepared via the controlled hydrolysis procedure (λ_{exc} = 978 nm).
(i) $^2H_{11/2}$, $^4S_{3/2} \rightarrow {}^4I_{15/2}$ (ii) $^4F_{9/2} \rightarrow {}^4I_{15/2}$.

6.3. Upconversion Spectroscopy of Bulk and Nanocrystalline $Lu_2O_3:Er^{3+}$

Our initial foray into rare earth doped nanocrystals was with the Y_2O_3 host, however, some researchers observed higher luminescence intensities when the Lu^{3+} cation replaced the Y^{3+} cation in the crystalline structure. Thus, the next phase of the research was to study $Lu_2O_3:Er^{3+}$ nanocrystals since upon comparing the emission properties of yttrium and lutetium containing oxide [262] and fluoride [263] single crystals, the lutetium based crystals always showed the stronger luminescence.

6.3.1. Visible Emission Spectroscopy and Decay Time Measurements in $Lu_2O_3:Er^{3+}$

On excitation with 488 nm at room temperature, the Er^{3+} doped bulk and nanocrystalline Lu_2O_3 (1 mol% Er^{3+}) yield distinct emission bands due to the intra-configurational *f-f* transitions (Figure 6.44) [264, 265]. Green emission was observed from the $(^2H_{11/2}, {}^4S_{3/2}) \rightarrow {}^4I_{15/2}$ transition between 500 and 580 nm. Red emission was observed from the $^4F_{9/2} \rightarrow {}^4I_{15/2}$ transition between 640 and 690 nm. NIR emission was observed in the ranges 785-825 nm and 840-870 nm assigned to the $^4I_{9/2} \rightarrow {}^4I_{15/2}$ and $^4S_{3/2} \rightarrow {}^4I_{13/2}$ transitions, respectively (Figure 6.44, inset). The transition energies are similar for both the bulk and nanocrystalline samples and no noticeable shifting of the peaks between bulk and nanocrystalline samples is observed. This observation indicates that the crystal field surrounding the Er^{3+} ions is in general similar in the nanocrystalline and the bulk materials. However, inspection of Figure 6.44 shows that at room temperature the intensity of the hypersensitive $^2H_{11/2} \rightarrow {}^4I_{15/2}$ transition located around 525 nm is higher with respect to the $^4S_{3/2} \rightarrow {}^4I_{15/2}$ transition for the nanocrystalline than for the bulk material as was observed in $Y_2O_3:Er^{3+}$ nanocrystals prepared by the same technique.

The overall shapes of the emission bands are similar in both bulk and nanocrystalline samples; however, there is a significant reduction of the overall luminescence in nanocrystalline $Lu_2O_3:Er^{3+}$ in comparison to the bulk sample. The $Lu_2O_3:Er^{3+}$ nanocrystals, like $Y_2O_3:Er^{3+}$ nanocrystals, adsorb atmospheric carbon dioxide and water. The MIR spectrum of the $Lu_2O_3:Er^{3+}$ (1 mol%) nanocrystals (see Figure 6.45) shows bands at approximately 1500 and 3300 cm^{-1} which indicate the presence of adsorbed CO_2 and water, respectively [265]. The intensities of these vibrational bands are much smaller than those due to the modes of the Lu_2O_3 lattice, denoting that the amount of adsorbed CO_2 and moisture is low. Moreover, the relative intensity of the band at about 1500 cm^{-1} is distinctly higher than the one at 3300 cm^{-1}, suggesting that CO_2 has been preferentially adsorbed over H_2O. From these findings, the decrease of the luminescence intensity in the nanocrystalline material could be explained by the presence of carbonate and hydroxyl ions on the surface of the nanocrystals. The presence of the large vibrational quanta in the nanocrystals makes multiphonon relaxation much more probable than in the bulk sample, where the maximum phonon energy, determined from Raman measurements, was approximately 620 cm^{-1} (see Figure 6.46).

The observed decay curves for the observed transitions following 488 nm excitation were fitted using a single exponential function (Table 6.7). The decay times for the nanocrystalline material are in general shorter than for the bulk, which could be attributed to a higher probability for multiphonon relaxation in the nanocrystalline material owing to the presence of contaminants on their surface. In the nanocrystalline material, the presence of vibrational quanta of about 1500 and 3350 cm^{-1} makes multiphonon relaxation much more probable than in the bulk material, increases the rate

of depopulation and therefore gives rise to a shorter observed decay time with respect to the bulk sample.

Table 6.7: Room temperature decay times for bulk and nanocrystalline $Lu_2O_3:Er^{3+}$ obtained from an exponential fit of the decay curves upon 488 excitation.

Transition	Decay Time (μs)	
	Bulk $Lu_2O_3:Er^{3+}$	Nanocrystalline $Lu_2O_3:Er^{3+}$
$^2H_{11/2} \rightarrow {}^4I_{15/2}$	63	53
$^4S_{3/2} \rightarrow {}^4I_{15/2}$	62	55
$^4F_{9/2} \rightarrow {}^4I_{15/2}$	74	42
$^4I_{9/2} \rightarrow {}^4I_{15/2}$	61	47
$^4S_{3/2} \rightarrow {}^4I_{13/2}$	63	54

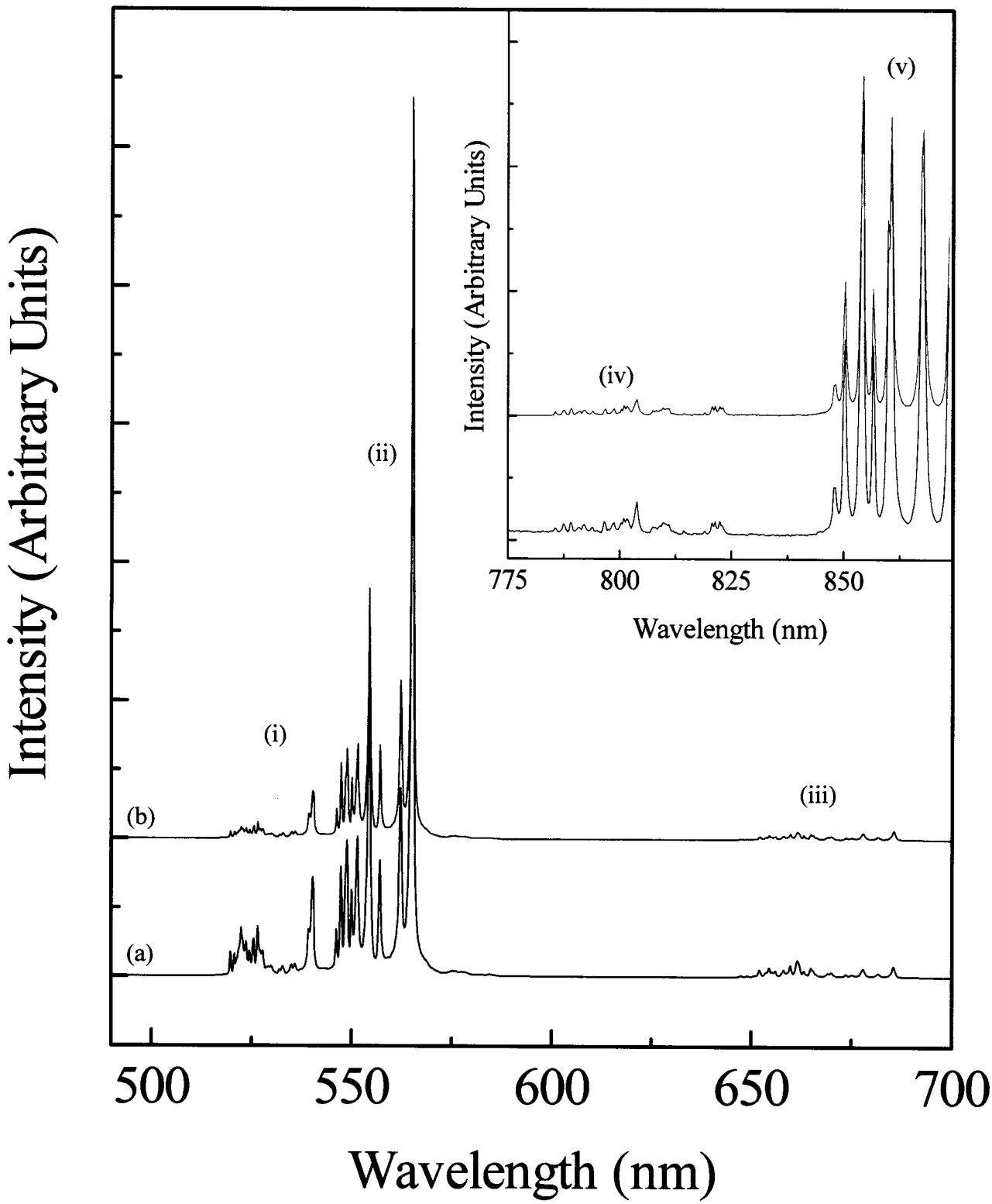

Figure 6.44: Room temperature luminescence of (a) nanocrystalline and (b) bulk $Lu_2O_3:Er^{3+}$ (1 mol%) following 488 nm excitation. (i) $^2H_{11/2} \rightarrow {}^4I_{15/2}$ (ii) $^4S_{3/2} \rightarrow {}^4I_{15/2}$ (iii) $^4F_{9/2} \rightarrow {}^4I_{15/2}$ Inset: (iv) $^4I_{9/2} \rightarrow {}^4I_{15/2}$ (v) $^4S_{3/2} \rightarrow {}^4I_{13/2}$.

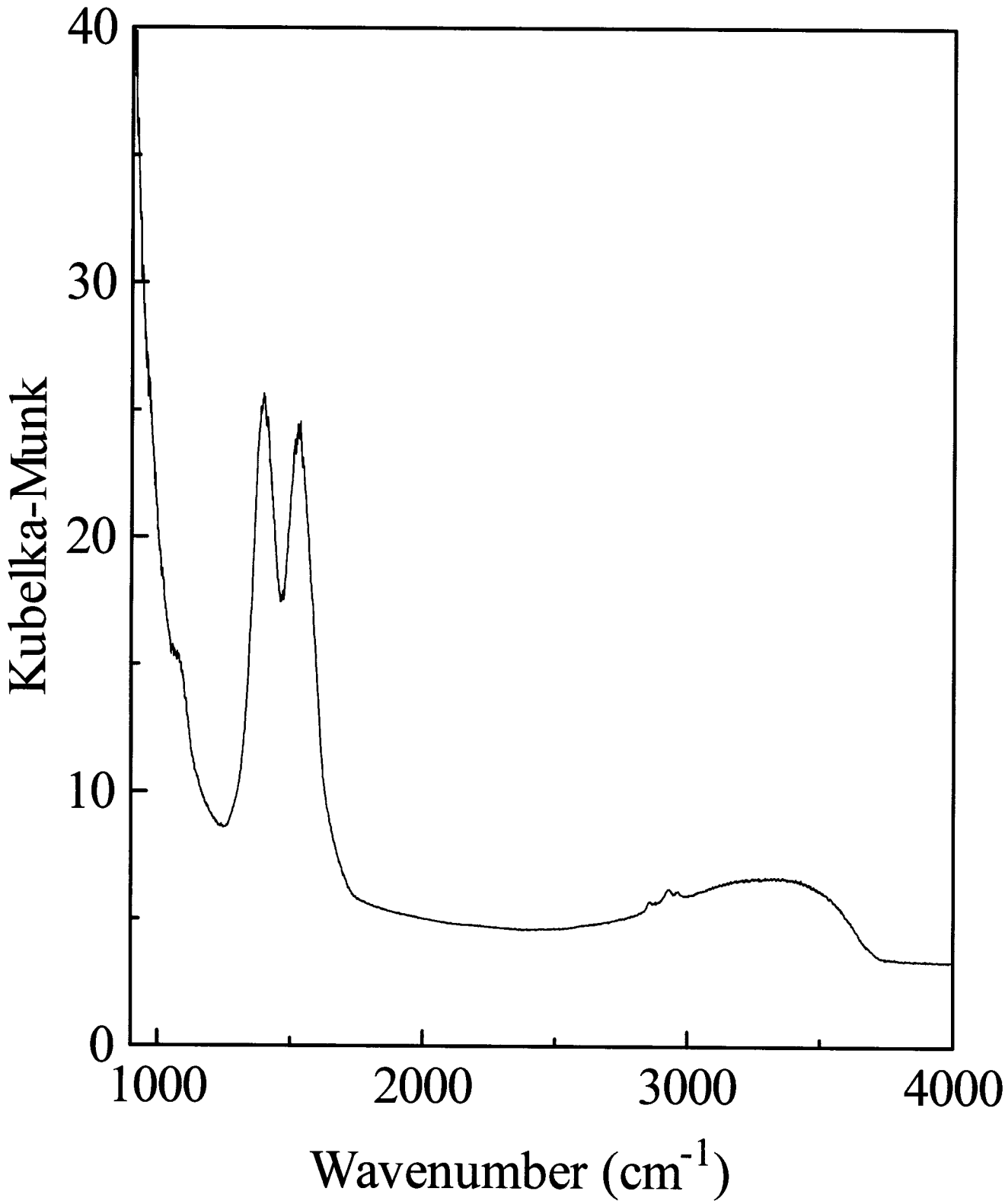

Figure 6.45: Diffuse reflectance medium-infrared (MIR) spectrum of nanocrystalline $Lu_2O_3:Er^{3+}$ (1 mol%).

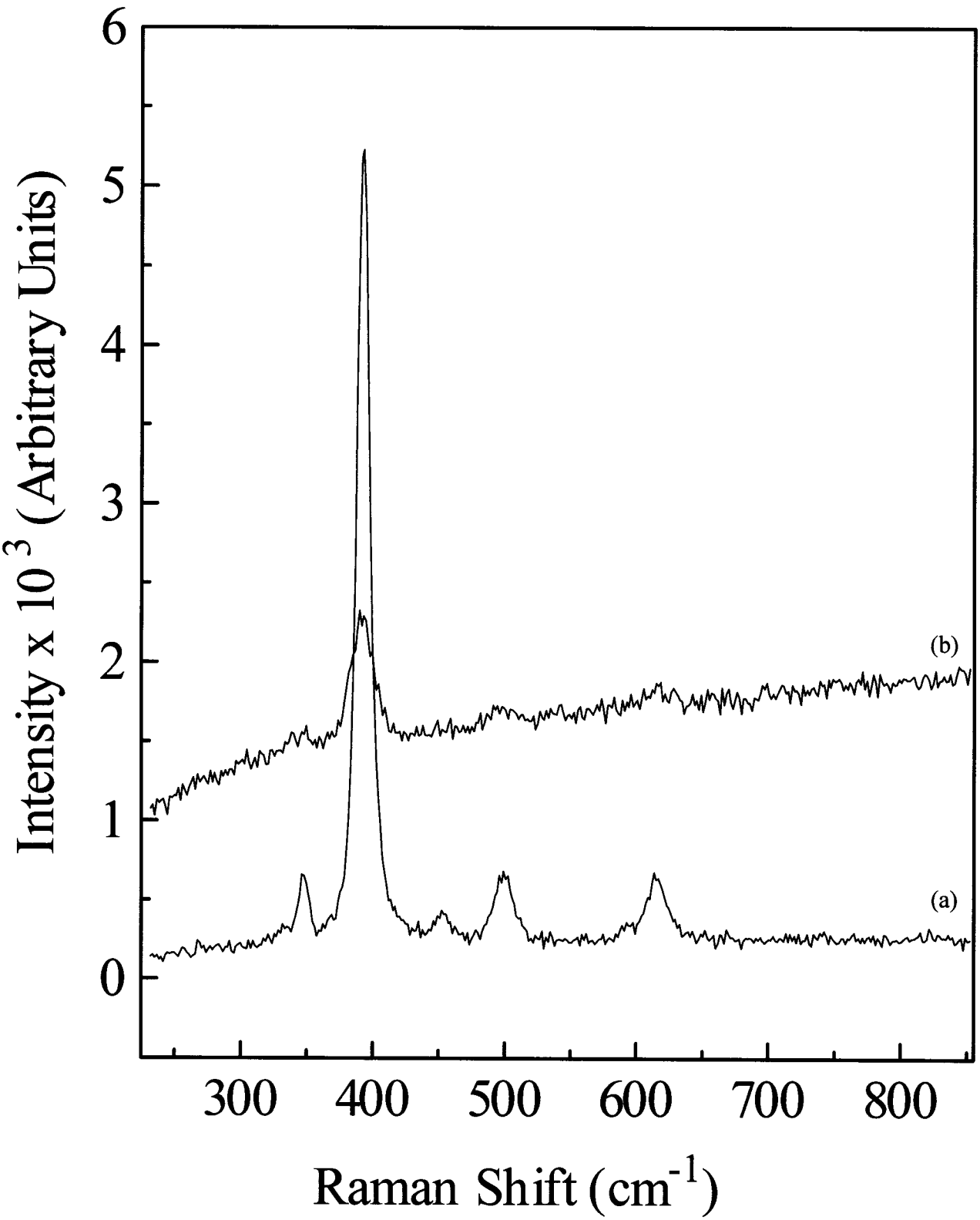

Figure 6.46: Raman spectrum of (a) commercial and (b) nanocrystalline undoped Lu_2O_3.

6.3.2. Near-Infrared Emission Spectroscopy

Figure 6.47 shows the near-infrared (NIR) luminescence spectra excited at 488 nm in the range 900-1800 nm for the samples under investigation [265]. The following transitions were observed: $^4I_{11/2} \rightarrow {}^4I_{15/2}$ (~ 1000 nm), $^4S_{3/2} \rightarrow {}^4I_{11/2}$ (~ 1260 nm) and $^4I_{13/2} \rightarrow {}^4I_{15/2}$ (~ 1540 nm). The NIR spectrum of the nanocrystalline sample differs from its bulk counterpart. In the bulk sample, the relative integrated intensity of the $^4I_{11/2} \rightarrow {}^4I_{15/2}$ and $^4I_{13/2} \rightarrow {}^4I_{15/2}$ transitions is about 3:1 while in the nanocrystals, this ratio is approximately 1:1. We again attribute this behavior to the presence of carbonates and hydroxyl groups on the nanocrystalline surface. In the nanocrystalline sample, the multiphonon relaxation from the higher lying levels to the $^4I_{13/2}$ level is more probable due to the presence of the vibrational quanta of 1500 and 3300 cm^{-1}, resulting in an increased population of the $^4I_{13/2}$ state. In the bulk sample, the probability of multiphonon relaxation is significantly reduced, as significantly more phonons are required in order to bridge the gaps from the upper lying states to the $^4I_{13/2}$ level.

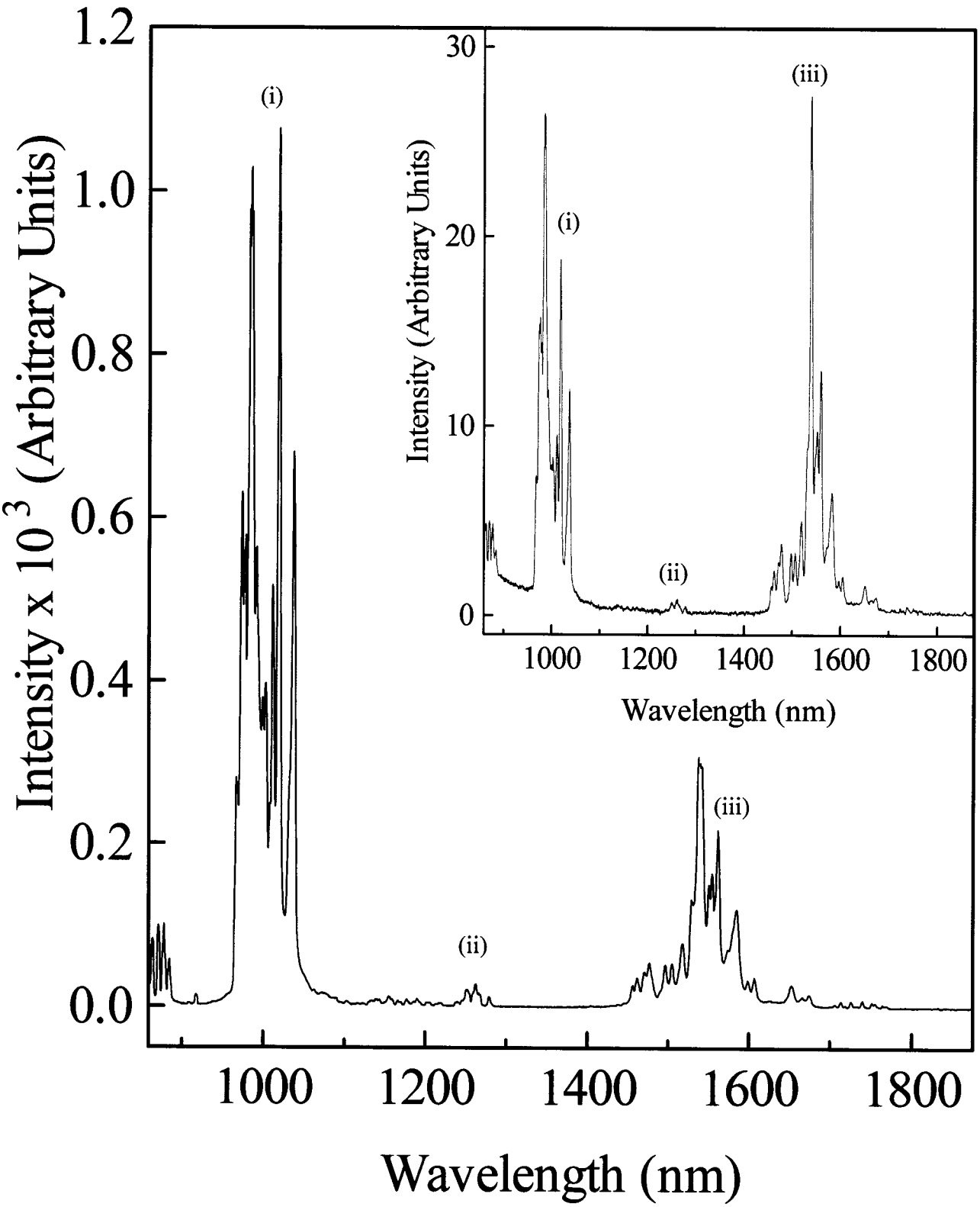

Figure 6.47: NIR luminescence of bulk $Lu_2O_3:Er^{3+}$ (1 mol%) upon excitation at 488 nm. Inset: NIR luminescence of $Lu_2O_3:Er^{3+}$ (1 mol%) nanocrystals upon excitation at 488 nm. (i) $^4I_{11/2} \rightarrow {}^4I_{15/2}$ (ii) $^4S_{3/2} \rightarrow {}^4I_{11/2}$ (iii) $^4I_{13/2} \rightarrow {}^4I_{15/2}$.

6.3.3. Upconversion Upon Excitation into the $^4F_{9/2}$ Manifold (λ_{exc} = 650 nm)

Room temperature laser excitation at 650 nm of the bulk and nanocrystalline samples into the $^4F_{9/2} \leftarrow {}^4I_{15/2}$ absorption transition produced intense upconversion luminescence bands in the blue and green regions [265]. The observed bands in the green region centered at 525 and at 550 nm are assigned to the $^2H_{11/2} \rightarrow {}^4I_{15/2}$ and $^4S_{3/2} \rightarrow {}^4I_{15/2}$ transitions, respectively. The luminescence bands in the blue region centered at 460, 495 and 475 nm are assigned to the $^4F_{5/2} \rightarrow {}^4I_{15/2,}$ $^4F_{7/2} \rightarrow {}^4I_{15/2}$ and $^2P_{3/2} \rightarrow {}^4I_{11/2}$ transitions, respectively. The mechanisms of upconversion responsible for populating the blue ($^4F_{5/2,}$ $^4F_{7/2}$ and $^2P_{3/2}$) and green ($^2H_{11/2}$ and $^4S_{3/2}$) emitting states were already discussed in section 6.2.2. However, in $Y_2O_3:Er^{3+}$ nanocrystals, upconversion in the blue region of the spectrum was not observed.

6.3.4. Upconversion Upon Excitation into the $^4I_{9/2}$ Manifold (λ_{exc} = 804 nm)

Room temperature laser excitation at 804 nm of the bulk and nanocrystalline samples into the $^4I_{9/2} \leftarrow {}^4I_{15/2}$ absorption transition produced intense upconversion luminescence bands in the blue, green and red regions, as shown in Figure 6.49. The observed bands in the green region centered at 525 nm and 550 nm are assigned to the $^2H_{11/2} \rightarrow {}^4I_{15/2}$ and $^4S_{3/2} \rightarrow {}^4I_{15/2}$ transitions respectively, while the bands in the red region centered at 660 nm are assigned to the $^4F_{9/2} \rightarrow {}^4I_{15/2}$ transition [265].

The intensity of the upconverted green and red emissions have been measured as a function of the pump power at 804 nm. From a fit of the curve $\ln(I_i)$ vs $\ln(I_o)$ we have obtained a slope of 1.9, which indicates a two photon upconversion process. It is worth pointing out that under identical conditions, the nanocrystalline $Lu_2O_3:Er^{3+}$ under

investigation shows upconversion intensities approximately 100 times greater than $Y_2O_3:Er^{3+}$ [238]. A possible explanation could be found on the basis of an intensity-borrowing mechanism mixing the 4*f* and 5*d* orbitals of the RE^{3+} ion via the lattice valence band levels, as proposed by Guillot-Noël et al. [266]. In Y-based compounds, the valence band energy levels are due predominantly to the oxygen or fluorine 2*p* orbitals whereas in Lu crystals, the top of the valence band would be composed mainly of Lu 4*f* orbitals [267]. It follows that lutetium could be a more favorable cation than yttrium for trivalent rare earth dopant emission [268].

Very interestingly, we have observed bands also in the blue region (450-500 nm) exciting at 804 nm for both the bulk and nanocrystalline samples, as shown in the inset of Figure 6.49. We have observed very weak bands centered at 460 and 495 nm which could be assigned to the $^4F_{5/2} \rightarrow {}^4I_{15/2}$ and $^4F_{7/2} \rightarrow {}^4I_{15/2}$ transitions, respectively. Moreover, a relatively stronger emission was observed centered at 475 nm which could be assigned to the $^2P_{3/2} \rightarrow {}^4I_{11/2}$ transition. The intensity of this latter transition has been measured as a function of the pump power at 804 nm. From a fit of the curve $\ln(I_i)$ vs $\ln(I_0)$ we have obtained a slope of 3.2, which strongly suggests the occurrence of a three photon upconversion process. The details of this mechanism will be discussed later. It should be noted that we have observed blue upconversion also in bulk samples of $Y_2O_3:Er^{3+}$. On the contrary, nanocrystalline Er^{3+} doped Y_2O_3 did not produce any noticeable blue upconversion.

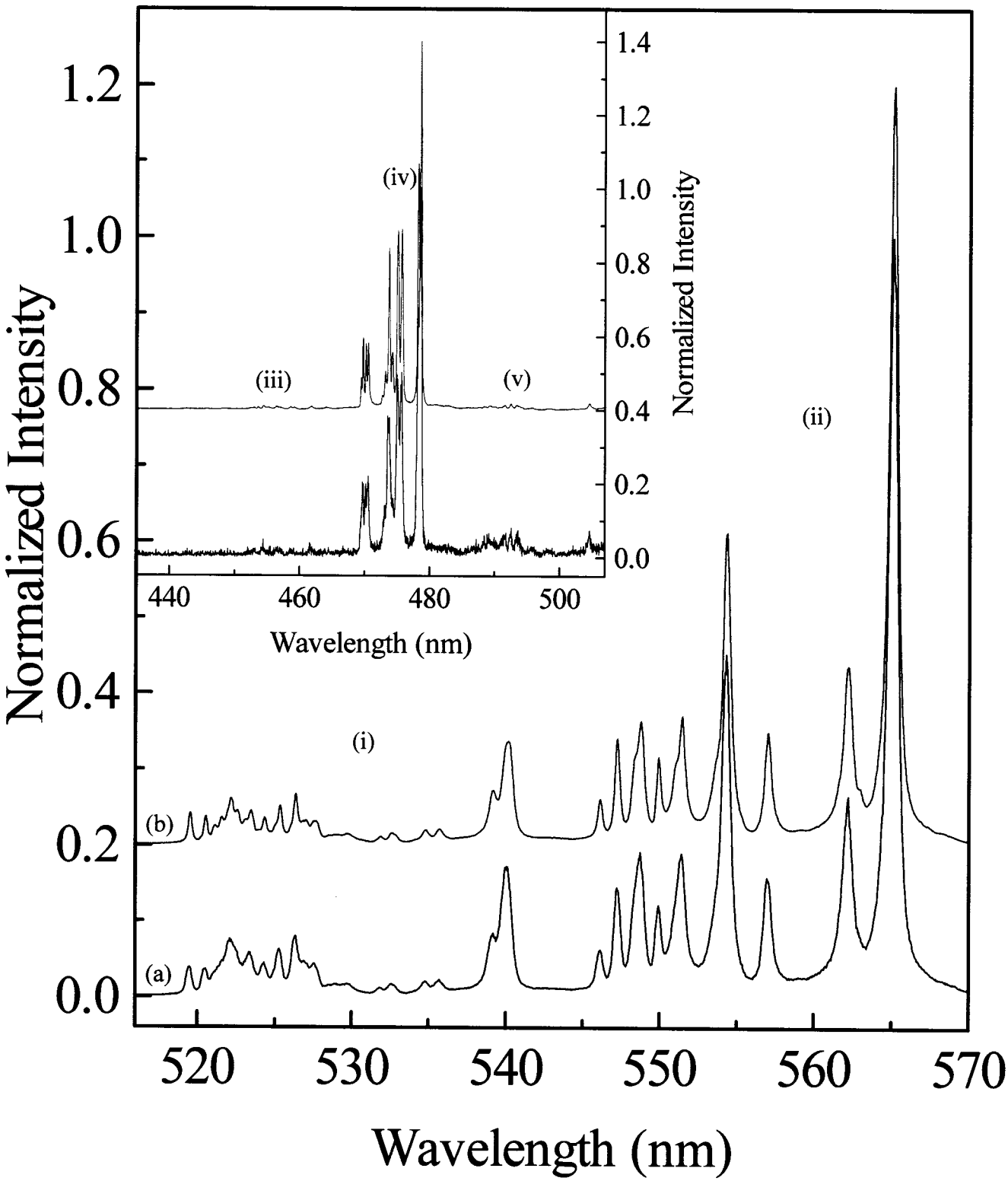

Figure 6.48: Upconversion luminescence of (a) nanocrystalline and (b) bulk $Lu_2O_3:Er^{3+}$ (1 mol%) following excitation with 650 nm. (i) $^2H_{11/2} \rightarrow {}^4I_{15/2}$ (ii) $^4S_{3/2} \rightarrow {}^4I_{15/2}$ (iii) $^4F_{5/2} \rightarrow {}^4I_{15/2}$ (iv) $^2P_{3/2} \rightarrow {}^4I_{15/2}$ (v) $^4F_{7/2} \rightarrow {}^4I_{15/2}$.

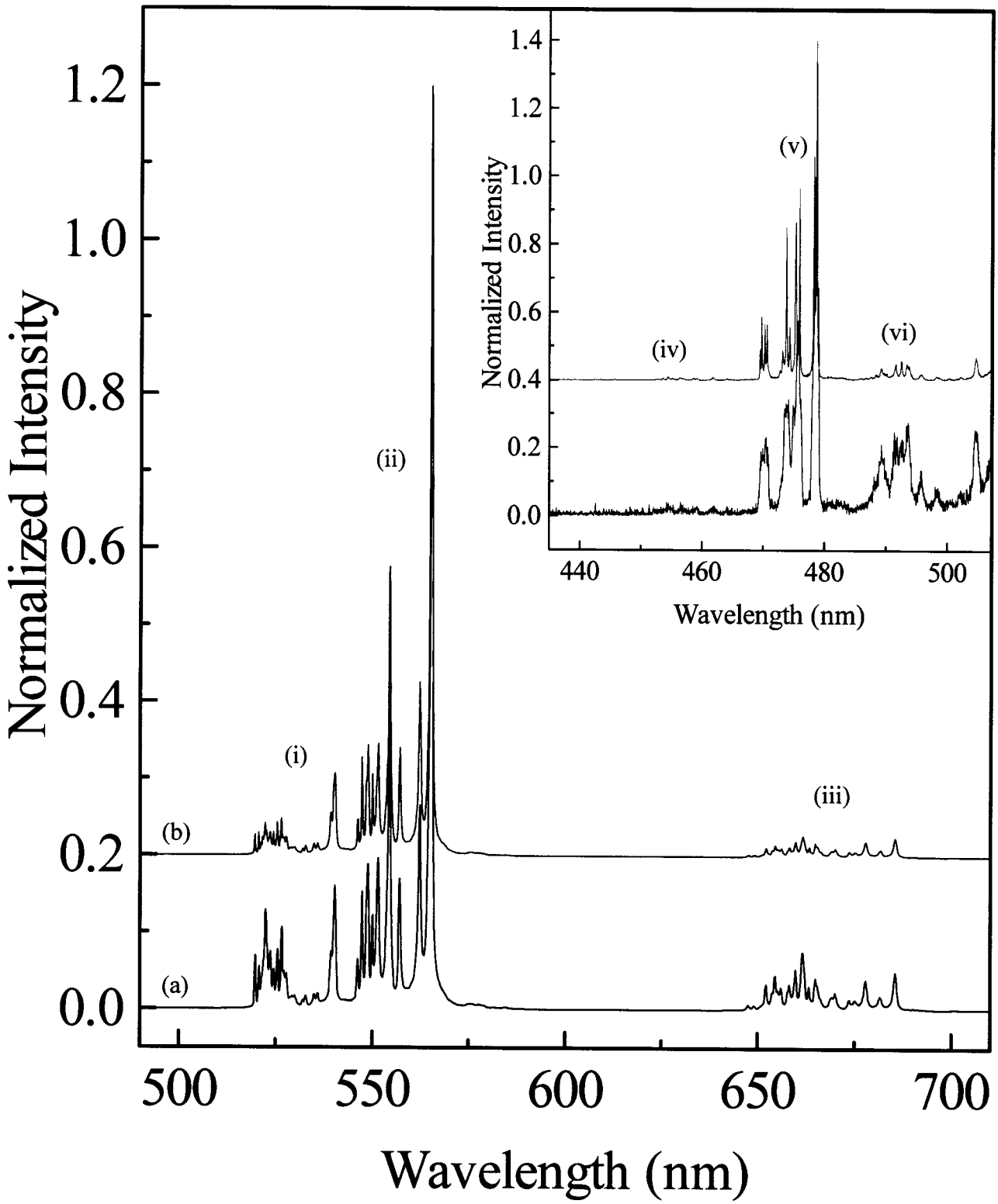

Figure 6.49: Upconversion luminescence of (a) nanocrystalline and (b) bulk $Lu_2O_3:Er^{3+}$ (1 mol%) following excitation with 804 nm. (i) $^2H_{11/2} \rightarrow {}^4I_{15/2}$ (ii) $^4S_{3/2} \rightarrow {}^4I_{15/2}$ (iii) $^4F_{9/2} \rightarrow {}^4I_{15/2}$ (iv) $^4F_{5/2} \rightarrow {}^4I_{15/2}$ (v) $^2P_{3/2} \rightarrow {}^4I_{15/2}$ (vi) $^4F_{7/2} \rightarrow {}^4I_{15/2}$.

6.3.5. Temperature Dependence of the Transition Probabilities

The decay times for the bulk sample of Er^{3+} doped lutetia obtained from the decay curves for the $^4S_{3/2} \rightarrow {}^4I_{15/2}$ transition at various temperatures, upon 804 nm excitation, are reported in Table 6.8. Since the present dopant concentration is relatively small, it is reasonable to assume that the energy transfer processes are not very important. Under this assumption, the rate of depopulation W of an excited state can be expressed as the sum of the radiative and non-radiative (or multiphonon) transition probabilities (see section 6.2.1). Unlike the radiative transition probability, which is independent of temperature, the multiphonon transition probability is in fact temperature dependent. The temperature dependence of W_{MPR}, in the case of a transition between states belonging to a $4f^N$ configuration, is given by [106]:

$$W_{MPR}(\mathrm{T}) = W_{MPR}(0)\left(1 + n_{eff}\right)^p \qquad 6.3.1$$

where

$$n_{eff} = \left[\exp(\hbar\omega_{eff} / kT) - 1\right]^{-1} \qquad 6.3.2$$

is the occupancy of the effective phonon mode of energy $\hbar\omega_{eff}$ and p is the number of phonons necessary to bridge the energy gap between the emitting state and the state directly beneath it. The observed decay time is equal to the reciprocal of the total transition probability W. Unfortunately, the value of W_R is not known and therefore we cannot obtain the behavior of W_{MPR} as a function of the temperature. In any case, the decay times become shorter on increasing the temperature (see Table 6.8), in agreement with eq. 6.3.1, and as reported for other systems [269].

Table 6.8: Room temperature decay times for bulk and nanocrystalline $Lu_2O_3:Er^{3+}$ obtained from an exponential fit of the decay curves upon 488 excitation.

Temperature (K)	Decay Time (μs)
78	914.6
120	510.1
140	309.6
180	218.4
240	163.3
298	127.6

Figure 6.50 shows the upconversion luminescence spectra for the bulk sample of $Lu_2O_3:Er^{3+}$ obtained at temperatures ranging from 77 to 298 K and excited at 804 nm. The upconversion efficiency for the $^4F_{9/2} \rightarrow {}^4I_{15/2}$ and $^4S_{3/2} \rightarrow {}^4I_{15/2}$ emissions present maxima at 140 and 180 K, respectively. This behavior could be due to the competition of two different phonon-assisted processes. The drop in the upconversion intensity when temperature is increased above 140-180 K is probably caused by the temperature dependence of the multiphonon relaxation of the ($^2H_{11/2}$, $^4S_{3/2}$) and $^4F_{9/2}$ levels, which increases significantly above 100 K [270], as observed above. However, both the ETU and ESA mechanisms promoting the upconversion involve phonon emission to populate the intermediate excited states, and therefore their probability should increase when the temperature is increased. The simultaneous occurrence of these two mechanisms could explain the presence of maxima for the upconversion intensities at about 140 and 180 K.

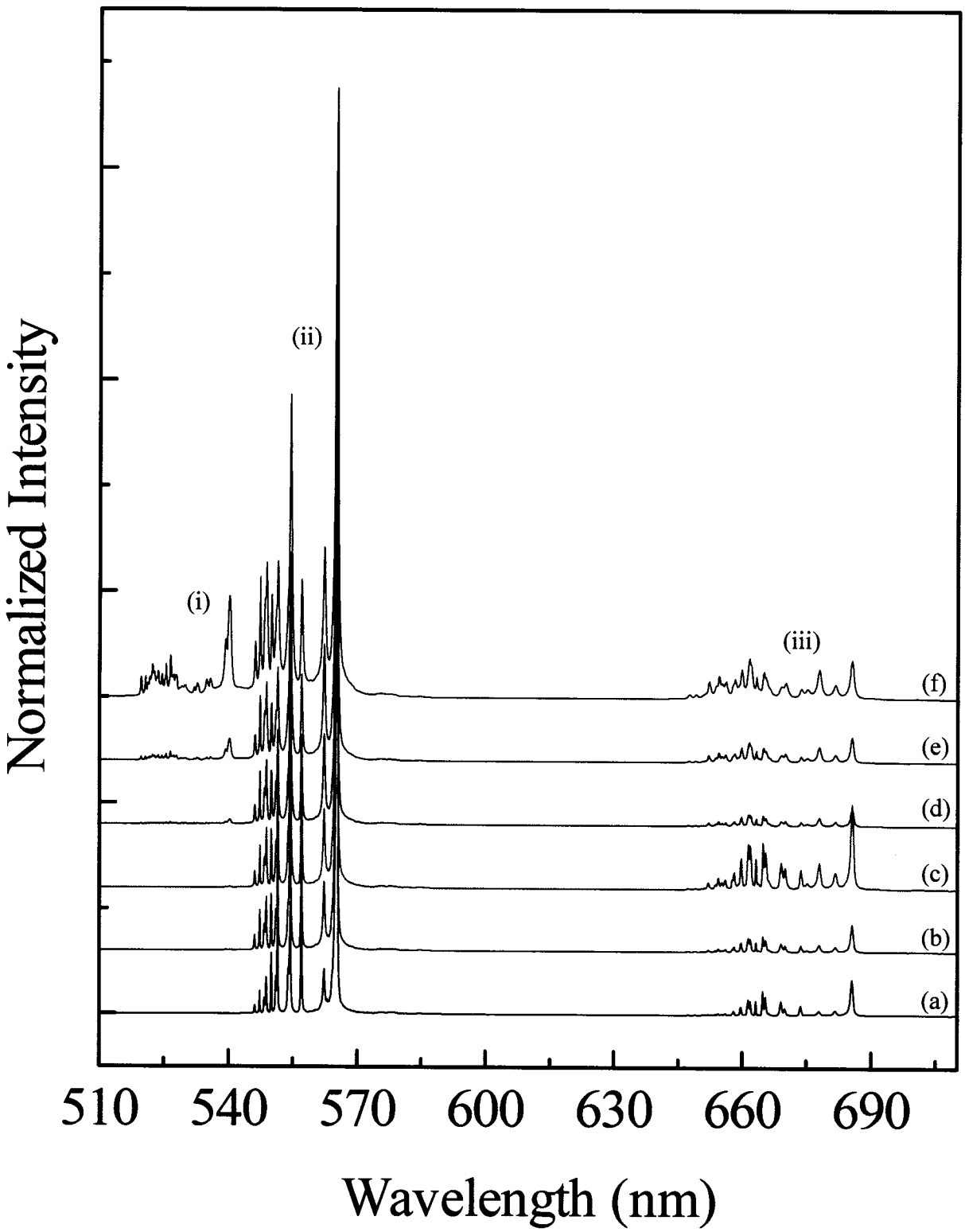

Figure 6.50: Upconversion luminescence spectra of bulk $Lu_2O_3:Er^{3+}$ at different temperatures (λ_{exc} = 804 nm): (a) 78 K, (b) 120 K, (c) 140 K, (d) 180 K, (e) 240 K, (f) 298 K. (i) $^2H_{11/2} \rightarrow {}^4I_{15/2}$ (ii) $^4S_{3/2} \rightarrow {}^4I_{15/2}$ (iii) $^4F_{9/2} \rightarrow {}^4I_{15/2}$. The intensities of emission are normalized to green ($^4S_{3/2} \rightarrow {}^4I_{15/2}$) transition.

6.3.6. Mechanisms of Upconversion

In bulk and nanocrystalline Er^{3+} doped Y_2O_3, we have shown that the mechanism resulting in green and red upconversion occurs via ESA and ETU processes. Similarly to what has been proposed for Y_2O_3, the mechanism by which the ($^2H_{11/2}$, $^4S_{3/2}$) and $^4F_{9/2}$ levels are populated in Lu_2O_3 is assigned as follows. The laser light at 804 nm brings the Er^{3+} ion to the $^4I_{9/2}$ level, which then non-radiatively decays into the $^4I_{11/2}$ level after which energy transfer from a neighboring Er^{3+} ion brings it to the $^4F_{3/2}$ level. Then, the Er^{3+} ion decays into the emitting the ($^2H_{11/2}$, $^4S_{3/2}$) and $^4F_{9/2}$ levels by multiphonon relaxation. Alternatively, after the initial excitation, the Er^{3+} ion can non-radiatively decay down to the $^4I_{13/2}$ level. Again, an energy transfer process brings the ion to the $^2H_{11/2}$ level. Emission from the latter and the lower lying $^4F_{9/2}$ level can then be observed. While it has been shown that upconversion to the ($^2H_{11/2}$, $^4S_{3/2}$) and $^4F_{9/2}$ levels occurs via a two photon process other different competitive mechanisms occurring simultaneously could be invoked to generate the upconverted green and red luminescence [270]. This observation was brought to light with this study as very intense upconversion has been observed in these samples with relatively low (1 mol%) Er^{3+} concentration. We therefore assume that both energy transfer upconversion (ETU) and excited state absorption (ESA) occur simultaneously.

The results of the power study of the $^2P_{3/2} \rightarrow {}^4I_{11/2}$ transition indicated that a three-photon mechanism was at play. This mechanism may occur via a sequential absorption of photons and is shown in Figure 6.51. First, the 804 nm light excites the Er^{3+} ion to the $^4I_{9/2}$ multiplet, after which, the Er^{3+} ion relaxes to the $^4I_{11/2}$ level by a non-radiative process. A second and third photon excites the Er^{3+} ion to the $^4G_{7/2}$ level. Again, non-

radiative decay results in the population of the $^2P_{3/2}$ level and of course the ($^2H_{11/2}$, $^4S_{3/2}$) and $^4F_{9/2}$ levels.

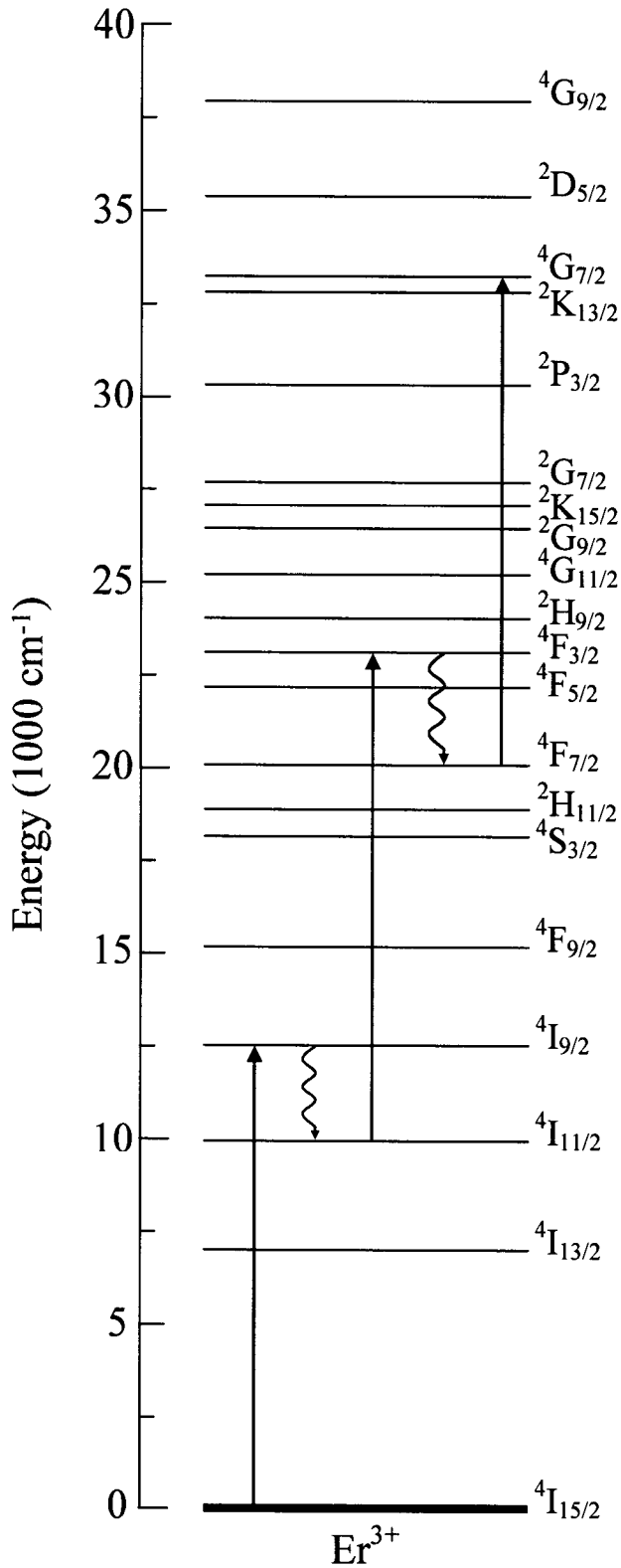

Figure 6.51: Energy level diagram of Er^{3+} ions in Lu_2O_3 showing the three photon upconversion process responsible for populating the $^4G_{7/2}$ level (λ_{exc} = 804 nm).

6.3.7. Upconversion Upon Excitation into the $^4I_{11/2}$ Manifold (λ_{exc} = 980 nm)

Excitation of bulk and nanocrystalline Lu_2O_3 with NIR light (λ_{exc} = 980 nm) into the $^4I_{11/2}$ level of the Er^{3+} ion produced intense upconversion luminescence spectra (Figure 6.52) [264]. Blue upconversion was observed with bands centered at 460, 475 and 495 nm, which are assigned to the $^4F_{5/2} \rightarrow {}^4I_{15/2}$, $^2P_{3/2} \rightarrow {}^4I_{11/2}$ and $^4F_{7/2} \rightarrow {}^4I_{15/2}$ transitions, respectively. Similar to the direct emission spectra, upconverted green emission was observed from the thermalized $^2H_{11/2} \rightarrow {}^4I_{15/2}$ and $^4S_{3/2} \rightarrow {}^4I_{15/2}$ transitions centered at 525 nm and 550 nm, respectively. Upconverted red emission centered at 660 nm was assigned to the $^4F_{9/2} \rightarrow {}^4I_{15/2}$ transition. The bulk and nanocrystalline samples exhibit a visually dominant green emission following 980 nm excitation ascribed to the spin allowed $^4S_{3/2} \rightarrow {}^4I_{15/2}$ transition.

To better understand the mechanism by which the $^4S_{3/2}$ and $^4F_{9/2}$ levels are populated, the upconverted luminescence intensity I_o of the green ($^4S_{3/2} \rightarrow {}^4I_{15/2}$) and red ($^4F_{9/2} \rightarrow {}^4I_{15/2}$) transitions was measured as a function of the NIR pump power I_i. The slope of the curve ln(Intensity) vs. ln(Power) was 1.9 and 1.6, respectively (Figure 6.53) so we can therefore propose that two photons partake in the upconversion processes involved in the population of the $^4S_{3/2}$ and $^4F_{9/2}$ levels. As all other samples, the PA mechanism was eliminated as a possible mechanism as no inflection point was observed in the power study [148, 247]. In the bulk and nanocrystalline material, upconversion can therefore only occur via an ESA or ETU process.

The ESA model involves only a single ion and it is usually the only upconversion process, which occurs in materials at low dopant concentrations. In this process, an incoming photon from the pump beam will bring the ion already in an intermediate

excited level (|1>), to an upper level (|2>). In the framework of the proposed model, the population N_2 of level |2> is given by:

$$N_2(t) = \frac{N_0 A_{01} A_{12} I_0^2}{\tau_2^{-1}\left(\tau_1^{-1} + A_{12} I_0\right)} \qquad 6.3.3$$

where N_0 is the initial population of the ion in the ground state (|0>), A_{ij} is a characteristic constant involving the oscillator strengths for the transitions from the initial state |i> to the final state |j>. I_0 describes the density of photons in the pump beam while τ_1^{-1} and τ_2^{-1} are the intrinsic relaxation rates of levels |1> and |2>, respectively. According to eqn. 6.3.3, we note that the upconverted luminescence varies quadratically with the pump beam (I_0) but varies linearly with the concentration of the emitting particle.

Using the proposed model, one photon at 980 nm from the pump beam will excite the Er^{3+} ion from the $^4I_{15/2}$ ground state (|0>) to the $^4I_{11/2}$ intermediate excited state (|1>). A second photon of equal energy brings the ion to the $^4F_{7/2}$ level (|2>), which has an energy exactly twice that of the excitation pump beam (see Figure 6.54). Multiphonon relaxation will then populate the $^2H_{11/2}$, $^4S_{3/2}$ and $^4F_{9/2}$ levels.

However, we cannot readily exclude the presence of the ETU mechanism acting in conjunction with the ESA process. It has been shown that in samples having a dopant concentration of 0.5 mol% or less, the energy transfer between dopant ions can be considered as negligible [271], as the ions are too far apart and therefore the interaction with one another is very weak. The bulk and nanocrystalline samples used in this study have a dopant Er^{3+} concentration of 1 mol% and therefore, it is conceivable that the ETU process could be efficient. ETU proceeds according to a scheme in which two ions in close proximity are excited in an intermediate level |1> and are coupled by a non-

radiative process in which one ion returns to the ground state |0> while the other is promoted to the upper level |2>. Using the same symbols as above, population of level |2> can be written as:

$$N_2(t) = \frac{(N_0 A_{01} I_0)^2 \sigma_u}{\tau_2^{-1}(\tau_1^{-1})^2} \qquad 6.3.4$$

where σ_u is the rate constant for the ETU process. Similar to ESA, in the ETU process the population of level |2> varies quadratically with the density of photons in the pump beam (I_0), but, at variance with ESA, also varies quadratically with the dopant concentration N_0. Using the proposed model, the ETU process (see Figure 6.54) occurs as follows: one Er^{3+} ion is excited to the $^4I_{11/2}$ level by the pump laser beam. A neighboring Er^{3+} ion also in the $^4I_{11/2}$ level, transfers its energy to the initial ion thereby exciting it to the $^4F_{7/2}$ level while it returns to the ground state. Again, non-radiative phonon decay populates the green and red emitting levels.

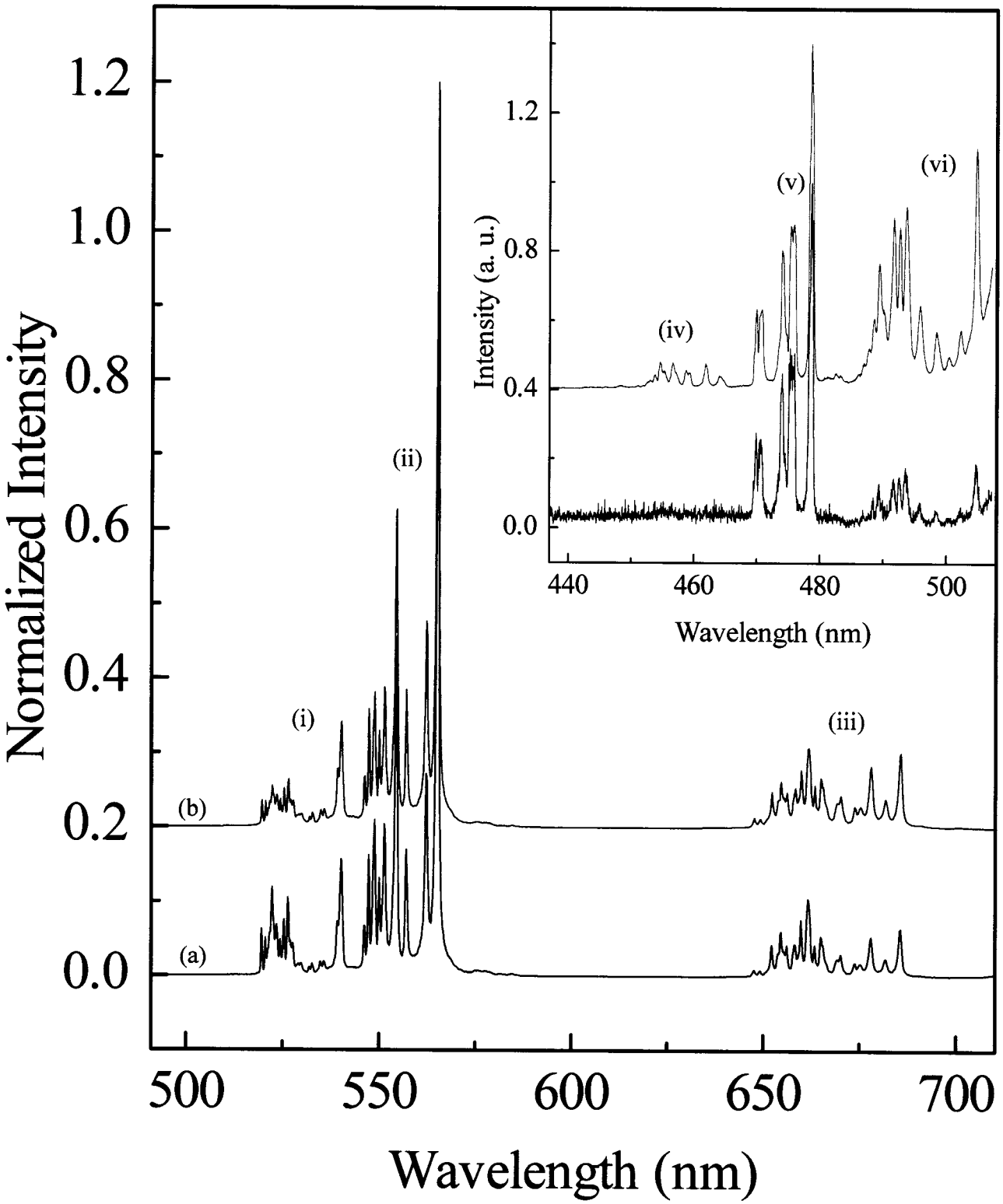

Figure 6.52: Room temperature upconversion luminescence of (a) nanocrystalline and (b) bulk $Lu_2O_3:Er^{3+}$ following 980 nm excitation. (i) $^2H_{11/2} \rightarrow {}^4I_{15/2}$ (ii) $^4S_{3/2} \rightarrow {}^4I_{15/2}$ (iii) $^4F_{9/2} \rightarrow {}^4I_{15/2}$. Inset: (iv) $^4F_{5/2} \rightarrow {}^4I_{15/2}$ (v) $^2P_{3/2} \rightarrow {}^4I_{11/2}$ (vi) $^4F_{7/2} \rightarrow {}^4I_{15/2}$.

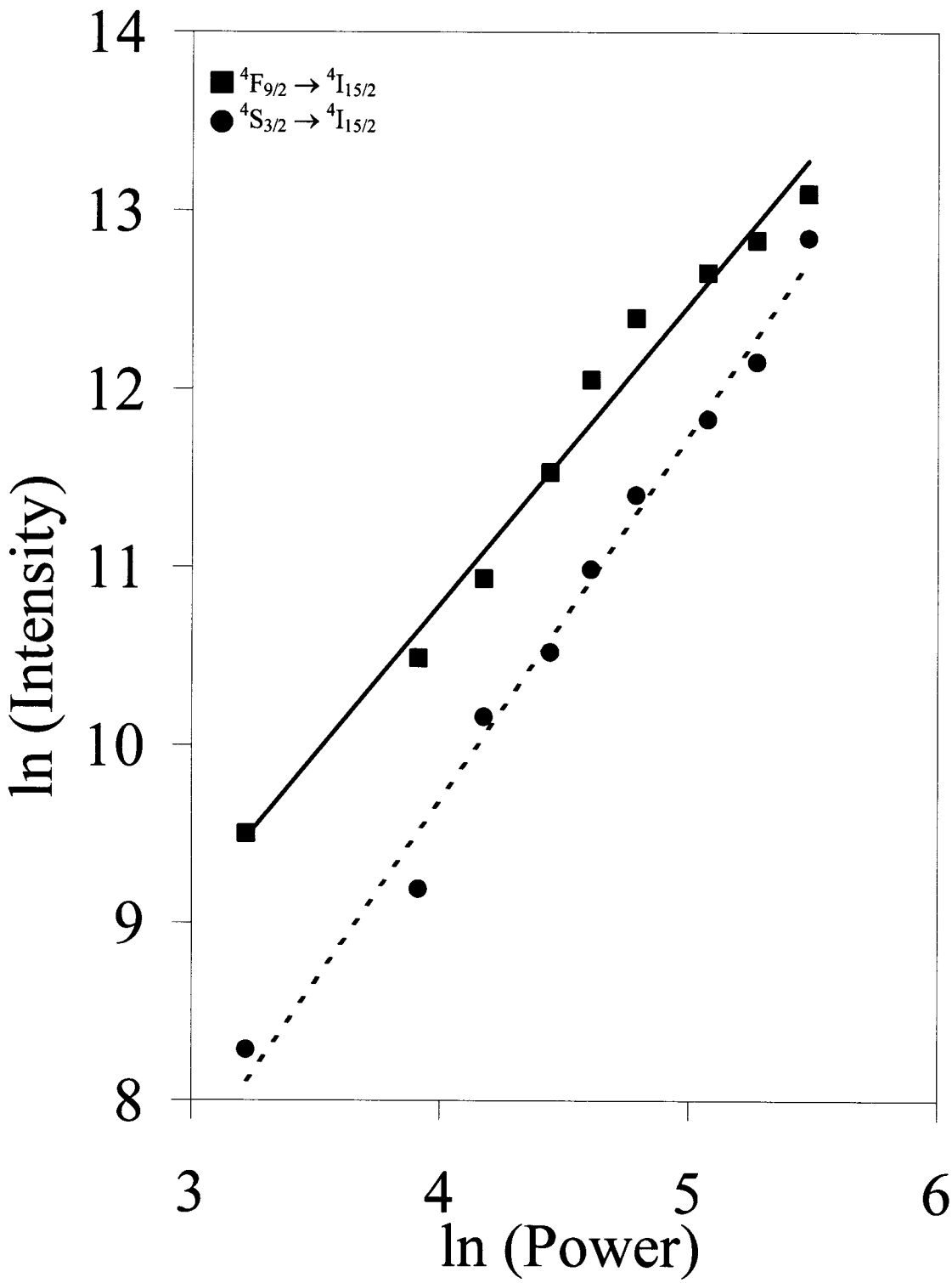

Figure 6.53: Power dependence of the green and red upconversion luminescence intensity of nanocrystalline $Lu_2O_3:Er^{3+}$ observed following 980 nm excitation.

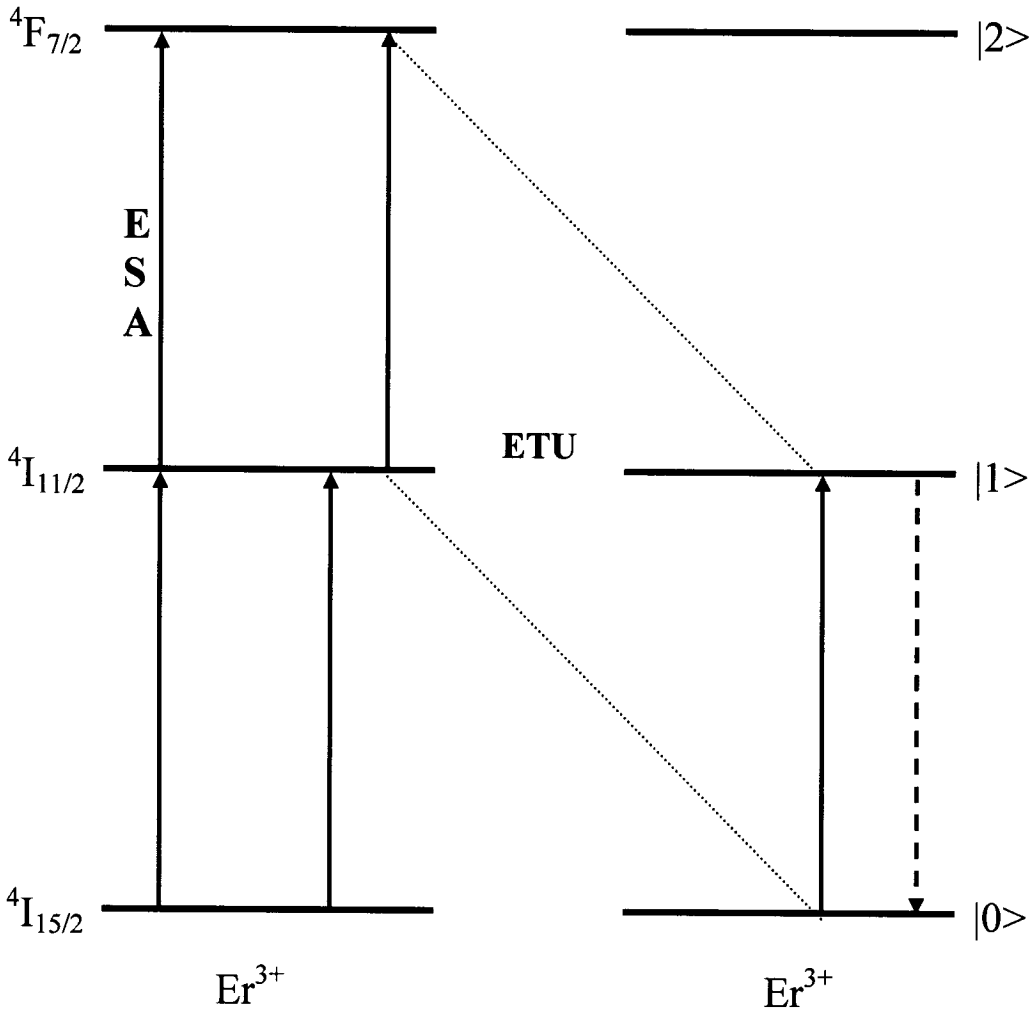

Figure 6.54: Schematic representation of the ESA and ETU processes in bulk and nanocrystalline $Lu_2O_3:Er^{3+}$. Note: only the relevant Er^{3+} energy levels are shown.

Table 6.9 shows the room temperature emission lifetimes of the $^4S_{3/2}$ and $^4F_{9/2}$ levels following excitation with 980 nm radiation. While the decay curves of the $Lu_2O_3:Er^{3+}$ excited states following 488 nm excitation were exponential (Table 6.7), the same is not true following 980 nm excitation, which showed a slight deviation from single exponential decay. In the bulk and nanocrystalline samples, the decay times in the case of anti-Stokes emission (λ_{exc} = 980 nm) are significantly longer than the ones measured for the same states when exciting directly (λ_{exc} = 488 nm). Lengthening of the decay times following upconversion pumping is a clear indication of the presence of an ETU process. Excitation with either 488 or 980 nm could populate the $^4F_{7/2}$ state, albeit via different mechanisms. However, in the case of the upconversion process (λ_{exc} = 980 nm), it could be assumed that the decays of the emitting levels reflect the feeding from longer-lived states.

Table 6.9: Room temperature decay times for bulk and nanocrystalline $Lu_2O_3:Er^{3+}$ obtained from an exponential fit of the decay curves upon 980 excitation.

Transition	Decay Time (μs)	
	Bulk $Lu_2O_3:Er^{3+}$	Nanocrystalline $Lu_2O_3:Er^{3+}$
$^4S_{3/2} \rightarrow {}^4I_{15/2}$	190	246
$^4F_{9/2} \rightarrow {}^4I_{15/2}$	334	315

6.3.8. Blue Upconversion in $Lu_2O_3:Er^{3+}$

A power study was also performed on the blue emitting levels of bulk $Lu_2O_3:Er^{3+}$. From the fitting of the ln(Intensity) vs. ln(Power) curves for the $^4F_{7/2} \rightarrow {}^4I_{15/2}$ and $^4F_{5/2} \rightarrow {}^4I_{15/2}$ emission transitions the slopes were found to be 1.8 and 1.7, respectively (Figure 6.55) and therefore two photons partake in the upconversion processes involved in the population of the $^4F_{7/2}$ and $^4F_{5/2}$ levels. The $^4F_{7/2}$ level is therefore likely to be populated via an ESA and/or ETU process involving two photons of 980 nm, as described above (see Figure 6.54). On the other hand, the $^4F_{5/2}$ level is approximately 1400 cm^{-1} higher in energy than the $^4F_{7/2}$ level and so in order for this level to be populated via two photons, a phonon-assisted process must be operative. Pure lutetia possesses a maximum phonon energy of approximately 620 cm^{-1} and therefore 2 or 3 phonons of such energy would be required to bridge the 1400 cm^{-1} energy gap, resulting in a phonon assisted upconversion process. Moreover, carbonate ions are adsorbed on the surface of the nanoparticles and therefore one 1500 cm^{-1} phonon could possibly be involved as well in the phonon-assisted upconversion.

The slope of the ln(Intensity) vs. ln(Power) curve for the $^2P_{3/2} \rightarrow {}^4I_{11/2}$ transition (shown in Figure 6.55) was found to be 2.8, denoting that three photons were responsible for the upconversion process. In bulk $Y_2O_3:Er^{3+}$, we have studied the blue upconversion following 804 nm excitation as a function of the Er^{3+} concentration and have showed that ETU and ESA mechanisms were operating simultaneously. In particular, it was observed that at low Er^{3+} concentrations (< 1 mol%), the dominant mechanism is ESA, the reason being that the Er^{3+} ions are not very close to one another and the inter-ionic interactions

are very small. As the erbium concentration is increased, the inter-ionic interaction increases and the ETU process becomes more and more important.

In the present case we excited at 980 nm and thus, the mechanism that we propose to be responsible for populating the $^2P_{3/2}$ level is slightly different. The Er^{3+} energy level diagram reveals that there is no energy level, which could be populated by a sequential absorption of three pump photons. In fact, if the $^4F_{7/2}$ level is populated by the simultaneous absorption of two photons, (ESA mechanism, see Figure 6.54), there is no energy level that could be populated by the absorption of another photon. Similarly, if the ion in the ground state is excited by one photon to the $^4I_{11/2}$ level and then non-radiatively decays to the $^4I_{13/2}$ level, a second photon has no resonant energy level for which to populate. Therefore, we propose a phonon assisted ETU mechanism (Figure 6.19), in which 1-2 maximum energy phonons are requested to compensate the mismatch in energy (approximately 690 cm^{-1}).

The blue upconversion spectrum obtained at 77 K can be used to further illustrate that the population of the $^4F_{5/2}$ and $^2P_{3/2}$ energy levels can be caused by a phonon assisted process. In fact, at 77 K, emission from the $^4F_{5/2}$ level is not observed while emission from the $^2P_{3/2}$ level is only barely detectable. This experimental evidence could be well explained by the proposed mechanisms required to populate the $^4F_{5/2}$ and $^2P_{3/2}$ levels. In the former mechanism, 2-3 lattice phonons are involved while 1-2 phonons are required for the latter one. Then, the decrease of the temperature induces a stronger decrease of the population of the $^4F_{5/2}$ level with respect to the $^2P_{3/2}$ level. Therefore, a corresponding decrease of the emission intensity of the $^4F_{5/2} \rightarrow {}^4I_{15/2}$ transition with respect to the $^2P_{3/2} \rightarrow {}^4I_{15/2}$ transition is observed.

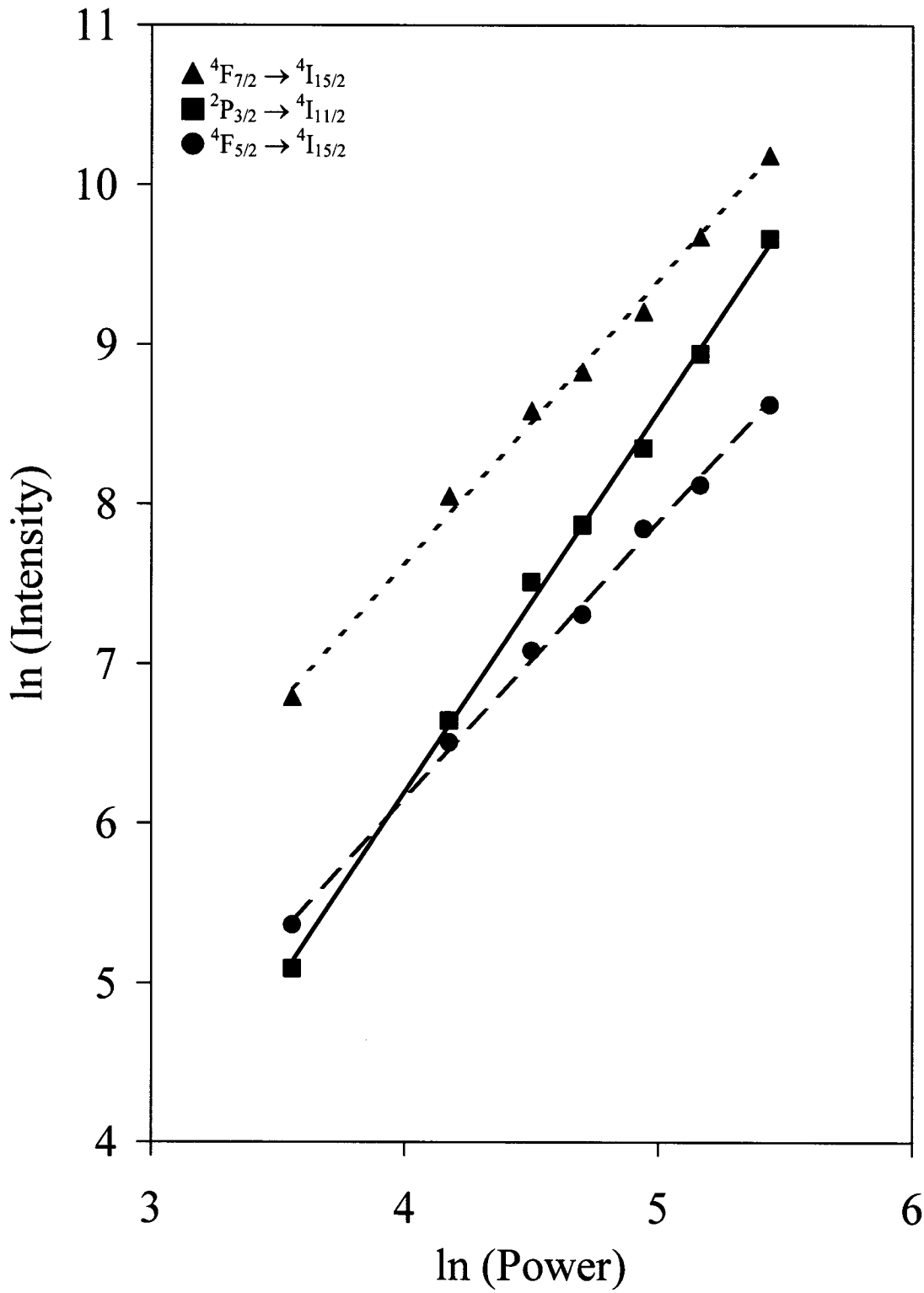

Figure 6.55: Power dependence of the blue upconversion luminescence intensity of bulk $Lu_2O_3:Er^{3+}$ observed following 980 nm excitation.

6.3.9. Temperature Dependence of the Upconversion Luminescence

The temperature dependence of the green and red upconversion luminescence for bulk and nanocrystalline $Lu_2O_3:Er^{3+}$ following 980 nm was studied (Figure 6.56). At 77K, transitions to the ground state originating from the $^2H_{11/2}$ level were not observed. However, as the temperature was increased to 298K, we observed an increase in the luminescence intensity of the $^2H_{11/2} \rightarrow {}^4I_{15/2}$ transition and a decrease of the $^4S_{3/2} \rightarrow {}^4I_{15/2}$ intensity. This occurs because the $^4S_{3/2}$ level is the feeding level for the $^2H_{11/2}$ level and as a result of the population of the $^2H_{11/2}$ level, the $^4S_{3/2}$ level is depopulated. As the energy gap between the $^4S_{3/2}$ and $^2H_{11/2}$ levels is about 700 cm^{-1}, at room temperature both are populated while at 77 K, the thermalization is very small. The temperature dependence of the $(^2H_{11/2}, {}^4S_{3/2}) \rightarrow {}^4I_{15/2}$ transition in the nanocrystalline sample can be seen in Figure 6.56 (the bulk sample shows the same spectral temperature dependence). If we denote as A_1 and A_2 the experimental integrated luminescence intensities of the $^4S_{3/2} \rightarrow {}^4I_{15/2}$ and $^2H_{11/2} \rightarrow {}^4I_{15/2}$ transitions respectively, the thermalization of the $^2H_{11/2}$ level may be expressed by the following equation [272]:

$$\frac{A_2}{A_1} = C\exp(-\Delta E / kT) \qquad 6.3.5$$

where C is a constant, k is the Boltzmann constant, T is the absolute temperature and ΔE is the energy gap separating levels $^4S_{3/2}$ and $^2H_{11/2}$. The calculated values of ln (A_2 / A_1) as a function of $1/T$ were fitted using a straight line and from the slope, an energy gap of 689 cm^{-1} was obtained. This value is in good agreement with the difference between the lowest energy $^2H_{11/2}$ Stark level and the highest energy $^4S_{3/2}$ Stark level determined from the luminescence spectra (ΔE = 720 cm^{-1}).

Table 6.10 presents the upconversion decay times for bulk and nanocrystalline $Lu_2O_3:Er^{3+}$ as a function of temperature. We observe that for the $^4F_{9/2}$ and $^4S_{3/2}$ states in both bulk and nanocrystalline samples, the decay times lengthen as the temperature is decreased. However, there is a difference in the behavior of the decay times for the bulk and nanocrystalline samples as a function of temperature. For the bulk sample, the $^4S_{3/2}$ level decay times decrease more rapidly on increasing the temperature with respect to the $^4F_{9/2}$ level. This is different from the nanocrystalline sample in which this behavior is not observed (see Table 6.10). W_{MPR} is temperature dependent and thus, as the temperature is raised, W_{MPR} would increase thus increasing the total rate of depopulation (W) and lowering the observed decay time, where $\tau = W^{-1}$ (see eqns. 6.2.1 and 6.3.1-6.3.2). If we consider the energy gap between the $^4S_{3/2}$ and $^4F_{9/2}$ levels to be about 3000 cm^{-1} and thus allowing for 5 maximum energy phonons to participate in the non-radiative relaxation, then the variation in the decay time of the $^4S_{3/2}$ level is not well explained by eqn. 6.3.1 alone. In fact, the thermalization of the $^2H_{11/2}$ level by the $^4S_{3/2}$ level is also involved in determining the observed behavior of the decay times, as the radiative lifetime of the upper lying state ($^2H_{11/2}$) is distinctly shorter than the one of the lower level ($^4S_{3/2}$) [105]. Therefore, it is expected that the lowering of the temperature induces the depopulation of the short lived $^2H_{11/2}$ level and consequently an increase of the observed decay time. In the present case, both mechanisms are active; the relatively high number of phonons required for the multiphonon relaxation probably makes the thermalization process more important. Also of note is the variation, with temperature, of the emission from the $^4F_{9/2}$ level. On passing from room to lower temperature, the $^4F_{9/2}$ level is populated by a weaker multiphonon relaxation from the $^4S_{3/2}$ level above. Since the energy gap between

the $^4F_{9/2}$ level and the next lower $^4I_{9/2}$ level is about 2500 cm^{-1}, and if the intrinsic decay rate of the $^4F_{9/2}$ is higher than that of the thermalized $^4S_{3/2}$ level, then the multiphonon relaxation from the $^4S_{3/2}$ level will be the bottleneck, causing the decay times from both levels to be identical. The longer observed decay time from the $^4F_{9/2}$ level may reflect a weaker decay rate from this level.

Table 6.10: Decay times for bulk and nanocrystalline $Lu_2O_3:Er^{3+}$ for the $^4S_{3/2} \rightarrow {}^4I_{15/2}$ and $^4F_{9/2} \rightarrow {}^4I_{15/2}$ transitions upon 980 nm excitation at various temperatures.

Temperature (K)	Decay Time (μs)			
	$^4S_{3/2} \rightarrow {}^4I_{15/2}$		$^4F_{9/2} \rightarrow {}^4I_{15/2}$	
	Bulk	Nanocrystal	Bulk	Nanocrystal
77	414	447	423	692
100	372	406	415	664
130	349	393	409	628
160	311	381	400	575
190	277	353	389	553
220	254	339	373	540
250	226	266	352	450
298	190	246	334	315

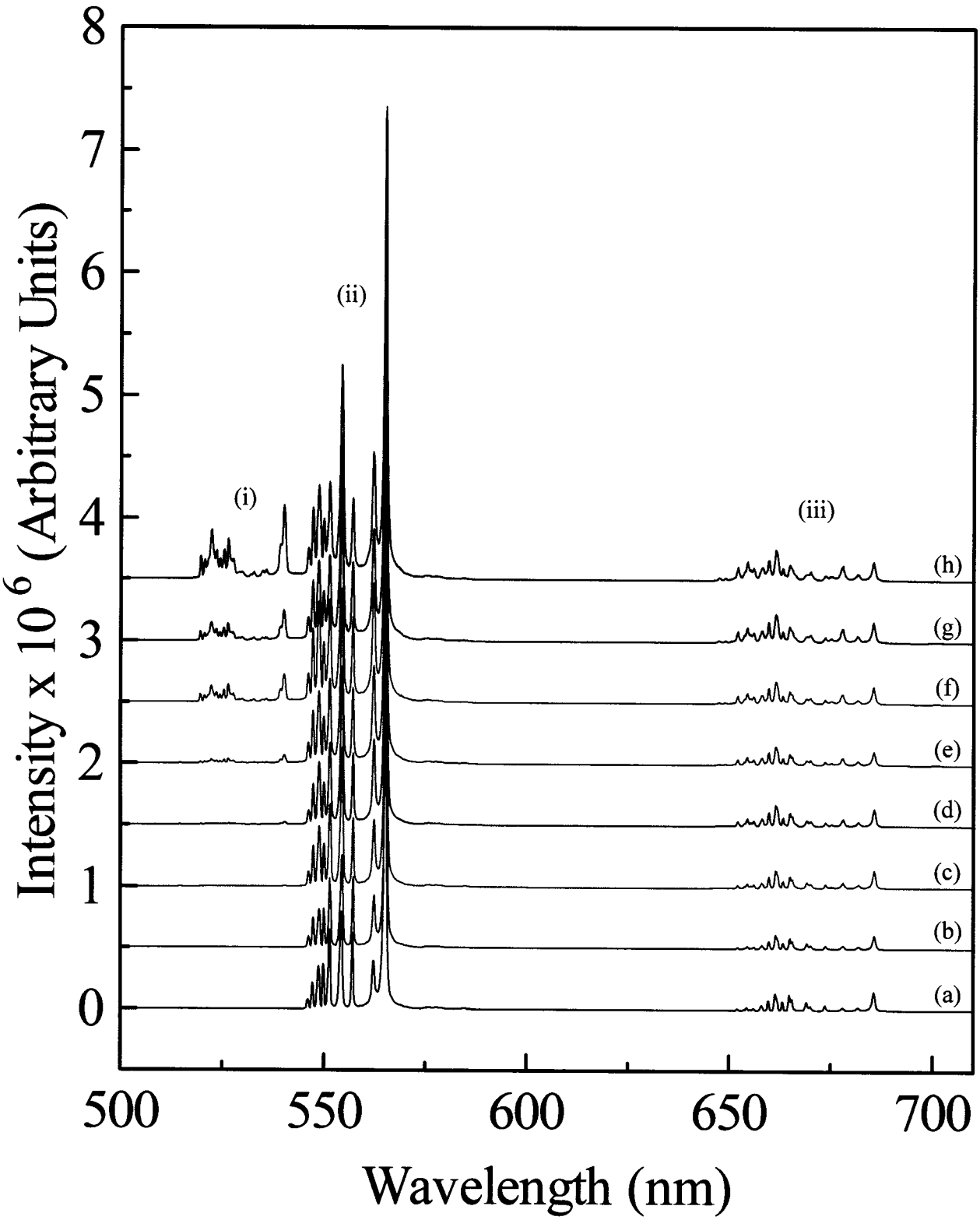

Figure 6.56: Upconversion luminescence spectra of nanocrystalline $Lu_2O_3:Er^{3+}$ at different temperatures (λ_{exc} = 980 nm): (a) 77 K, (b) 100 K, (c) 130 K, (d) 160 K, (e) 190 K, (f) 220 K, (g) 250 K, (h) 298 K. (i) $^2H_{11/2} \rightarrow {}^4I_{15/2}$ (ii) $^4S_{3/2} \rightarrow {}^4I_{15/2}$ (iii) $^4F_{9/2} \rightarrow {}^4I_{15/2}$. The intensities of emission are normalized to green ($^4S_{3/2} \rightarrow {}^4I_{15/2}$) transition.

6.4. Comparative Analysis of the Upconversion (Anti-Stokes) Emission of Nanocrystalline $Sc_2O_3:Er^{3+}$

The rationale for studying Sc_2O_3 stems from the fact that while it is isostructural to cubic Y_2O_3, its lattice constant is smaller. Moreover, the Sc^{3+} ion is much smaller than Y^{3+}, which induces a stronger crystal field and a larger Stark splitting of the multiplets.

6.4.1. Stokes (λ_{exc} = 488 nm) and Anti-Stokes Emission Spectroscopy of $Sc_2O_3:Er^{3+}$ Nanocrystals (λ_{exc} = 980 nm)

The Stokes luminescence spectra of the $Sc_2O_3:Er^{3+}$ nanocrystal samples under investigation (0.1, 1 and 10 mol% Er^{3+}) are presented in Figure 6.57 following the direct excitation of the $^4F_{7/2}$ state with 488 nm. Green emission is observed between 515 and 580 nm and attributed to the $^2H_{11/2} \rightarrow {}^4I_{15/2}$ and $^4S_{3/2} \rightarrow {}^4I_{15/2}$ transitions centered at approximately 530 and 560 nm, respectively. Red emission, ascribed to the $^4F_{9/2} \rightarrow {}^4I_{15/2}$ transition, was observed between 640 – 700 nm. Furthermore, NIR emission (not shown) was observed between 780 and 880 nm from the $^4I_{9/2} \rightarrow {}^4I_{15/2}$ (centered at 800 nm) and $^4S_{3/2} \rightarrow {}^4I_{13/2}$ (centered at 860 nm) transitions.

Following continuous wave excitation with 980 nm into the $^4I_{11/2}$ intermediate excited state (approximately 10200 cm^{-1}), blue, green, and red upconverted emission was observed in all nanocrystalline $Sc_2O_3:Er^{3+}$ samples under investigation (Figure 6.58). A weak upconverted blue emission was observed centered at approximately 495 nm and occurs via the $^4F_{7/2} \rightarrow {}^4I_{15/2}$ transition. Upconversion emission in the green portion of the electromagnetic spectrum was observed between 515 and 580 nm and was ascribed to the transitions from the $^2H_{11/2}$ and $^4S_{3/2}$ excited states to the $^4I_{15/2}$ ground state and centered at

530 and 560 nm, respectively. Finally, red anti-Stokes emission was also observed centered at 670 nm from the $^4F_{9/2} \rightarrow {}^4I_{15/2}$ transition.

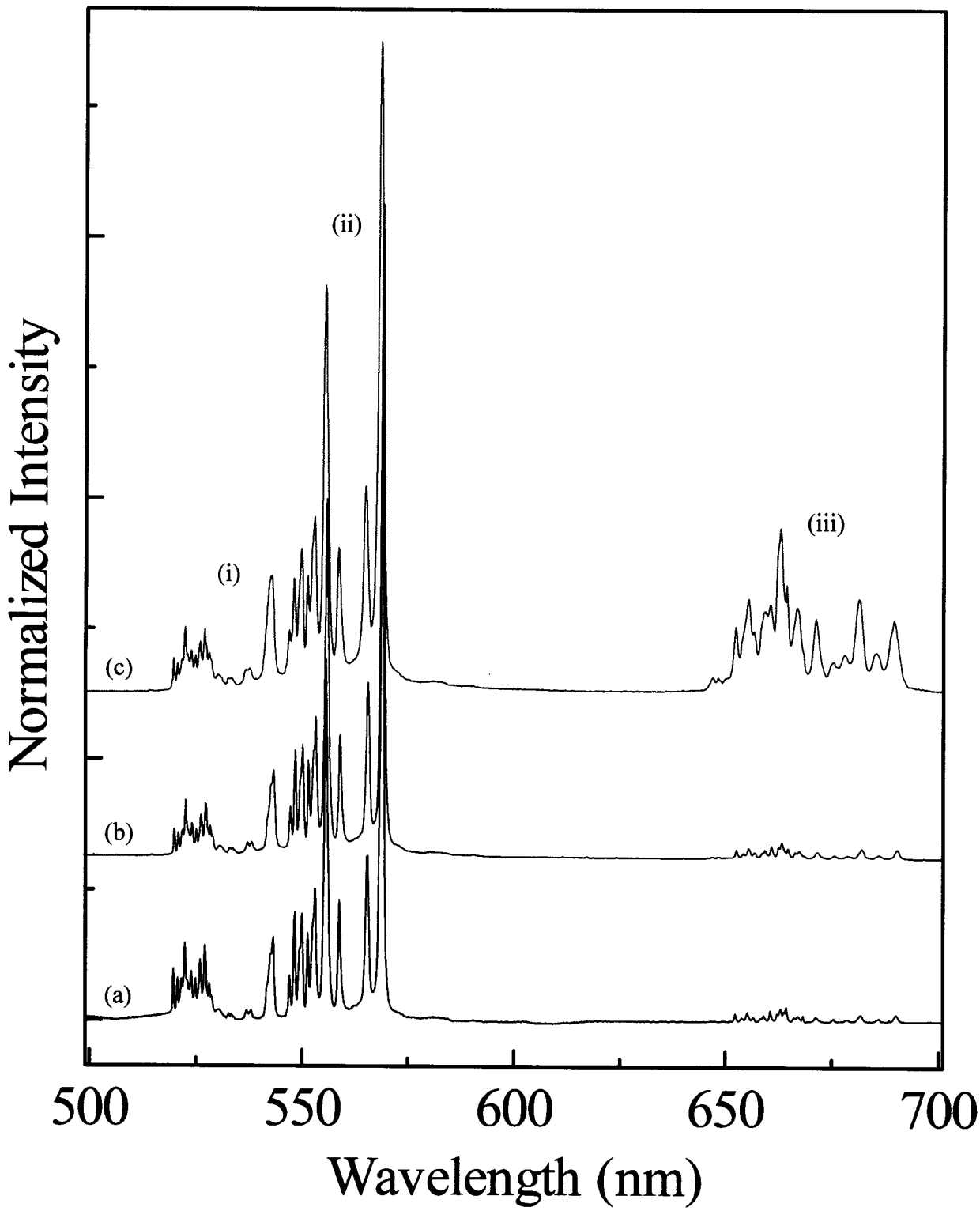

Figure 6.57: Stokes emission spectra of nanocrystalline Sc_2O_3 doped with (a) 0.1 mol%, (b) 1 mol%, (c) 10 mol% Er^{3+} following excitation with 488 nm. Shown are the (i) $^2H_{11/2} \rightarrow {}^4I_{15/2}$ (ii) $^4S_{3/2} \rightarrow {}^4I_{15/2}$ (iii) $^4F_{9/2} \rightarrow {}^4I_{15/2}$ transitions.

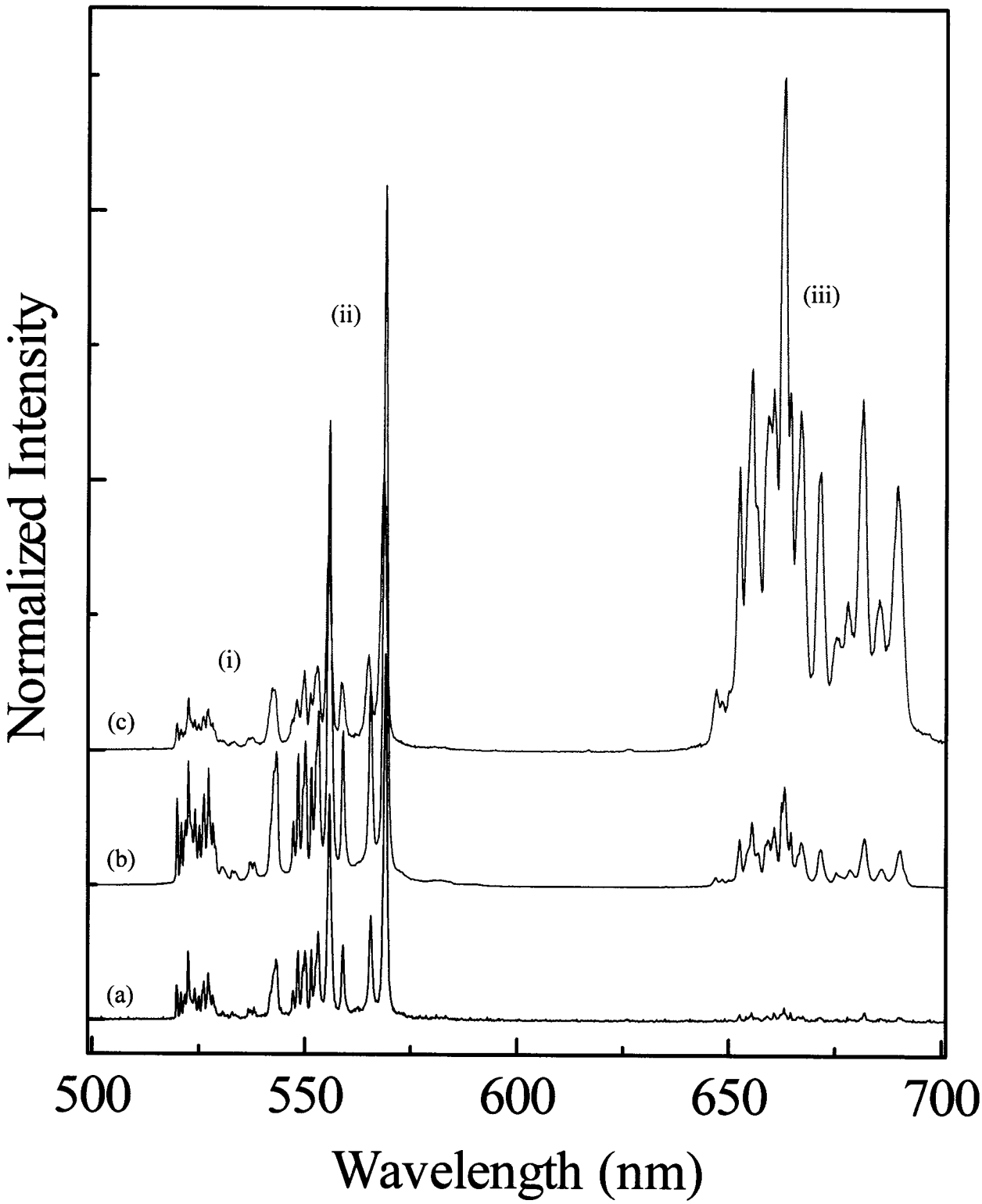

Figure 6.58: Upconversion emission spectra of nanocrystalline Sc_2O_3 doped with (a) 0.1 mol%, (b) 1 mol%, (c) 10 mol% Er^{3+} following excitation with 980 nm. Shown are the (i) $^2H_{11/2} \rightarrow {}^4I_{15/2}$ (ii) $^4S_{3/2} \rightarrow {}^4I_{15/2}$ (iii) $^4F_{9/2} \rightarrow {}^4I_{15/2}$ transitions.

6.4.2. Elucidation of the Mechanism of Upconversion – Power Study and Upconversion Decay Times

To fully elucidate the mechanisms responsible for the upconverted luminescence, a systematic study was undertaken. The first step was to perform an excitation power dependence study on the upconverted emission (Figure 6.59). From the plot of $\ln(I_{vis})$ versus $\ln(I_{NIR})$, we determined that $n = 2$ for all anti-Stokes transitions in all nanocrystalline samples under investigation and that PA was not the upconversion mechanism (Figure 6.59). Thus, the upper emitting levels are populated via an ESA or ETU two-photon upconversion process. In order to distinguish the two possible mechanisms (ESA and ETU), we obtained the decay curves following pumping with the upconversion wavelength (λ_{exc} = 980 nm) and compared them to the curves acquired following direct excitation of the $^4F_{7/2}$ state with 488 nm (Table 6.11).

Table 6.11: Effective decay time constants, τ_m, of the $^4S_{3/2}$ emitting state in $Sc_2O_3:Er^{3+}$ nanocrystals.

Er^{3+} Concentration (mol%)	Decay Time Constant (τ_m)	
	λ_{exc} = 488 nm	λ_{exc} = 980 nm
0.1	212	216
1	98	182
10	22	92

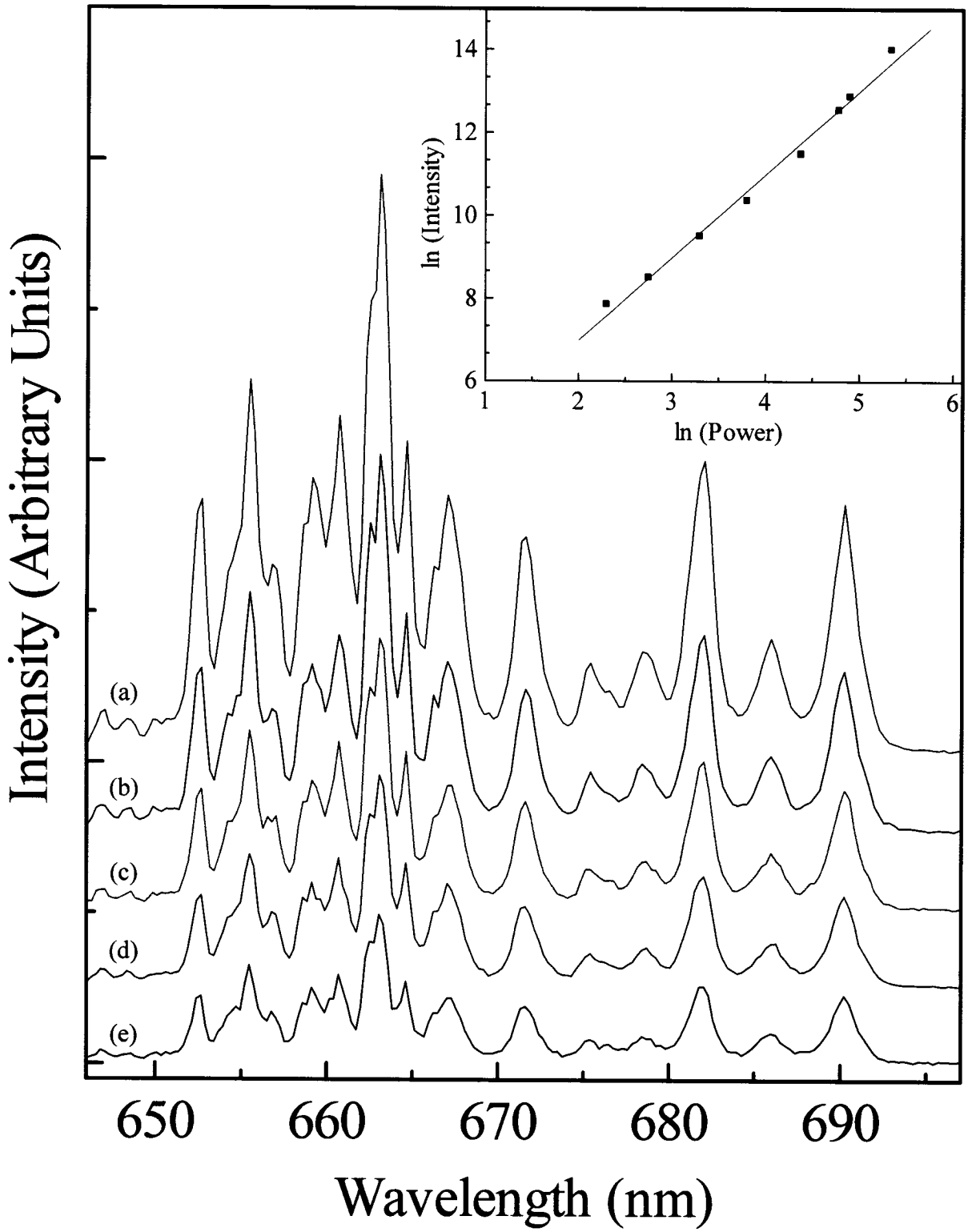

Figure 6.59: Power dependence study of the $^4F_{9/2} \rightarrow {}^4I_{15/2}$ upconverted emission following excitation with 980 nm. (a) 210 mW (b) 135 mW (c) 80 mW (d) 45 mw (e) 10 mW. Inset: Graph of ln (Intensity) versus ln (Power) (slope $n = 2$).

These results indicated that the dominant mechanism leading to the upconversion emission is dependent upon the Er^{3+} dopant concentration. In the 0.1 mol% nanocrystalline $Sc_2O_3:Er^{3+}$ sample, the decay curves at both wavelengths were single exponential and the obtained decay time constants after excitation with 488 or 980 nm were identical indicating that the upconversion is due only to excited state absorption. The ESA process consists of two sequential excitation steps in a single ion and thus, the decay times are not affected when pumping with an upconversion wavelength. In this mechanism (Figure 6.60), the Er^{3+} ion is excited from the ground state ($^4I_{15/2}$) to an intermediate excited state ($^4I_{11/2}$) following the absorption of a single 980 nm photon (ground state absorption, GSA). A second photon is subsequently and immediately absorbed, further exciting the ion from the intermediate excited state (population reservoir) to the upper excited state ($^4F_{7/2}$).

On the other hand, the decay curves of the 1 and 10 mol% nanocrystals demonstrated a deviation from single exponential behavior principally caused by ion-ion interactions at higher dopant concentrations. Thus, the effective decay time constants, τ_m, were determined. The results of the fit are presented in Table 6.11 and it is evident that we observe a lengthening of the decay times following excitation with 980 nm. This lengthening of the anti-Stokes decay times is a clear indication of the presence of energy transfer upconversion. In the ETU process (Figure 6.60), an ion excited to its intermediate state (population reservoir, $^4I_{11/2}$) transfers its energy to a neighboring ion in close proximity, also in its intermediate excited state ($^4I_{11/2}$). This further excites the ion to the upper excited state ($^4F_{7/2}$) while the initial ion decays non-radiatively to the ground state. In the presence of ETU, the observed decay times can be lengthened as they

depend on the lifetime of the excited state from which the energy transfer originates at the donor ion.

The efficiency of this mechanism is strongly dependent on the ion-ion distances and in turn on the concentration of the dopant. Thus, the probability that an Er^{3+} ion will interact with its neighbor strongly depends on the separation between the two ions [273]. If the critical distance is achieved, then the probability of the energy transfer is identical to the probability of the internal decay of the isolated donor. The critical distance is dependent upon a variety of factors and for a rare earth ion is on the order of 10 Å [274]. As the concentration of the RE^{3+} dopant increases, the average distance between ions decreases thus favoring the ETU mechanism. Moreover, the upconversion decay time lengthening is much more drastic in the 10 mol% nanocrystals indicating that ETU is the dominant mechanism in this sample. However, in the 1 mol% sample, it is most likely that a combination of both ESA and ETU mechanisms are responsible for populating the emitting states.

6.4.3. Enhancement of Red Emission ($^4F_{9/2} \rightarrow {}^4I_{15/2}$) – Comparison to $Y_2O_3:Er^{3+}$

As the upconversion spectra clearly demonstrate, the red emission ($^4F_{9/2} \rightarrow {}^4I_{15/2}$) shows an enhancement relative to the green emission ($^2H_{11/2}$, $^4S_{3/2} \rightarrow {}^4I_{15/2}$) as the concentration of Er^{3+} increases. For example, the upconversion spectrum of the 0.1 mol% nanocrystalline $Sc_2O_3:Er^{3+}$ shows a dominant green emission while in the 10 mol% sample, the red emission is most prominent. This enhancement of the red emission has been previously discussed in detail following excitation with 980 nm in $Y_2O_3:Er^{3+}$ and

$Y_2O_3:Er^{3+}$, Yb^{3+} nanocrystals [239, 249]. We proposed two distinct mechanisms, which were directly responsible for populating the $^4F_{9/2}$ level and bypassing the green emitting states ($^2H_{11/2}$ and $^4S_{3/2}$). Initially, it was proposed that a cross-relaxation mechanism of the type $^4F_{7/2} + {}^4I_{11/2} \rightarrow {}^4F_{9/2} + {}^4F_{9/2}$ could populate the $^4F_{9/2}$ state directly (Figure 6.60). In agreement with the experimental data, the efficiency of this process would increase with decreasing the average distance between Er^{3+} ions and thus with increasing erbium concentration [239]. In $Y_2O_3:Er^{3+}$, Yb^{3+} (1 mol% each of Er^{3+} and Yb^{3+}) we observed an even stronger enhancement of the red emission compared to the singly doped $Y_2O_3:Er^{3+}$ (10 mol%) nanocrystals. Furthermore, the red enhancement was much more pronounced in the $Y_2O_3:Er^{3+}$ nanocrystals compared to the identically doped bulk (microcrystalline) material allowing us to determine that an additional mechanism was active, which utilized the high energy phonons inherently present in the sesquioxide nanocrystalline material [249].

It is quite feasible that in the singly doped scandia nanocrystalline host, with sufficiently high Er^{3+} concentration, the following mechanism is also present to directly populate the $^4F_{9/2}$ state (see Figure 6.60). The 980 nm photons will excite two neighboring Er^{3+} ions to the $^4I_{11/2}$ state. Due to the presence of carbonate and hydroxyl ions on the particle surface providing high vibrational energies to the nanocrystalline lattice (1500 and 3350 cm^{-1}, respectively), one of the excited ions will quickly and efficiently decay non-radiatively to the $^4I_{13/2}$ state. The neighboring ion (in the $^4I_{11/2}$ state) will transfer its energy exciting it to the $^4F_{9/2}$ state. However, there is approximately 1600 cm^{-1} of excess energy, which is easily dissipated by the nanocrystal lattice to conserve energy [249]. This mechanism is much less probable in the bulk material as it possesses

only the intrinsic phonons of the sesquioxide host (maximum phonon energy about 600 cm^{-1}).

However, it should be noted that comparing identically doped (10 mol%) $Y_2O_3:Er^{3+}$ and $Sc_2O_3:Er^{3+}$ prepared by the same combustion synthesis, the red enhancement is much more pronounced in the scandia nanocrystals. We attribute this behavior to the difference of the average distances between the Er^{3+} ions in the host lattice. In fact, the ion distance d in a crystalline host can be estimated using the equation [275]:

$$d = \left(\frac{3}{4\pi N}\right)^{1/3} \qquad 6.4.1$$

where N is the ion density. From the X-ray diffraction results, it was determined that the 10 mol% Er^{3+} doped Sc_2O_3 nanocrystals under investigation had a unit cell volume (971.95 $Å^3$), which was smaller with respect to that of the isostructural 10 mol% Er^{3+} doped Y_2O_3 nanocrystalline material [191] (1193.38 $Å^3$). Then, considering the same 10 mol% dopant concentration for both sesquioxides, an Er^{3+} ion average distance of 4.47 and 4.17 Å results for the 10 mol% Er^{3+} doped Y_2O_3 and Sc_2O_3 nanocrystalline hosts, respectively, using eqn. 6.4.1. Therefore, shorter Er^{3+} - Er^{3+} distances will result in Sc_2O_3 compared to Y_2O_3. The shorter ion-ion distances will result in a much higher transfer probability between the Er^{3+} ions, which is dependent upon the sixth power of the inverse of the dopant distance (for dipole-dipole interactions) [140], and consequently, the red enhancement will be greater in $Sc_2O_3:Er^{3+}$ as both mechanisms responsible for populating the $^4F_{9/2}$ state will be more efficient.

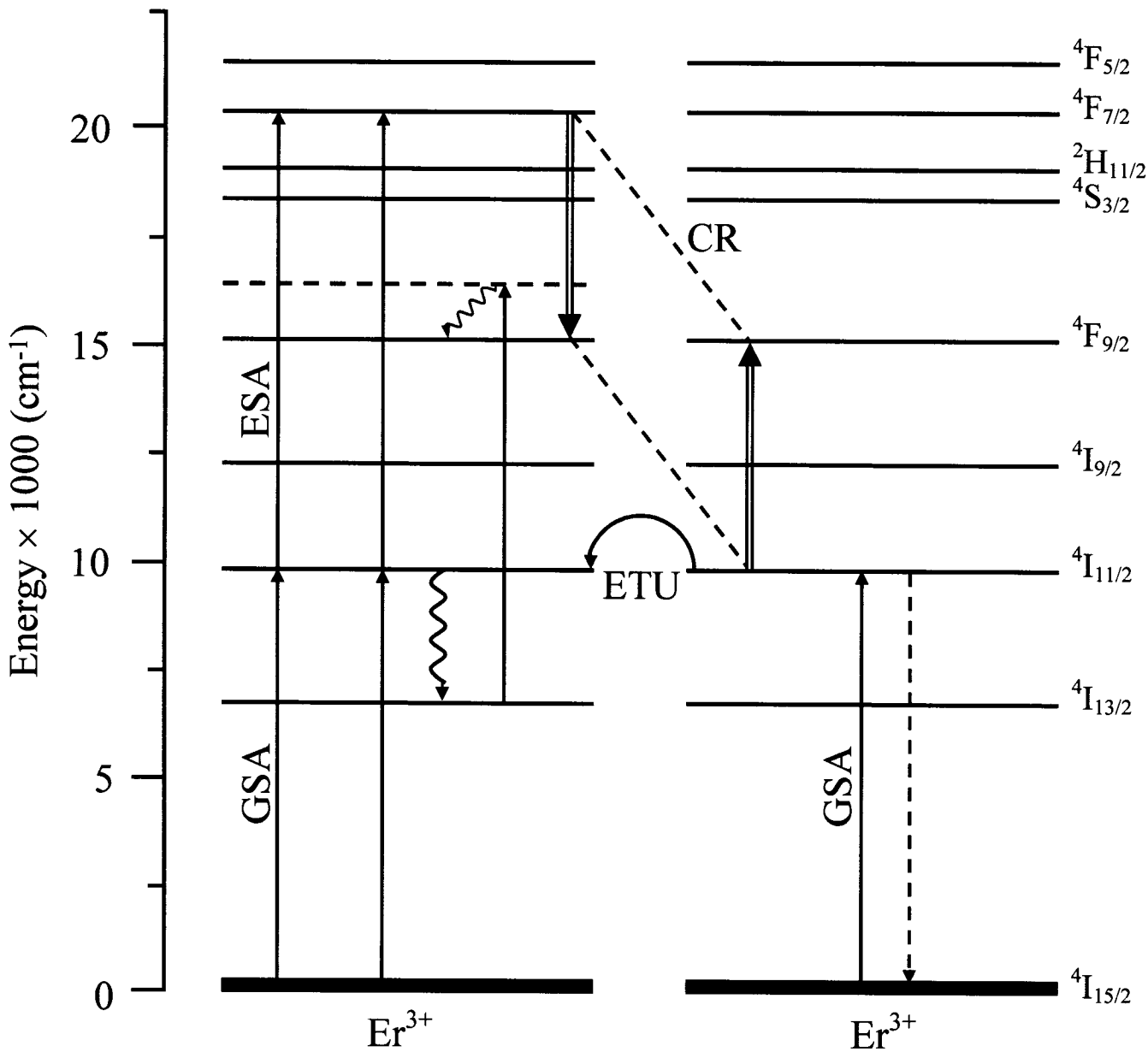

Figure 6.60: Schematic representation of the different mechanisms responsible for the anti-Stokes emission.

6.5. Luminescence Spectroscopy and NIR-to-Visible Upconversion of $Gd_3Ga_5O_{12}:Er^{3+}$ Nanocrystals

Other than yttrium aluminum garnet (YAG, $Y_3Al_5O_{12}$) [75, 206, 276, 277], very little work on rare earth doped nanocrystalline garnets has been done. Furthermore, existing work on the garnet nanocrystals has focused on the Stokes emission whereas the anti-Stokes (or upconversion) properties have been largely overlooked. Without doubt, the best known garnet is $Y_3Al_5O_{12}$ (YAG, yttrium aluminum garnet) however, $Gd_3Ga_5O_{12}$ (GGG, gadolinium gallium garnet) possesses several advantages [278, 279]. Thus, we investigate the optical properties of the ternary nanocrystalline $Gd_3Ga_5O_{12}:Er^{3+}$ oxide, focusing on the upconversion luminescence and compare it to the well known binary $Y_2O_3:Er^{3+}$ oxide.

6.5.1. Visible and NIR Emission in $Gd_3Ga_5O_{12}:Er^{3+}$ Nanocrystals (λ_{exc} = 488 nm)

Following the direct excitation of the $^4F_{7/2} \leftarrow {}^4I_{15/2}$ transition of the erbium ion with 488 nm, green, red, and NIR emission was observed in nanocrystalline gadolinium gallium garnet doped with 1 and 5 mol% Er^{3+} (Figure 6.61). Green emission was observed between 510-580 nm and was ascribed to the transition from the thermalized $^2H_{11/2}$, $^4S_{3/2}$ excited states to the $^4I_{15/2}$ ground state. Red emission between 630-700 nm was observed and attributed to the $^4F_{9/2} \rightarrow {}^4I_{15/2}$ transition. The shape of the emission bands of the $^4S_{3/2} \rightarrow {}^4I_{15/2}$ and $^4F_{9/2} \rightarrow {}^4I_{15/2}$ transitions were identical to those published previously on $GGG:Er^{3+}$ single crystals [244]. Furthermore, NIR emission was observed from the $^4I_{9/2} \rightarrow {}^4I_{15/2}$ transition between 780-820 nm and from the $^4S_{3/2} \rightarrow {}^4I_{13/2}$ transition between 830-870 nm (Figure 6.61, inset). Similarly, NIR emission was also observed

between 900-1075 nm and from 1400-1700 nm ascribed to the transitions from the $^4I_{11/2}$ and $^4I_{13/2}$ excited states to the $^4I_{15/2}$ ground state as well as a very weak emission from the $^4S_{3/2} \rightarrow {}^4I_{11/2}$ transition between 1225-1275 nm (Figure 6.62). As can be seen from Figures 6.61 and 6.62, the overall Stark structures of the emission bands in the 1 and 5 mol% samples are identical.

In previous studies on Er^{3+} doped nanocrystalline cubic sesquioxides (Y_2O_3 and Lu_2O_3) prepared using a similar synthesis procedure, we showed that the medium infrared (MIR) spectra of the nanocrystals contained intense bands centered around 1500 and 3350 cm^{-1}, which were assigned to vibrations from the CO_3^{2-} and OH^- species present on the particle surface [233, 238, 265]. The emission intensity from the $(^2H_{11/2}, {}^4S_{3/2}) \rightarrow {}^4I_{15/2}$ and $^4F_{9/2} \rightarrow {}^4I_{15/2}$ transitions in the nanocrystalline material was significantly lower than the bulk material, where no bands were observed in the MIR spectra. The reduction in intensity was attributed to an increase in the non-radiative decay from the emitting states as it is well known that an increase in the effective phonon energy of the material will have the resultant effect of increasing the rate of multiphonon relaxation (W_{MPR}) [106]. Interestingly enough as can be seen from Figure 6.63, the MIR spectrum of nanocrystalline $Gd_3Ga_5O_{12}:Er^{3+}$ shows that the bands at 1500 and 3350 cm^{-1} are significantly reduced compared to the Eu^{3+} and Er^{3+} doped Y_2O_3 nanocrystals, for example. This has the desired effect of considerably increasing the luminescence efficiency of nanocrystalline GGG:Er^{3+} in comparison to either $Y_2O_3:Er^{3+}$ or $Lu_2O_3:Er^{3+}$ nanocrystals.

The decay times following excitation with 488 nm, are presented in Table 6.12. The decay curves for the 1 mol% nanocrystalline GGG:Er^{3+} were exponential and thus

could be fit with a single exponential model. However, when the concentration of Er^{3+} was increased to 5 mol%, the decay curves deviated from single exponentiality. At low erbium ion concentrations, the Er^{3+} – Er^{3+} interactions are negligible and as a result, the decay curves will be exponential. At higher Er^{3+} concentrations, the ion-ion interactions increase and thus the interactions between dopant ions become more prominent. These ion-ion interactions causes the observed deviation from exponentiality in the 5 mol% GGG:Er^{3+} sample and the degree of non-exponentiality increases with increasing dopant concentration. Therefore, fitting the decay curves of the 5 mol% sample with a single exponential function was no longer a valid option and we determined the emission decay time constant, τ_m, using the model proposed by Nakazawa [246]. As seen from Table 6.12, the decay times for the more heavily doped sample are considerably shorter in comparison to the more weakly doped sample. In the 5 mol% sample the dynamics become influenced by the aforementioned energy transfer processes which makes the decay time shorter [280].

Table 6.12: Decay times of nanocrystalline GGG:Er^{3+} following excitation with 488 nm. In the case of the 5 mol% doped sample, the values of the decay time constant, τ_m, are reported.

Transition	Nanocrystalline $Gd_3Ga_5O_{12}:Er^{3+}$ Decay Times (μs)	
	1 mol% Er^{3+}	5 mol% Er^{3+}
$^2H_{11/2} \rightarrow {}^4I_{15/2}$	122	89
$^4S_{3/2} \rightarrow {}^4I_{15/2}$	123	81
$^4F_{9/2} \rightarrow {}^4I_{15/2}$	117	58
$^4S_{3/2} \rightarrow {}^4I_{13/2}$	113	81

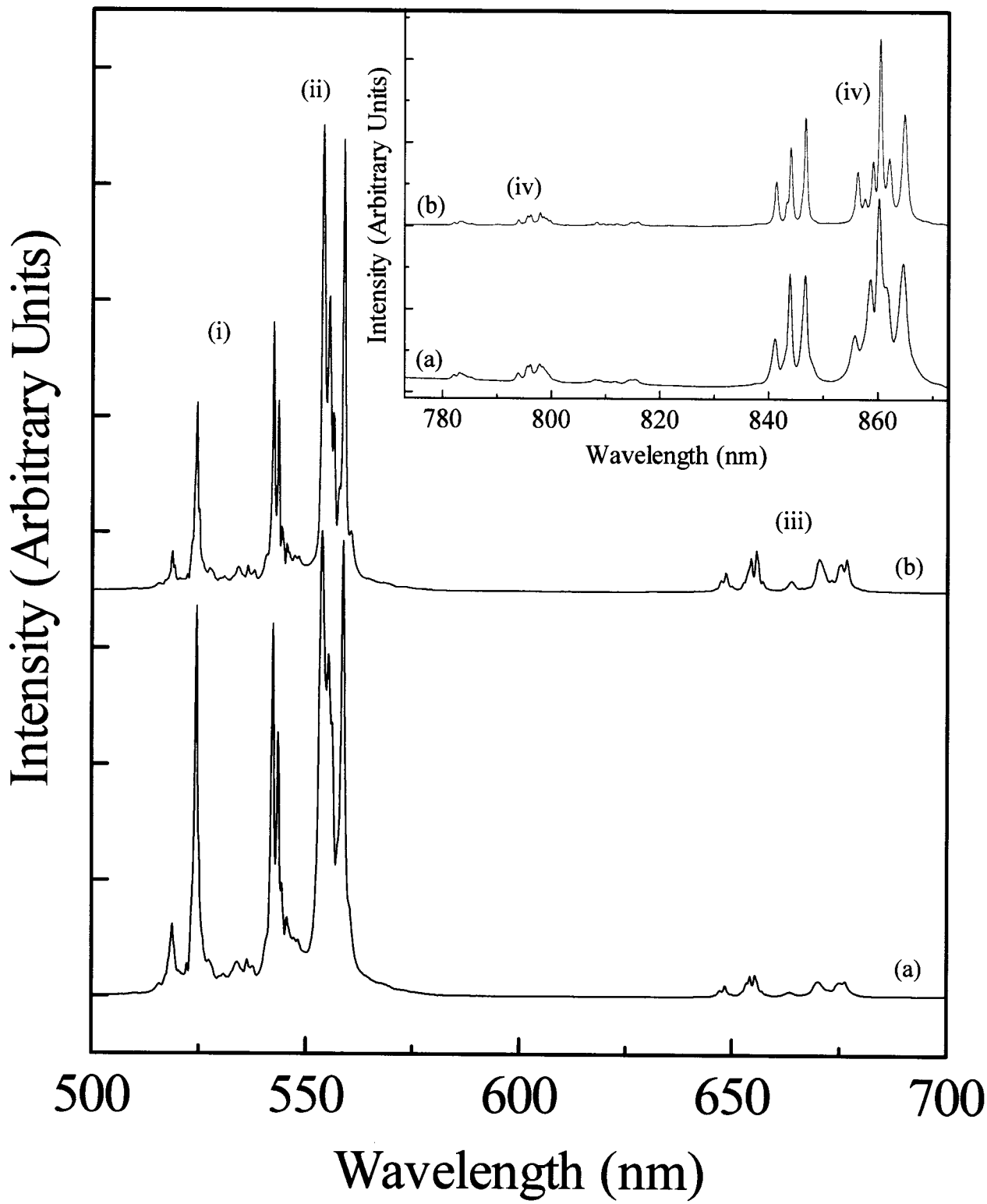

Figure 6.61: Emission spectrum of nanocrystalline GGG:Er^{3+} doped with (a) 1 mol% and (b) 5 mol% Er^{3+} following excitation with 488 nm and showing the following transitions: (i) $^2H_{11/2} \rightarrow {}^4I_{15/2}$ (ii) $^4S_{3/2} \rightarrow {}^4I_{15/2}$ (iii) $^4F_{9/2} \rightarrow {}^4I_{15/2}$. Inset: (iv) $^4I_{9/2} \rightarrow {}^4I_{15/2}$ (v) $^4S_{3/2} \rightarrow {}^4I_{13/2}$.

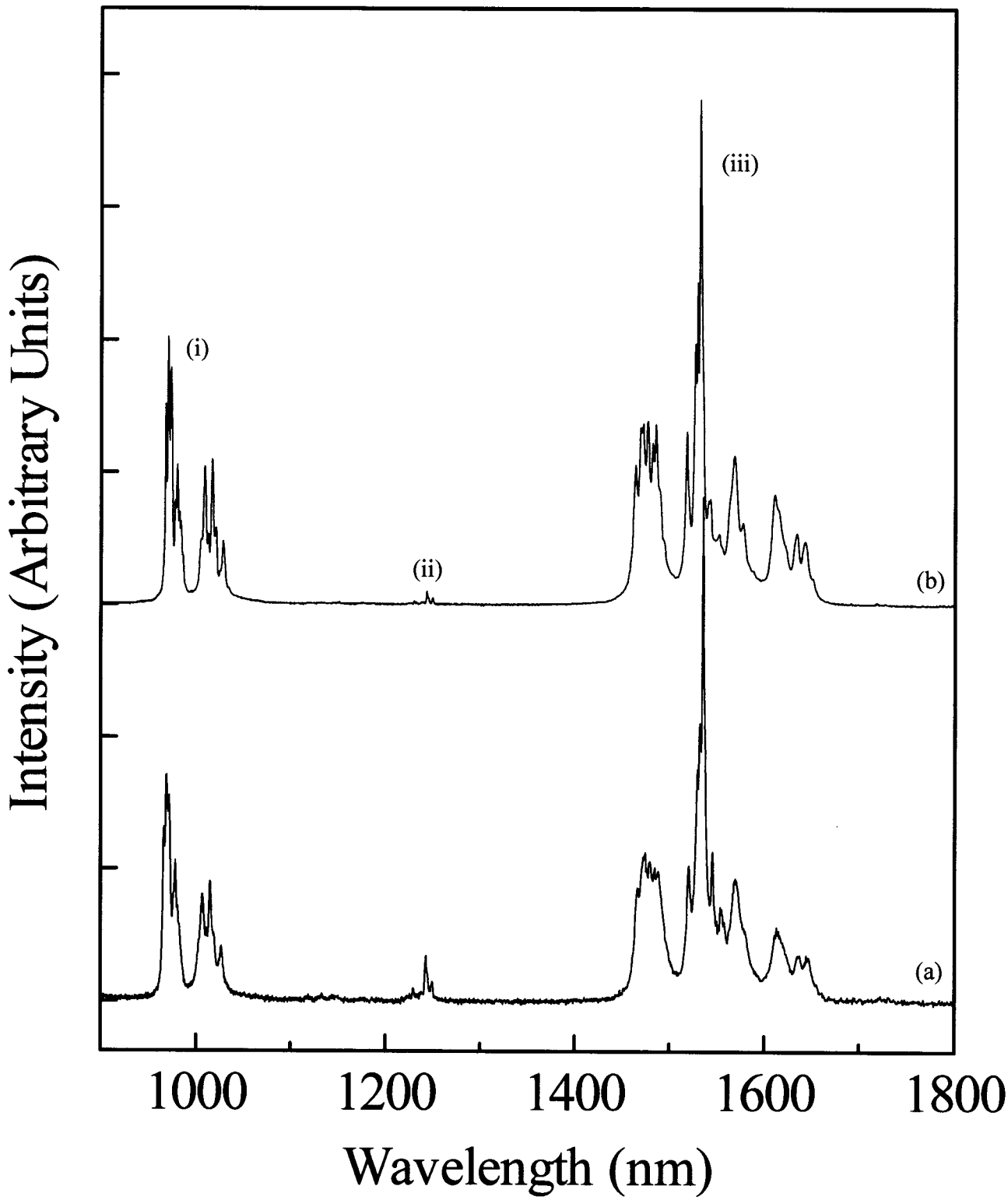

Figure 6.62: NIR emission spectrum of nanocrystalline GGG:Er^{3+} doped with (a) 1 mol% and (b) 5 mol% Er^{3+} following excitation with 488 nm and showing the following transitions: (i) $^4I_{11/2} \rightarrow {}^4I_{15/2}$ (ii) $^4S_{3/2} \rightarrow {}^4I_{11/2}$ (iii) $^4I_{13/2} \rightarrow {}^4I_{15/2}$.

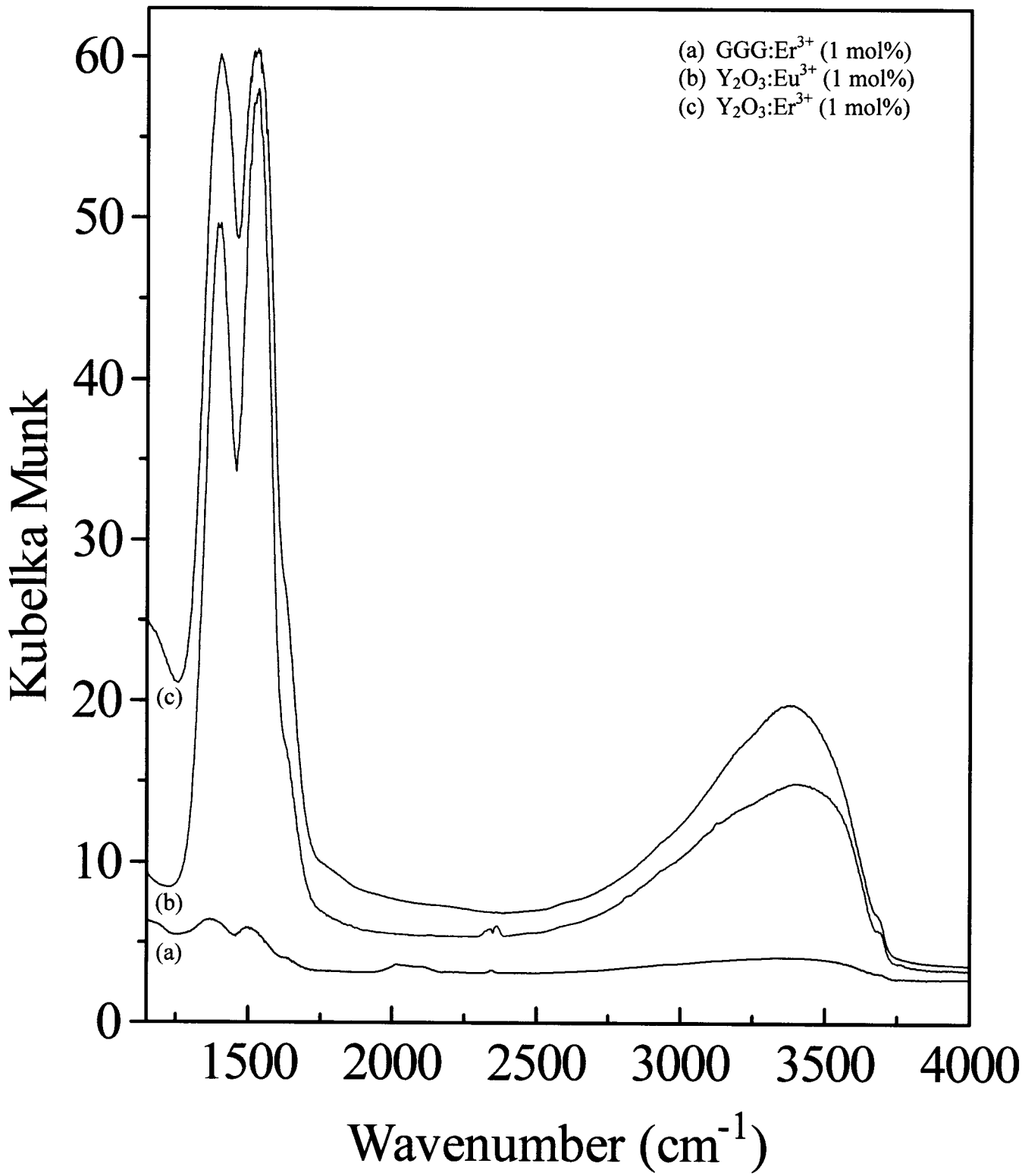

Figure 6.63: Medium-Infrared (MIR) reflectance spectra of nanocrystalline (a) GGG:Er 1 mol%, (b) Y_2O_3:Eu 1 mol%, and (c) Y_2O_3:Er 1 mol%.

6.5.2. Efficient NIR-to-Visible Upconversion in GGG:Er^{3+} Nanocrystals (λ_{exc} = 800 nm)

Following excitation of the $^4I_{9/2} \leftarrow {}^4I_{15/2}$ transition using 800 nm radiation, intense upconverted emission was observed in both 1 and 5 mol% nanocrystalline GGG:Er^{3+} samples (Figure 6.64). Green emission from the thermalized ($^2H_{11/2}$, $^4S_{3/2}$) $\rightarrow$ $^4I_{15/2}$ transition and red emission from the $^4F_{9/2} \rightarrow {}^4I_{15/2}$ transition was observed centered at approximately 540 and 660 nm, respectively. Similarly, a relatively weak blue emission assigned to the transition from the $^4F_{7/2}$ excited state to the $^4I_{15/2}$ ground state was observed centered at approximately 492 nm (Figure 6.64, inset). It is worth mentioning that the visually dominant green emission was still observed when pumping with < 5 mW of excitation power.

In order to obtain a better understanding of the process of upconversion, a power dependence study of the upconverted emission intensity was performed (Figure 6.65). Fitting the data to a straight line yielded slopes of approximately 2 for the ($^2H_{11/2}$, $^4S_{3/2}$) $\rightarrow$ $^4I_{15/2}$ and $^4F_{9/2} \rightarrow {}^4I_{15/2}$ transitions for both 1 and 5 mol% GGG:Er^{3+} nanocrystal samples (Figure 6.65, inset) therefore indicating that the upconversion process was achieved via a two-photon process. Since no inflection point was observed in the graph of $\ln(I_i)$ versus $\ln(I_o)$, PA was discounted as a mechanism of upconversion thus indicating that it could occur via ESA or ETU mechanisms. Table 6.12 presents the decay times of $Gd_3Ga_5O_{12}$:Er^{3+} (1 and 5 mol%) following excitation with 800 nm. As with the decay times obtained following 488 nm excitation, the upconverted decay curves of the 5 mol% sample deviated from exponentiality. It is worth mentioning that the decay times in the 1 mol% sample were identical at both pumping wavelengths. However in the 5 mol%

sample, the decay times obtained following excitation with 800 nm were lengthened compared to those obtained following direct excitation (λ_{exc} = 488 nm). This decay lengthening is a clear indication of the presence of ETU.

Table 6.13: Decay times of nanocrystalline GGG:Er^{3+} following excitation with 800 nm. In the case of the 5 mol% doped sample, the values of the decay time constant, τ_m, are reported.

Transition	Nanocrystalline $Gd_3Ga_5O_{12}:Er^{3+}$ Decay Times (μs)	
	1 mol% Er^{3+}	5 mol% Er^{3+}
$^2H_{11/2} \rightarrow {}^4I_{15/2}$	119	172
$^4S_{3/2} \rightarrow {}^4I_{15/2}$	123	167
$^4F_{9/2} \rightarrow {}^4I_{15/2}$	117	830

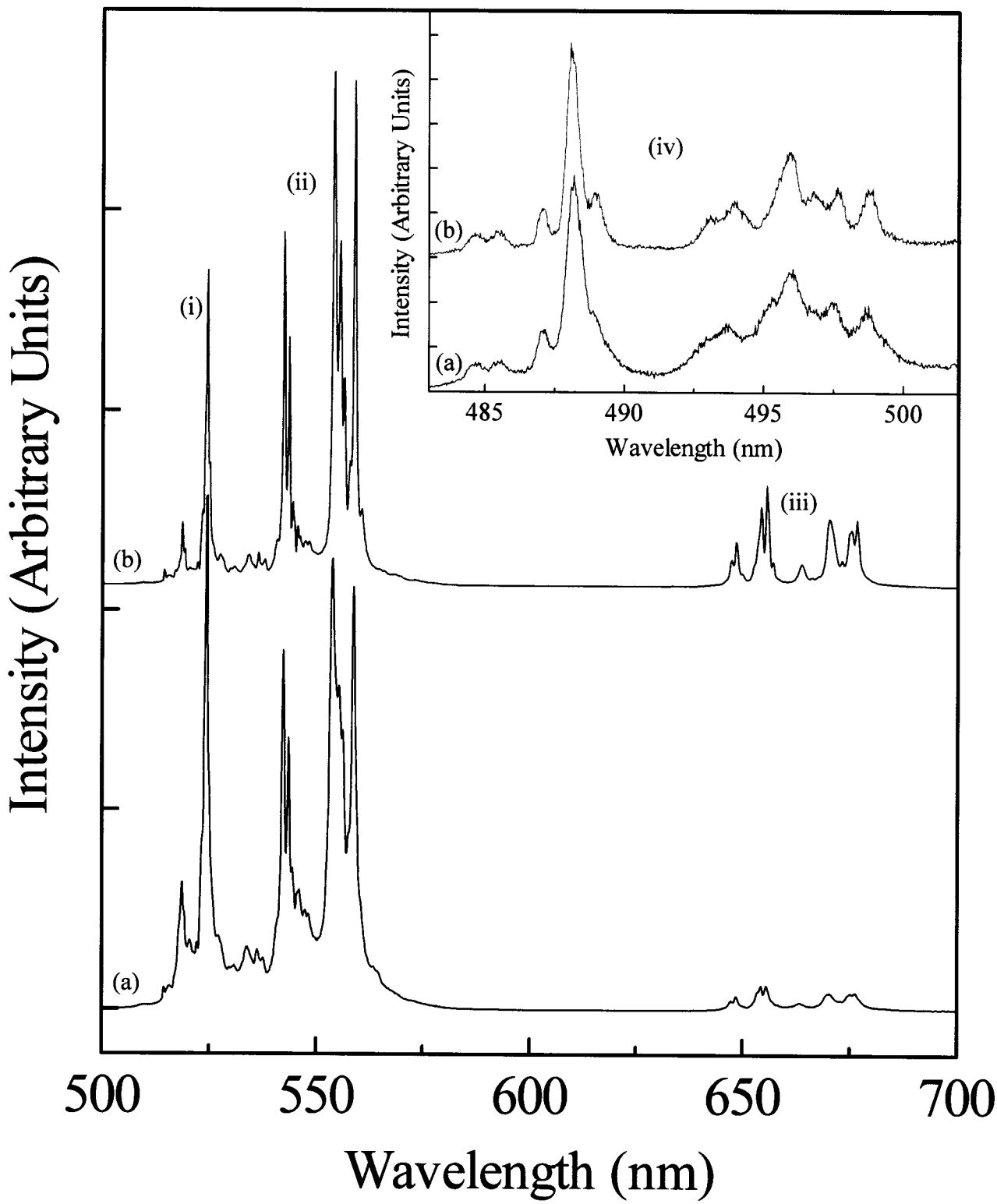

Figure 6.64: Upconversion spectrum of nanocrystalline gadolinium gallium garnet doped with (a) 1 mol% and (b) 5 mol% Er^{3+} following excitation with 800 nm and showing the following transitions: (i) $^2H_{11/2} \rightarrow {}^4I_{15/2}$ (ii) $^4S_{3/2} \rightarrow {}^4I_{15/2}$ (iii) $^4F_{9/2} \rightarrow {}^4I_{15/2}$. Inset: (iii) $^4F_{7/2} \rightarrow {}^4I_{15/2}$.

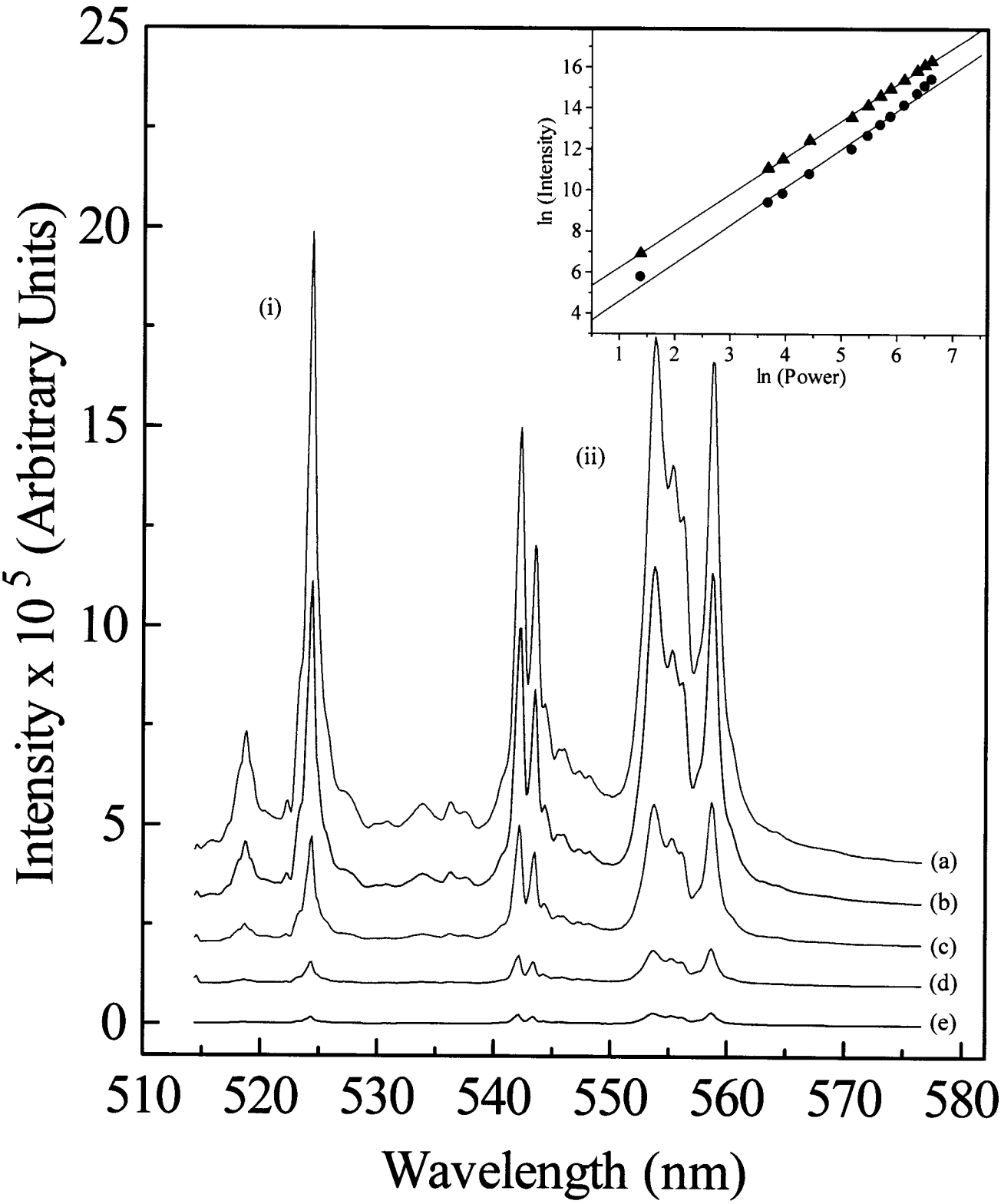

Figure 6.65: Power dependence of the upconverted (i) $^2H_{11/2} \rightarrow {}^4I_{15/2}$ and (ii) $^4S_{3/2} \rightarrow {}^4I_{15/2}$ emission in nanocrystalline gadolinium gallium garnet doped 1 mol% Er^{3+} following excitation with 800 nm. (a) 750 mW (b) 580 mW (c) 360 mW (d) 180 mW (e) 84 mW. Inset: Graph of $\ln(I_i)$ versus $\ln(I_o)$ yielding slopes of approximately 2 for both transitions

From the upconversion decay times, it is clear that excited state absorption is the dominant mechanism in the nanocrystalline 1 mol% GGG:Er^{3+} sample (Figure 6.66). In this process, an 800 nm photon from the pump beam excites the ion to the $^4I_{9/2}$ excited state. However, rapid multiphonon relaxation from $^4I_{9/2}$ to $^4I_{11/2}$ is a property common to all fluorides and oxides [281, 282] and thus, the resonant $^2H_{9/2} \leftarrow {}^4I_{9/2}$ transition, which occurs following absorption of a second photon, is not the most probable forcing us to consider alternate upconversion pathways. Therefore, once the ion is excited to the $^4I_{9/2}$ intermediate level, it will non-radiatively decay to the $^4I_{11/2}$ state. A second photon from the pump beam will then excite the Er^{3+} ion to the $^4F_{3/2}$ state. Non-radiative relaxation in turn populates the lower emitting states. Alternately, the ion can decay non-radiatively to the $^4I_{13/2}$ state and a second 800 nm photon will populate the $^2H_{11/2}$ state. The upconverted emission is then observed from this and the lower emitting states.

As evidenced by the decay time lengthening following excitation with 800 nm, energy transfer upconversion becomes more efficient and thus is presumably the dominant mechanism in the 5 mol% nanocrystalline sample (Figure 6.66). In this process, two Er^{3+} ions in close proximity are excited to the $^4I_{9/2}$ intermediate state following absorption of 800 nm radiation. One Er^{3+} ion non-radiatively decays to the $^4I_{11/2}$ state and is excited to the $^4F_{3/2}$ state via the transfer of energy from the neighboring Er^{3+} ion in the $^4I_{9/2}$ state, which then returns to the $^4I_{15/2}$ ground state. Alternatively, the initial ion can decay to the $^4I_{13/2}$ state and following energy transfer from another ion in the $^4I_{9/2}$ state, the $^2H_{11/2}$ level is populated. Upconverted emission is subsequently observed from this and the lower lying excited states.

We notice from the upconversion spectra, which are normalized to the green ($^2H_{11/2}$, $^4S_{3/2} \rightarrow {}^4I_{15/2}$) transition, that the ($^4F_{9/2} \rightarrow {}^4I_{15/2}$) transition is more intense in the 5 mol% nanocrystalline GGG:Er^{3+} sample. If the ESA and ETU mechanisms described earlier are the only processes operative, we would expect the green ($^2H_{11/2}$, $^4S_{3/2}$) $\rightarrow {}^4I_{15/2}$ and red $^4F_{9/2} \rightarrow {}^4I_{15/2}$ transitions in the upconversion spectrum to have identical relative intensities as in the direct emission (λ_{exc} = 488 nm) spectrum. However, this is not the case as the intensity of the $^4F_{9/2} \rightarrow {}^4I_{15/2}$ transition grows at a more rapid rate than the green ($^2H_{11/2}$, $^4S_{3/2}$) $\rightarrow {}^4I_{15/2}$ transition. We similarly observed an enhancement of the red $^4F_{9/2} \rightarrow {}^4I_{15/2}$ emission in Y_2O_3:Er^{3+} nanocrystals (1, 2, 5, and 10 mol%) synthesized by identical techniques. Chen et al. [244] studied the upconversion properties of single crystal $Gd_3Ga_5O_{12}$ doped with 1, 10, and 30 % Er^{3+} following excitation with 790 nm from a semiconductor diode. They observed that when the GGG:Er^{3+} single crystals were pumped with 790 nm, both the green and red upconverted emission became much more intense with increasing concentration of erbium ions. However, they also observed that the red emission became stronger by a greater factor than the green emission. Thus, it was postulated that a second mechanism was responsible for populating the $^4F_{9/2}$ level only. In 5 mol% nanocrystalline $Gd_3Ga_5O_{12}$:Er^{3+}, it is therefore probable that an additional mechanism is operative, which directly populates the $^4F_{9/2}$ state. In this mechanism, 800 nm photons excite two neighboring ions in close proximity to the $^4I_{9/2}$ level followed by the quick non-radiative decay of one of the ions to the $^4I_{11/2}$ state. Since the energy gap from this state to the $^4F_{9/2}$ level is identical to the gap from the intermediate $^4I_{9/2}$ state to the $^4I_{13/2}$ level, the two ions undergo an ion-pair process of the type; ($^4I_{9/2}$, $^4I_{11/2}$) $\rightarrow$ ($^4I_{13/2}$, $^4F_{9/2}$). This additional upconversion mechanism is wholly

responsible for populating the $^4F_{9/2}$ level and results in the observed phenomenon of $^4F_{9/2} \rightarrow {}^4I_{15/2}$ emission enhancement (Figure 6.66). Moreover, the upconverted decay time of the $^4F_{9/2}$ excited state in the 5 mol% nanocrystal sample is severely lengthened compared to the decay obtained with 488 nm excitation (830 μs compared to 58 μs). This is indicative of the presence of a very efficient energy transfer process and clearly illustrates that the mechanism responsible for the enhancement of the red emission is a highly concentration dependent process.

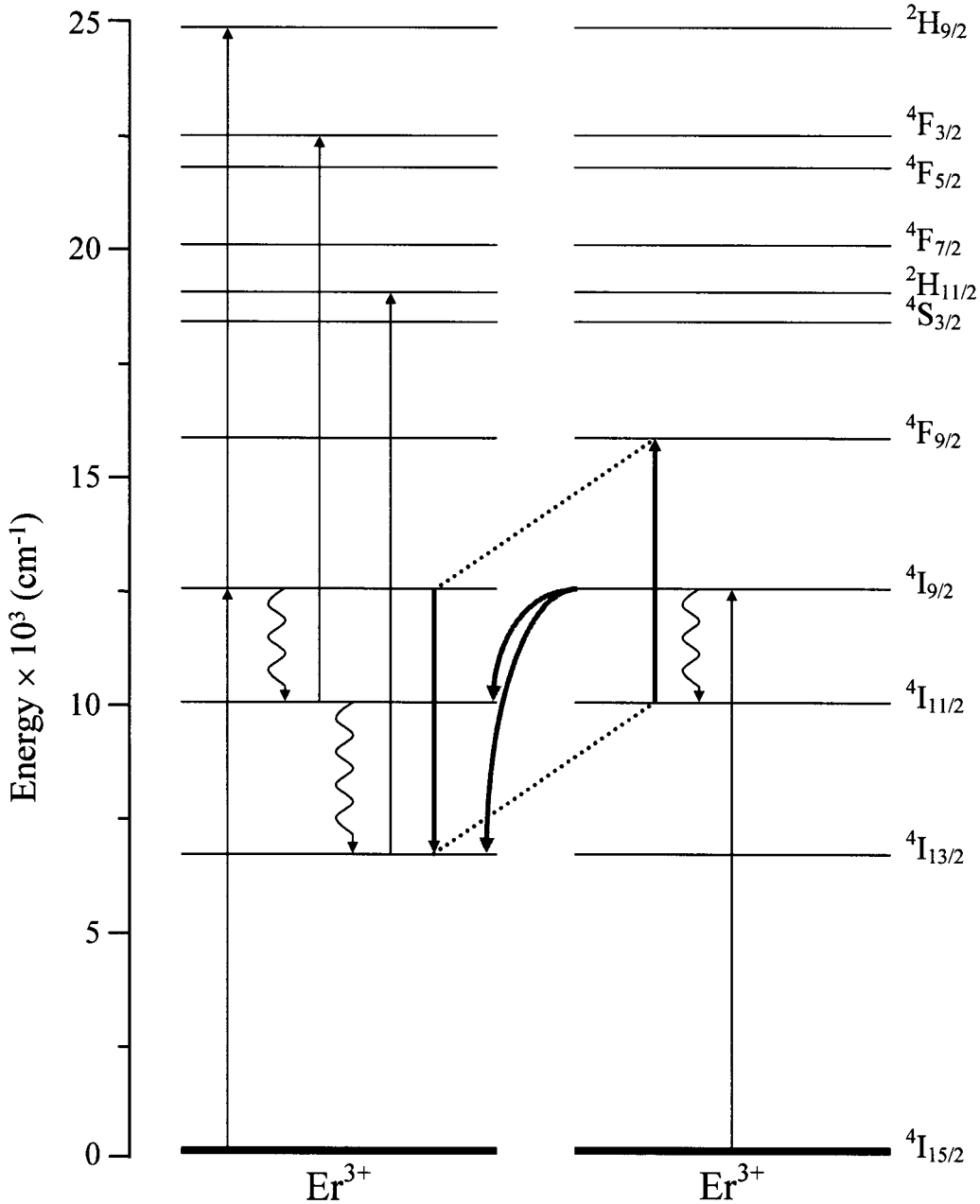

Figure 6.66: Diagram showing the excited state absorption and energy transfer upconversion mechanisms in nanocrystalline GGG:Er^{3+} following excitation with 800 nm into the $^4I_{9/2}$ state. Also shown is the ($^4I_{9/2}$, $^4I_{11/2}$) → ($^4I_{13/2}$, $^4F_{9/2}$) ion pair process responsible for $^4F_{9/2}$ state.

6.6. Laser Spectroscopy of Sesquioxide Nanocrystals Doped With Other Rare Earth Ions

The spectroscopic properties of other nanocrystal sesquioxide hosts prepared via combustion and doped with rare earth ions other than Er^{3+} and Yb^{3+}, were investigated to ascertain whether there was a difference compared to the respective bulk material. In each case, effects due to the reduction of the crystal size to the nanoscale were observed.

6.6.1. Spectroscopic Properties of $Lu_2O_3:Nd^{3+}$ and the *X* Parameter

The NIR emission spectra of bulk and nanocrystalline $Lu_2O_3:Nd^{3+}$ are composed of four distinct emission bands centered at approximately 920, 1100, 1400, and 1800 nm and are assigned to transitions from the $^4F_{3/2}$ excited state to the lower ^4I_J states (Figure 6.67) [220]. The spectra are dominated by the bands between 860-980 nm, which correspond to the $^4F_{3/2} \rightarrow {}^4I_{9/2}$ transition and between 1000-1200 nm corresponding to the $^4F_{3/2} \rightarrow {}^4I_{11/2}$ transition. Furthermore, less intense bands between 1300-1500 and 1700-1900 nm were also observed and attributed to the $^4F_{3/2} \rightarrow {}^4I_{13/2}$ and $^4F_{3/2} \rightarrow {}^4I_{15/2}$ transitions, respectively.

Upon comparing the NIR emission spectra of the bulk and nanocrystalline material, we observe no noticeable shift in the transition energies between the two samples, which indicates that the crystal fields surrounding the ions in the two different materials are reasonably similar. As in the other samples studied, we observed that the overall luminescence is lower in the nanocrystalline material, relative to the bulk and is of course ascribed to the adsorption of atmospheric CO_2 and H_2O on the surface of the nanocrystal.

The decay times of the $^4F_{3/2}$ level for the bulk and nanocrystalline $Lu_2O_3:Nd^{3+}$ samples were obtained by measuring the luminescence decay curves of the $^4F_{3/2} \rightarrow {}^4I_{9/2}$ transition following excitation with 488 nm. In the case of nanocrystalline $Lu_2O_3:Nd^{3+}$, the decay time of the $^4F_{3/2}$ excited is shorter (0.25 ms) than that of the corresponding bulk material (0.40 ms). Again, this behavior has been observed for other trivalent rare earth ion doped sesquioxides, for which the nanocrystalline material is usually found to have shorter decay times than the similarly doped bulk sample due to the adsorbed surface species.

More strikingly, we observed differences in the relative intensity of the $^4F_{3/2} \rightarrow {}^4I_{9/2}$ and $^4F_{3/2} \rightarrow {}^4I_{11/2}$ transitions between bulk and nanocrystalline $Lu_2O_3:Nd^{3+}$. In $Lu_2O_3:Er^{3+}$, the NIR emission of the nanocrystalline material differed significantly from its bulk counterpart and was attributed to the presence of the adsorbed species on the surface of the nanocrystal particle, which increased the rate of multiphonon relaxation [265]. In nanocrystalline $Lu_2O_3:Nd^{3+}$, this is not the case as all the NIR luminescence is coming from the same initial excited state to different lower lying states. Thus, the increase in the probability of the multiphonon relaxation rate due to the presence of the CO_3^{2-} and OH^- groups on the surface of the nanocrystal is of little consequence in explaining the difference in the relative intensities of the $^4F_{3/2} \rightarrow {}^4I_{9/2}$ and $^4F_{3/2} \rightarrow {}^4I_{11/2}$ transitions. A very similar behavior was also observed $Y_2O_3:Nd^{3+}$ nanocrystals where the relative intensity of the $^4F_{3/2} \rightarrow {}^4I_{9/2}$ and $^4F_{3/2} \rightarrow {}^4I_{11/2}$ transitions was significantly higher for the nanocrystalline 10 mol% doped $Y_2O_3:Nd^{3+}$ sample compared to the identically doped bulk material [189].

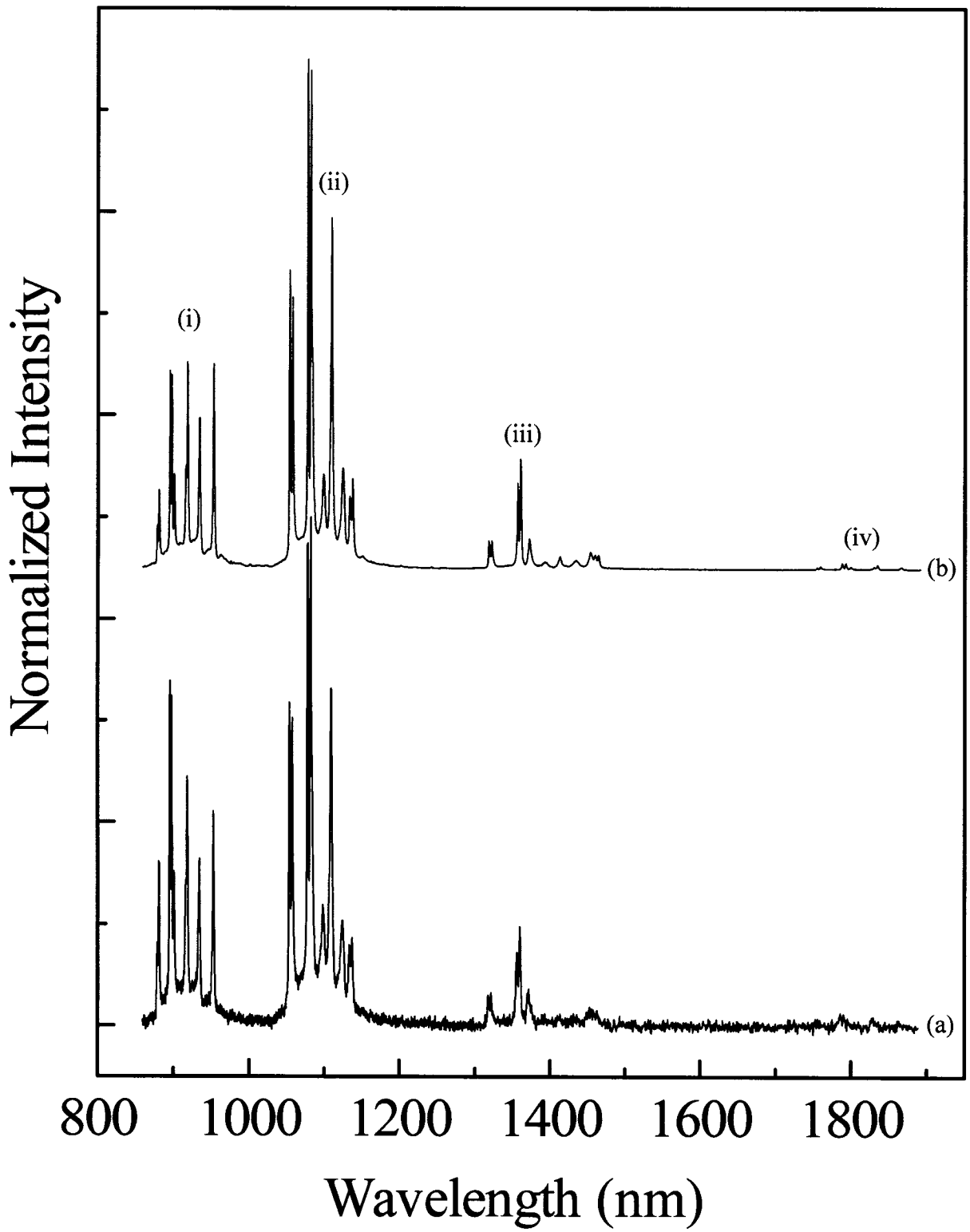

Figure 6.67: NIR luminescence spectra of (a) nanocrystalline and (b) bulk $Lu_2O_3:Nd^{3+}$, showing (i) $^4F_{3/2} \rightarrow {}^4I_{9/2}$, (ii) $^4F_{3/2} \rightarrow {}^4I_{11/2}$, (iii) $^4F_{3/2} \rightarrow {}^4I_{13/2}$ and (iv) $^4F_{3/2} \rightarrow {}^4I_{15/2}$ (λ_{exc} = 488 nm).

The branching ratio $\beta_{J,J'}$ for a $J \rightarrow J'$ luminescence transition is defined as:

$$\beta_{JJ'} = \frac{A(J,J')}{\sum_{J'} A(J,J')} \qquad 6.6.1$$

where $A(J, J')$ is the spontaneous emission probabilities associated to the $J \rightarrow J'$ transition and the sum is extended to all the lower lying J' levels . In the case of the Nd^{3+} ion, the intensity of the $^4F_{3/2} \rightarrow {}^4I_{J'}$ (J' = 9/2, 11/2, 13/2 and 15/2) transitions depend only on the Ω_4 and Ω_6 Judd-Ofelt intensity parameters given that the doubly reduced matrix element of rank 2 for transitions between these states is equal to zero [283]. Therefore, the luminescence branching ratios $\beta_{^4F_{3/2},\,J'}$ depend only on only one parameter $X = \Omega_4/\Omega_6$, as follows [284]:

$$\beta_{JJ'}(X) = \frac{(a_J X + b_J)/\bar{\lambda}_J^{\,3}}{\sum_{J'}(a_{J'} X + b_{J'})/\bar{\lambda}_{J'}^{\,3}} \qquad 6.6.2$$

where the a_J and b_J constants are defined as the squared matrix elements of the irreducible tensor operators of rank 4 and 6

$$a_J = \left|\left\langle {}^4F_{3/2}\right\| U^{(4)} \left\|{}^4I_J\right\rangle\right|^2 \qquad 6.6.3$$

$$b_J = \left|\left\langle {}^4F_{3/2}\right\| U^{(6)} \left\|{}^4I_J\right\rangle\right|^2 \qquad 6.6.4$$

The X parameter is called the spectroscopic-quality parameter which has been employed to study the differences in the relative $^4F_{3/2} \rightarrow {}^4I_{9/2}$: $^4F_{3/2} \rightarrow {}^4I_{11/2}$ intensities in several Nd^{3+} doped laser crystals [284]. Each crystal has its own X parameter, which determines a set of four $\beta_{J,J'}$ coefficients. From the ratio of the integrated emission intensities of the $^4F_{3/2} \rightarrow {}^4I_{9/2}$: $^4F_{3/2} \rightarrow {}^4I_{11/2}$ emission transitions, we have obtained the X

values for the bulk (0.683 ± 0.03) and nanocrystalline (0.825 ± 0.03) $Lu_2O_3:Nd^{3+}$ materials under investigation. These X values are in the range usually obtained for other oxide hosts (0.3-1.5) [284]. The variation of the Ω_4/Ω_6 ratio on passing from the nanocrystalline to the bulk sample indicates that the Nd^{3+} average coordination could be different for the two materials. This could be due to the fact that in the case of the nanocrystalline material a higher fraction of the dopant ions are on the surface of the particles with respect to the bulk one and therefore the average crystal field experienced by the ions in the nanoparticles is different with respect to that of the bulk sample. Moreover, as discussed above, at the surface of the nanoparticles contaminants such as CO_2 and water could contribute to vary the crystal field experienced by the Nd^{3+} ion. We also note that Jorgensen and Reisfeld pointed out that the Ω_6 parameter is related to the rigidity of the host [285]. Therefore, it could be possible that the variation of the X parameter is correlated with a difference of the average rigidity in the nanocrystalline and bulk Lu_2O_3 host [286].

6.6.2. Effect of the Surrounding Media on the Decay Times of Nanocrystalline $Y_2O_3:Sm^{3+}$

The visible emission of trivalent samarium (Sm^{3+}) consists of transitions from the $^4G_{5/2}$ excited state to the lower ^6H_J (J = 5/2, 7/2, 9/2 and 11/2) energy levels. The visible emission spectra of 0.1 and 1 mol% nanocrystals (Figure 6.68), following excitation with 476.5 nm, are dominated by the red $^4G_{5/2} \rightarrow {}^6H_{7/2}$ transition centered at approximately 610 nm. Additional emissions were observed centered at 570 and 660 nm and ascribed to the $^4G_{5/2} \rightarrow {}^6H_{5/2}$ and $^6H_{7/2} \rightarrow {}^6H_{9/2}$ transitions, respectively. Furthermore, the relatively weaker $^4G_{5/2} \rightarrow {}^6H_{11/2}$ transition was observed centered at approximately 730 nm. The visible emission spectrum of a 1 mol% microcrystalline (bulk) sample was obtained for comparison and was identical to that of the nanocrystals. However, the features in the spectra of the nanocrystalline material were slightly broadened compared to the bulk. Different concentrations (0.1, 1 and 10 mol%) of nanocrystalline $Y_2O_3:Sm^{3+}$ were studied and a strong concentration dependence of the emission spectrum was observed [287]. The luminescence intensity increased from 0.1 to 1 mol% but was reduced drastically in the 10 mol% sample. In fact, so much so that the emission signal of the 10 mol% nanocrystalline sample was almost completely quenched and the sample appeared nearly non-luminescent. Table 6.14 presents the decay times of the $^4G_{5/2}$ excited state in both bulk and nanocrystalline $Y_2O_3:Sm^{3+}$ following excitation with 476.5 nm, which were obtained by fitting the exponential decay curves with a single exponential function. As was observed with the emission spectra, the decay times were also severely affected by the concentration of Sm^{3+} dopant. In 0.1 mol% $Y_2O_3:Sm^{3+}$ nanocrystals, a decay time of approximately 3.2 ms was obtained compared to a time of 1.6 ms for the 1 mol% sample. The decrease of the decay time of the $^4G_{5/2}$ state as the concentration of Sm^{3+} ions was

increased was caused by an increased interaction between dopant ions. It is known that many cross-relaxation processes involving the $^4G_{5/2}$ to ^6F_J relaxation at the donor and $^6H_{5/2}$ to ^7F_J transitions at the acceptor (J = 5/2, 7/2, 9/2 and 11/2) can be involved in quenching the luminescence of Sm^{3+} doped materials [288]. As the concentration was increased from 0.1 to 1 mol%, the Sm^{3+}–Sm^{3+} interactions are no longer negligible and quenching of the emission occurs due to cross-relaxation processes between neighboring Sm^{3+} ions. Furthermore, in the 1 mol% nanocrystalline Y_2O_3:Sm^{3+} sample, the decay time was observed to be considerably longer than that of the bulk (1.5 ms versus 990 μs). This is contrary to what we observed in Er^{3+} and Ho^{3+} doped nanocrystalline yttria, where the lifetimes of the excited states were significantly shorter than in the corresponding bulk material [233, 245]. In Y_2O_3 nanocrystals doped with either Er^{3+}, Ho^{3+}, or Tm^{3+}, it was determined that the cause of this phenomenon was the presence of adsorbed CO_2 and H_2O molecules on the surface of the nanocrystal, which increased the probability of multiphonon decay.

Table 6.14: Decay times of bulk and nanocrystalline Y_2O_3:Sm^{3+} following excitation with 476.5 nm.

Sample	Decay Time (μs)
Nanocrystal	
Y_2O_3:Er^{3+} (0.1 mol%)	3219
Y_2O_3:Er^{3+} (1 mol%)	1570
Bulk	
Y_2O_3:Er^{3+} (1 mol%)	986

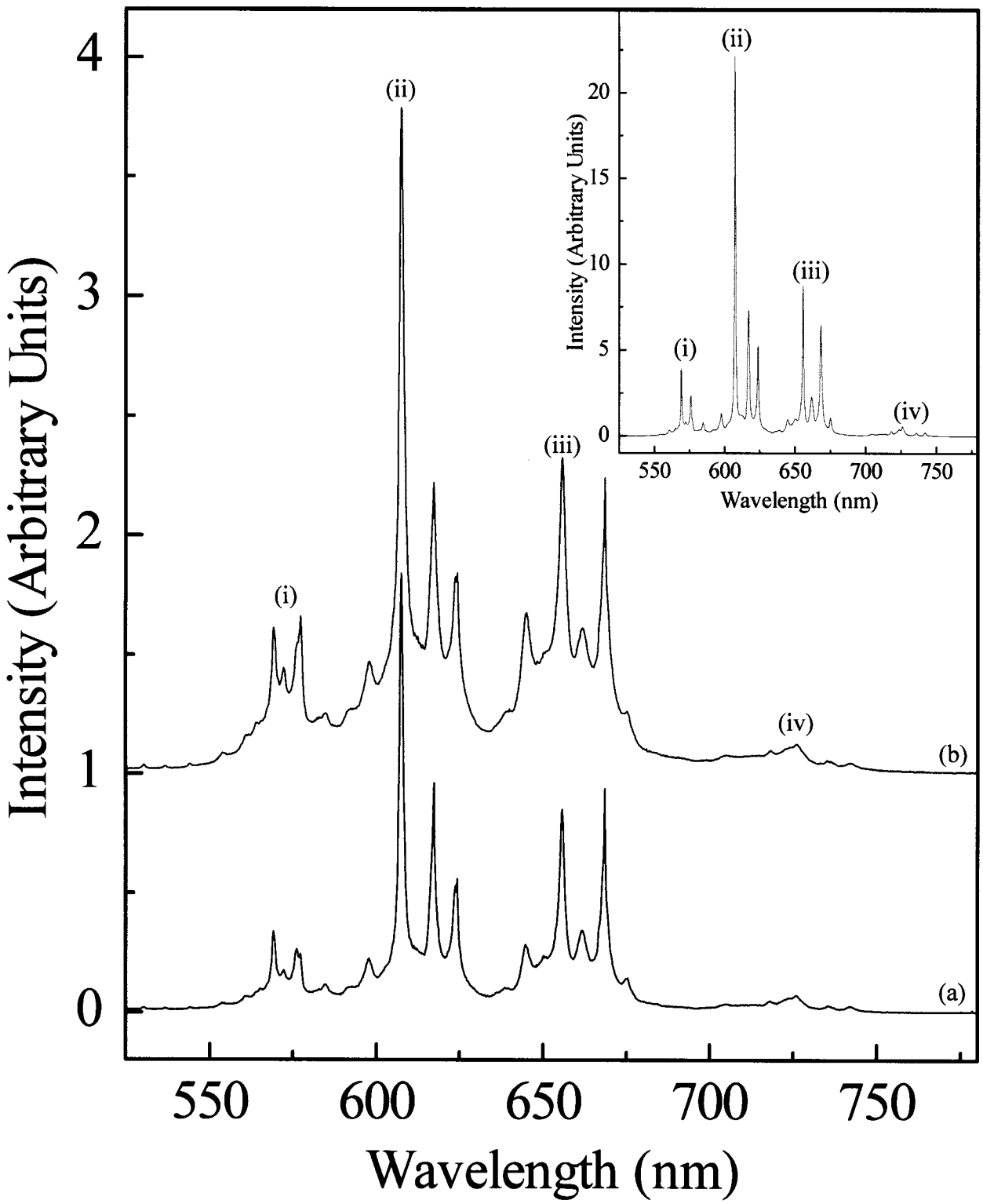

Figure 6.68: Visible emission spectrum of (a) 0.1 and (b) 1 mol% nanocrystalline $Y_2O_3:Sm^{3+}$ following excitation with 476.5 nm at room temperature. Inset: Visible emission spectrum of 1 mol% bulk $Y_2O_3:Sm^{3+}$ (λ_{exc} = 476.5 nm). (i) $^4G_{5/2} \rightarrow {}^6H_{5/2}$ (ii) $^4G_{5/2} \rightarrow {}^6H_{7/2}$ (iii) $^4G_{5/2} \rightarrow {}^6H_{9/2}$ (iv) $^4G_{5/2} \rightarrow {}^6H_{11/2}$.

Of course, the Er^{3+} and Ho^{3+} ions possess closely spaced electronic energy levels and thus non-radiative decay dominates as a result of very efficient multiphonon relaxation. However, the Sm^{3+} ion has fewer electronic energy levels in the visible and thus multiphonon decay should be minimized. So, we would expect the lifetime of the $^4G_{5/2}$ state to be similar in both bulk and nanocrystalline Y_2O_3:Sm^{3+}. Clearly, this was not the case and an alternative explanation was sought. Meltzer and co-workers [114] observed a similar phenomenon in monoclinic Y_2O_3:Eu^{3+} and explained this behavior as being due to changes produced by the medium surrounding the nanocrystal when the size of the particle was much smaller than the excitation wavelength. In this case, the local electric field acting on the Eu^{3+} ion was determined by the combined effects of the Y_2O_3 medium contained within the nanocrystal and that of the medium filling the voids. The radiative lifetime of electric dipole transitions of an ion embedded in a medium may be expressed by the formula [114]:

$$\tau_R \sim \frac{1}{f(\mathrm{ED})} \frac{\lambda_0^2}{\left[\frac{1}{3}\left(n^2+2\right)\right]^2 n} \qquad 6.6.5$$

where f (ED) is the oscillator strength for the electric dipole transition, λ_0 is the wavelength in vacuum and n is the refractive index of the medium. The dependence of τ_R on the refractive index, n, was caused by the change in the density of states for the photons in a medium of reduced light velocity and the modification of the polarizability of the surrounding medium. In the case where the particle size of the nanocrystals is considerably smaller than the wavelength of light, the refractive index, n, may be replaced by n_{eff}, the effective index of refraction of the medium:

$$n_{\mathrm{eff}}(x) = x \cdot n_{Y_2O_3} + (1-x) \cdot n_{\mathrm{med}} \qquad 6.6.6$$

where x is the "filling factor", which shows what fraction of space is occupied by the Y_2O_3 nanocrystals, $n_{Y_2O_3}$ is the refractive index of yttrium oxide (n = 1.91) and n_{med} is the refractive index of the medium surrounding the nanocrystals. We undertook similar experiments with $Y_2O_3:Sm^{3+}$ in order to attempt to explain the lengthening of the decay time of the nanocrystalline material compared to the bulk. We studied the lifetime of the $^4G_{5/2}$ excited state of $Y_2O_3:Sm^{3+}$ when the nanocrystals were surrounded by different media having considerably different refractive indices; air (n = 1), methanol (CH_3OH, n = 1.326) and carbon disulfide (CS_2, n = 1.628). In fact, the decay of the $^4G_{5/2}$ level is not strongly affected by multiphonon relaxation, as the energy gap separating it from the lower lying state ($^6F_{11/2}$) amounts to about 7500 cm^{-1} and therefore cannot be easily bridged by the emission of phonons. Figure 6.69 presents the lifetime of the $^4G_{5/2}$ excited state of nanocrystalline $Y_2O_3:Sm^{3+}$ (1 mol%) plotted versus the refractive index of the media (n_{med}) using x as an adjustable parameter until a reasonable fit was obtained. Our results showed that the lifetime of the $^4G_{5/2}$ state was strongly dependent on the index of refraction of the media, n_{med}, and the substance filling the space between the particles. We found that a filling factor (x) of 0.75 gave the best fit, indicating that the nanocrystals occupied 75% of the sample space.

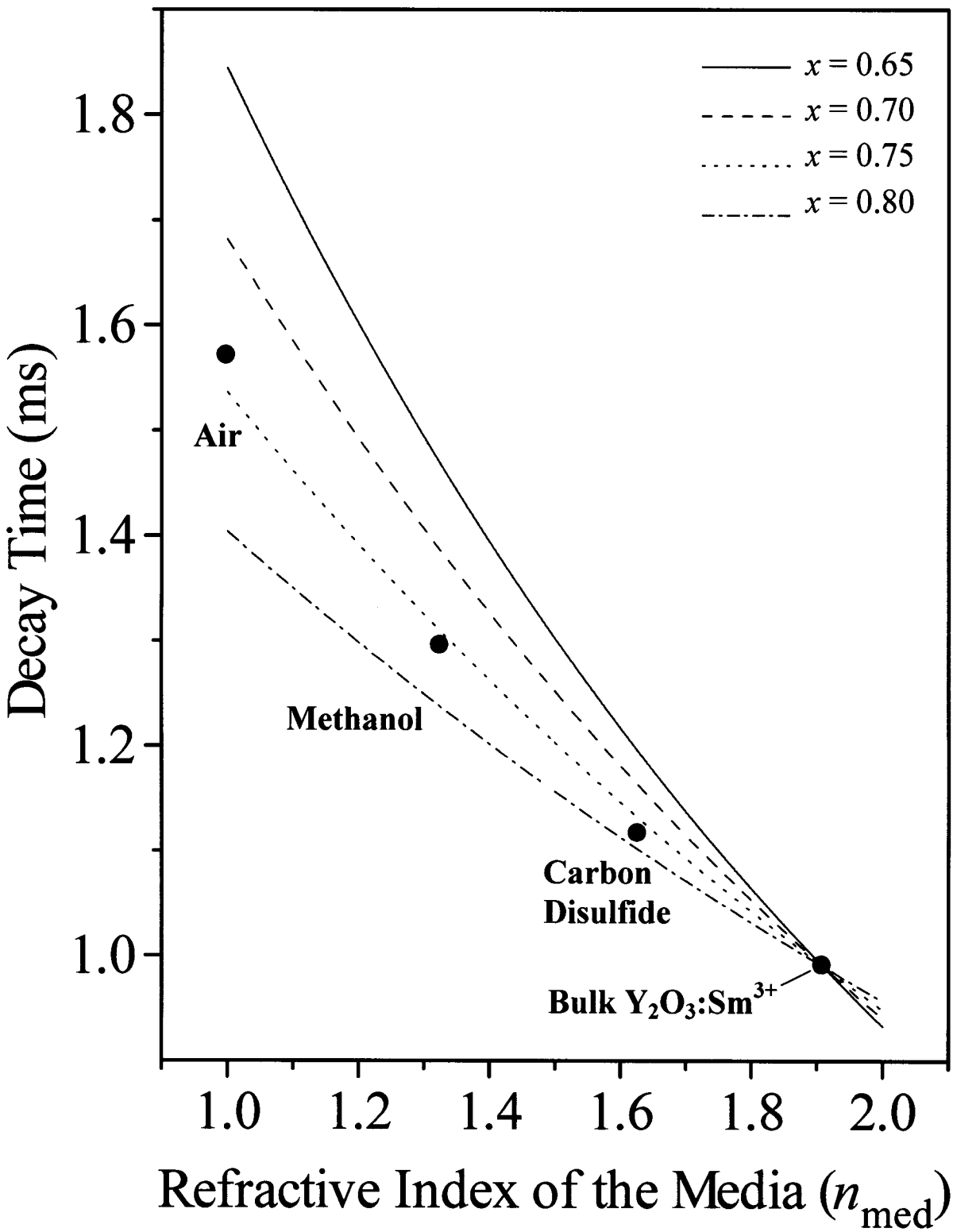

Figure 6.69: Dependence of the $^4G_{5/2}$ decay time of nanocrystalline $Y_2O_3:Sm^{3+}$ (1 mol%) on the index of refraction of the medium surrounding the nanocrystals as a function of different filling factors (x) following excitation with 476.5 nm at room temperature.

6.6.3. Decay Times of Nanocrystalline $Y_2O_3:Dy^{3+}$ Using the Inokuti – Hirayama Model

The 298 K visible emission spectrum of nanocrystalline $Y_2O_3:Dy^{3+}$, presented in Figure 6.70, was obtained following excitation with 457.9 nm [287]. The visible emission from the $Y_2O_3:Dy^{3+}$ nanocrystals was predominantly yellow from the $^4F_{9/2} \rightarrow {}^6H_{13/2}$ transition centered at approximately 575 nm. This visible transition makes the Dy^{3+} ion doped into solid state materials an attractive choice for technological applications, which require the emission of yellow light. The visible spectrum also consists of four other relatively weaker emission bands in the blue-green, red and NIR portions of the spectrum centered at about 485, 675, 760 and 850 nm assigned to the transitions from the $^4F_{9/2}$ excited state to the $^6H_{15/2}$, $^6H_{11/2}$, $^6H_{9/2} + {}^6F_{11/2}$ and $^6H_{7/2} + {}^6F_{9/2}$ levels, respectively. The decay curves of the luminescence originating from the $^4F_{9/2}$ excited state were obtained and we observed that they deviated from exponentiality. As seen from Figure 6.71, a single exponential function was deemed unsuitable to fit the decay curves (Table 6.15). The non-exponentiality in the decay curves of rare earth doped materials usually arises from ion-ion interactions as the concentration of dopant is increased, usually due to cross- relaxation processes.

Table 6.15: Decay times of the $^4F_{9/2}$ state of $Y_2O_3:Dy^{3+}$ nanocrystals following excitation with 457.9 nm.

Single Exponential Fit	$\tau = 606$ μs
Inokuti-Hirayama Fit	
$S = 6$	$\tau_0 = 706$ μs
$S = 8$	$\tau_0 = 667$ μs
$S = 10$	$\tau_0 = 650$ μs

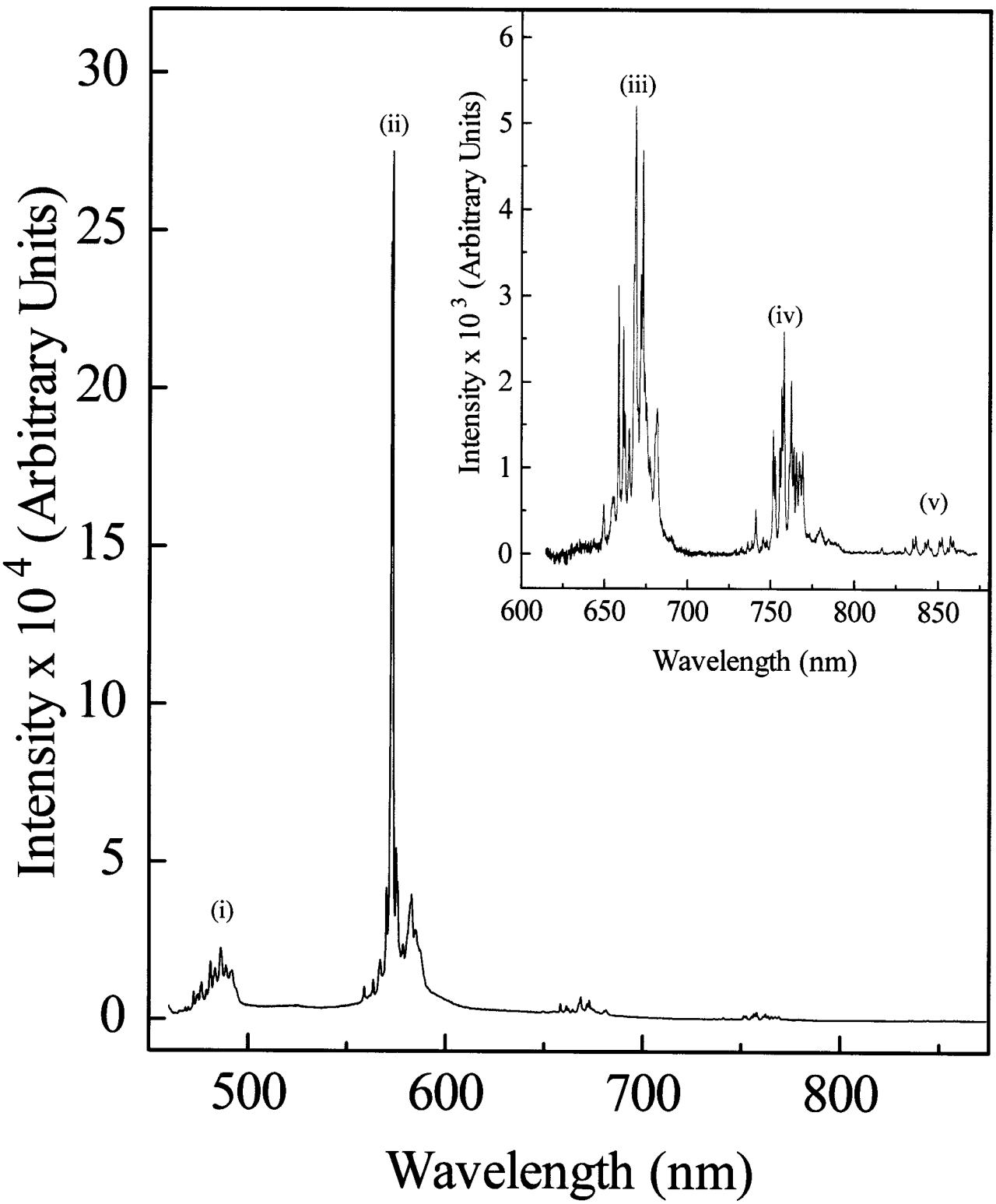

Figure 6.70: Visible emission spectrum of 1 mol% nanocrystalline $Y_2O_3:Dy^{3+}$ following excitation with 457.9 nm at room temperature. (i) $^4F_{9/2} \rightarrow {}^6H_{15/2}$ (ii) $^4F_{9/2} \rightarrow {}^6H_{13/2}$ (iii) $^4F_{9/2} \rightarrow {}^6H_{11/2}$ (iv) $^4F_{9/2} \rightarrow {}^6H_{9/2} + {}^6F_{11/2}$ (v) $^4F_{9/2} \rightarrow {}^6H_{7/2} + {}^6F_{9/2}$.

In the case of Dy^{3+} doped materials for example, the presence of a cross-relaxation process of the form $^4F_{9/2} + {}^6H_{15/2} \rightarrow ({}^6F_{3/2}, {}^6F_{1/2}) + ({}^6H_{9/2}, {}^6F_{11/2})$ has been previously observed [289]. Therefore, to obtain a more thorough understanding of the energy transfer processes, we applied the Inokuti–Hirayama (IH) model to the analysis of the decay curves. This model is adequate in describing energy transfer processes in which the transfer of energy from the donor to the acceptor is significantly faster than the diffusion amongst donors. Thus, the IH expression for the time evolution of the luminescence intensity in the presence of energy transfer resulting from electric-multipolar interactions between donor and acceptor ions in the absence of migration among the donors [290] is given by:

$$\phi(t) = A\exp\left[-\frac{t}{\tau_o} - \alpha\left(\frac{t}{\tau_o}\right)^{3/S}\right] \qquad 6.6.7$$

where $\phi(t)$ is the luminescence intensity at time t, A is the luminescence intensity at $t = 0$ and τ_o is the intrinsic lifetime of the donors in the absence of acceptors. Furthermore, $S = 6$ for dipole–dipole (D–D) interactions, $S = 8$ for dipole–quadrupole (D–Q) interactions and $S = 10$ for quadrupole–quadrupole (Q–Q) interactions while α is a parameter containing the energy transfer probability. We fit the decay curves using eqn. 6.6.7 in order to obtain the parameters α and τ_o, considering the three possible interaction mechanisms (D–D, D–Q or Q–Q). Analysis revealed that the best fit was obtained with $S = 6$ as opposed to $S = 8$ or 10 and the calculated lifetime was determined to be 705 μs (Figure 6.71). The IH model fits the data better than the single exponential model although it is not an ideal fit. It is therefore conceivable that the cross-relaxation processes between dopant dysprosium ions could involve a D–D interaction. The

parameter α describes the interaction between the donor and acceptor ions and is given by the relation:

$$\alpha = \frac{4}{3}\pi\,\Gamma\left(1-\frac{3}{s}\right)N_a R_0^3 \qquad 6.6.8$$

where Γ is the gamma function, R_0 is the critical donor-acceptor distance where the rate of energy transfer to the acceptor is equal to the rate of intrinsic decay of the donor and N_a is the concentration of acceptor ions (ions cm^{-3}). Given the value we obtained for α (0.218) from the fit, the calculated critical distance, R_0, was determined to be approximately 6.05 Å, which is typical for energy transfer processes involving rare earth ions [291]. In single crystals of $CaMoO_4:Dy^{3+}$, a critical distance of between 9.5 and 9.8 Å was obtained [289], which indicates that the energy transfer process in $Y_2O_3:Dy^{3+}$ nanocrystals is less probable compared to the single crystals of calcium molybdate doped with dysprosium. Once R_0 was obtained, the D–D coupling parameter, C, can be calculated using [292]:

$$C = R_0^6 k \qquad 6.6.9$$

where k is the intrinsic decay constant of the donor ion involved in the energy transfer process in the absence of the acceptor. A value of 6.956×10^{-53} m^6 s^{-1} was obtained. It must be stated that the results of the fit represent a qualitative assessment of the data and should be treated as such. A model, which will better represent the dynamics of nanocrystalline Y_2O_3 doped with rare earth ions is currently being developed.

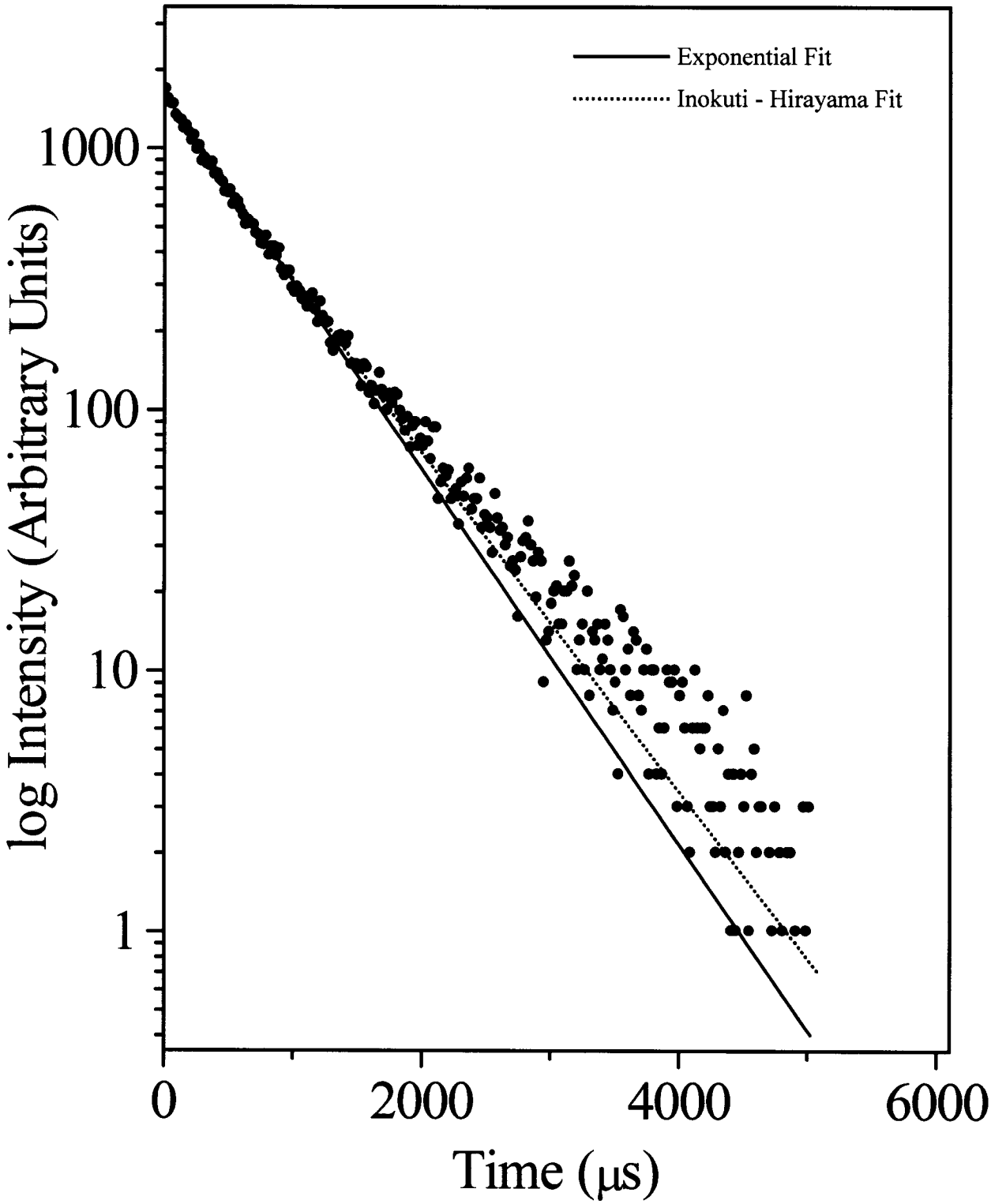

Figure 6.71: Results of the single exponential and Inokuti-Hirayama fits to the decay curve of the $^4F_{9/2}$ emission in nanocrystalline $Y_2O_3:Dy^{3+}$.

CHAPTER 7

7. Conclusion

In this thesis, we have investigated the luminescence properties of rare earth doped inorganic nanocrystals, specifically the sesquioxides Y_2O_3, Lu_2O_3, and Sc_2O_3 as well as the $Gd_3Ga_5O_{12}$ garnet. We explored two diverse synthesis techniques (for Y_2O_3), which resulted in distinct morphological properties. The nanocrystals prepared via the propellant synthesis had a microscopic, open, sponge like morphology, which was observed over different scales, thus suggesting a fractal behavior. Conversely, the Y_2O_3 nanocrystals prepared via the controlled hydrolysis procedure were compact with no fractal dimensions. Furthermore, at the nanometer scale, the powders were built up of crystalline platelets with a porous structure resulting in large partially ordered aggregates at the micrometer scale.

The luminescence spectra of $Y_2O_3:Er^{3+}$ nanocrystals (10 mol%) prepared via the propellant synthesis showed the characteristic Er^{3+} emissions in the visible and NIR region ascribed to the emissions from the $^2H_{11/2}$, $^4S_{3/2}$, $^4F_{9/2}$, and $^4I_{9/2}$ excited states to the $^4I_{15/2}$ ground state centered at 530, 550, 660, and 810 nm, respectively. Additionally, the $^4S_{3/2} \rightarrow {}^4I_{13/2}$ transition was observed centered at 860 nm. The luminescence was compared to that of a bulk (microcrystalline) material, with an identical doping level, and it was observed that while the shapes of the emission bands were identical, the nanocrystals had much lower luminescence intensities. Diffuse reflectance spectra revealed the presence of two bands centered at 1500 and 3350 cm^{-1} due to adsorbed CO_3^{2-} and OH^- ions, respectively. The presence of these bands increase the non-radiative decay in the nanocrystalline material thereby lowering the luminescence intensities. This was

manifested upon comparing the decay times of bulk and nanocrystalline $Y_2O_3:Er^{3+}$ (10 mol%) following excitation with 488 nm. The decay time of the $^4S_{3/2}$ state was observed to be one order of magnitude shorter in the nanocrystals compared to the bulk. The adsorbed surface species increased the rate of multiphonon relaxation, which in turn reduced the observed decay time. An attempt was made to reduce the overall surface contamination by various heat treatments and while a reduction in the amount of contaminants was observed, the luminescence intensity was only marginally improved.

The dependence of Er^{3+} concentration (1, 2, 5, and 10 mol%) was studied in $Y_2O_3:Er^{3+}$ nanocrystals and we observed that the crystal field was not significantly altered up to a 10 mol% doping level. However, the decay times of the $^4S_{3/2}$ excited state showed a significant concentration dependence. The decay time of the 1 mol% was almost one order of magnitude longer than the 10 mol% sample and was attributed to a reduction of the $^2H_{11/2} + {}^4I_{15/2} \rightarrow {}^4I_{9/2} + {}^4I_{13/2}$ cross-relaxation pathway.

Continuous wave excitation with 815 nm produced upconverted green ($^2H_{11/2}$, $^4S_{3/2} \rightarrow {}^4I_{15/2}$) and red ($^4F_{9/2} \rightarrow {}^4I_{15/2}$) emission in both bulk and nanocrystalline $Y_2O_3:Er^{3+}$ and blue upconversion from the $^4F_{5/2} \rightarrow {}^4I_{15/2}$ (450 - 465 nm), $^4F_{7/2} \rightarrow {}^4I_{15/2}$ (485 - 505 nm), and $^2P_{3/2} \rightarrow {}^4I_{11/2}$ (468 - 480 nm) transitions in the bulk material only. Power studies revealed that in all transitions, except the $^2P_{3/2} \rightarrow {}^4I_{11/2}$, which followed a cubic dependence, two photons were responsible for the population of the emitting states. No inflection point was observed allowing us to rule out photon avalanche as the mechanism of upconversion. We determined that the $^4S_{3/2}$ and $^4F_{9/2}$ emitting levels were populated via excited state absorption and energy transfer upconversion processes. However, in the upconversion spectra, the presence of an enhancement of the red ($^4F_{9/2} \rightarrow {}^4I_{15/2}$) emission

was observed indicating that even more processes were operative. We determined that an ion pair process of the type; ($^4I_{9/2}$, $^4I_{11/2}$) → ($^4I_{13/2}$, $^4F_{9/2}$) was responsible for directly populating the $^4F_{9/2}$ state.

In the bulk material, the $^2P_{3/2}$ state was populated via a three photon ESA process, while the $^4F_{5/2,\ 7/2}$ states were populated via a concentration dependent ETU process. This was elucidated from the upconversion spectra of various Er^{3+} doped bulk samples where in the most dilute sample (1 mol%), the relative intensity of all the blue upconverted emissions was 1:1:1. Conversely, in the 10 mol% sample, both the $^4F_{5/2}$ and $^4F_{7/2}$ emissions increased while the $^2P_{3/2}$ emission remained relatively constant.

Similar to excitation with 815 nm, red and green upconverted emission was observed in both bulk and nanocrystalline Y_2O_3:Er^{3+} and upconverted blue emission in the bulk material only, following excitation of the $^4I_{11/2}$ state with 980 nm. Upconverted decay curves for the green and red emissions of the Y_2O_3:Er^{3+} nanocrystals deviated from exponential behavior and were fit with Nakazawa's model. A lengthening of the decay times, following 980 nm excitation, was observed indicating the presence of a two photon ETU process. Furthermore, an enhancement of the red emission was again observed and attributed to the direct population of the $^4F_{9/2}$ state via two resonant transitions: $^4F_{7/2}$ → $^4F_{9/2}$ and $F_{9/2}$ ← $^4I_{11/2}$. Again in the bulk material, the $^2P_{3/2}$ → $^4I_{11/2}$ transition obeyed a cubic dependence on the NIR pump power versus the quadratic dependence for the $^4F_{7/2}$ → $^4I_{15/2}$ and $^4F_{5/2}$ → $^4I_{15/2}$ transitions. The blue upconversion spectra showed a decrease in the intensities of the $^2P_{3/2}$ → $^4I_{11/2}$ and $^4F_{7/2}$ → $^4I_{15/2}$ transitions while the intensity of the $^4F_{5/2}$ → $^4I_{15/2}$ transition increased. This behavior was explained by an increase in the efficiency of the above cross-relaxation ($^4F_{7/2}$ → $^4F_{9/2}$ and $F_{9/2}$ ← $^4I_{11/2}$) process, which

while populating the $^4F_{9/2}$ state, consequently depopulated the $^4F_{9/2}$ level. Since the $^2P_{3/2}$ state was populated by $^4F_{7/2}$, its intensity decreased accordingly.

We also investigated the effect of co-doping bulk and nanocrystalline $Y_2O_3:Er^{3+}$ with Yb^{3+}. The visible emission spectrum of $Y_2O_3:Er^{3+}$, Yb^{3+} (1 mol% each of Er^{3+} and of Yb^{3+}) following excitation with 488 nm remained relatively unchanged compared to singly doped $Y_2O_3:Er^{3+}$ (1 mol%). However, the NIR emission spectrum (λ_{exc} = 488 nm) showed emission from the Yb^{3+} ion. This emission was attributed to an energy transfer from Er^{3+} to Yb^{3+} since the ytterbium ion has only one excited state at approximately 10, 000 cm^{-1} and could not have been excited with 488 nm. The upconversion (λ_{exc} = 978 nm) in bulk and nanocrystalline $Y_2O_3:Er^{3+}$, Yb^{3+} was determined to occur via two successive transfers of energy from the Yb^{3+} ion to the Er^{3+} ion. Once again, the upconverted red emission was enhanced compared to the direct emission spectrum. Like in the singly doped material, the red enhancement was much more pronounced in the nanocrystalline material. The ($^4F_{7/2}$, $^4I_{11/2}$) $\rightarrow$ ($^4F_{9/2}$, $F_{9/2}$) cross-relaxation process described for $Y_2O_3:Er^{3+}$ as being responsible for the phenomenon, did not account for stronger enhancement in the nanocrystalline material. Thus, we proposed that another process was operative to populate the $^4F_{9/2}$ that used the inherent CO_3^{2-} and OH^- adsorbed species present only in the nanomaterial. The transition $^4F_{9/2} \leftarrow {}^4I_{13/2}$ was more efficient in the nanocrystals since the non-radiative decay from $^4I_{11/2}$ to $^4I_{13/2}$ was more efficient and since $^4F_{9/2} \leftarrow {}^4I_{13/2}$ is non-resonant, the extra 1600 cm^{-1} in energy can be more easily dissipated by the nanocrystal lattice.

The effect of Yb^{3+} concentration on the spectroscopic properties of $Y_2O_3:Er^{3+}$, Yb^{3+} nanocrystals was investigated. Decay times of nanocrystalline $Y_2O_3:Er^{3+}$, Yb^{3+}

were obtained following 488 nm excitation and we observed that increasing the Yb^{3+} concentration (1, 5, and 10 mol% Yb^{3+}) while keeping Er^{3+} constant at 1 mol%, resulted in a reduction of the decay times of the $^4S_{3/2}$ and $^4F_{9/2}$ states. This was believed to be due to the pairing or aggregation of donor Yb^{3+} ions, which induced a quenching effect and dissipated the energy non-radiatively. Similarly, upconverted decay times of the $^4S_{3/2}$ and $^4F_{9/2}$ excited states followed the same trend as the decay times obtained with 488 nm radiation. However a lengthening of the upconverted decay times was observed confirming ETU.

Interestingly, a power study of the nanocrystalline $Y_2O_3:Er^{3+}$, Yb^{3+} sample (containing 1 mol% Er^{3+} and 10 mol% Yb^{3+}) revealed that the $^4S_{3/2}$ state was populated via a three photon process as opposed to the $Y_2O_3:Er^{3+}$, Yb^{3+} sample, with 1 mol% each of Er^{3+} and Yb^{3+}, where the $^4S_{3/2}$ state was populated by a two photon process. This confirmed the presence of the $^4F_{9/2} \leftarrow {}^4I_{13/2}$ transition, which became very efficient at higher Yb^{3+} concentrations and as a result, bypassed the green ($^4S_{3/2}$) state and preferentially populated the $^2H_{9/2}$ state.

We studied $Y_2O_3:Er^{3+}$ nanocrystals prepared utilizing a controlled hydrolysis procedure (wet chemical synthesis) to determine if the synthesis method played any role in the spectroscopic behavior. The diffuse reflectance spectra of the nanocrystalline samples exhibited slightly broadened peaks (compared to the bulk material), which corresponded to the intraconfigurational $f-f$ transitions from the $^4I_{15/2}$ ground state to the various excited states of the Er^{3+} ion. The 77 K luminescence spectrum of the nanocrystalline material also demonstrated inhomogeneously broadened emission bands, which were attributed to Er^{3+} ions located on the surface of the nanomaterial that

experienced different crystal field effects than the ions in the C_2 and C_{3i} sites. The room temperature luminescence spectrum showed green ($^2H_{11/2}$, $^4S_{3/2} \rightarrow {}^4I_{15/2}$), red ($^4F_{9/2} \rightarrow {}^4I_{15/2}$) and NIR ($^4I_{9/2} \rightarrow {}^4I_{15/2}$ and $^4S_{3/2} \rightarrow {}^4I_{13/2}$) emission in both the bulk and nanocrystalline material. The decay time of the $^4S_{3/2}$ state in nanocrystalline $Y_2O_3:Er^{3+}$ (10 mol%), obtained with 488 nm radiation, was compared to the identically doped bulk material and was one order of magnitude shorter. Like $Y_2O_3:Er^{3+}$ nanocrystals prepared by propellant synthesis, nanocrystalline $Y_2O_3:Er^{3+}$ prepared via wet chemical synthesis contained the presence of CO_3^{2-} and OH^- anions adsorbed on their surface, which increased the rate of multiphonon relaxation and as a result, decreased the observed decay times.

Furthermore, upconverted luminescence was also observed following 650 nm excitation into the $^4F_{9/2}$ state as well as following 800 nm excitation into the $^4I_{9/2}$ state. The upconverted decay times of the $^4S_{3/2}$ state in nanocrystalline $Y_2O_3:Er^{3+}$ obtained at both 650 and 800 nm wavelengths were compared with the decay times obtained using 488 nm excitation. At low Er^{3+} dopant concentrations (0.1 mol%) the $^4S_{3/2}$ decay time at all pump wavelengths (488, 650, or 800 nm) was identical, indicating that ESA was the dominant mechanism of upconversion. At an intermediate Er^{3+} concentration (1 mol%), the upconverted decay times were slightly lengthened and indicated that both ESA and ETU were operative. Finally, in the heavily doped $Y_2O_3:Er^{3+}$ (10 mol%) nanocrystals, the decay times were considerably longer indicating that ETU was the dominant upconversion mechanism. An enhancement of the red upconverted luminescence was observed following NIR excitation (λ_{exc} = 800 nm) in both bulk and nanocrystalline $Y_2O_3:Er^{3+}$ (10 mol%) and was caused by an ion-pair process of the type; ($^4I_{9/2}$, $^4I_{11/2}$) $\rightarrow$

($^4I_{13/2}$, $^4F_{9/2}$). It was observed that the magnitude of the red enhancement was greater in the bulk material and greater still in $Y_2O_3:Er^{3+}$ nanocrystals prepared by a different technique (combustion). The lower magnitude of the red enhancement was ascribed to a decrease in the efficiency of the ion-pair process caused by either a change in the average $Er^{3+} - Er^{3+}$ distances or an increase in the multiphonon relaxation probability.

Nanocrystals of $Y_2O_3:Er^{3+}$, Yb^{3+} synthesized via the wet chemical synthesis (with 1 mol% each of Er^{3+} and Yb^{3+}) also showed an enhancement of the red ($^4F_{9/2} \rightarrow {}^4I_{15/2}$) emission. However, in this case the magnitude of red enhancement was greater than in identically doped nanocrystals but prepared via propellant synthesis. An increase in the multiphonon relaxation probability was hypothesized to reduce the red enhancement in $Y_2O_3:Er^{3+}$ nanocrystals (λ_{exc} = 800 nm) prepared via wet chemical synthesis. In the co-doped material, an increase in the multiphonon relaxation led to an increase in the non-radiative decay from $^4I_{11/2}$ to $^4I_{13/2}$ and thus, resulted in an increase of the $^4F_{9/2} \leftarrow {}^4I_{13/2}$ transition, which directly populated the $^4F_{9/2}$ state.

We have examined the effect of replacing the Y^{3+} cation with Lu^{3+} in the sesquioxide nanocrystal host. We discussed the visible upconversion emission (λ_{exc} = 800 nm) as well as the mechanisms responsible for pumping the upper levels in bulk and nanocrystalline $Lu_2O_3:Er^{3+}$ (1 mol%) prepared by propellant synthesis. The general spectroscopic behavior of $Lu_2O_3:Er^{3+}$ is similar to the one displayed by identically doped $Y_2O_3:Er^{3+}$; however, relatively strong blue upconversion is observed in the case of erbium doped nanocrystalline lutetia, whilst in $Y_2O_3:Er^{3+}$ obtained in the same experimental conditions no upconversion was observed. However, most importantly, $Lu_2O_3:Er^{3+}$ nanocrystals (1 mol%) had upconversion luminescence intensities which were

approximately 100 times greater, under identical experimental conditions, than identically doped $Y_2O_3:Er^{3+}$ synthesized via the same technique.

Furthermore, we discussed NIR to visible upconversion in bulk and nanocrystalline $Lu_2O_3:Er^{3+}$ following 980 nm continuous wave excitation. Power studies revealed that the green ($^4S_{3/2} \rightarrow {}^4I_{15/2}$) and red ($^4F_{9/2} \rightarrow {}^4I_{15/2}$) upconversion occurred via a two-photon process. Lifetime measurements showed that energy transfer upconversion (ETU) was present as the lifetime of both green and red emitting levels were longer when exciting with 980 nm compared to direct excitation with 488 nm. Blue upconversion was observed, assigned to the $^4F_{5/2} \rightarrow {}^4I_{15/2}$, $^2P_{3/2} \rightarrow {}^4I_{11/2}$, and $^4F_{7/2} \rightarrow {}^4I_{15/2}$ transitions. A power study revealed that the $^2P_{3/2}$ emitting level was populated via a three-photon process. Population of the $^2P_{3/2}$ level via an ESA process is improbable as no resonance exists for a process involving the sequential absorption of three photons. Therefore, an ETU mechanism assisted by phonons was determined to be operative.

We measured the upconversion behavior as a function of temperature exciting with either 804 or 980 nm. We showed that the $^2H_{11/2}$ state was thermalized by the $^4S_{3/2}$ state since at 77 K, no emission from $^2H_{11/2}$ was observed. We calculated an energy gap of 689 cm^{-1} between the $^2H_{11/2}$ and $^4S_{3/2}$ levels, which compared favorably to the energy gap obtained from the spectrum (720 cm^{-1}). Furthermore, the upconversion decays as a function of temperature were measured and we observed a lengthening of the decay time with increasing temperature. At lower temperature, the multiphonon relaxation rate is less efficient and caused a decrease in the total rate of depopulation, and in turn caused an increase in the observed decay time.

We investigated $Sc_2O_3:Er^{3+}$, another nano sesquioxide isostructural to Y_2O_3, which was also prepared by the combustion synthesis. The Sc^{3+} ion is considerably smaller than Y^{3+} and we were interested in determining just how much of an effect on the spectroscopic properties of Er^{3+} the change in ionic size would have. The upconversion emission (λ_{exc} = 980 nm) was studied and it was determined that the mechanism responsible for populating the emitting states was dependent upon the concentration of the dopant ion. In 0.1 mol% $Sc_2O_3:Er^{3+}$ nanocrystals, upconversion was determined to occur via excited state absorption (ESA) since the decay time of the $^4S_{3/2}$ state obtained when directly populating the $^4F_{7/2}$ excited state with 488 nm was identical to that obtained when utilizing 980 nm as the pump wavelength. On the other hand, the 1 and 10 mol% samples showed a lengthening of the decay times obtained with 980 nm confirming the presence of energy transfer upconversion (ETU).

A concentration dependent enhancement of the red emission ($^4F_{9/2} \rightarrow {}^4I_{15/2}$) was observed in the upconverted emission spectra following excitation with 980 nm. A cross-relaxation mechanism of the type $^4F_{7/2} + {}^4I_{11/2} \rightarrow {}^4F_{9/2} + {}^4F_{9/2}$ was in part responsible for directly populating the $^4F_{9/2}$ state and bypassing the green emitting states ($^2H_{11/2}$ and $^4S_{3/2}$). Also, following excitation of the ion to the $^4I_{11/2}$ state (λ_{exc} = 980 nm) the large vibrational energies of the carbonate and hydroxyl ions impurities present in these nanocrystalline materials, induced efficient multiphonon decay to the $^4I_{13/2}$ state. The resulting non-resonant $^4F_{9/2} \leftarrow {}^4I_{13/2}$ transition was also responsible for the direct population of the $^4F_{9/2}$ level with the excess energy easily dissipated by the Sc_2O_3 lattice. Furthermore, the enhancement of the red emission was more prominent in $Sc_2O_3:Er^{3+}$ nanocrystals compared to identically doped $Y_2O_3:Er^{3+}$. This was caused by the shorter

Er^{3+} - Er^{3+} distances in the Sc_2O_3:Er^{3+} nanocrystals due to the lower unit cell volume (971.95 $Å^3$) compared to that of Y_2O_3:Er^{3+} nanocrystals (1193.38 $Å^3$).

The ternary $Gd_3Ga_5O_{12}$:Er^{3+} nanocrystal oxide was prepared using the combustion synthesis. Following the direct excitation of the $^4F_{7/2}$ excited state with 488 nm, green ($^2H_{11/2}$, $^4S_{3/2} \rightarrow {}^4I_{15/2}$) and red ($^4F_{9/2} \rightarrow {}^4I_{15/2}$) emission was observed centered at 535 and 660 nm, respectively. Furthermore, we observed NIR emission centered at 795, 850, 995, 1240, and 1560 nm ascribed to the $^4I_{9/2} \rightarrow {}^4I_{15/2}$, $^4S_{3/2} \rightarrow {}^4I_{13/2}$, $^4I_{11/2} \rightarrow {}^4I_{15/2}$, $^4S_{3/2} \rightarrow {}^4I_{11/2}$, and $^4I_{13/2} \rightarrow {}^4I_{15/2}$ transitions, respectively.

We demonstrated near-infrared to visible upconversion in nanocrystalline $Gd_3Ga_5O_{12}$ doped with Er^{3+} ions following excitation with 800 nm into the $^4I_{9/2}$ state. Power studies revealed that a visually dominant green emission was observed when pumping with less than 5 mW of NIR excitation power. Efficient upconversion was possible since the MIR spectra of the nanocrystal GGG host showed that the bands at 1500 and 3350 cm^{-1} attributed to the adsorbed CO_3^{2-} and OH^- surface contaminants, respectively, were significantly reduced compared to nanocrystalline Y_2O_3. Thus, the GGG nanocrystals had a lower probability for multiphonon relaxation, which increased the upconversion intensity. Nanocrystalline samples of GGG:Er^{3+} with 1 and 5 % Er^{3+} dopant concentrations were studied and it was determined that upconversion occurred via excited state absorption in the 1 mol% sample while energy transfer upconversion took over as the dominant mechanism as the concentration was increased to 5 mol% as evidenced from the lengthening of the upconverted decay times. Furthermore, an enhancement of the red ($^4F_{9/2} \rightarrow {}^4I_{15/2}$) emission was observed and hypothesized to occur

via the concentration dependent ($^4I_{9/2}$, $^4I_{11/2}$) → ($^4I_{13/2}$, $^4F_{9/2}$) ion pair process, which directly populated the $^4F_{9/2}$ state.

We studied the spectroscopic properties of nanocrystal sesquioxides doped with ions other than Er^{3+} and Yb^{3+}. The NIR emission of bulk and nanocrystalline $Lu_2O_3:Nd^{3+}$ showed four distinct bands ascribed to the transition from the $^4F_{3/2}$ excited state to the $^4I_{9/2}$ (920 nm), $^4I_{11/2}$ (1090 nm), $^4I_{13/2}$ (1360 nm), and $^4I_{15/2}$ (1800 nm) states. Differences between the bulk and nanomaterial were observed in the relative intensities of the $^4F_{3/2} \rightarrow {}^4I_{9/2}$ and $^4F_{3/2} \rightarrow {}^4I_{11/2}$ transitions. We calculated the spectroscopic quality parameter (X) and obtained a value of 0.68 ± 0.03 and 0.82 ± 0.03 for the bulk and nanocrystalline material, respectively. The X parameter is a measure of the variation of the ratios of Ω_4 and Ω_6 Judd-Ofelt parameters. This indicated that the average coordination of the Nd^{3+} ion was different in the nanocrystals due to the presence of a high fraction of dopant ions on the surface, which experienced a different crystal field.

Yttrium oxide doped with tripositive samarium ions had a predominantly red emission from the $^4G_{5/2} \rightarrow {}^6H_{7/2}$ transition and a severe dependence on the Sm^{3+} concentration was observed in the nanocrystalline material. Decay time measurements of the $^4G_{5/2}$ excited state revealed that the decay time of the 1 mol% $Y_2O_3:Sm^{3+}$ nanocrystals was significantly longer than in the corresponding bulk material. It was determined that the index of refraction of the medium surrounding the nanoparticles has a strong effect on the decay times. We showed via the fit of the experimental decays, obtained by immersing the nanocrystals in different media (air, methanol and carbon disulfide), that the nanocrystals occupied 75% of the sample space.

Dysprosium doped Y_2O_3 nanocrystals showed a visually dominant yellow emission from the $^4F_{9/2} \rightarrow {}^6H_{13/2}$ transition. The decay curves of the $^4F_{9/2}$ excited state were non-exponential and thus the Inokuti-Hirayama model was applied to analysis of the curves. We determined that the interactions between dopant Dy^{3+} ions was dipole-dipole (D-D) in nature and had a D-D coupling parameter of approximately 7×10^{-56} m^6 s^{-1}. Furthermore, a critical $Dy^{3+} - Dy^{3+}$ distance of 6.05 Å was calculated.

CHAPTER 8

8. Future Work

The study of rare earth doped inorganic nanocrystals is relative new, and thus, the results presented in this thesis only begin to scratch the surface of this young and vast field. There are a great many avenues still left to be explored. Below are some suggestions for future studies for the current body of work presented in this thesis as well as the next phase envisaged for upconverting nanoparticles.

8.1. Future Work on the Sesquioxides and Garnet Nanocrystals

No study on inorganic nanocrystals can ever be complete without investigating the effect of particle size. Studies have shown that changing the particle size will have an immense impact on the spectroscopic behavior in rare earth doped nanocrystals. In the sesquioxide and garnet nanocrystals, especially in the sesquioxides, reduction of particle size will result in a larger surface area. Consequently, more CO_3^{2-} and OH^- contaminants will be present on the particle surface.

While the upconversion behavior in the sesquioxide and garnet nanocrystals are well known, a few open questions still remain. It is imperative that we investigate the decay kinetics of these nanocrystals using pulsed laser excitation. The temporal studies will be invaluable to elucidate the behavior and efficiency of the different upconversion mechanisms.

In order to quantify the upconversion process, the determination of the upconversion efficiencies, η, is of the essence. While it is not trivial to do so in powdered materials, a few methods are available. The determination of the upconversion

efficiency will aid in assessing the potential of a certain upconverting nanomaterial for use in a FRET assay.

It has been shown that Y_2O_3 nanocrystals left exposed to the atmosphere suffer aging effects. That is, their luminescence efficiency diminishes due to more adsorbed surface species, which quench the luminescence. If these nanocrystals are to be used in technological applications, it is imperative that we probe deeper and understand the aging process.

Finally, crystal field studies will compliment the spectroscopic results and enable us to gain a better understanding of the crystalline environments surrounding the rare earth ion in both the bulk and nanomaterial.

8.2. Colloidal Nanoparticles

The current crop of upconverting nanomaterials described in this thesis are in the "powdered" state and furthermore, have lower upconversion efficiencies than their micrometer counterparts (bulk). It is of the essence that upconverting nanomaterials of uniform size distribution are developed, which have equal or greater efficiencies compared to the bulk material. Moreover, to utilize the upconverting labels in real bioassays, the nanoparticles would have to be transparently dispersed in solution. Thus, colloidal solutions of efficiently upconverting nanoparticles are needed.

It is of course of great significance to investigate colloidal solutions of nanoparticles with low phonon energies. Promising candidates include fluoride based nanoparticles, namely, $LaF_3:Er^{3+}$, Yb^{3+} and $NaYF_4:Er^{3+}$, Yb^{3+} since their upconversion properties are well known in single crystal and microcrystalline hosts. Their low phonon

energies minimize the rate of multiphonon relaxation in turn leading to much higher upconversion efficiencies compared to the oxides.

8.3. FRET

Once suitable colloidal upconverting nanoparticles have been developed, which meet the requirements for an upconversion FRET assay, it is vital that we simulate in the laboratory the usability, utility and feasibility of the proposed assay. Model assays must be conducted where binding interactions between well-characterized pairs of upconverting nanoparticles and labels are investigated. To accomplish this, a monolayer of a biological macromolecule such as albumin, avidin or an immunoglobulin must be adsorbed onto the particle surface. Many such biological macromolecules will adsorb strongly to surfaces if incubated near their isoelectric point for an extended period of time. If the surface of a nanoparticle has functionality (e.g. carboxylate groups) the physisorbed macromolecule can often be covalently bound either by direct linkage (e.g. using water-soluble carbodiimide) or indirectly using a commercially available bifunctional cross-linking agent. A very convenient molecule from this standpoint is avidin, which binds biotinylated materials very tightly in four distinct sites on its surface. Avidin is widely used as a component of a large number of biological assays and many biotinylated or avidin-labeled reagents are easily available. Nanoparticles will be coated with avidin by physisorption from alkaline solution in the first instance and the extent of binding will be assessed using biotinylated fluorescent labels followed by centrifugation and/or gel filtration to remove unbound labels. Biotinylated fluorescent molecules are commercially available over a very wide range of excitation and emission wavelengths so

that it is easy to select a marker that will be distinctly detectable in the presence of the fluorescent nanoparticle itself. The nanoparticles can then be excited at 980 nm, which gives no detectable emission from conventional labels thus showing the potential of this system.

CHAPTER 9

9. References

1. J. B. Hedrick, *J. Alloy Compd.* **225**, 609-618 (1995).
2. S. D. Barrett, S. S. Dhesi, *The Structure of Rare-Earth Metal Surfaces* (Imperial College Press, London, 2001).
3. D. Lutz, in *The Industrial Physicist.* (1996), vol. 2, pp. 28, 30.
4. C. K. Jørgensen, *Inorg. Chem. Acta* **139**, 1-5 (1987).
5. M. E. Weeks, *J. Chem. Ed.* **9**, 1751-1773 (1932).
6. L. F. Yntema, *J. Am. Chem. Soc.* **46**, 37-39 (1924).
7. J. A. Marinsky, L. E. Glendenin, C. D. Coryell, *J. Am. Chem. Soc.* **69**, 2781-2785 (1947).
8. Los Alamos National Labs-Chemistry Division, *Periodic Table of the Elements*, http://pearl1.lanl.gov/periodic/elements/61.html
9. J. A. Marinsky, L. E. Glendenin, *Chem. Eng. News* **26**, 2346-2348 (1948).
10. F. M. Aller, *Sky Telesc.* **41**, 220-222 (1971).
11. N. Koertge, *Science as Problem-Solving: How Values Affect the Direction of Scientific Research*, http://www.indiana.edu/~koertge/rIPChV.html
12. F. A. Cotton, G. Wilkinson, *Advanced Inorganic Chemistry - 5th Edition* (John Wiley & Sons, New York, 1988).
13. I. Newton, *Opticks or, A Treatise of the Reflections, Refractions, Inflections & Colours of Light: Also Two Treatises of the Species and Magnitude of Curvilinear Figures* (Sam. Smith, and Benj. Walford, London, 1704).
14. J. Keats, *Poems of John Keats*. G. Thorn-Drury, Ed. (Lawrence & Bullen, London, 1896), vol. 2.
15. E. Katz, *Gustav Robert Kirchhoff*, http://chem.ch.huji.ac.il/~eugeniik/history/kirchhoff.htm
16. E. Katz, *Robert Wilhelm Eberhard von Bunsen*, http://chem.ch.huji.ac.il/~eugeniik/history/bunsen.html
17. C. Dickens, *Our Mutual Friend* (Chapman and Hall, London, 1865).
18. J. M. Thomas, *Angew. Chem. Int. Ed.* **41**, 2059-2065 (2002).
19. S. Freed, *Rev. Mod. Phys.* **14**, 105-111 (1942).
20. H. Becquerel, *Ann. Chim. Phys.* **6**, 170 (1888).
21. J. Becquerel, *le Radium* **4**, 328 (1907).
22. J. Becquerel, *Physik. Z.* **9**, 94-100 (1908).
23. J. Becquerel, H. K. Onnes, W. J. de Haas, *Compt. Rend.* **181**, 758-760 (1925).

24. H. K. Onnes, J. Becquerel, W. J. de Haas, *Compt. Rend.* **181**, 838-841 (1925).

25. F. Hund, *Z. Physik* **33**, 855-859 (1925).

26. H. Bethe, *Ann. Physik* **3**, 133-208 (1929).

27. H. Bethe, *Ann. Physik* **60**, 218-233 (1930).

28. H. A. Kramers, *Proc. Acad. Sci. Amsterdam* **33**, 959-972 (1930).

29. N. C. Chang, J. B. Gruber, R. P. Leavitt, C. A. Morrison, *J. Chem. Phys.* **76**, 3877-3889 (1982).

30. J. H. Van Vleck, A. Frank, *Phys. Rev.* **34**, 1494-1496 (1929).

31. J. H. Van Vleck, *The Theory of Electric and Magnetic Susceptibilities* (Oxford University Press, New York, 1932).

32. W. G. Penney, R. Schlapp, *Phys. Rev.* **41**, 194-207 (1932).

33. E. P. Wigner, *Group Theory and its Application to the Quantum Mechanics of Atomic Spectra* (Academic Press, New York, 1959).

34. A. Frank, *Phys. Rev.* **39**, 119-129 (1932).

35. A. Frank, *Phys. Rev.* **48**, 765-771 (1935).

36. B. G. Wybourne, *J. Alloy Compd.* **380**, 96-100 (2004).

37. S. Freed, F. H. Spedding, *Nature* **123**, 525-526 (1929).

38. S. Freed, F. H. Spedding, *Phys. Rev.* **34**, 945-953 (1929).

39. S. Freed, *Phys. Rev.* **38**, 2122-2130 (1931).

40. H. A. Bethe, F. H. Spedding, *Phys. Rev.* **52**, 454-455 (1937).

41. J. H. Van Vleck, *J. Phys. Chem.* **41**, 67-80 (1936).

42. G. Racah, *Phys. Rev.* **76**, 1352-1365 (1949).

43. R. J. Elliott, K. W. H. Stevens, *Proc. Roy. Soc. (London)* **215A**, 437-453 (1952).

44. R. J. Elliott, K. W. H. Stevens, *Proc. Roy. Soc. (London)* **219A**, 387-404 (1953).

45. B. R. Judd, *Mol. Phys.* **2**, 407-414 (1959).

46. J. S. Margolis, *J. Chem. Phys.* **35**, 1367-1373 (1961).

47. J. D. Axe, G. H. Dieke, *J. Chem. Phys.* **37**, 2364-2371 (1962).

48. G. H. Dieke, *Spectra and Energy Levels of Rare Earth Ions in Crystals* (Interscience Publishers, New York, 1968).

49. G. N. Sauvion, P. Ducros, *J. Less-Common Met.* **111**, 23-35 (1985).

50. J. A. Peters, D. J. Raber, *Chem. Eng. News* **81**, 136-137 (2003).

51. B. Locardi, E. Guadagnino, *Mater. Chem. Phys.* **31**, 45-49 (1992).

52. J. A. Peters, J. Huskens, D. J. Raber, *Prog. Nucl. Magn. Reson. Spectrosc.* **28**, 283-350 (1996).

53. F. Suyver, A. Meijerink, *Chemisch2Weekblad* **98**, 12-13 (2002).

54. A. L. Schawlow, C. H. Townes, *Phys. Rev.* **112**, 1940-1949 (1958).

55. A. L. Schawlow, *Rev. Mod. Phys.* **54**, 697-707 (1982).

56. T. H. Maiman, *Brit. Commun. & Electronics* **7**, 674-675 (1960).

57. T. H. Maiman, *Phys. Rev.* **123**, 1145-1150 (1961).

58. M. Zambelli, A. Speghini, G. Ingletto, M. Bettinelli, F. Vetrone, J. C. Boyer, J. A. Capobianco, *Opt. Mater.* **25**, 215-222 (2004).

59. A. J. Kenyon, *Prog. Quant. Electr.* **26**, 225-284 (2002).

60. E. Desurvire, *Phys. Today* **47**, 20-27 (1994).

61. C. R. Ronda, T. Jüstel, H. Nikol, *J. Alloy Compd.* **275-277**, 669-676 (1998).

62. D. J. Lockwood, in *Interface (The Electrochemical Society)*. Summer 2003, pp. 35 & 66-67.

63. E. N. Harvey, *A History of Luminescence from the Earliest Times Until 1900* (American Philosophical Society, Philadelphia, 1957).

64. C. Feldmann, T. Jüstel, C. R. Ronda, P. J. Schmidt, *Adv. Funct. Mater.* **13**, 511-516 (2003).

65. A. K. Levine, F. C. Palilla, *Appl. Phys. Lett.* **5**, 118-120 (1964).

66. B. Moine, G. Bizarri, *Mater. Sci. Eng. B* **105**, 2-7 (2003).

67. R. Chen, D. J. Lockwood, *J. Electrochem. Soc.* **149**, S69-S78 (2002).

68. W. J. van den Hoek, A. G. Jack, G. M. J. F. Luijks, in *Ullmann's Encyclopedia of Industrial Chemistry*. (Weinheim: Wiley-VCH, 1990), vol. A15, pp. 115.

69. A. M. Srivastava, T. J. Sommerer, *Interface (The Electrochemical Society)*. Summer 1998, 28-31.

70. T. Jüstel, H. Nikol, C. Ronda, *Angew. Chem. Int. Ed.* **37**, 3084-3103 (1998).

71. L. Ozawa, M. Itoh, *Chem. Rev.* **103**, 3835-3855 (2003).

72. X. Jing, T. Ireland, C. Gibbons, D. J. Barber, J. Siver, A. Vecht, G. Fern, P. Trowga, D. C. Morton, *J. Electrochem. Soc.* **146**, 4654-4658 (1999).

73. G. Blasse, *J. Alloy Compd.* **225**, 529-533 (1995).

74. C. Fouassier, *Curr. Opin. Solid State Mater. Sci.* **2**, 231-235 (1997).

75. L. E. Shea, J. McKittrick, O. A. Lopez, *J. Am. Ceram. Soc.* **79**, 3257-3265 (1996).

76. M. Leskelä, *J. Alloy Compd.* **275-277**, 702-708 (1998).

77. R. P. Feynman, *Plenty of Room at the Bottom*, http://www.its.caltech.edu/~feynman/plenty.html

78. M. Roukes, in *Scientific American*. (2001), vol. 285, pp. 48-57.

79. A. P. Alivisatos, *Endeavour* **21**, 56-60 (1996).

80. B. M. Tissue, *Chem. Mater.* **10**, 2837-2845 (1998).

81. A. P. Alivisatos, *J. Phys. Chem.* **100**, 13226-13239 (1996).

82. L. Brus, *J. Phys. Chem.* **90**, 2555-2560 (1986).

83. Y. Shen, C. S. Friend, Y. Jiang, D. Jakubczyk, J. Swiatkiewicz, P. N. Prasad, *J. Phys. Chem. B* **104**, 7577-7587 (2000).

84. Y. L. Soo, Z. H. Ming, S. W. Hunag, Y. H. Kao, R. N. Bhargava, D. Gallagher, *Phys. Rev. B* **50**, 7602-7607 (1994).

85. R. N. Bhargava, D. Gallagher, T. Welker, *J. Lumin.* **60-61**, 275-280 (1994).

86. R. N. Bhargava, D. Gallagher, X. Hong, A. Nurmikko, *Phys. Rev. Lett.* **72**, 416-419 (1994).

87. R. N. Bhargava, *J. Lumin.* **72-74**, 46-48 (1997).

88. A. A. Bol, A. Meijerink, *Phys. Rev. B* **58**, R15997-R16000 (1998).

89. A. A. Bol, A. Meijerink, *J. Lumin.* **87-89**, 315-318 (2000).

90. W. Zhang, P. Xie, C. Duan, K. Yan, M. Yin, L. Lou, S. Xia, J.-C. Krupa, *Chem. Phys. Lett.* **292**, 133-136 (1998).

91. K. Riwotzki, M. Hasse, *J. Phys. Chem. B* **102**, 10129-10135 (1998).

92. C. M. Bender, J. M. Burlitch, D. Barber, C. Pollock, *Chem. Mater.* **12**, 1969-1976 (2000).

93. H. X. Zhang, C. H. Kam, Y. Zhou, H. Q. Han, S. Buddhudu, Y. L. Lam, *Opt. Mater.* **15**, 47-50 (2000).

94. X. Yu, P. Xie, Q. Su, *Phys. Chem. Chem. Phys.* **3**, 5266-5269 (2001).

95. G. K. Liu, H. Z. Zhuang, X. Y. Chen, *Nano Lett.* **2**, 535-539 (2002).

96. J. W. Stouwdam, F. C. J. M. van Veggel, *Nano Lett.* **2**, 733-737 (2002).

97. G. Yi, B. Sun, F. Yang, D. Chen, Y. Zhou, J. Cheng, *Chem. Mater.* **14**, 2910-2914 (2002).

98. T. Igarashi, M. Ihara, T. Kusunoki, K. Ohno, *Appl. Phys. Lett.* **76**, 1549-1551 (2000).

99. D. R. Tallant, C. H. Seager, R. L. in *Materials Research Society Spring Meeting*; K. L. Jensen, W. Mackie, D. Temple, J. Itoh, R. Nemanich, T. Trottier, P. Holloway, Eds.; Materials Research Society: San Francisco, CA, 2000; Vol. 621.

100. R. Schmechel, H. Winkler, L. Xaomao, M. Kennedy, M. Kolbe, A. Benker, M. Winterer, R. A. Fischer, H. Hahn, H. von Seggern, *Scripta Mater.* **44**, 1213-1217 (2001).

101. W. M. Yen, *Phys. Status Solidi A* **202**, 177-184 (2005).

102. B. M. Tissue, B. Bihari, *J. Fluoresc.* **8**, 289-294 (1998).

103. C. Xu, B. A. Watkins, R. E. Sievers, X. Jing, P. Trowga, C. S. Gibbons, A. Vecht, *Appl. Phys. Lett.* **71**, 1643-1645 (1997).

104. T. Hase, T. Kano, E. Nakazawa, H. Yamamoto, *Adv. Electron. Electron Phys.* **79**, 271-373 (1990).

105. M. J. Weber, *Phys. Rev.* **171**, 283-291 (1968).

106. L. A. Riseberg, H. W. Moos, *Phys. Rev.* **174**, 429-438 (1968).

107. N. Yamada, S. Shionoya, T. Kushida, *J. Phys. Soc. Japan* **32**, 1577-1586 (1972).

108. E. T. Goldburt, B. Kulkarni, R. N. Bhargava, J. Taylor, M. Libera, *J. Lumin.* **72-74**, 190-192 (1997).

109. D. K. Williams, H. Yuan, B. M. Tissue, *J. Lumin.* **83-84**, 297-300 (1999).

110. L. E. Brus, *J. Chem. Phys.* **80**, 4403-4409 (1984).

111. A. Konrad, U. Herr, R. Tidecks, F. Kummer, K. Samwer, *J. Appl. Phys.* **90**, 3516-3523 (2001).

112. D. K. Williams, B. Bihari, B. M. Tissue, J. M. McHale, *J. Phys. Chem. B* **102**, 916-920 (1998).

113. H.-S. Yang, S. P. Feofilov, D. K. Williams, J. C. Milora, B. M. Tissue, R. S. Meltzer, W. M. Dennis, *Physica B* **263-264**, 476-478 (1999).

114. R. S. Meltzer, S. P. Feofilov, B. M. Tissue, H. B. Yuan, *Phys. Rev. B* **60**, R14012-R14015 (1999).

115. R. S. Meltzer, W. M. Yen, H. Zheng, S. P. Feofilov, M. J. Dejneka, B. M. Tissue, H. B. Yuan, *J. Lumin.* **94&95**, 217-220 (2001).

116. F. Vetrone, J. C. Boyer, J. A. Capobianco, in *The Handbook of Luminescence, Display Materials and Devices* H. S. Nalwa, L. S. Rohwer, Eds. (American Scientific Publishers, Los Angeles, CA, 2003), vol. 2, pp. 141-186.

117. F. Vetrone, J. C. Boyer, J. A. Capobianco, in *The Encyclopedia of Nanoscience and Nanotechnology* H. S. Nalwa, Ed. (American Scientific Publishers, Stevenson Ranch, CA, 2004), vol. 10, pp. 725-765.

118. D. Matsuura, *Appl. Phys. Lett.* **81**, 4526-4528 (2002).

119. A. Patra, C. S. Friend, R. Kapoor, P. N. Prasad, *J. Phys. Chem. B* **106**, 1909-1912 (2002).

120. S. Heer, O. Lehmann, M. Haase, H.-U. Guedel, *Angew. Chem. Int. Ed.* **42**, 3179-3182 (2003).

121. E. De la Rosa-Cruz, L. A. Diaz-Torres, R. A. Rodriguez-Rojas, M. A. Meneses-Nava, O. Barbosa-Garcia, P. Salas, *Appl. Phys. Lett.* **83**, 4903-4905 (2003).

122. R. Francini, S. Pietrantoni, M. Zambelli, A. Speghini, M. Bettinelli, *J. Alloy Compd.* **380**, 34-38 (2004).

123. H. Guo, N. Dong, M. Yin, W. Zhang, L. Lou, S. Xia, *J. Phys. Chem. B* **108**, 19205-19209 (2004).

124. S. Heer, K. Koempe, H.-U. Guedel, M. Haase, *Adv. Mater.* **16**, 2102-2105 (2004).

125. T. Hirai, T. Orikoshi, *J. Colloid Interface Sci.* **273**, 470-477 (2004).

126. R. Naccache, F. Vetrone, J. C. Boyer, J. A. Capobianco, A. Speghini, M. Bettinelli, *J. Nanosci. Nanotechno.* **4**, 1025-1031 (2004).

127. H. Song, B. Sun, T. Wang, S. Lu, L. Yang, B. Chen, X. Wang, X. Kong, *Solid State Commun.* **132**, 409-413 (2004).

128. G. Yi, H. Lu, S. Zhao, Y. Ge, W. Yang, D. Chen, L. -H. Guo, *Nano Lett.* **4**, 2191-2196 (2004).

129. J. Zhang, S. Wang, T. Rong, L. Chen, *J. Am. Ceram. Soc.* **87**, 1072-1075 (2004).

130. J. C. Boyer, F. Vetrone, J. A. Capobianco, A. Speghini, M. Zambelli, M. Bettinelli, *J. Lumin.* **106**, 263-268 (2004).

131. J. C. Boyer, F. Vetrone, J. A. Capobianco, A. Speghini, M. Bettinelli, *Chem. Phys. Lett.* **390**, 403-407 (2004).

132. F. Vetrone, J. C. Boyer, J. A. Capobianco, A. Speghini, M. Bettinelli, *Appl. Phys. Lett.* **80**, 1752-1754 (2002).

133. J. C. Boyer, F. Vetrone, J. A. Capobianco, A. Speghini, M. Bettinelli, *J. Appl. Phys.* **93**, 9460-9465 (2003).

134. R. Naccache, F. Vetrone, J. C. Boyer, J. A. Capobianco, A. Speghini, M. Bettinelli, G. C. Righini, *Mater. Lett.* **58**, 2207-2212 (2004).

135. F. Auzel, *J. Lumin.* **45**, 341-345 (1990).

136. W. Lenth, R. M. Macfarlane, in *Optics and Photonics News*. (1992), vol. 3, pp. 8-15.

137. R. Scheps, *Prog. Quant. Electr.* **20**, 271-358 (1996).

138. X. Chen, in *Advances in Energy Transfer Processes, Proceedings of the 16th Course of the International School of Atomic and Molecular Spectroscopy* X. Chen, B. Di Bartolo, Eds. (World Scientific Publishing, River Edge, NJ, 2001) pp. 261-272.

139. S. G. Mackay, O. S. Wenger, K. W. Kramer, H. U. Güdel, *Curr. Opin. Solid State Mater. Sci.* **6**, 487-493 (2003).

140. F. Auzel, *Chem. Rev.* **104**, 139-173 (2004).

141. J. A. Capobianco, G. Prevost, P. P. Proulx, P. Kabro, M. Bettinelli, *Opt. Mater.* **6**, 175-184 (1996).

142. S. Taccheo, P. Laporta, S. Longhi, O. Svelto, C. Svelto, *Appl. Phys. B* **63**, 425-436 (1996).

143. G. M. Salley, R. Valiente, H. U. Güdel, *Phys. Rev. B* **67**, 134111/1-134111/9 (2003).

144. N. Bloembergen, *Phys. Rev. Lett.* **2**, 84-85 (1959).

145. F. Auzel, *C. R. Acad. Sci. (Paris)* **262**, 1016-1019 (1966).

146. J. S. Chivian, W. E. Case, D. D. Eden, *Appl. Phys. Lett.* **35**, 124-125 (1979).

147. J. Wright, in *Radiationless Processes in Molecules and Condensed Phases* F. K. Fong, Ed. (Springer, New York, 1976), vol. 15, pp. 239.

148. M. F. Joubert, *Opt. Mater.* **11**, 181-203 (1999).

149. F. E. Auzel, *Proc. IEEE* **61**, 758-786 (1973).

150. A. J. Silversmith, W. Lenth, R. M. Macfarlane, *Appl. Phys. Lett.* **51**, 1977-1979 (1987).

151. B. M. Antipenko, S. P. Voronin, T. A. Privalova, *Sov. Phys.-Tech. Phys.* **32**, 208-209 (1987).

152. R. M. Macfarlane, F. Tong, A. J. Silversmith, W. Lenth, *Appl. Phys. Lett.* **52**, 1300-1302 (1988).

153. S. A. Pollack, D. B. Chang, I. F. Shih, R. Tzeng, *Appl. Opt.* **26**, 4400-4406 (1987).

154. Q.-H. Wang, M. Bass, *Electron. Lett.* **40**, 987- 988 (2004).

155. A. Shalav, B. S. Richards, T. Trupke, K. W. Kramer, H. U. Güdel, *Appl. Phys. Lett.* **86**, 013505/013501-013505/013503 (2005).

156. E. Downing, L. Hesselink, J. Ralston, R. Macfarlane, *Science* **273**, 1185-1189 (1996).

157. F. van de Rijke, H. Zijlmans, S. Li, T. Vail, A. K. Raap, R. S. Niedbala, H. J. Tanke, *Nat. Biotechnol.* **19**, 273-276 (2001).

158. S. Y. Tetin, S. D. Stroupe, *Curr. Pharma. Biotech.* **5**, 9-16 (2004).

159. A. R. Clapp, I. L. Medintz, J. M. Mauro, B. R. Fisher, M. G. Bawendi, H. Mattoussi, *J. Am. Chem. Soc.* **126**, 301-310 (2003).

160. N. J. Turro, *Modern Molecular Photochemistry* (University Science Books, Mill Valley, CA, 1991).

161. J. R. Lakowicz, *Principles of Fluorescence Spectroscopy 2nd Ed.* (Kluwer Academic, New York, NY, 1999).

162. X. Michalet, F. Pinaud, T. D. Lacoste, M. Dahan, M. P. Bruchez, A. P. Alivisatos, S. Weiss, *Single Mol.* **2**, 261-276 (2001).

163. B. G. Wybourne, *Spectroscopic Properties of Rare Earths* (John Wiley & Sons, New York, 1965).

164. S. Hüfner, *Optical Spectra of Transparent Rare Earth Compounds* (Academic Press, New York, 1978).

165. B. Di Bartolo, *Optical Interactions in Solids* (John Wiley & Sons, New York, 1968).

166. C. W. Nielson, G. F. Koster, *Spectroscopic Coefficients for the p^n, d^n, and f^n Configurations* (M. I. T. Press, Cambridge, MA, 1963).

167. B. R. Judd, *Operator Techniques in Atomic Spectroscopy* (McGraw-Hill, New York, 1963).

168. L. J. F. Broer, C. J. Gorter, J. Hoogschagen, *Physica* **11**, 231-250 (1945).

169. B. R. Judd, *Phys. Rev.* **127**, 750-761 (1962).

170. G. S. Ofelt, *J. Chem. Phys.* **37**, 511-520 (1962).

171. G. Racah, *Phys. Rev.* **61**, 186-197 (1942).

172. G. Racah, *Phys. Rev.* **62**, 438-462 (1942).

173. G. Racah, *Phys. Rev.* **63**, 367-382 (1943).

174. A. R. Edmonds, *Angular Momentum in Quantum Mechanics* (Princeton University Press, Princeton, NJ, 1960).

175. W. T. Carnall, P. R. Fields, K. Rajnak, *J. Chem. Phys.* **49**, 4424-4442 (1968).

176. W. T. Carnall, P. R. Fields, K. Rajnak, *J. Chem. Phys.* **49**, 4443-4446 (1968).

177. W. T. Carnall, P. R. Fields, K. Rajnak, *J. Chem. Phys.* **49**, 4447-4449 (1968).

178. W. T. Carnall, P. R. Fields, K. Rajnak, *J. Chem. Phys.* **49**, 4450-4455 (1968).

179. C. Görller-Walrand, K. Binnemans, in *Handbook on the Physics and Chemistry of Rare Earths* K. A. Gschneidner, L. Eyring, Eds. (Elsevier, Amsterdam, 1998), vol. 25.

180. B. Di Bartolo, in *NATO Advanced Study Institute on Energy Transfer Processes in Condensed Matter* B. Di Bartolo, A. Karipidou, Eds. (Plenum Press, New York, 1984) pp. 1-71.

181. B. Di Bartolo, in *Advances in Energy Transfer Processes, Proceedings of the 16th Course of the International School of Atomic and Molecular Spectroscopy* X. Chen, B. Di Bartolo, Eds. (World Scientific Publishing, River Edge, NJ, 2001) pp. 1-71.

182. D. L. Dexter, *J. Chem. Phys.* **21**, 836-850 (1953).

183. A. J. Freeman, R. E. Watson, *Phys. Rev.* **127**, 2058-2075 (1962).

184. M. Stavola, D. L. Dexter, *Phys. Rev. B* **20**, 1867-1885 (1979).

185. E. Zych, *Opt. Mater.* **16**, 445-452 (2001).

186. K. C. Patil, S. T. Aruna, T. Mimani, *Curr. Opin. Solid State Mater. Sci.* **6**, 507-512 (2002).

187. G. A. Hirata, F. Ramos, R. Garcia, E. J. Bosze, J. McKittrick, O. Contreras, F. A. Ponce, *Phys. Status Solidi A* **188**, 179-182 (2001).

188. Y. Tao, G. Zhao, W. Zhang, S. Xia, *Mater. Res. Bull.* **32**, 501-506 (1997).

189. G. Tessari, M. Bettinelli, A. Speghini, D. Ajò, G. Pozza, L. E. Depero, B. Allieri, L. Sangaletti, *Appl. Surf. Sci.* **144-145**, 686-689 (1999).

190. G. Fagherazzi, S. Polizzi, M. Bettinelli, A. Speghini, *J. Mater. Res.* **15**, 586-589 (2000).

191. S. Polizzi, G. Fagherazzi, M. Battagliarin, M. Bettinelli, A. Speghini, *J. Mater. Res.* **16**, 146-154 (2001).

192. J. Poth, R. Haberkorn, H. P. Beck, *J. Eur. Ceram. Soc.* **20**, 715-723 (2000).

193. T. V. Anuradha, S. Ranganathan, T. Mimani, K. C. Patil, *Scripta Mater.* **44**, 2237-2241 (2001).

194. S. Shi, J. Wang, *J. Alloy Compd.* **327**, 82-86 (2001).

195. T. K. Anh, L. Q. Minh, N. Vu, T. T. Huong, N. T. Huong, C. Barthou, W. Strek, *J. Lumin.* **102-103**, 391-394 (2003).

196. L. Malavasi, M. C. Mozzati, S. Polizzi, C. B. Azzoni, G. Flor, *Chem. Mater.* **15**, 5036-5043 (2003).

197. T. Peng, H. Yang, X. Pu, B. Hu, Z. Jiang, C. Yan, *Mater. Lett.* **58**, 352-356 (2003).

198. Z. Fu, Z. Shihong, Y. Yu, S. Zhang, *Chem. Phys. Lett.* **395**, 285-289 (2004).

199. S. K. Ghosh, S. Datta, S. K. Roy, *Trans. Ind. Ceram. Soc.* **63**, 27-32 (2004).

200. F. Gu, S. F. Wang, M. K. Lu, W. G. Zou, G. J. Zhou, D. Xu, D. R. Yuan, *J. Cryst. Growth* **260**, 507-510 (2004).

201. K. Nagaveni, M. S. Hegde, N. Ravishankar, G. N. Subbanna, M. Giridhar, *Langmuir* **20**, 2900-2907 (2004).

202. F. S. Wuister, C. de Mello Donega, A. Meijerink, *Physical Chemistry Chemical Physics* **6**, 1633-1636 (2004).

203. S. R. Jain, K. C. Adiga, V. R. Pai Verneker, *Combust. Flame* **40**, 71-79 (1981).

204. L. Sun, J. Yao, C. Liu, C. Liao, C. Yan, *J. Lumin.* **87-89**, 447-450 (2000).

205. S. Ekambaram, K. C. Patil, *J. Mater. Chem.* **5**, 905-908 (1995).

206. J. McKittrick, L. E. Shea, C. F. Bacalski, E. J. Bosze, *Displays* **19**, 169-172 (1999).

207. P. K. Sharma, M. H. Jilavi, R. Nab, H. Schmidt, *J. Mater. Sci. Lett.* **17**, 823-825 (1998).

208. P. K. Sharma, M. H. Jilavi, R. Nass, H. Schmidt, *J. Lumin.* **82**, 187-193 (1999).

209. B. Allieri, L. E. Depero, A. Marino, L. Sangaletti, L. Caporaso, A. Speghini, M. Bettinelli, *Mater. Chem. Phys.* **66**, 164-171 (2000).

210. S. Polizzi, M. Battagliarin, M. Bettinelli, A. Speghini, G. Fagherazzi, *J. Mater. Chem.* **12**, 742-747 (2002).

211. R. P. I. Adler, C. N. J. Wagner, *J. Appl. Phys.* **33**, 3451-3458 (1962).

212. C. N. J. Wagner, in *Local Atomic Arrangements Studied by X-Ray Diffraction*, J. B. Cohen, J. E. Hilliard, Eds.; Metallurgical Society Conferences, Gordon & Breach, New York (1966).

213. S. Enzo, S. Polizzi, A. Benedetti, *Z. Kristallogr.* **170**, 275-287 (1985).

214. A. Benedetti, G. Fagherazzi, S. Enzo, M. Battagliarin, *J. Appl. Cryst.* **21**, 543-549 (1988).

215. B. E. Warren, B. L. Averbach, *J. Appl. Phys.* **21**, 595-598 (1950).

216. B. E. Warren, B. L. Averbach, *J. Appl. Phys.* **23**, 497 (1952).

217. D. Shindo, Y. Murakami, in *Morphology Control of Materials and Nanoparticles* Y. Waseda, A. Muramatsu, Eds. (Springer, 2004), vol. 64, pp. 153-181.

218. Z. L. Wang, *Adv. Mater.* **15**, 1497-1514 (2003).

219. R. Krsmanovic, P. Canton, A. Speghini, M. Bettinelli, S. Polizzi, *Mater. Sci. Forum* **453-454**, 251-256 (2004).

220. S. Polizzi, S. Bucella, A. Speghini, F. Vetrone, R. Naccache, J. C. Boyer, J. A. Capobianco, *Chem. Mater.* **16**, 1330-1335 (2004).

221. F. Vetrone, J. C. Boyer, J. A. Capobianco, A. Speghini, M. Bettinelli, R. Krsmanovic, S. Polizzi, *J. Electrochem. Soc.* **152**, H19-H24 (2005).

222. Y.-N. Xu, Z.-q. Gu, W. Y. Ching, *Phys. Rev. B* **56**, 14993-15000 (1997).

223. G. Concas, G. Spano, M. Bettinelli, A. Speghini, *Z. Naturforsch., A: Phys. Sci.* **58**, 551-557 (2003).

224. Powder Diffraction File, JCPDS International Centre for Diffraction Data, Swarthmore, PA, PDF n.42-1463.

225. *Handbook of Physics and Chemistry - 78th Edition*, D. R. Lide, Ed. (CRC Press, Boca Raton, FL, 1998) pp. 4-121.

226. Powder Diffraction File, JCPDS International Centre for Diffraction Data, Swarthmore, PA, PDF n.43-1036.

227. J. Dong, K. Lu, *Phys. Rev. B* **43**, 8808-8821 (1991).

228. Y.-N. Xu, W. Y. Ching, B. K. Brickeen, *Phys. Rev. B* **61**, 1817-1824 (2000).

229. V. Lupei, *Opt. Mater.* **19**, 95-107 (2002).

230. G. Blasse, L. H. Brixner, *Eur. Solid State Inorg. Chem.* **28**, 767-771 (1991).

231. L. E. Brus, *J. Chem. Phys.* **79**, 5566-5571 (1983).

232. Y. Kayanuma, *Phys. Rev. B* **38**, 9797-9805 (1988).

233. J. A. Capobianco, F. Vetrone, T. D'Alesio, G. Tessari, A. Speghini, M. Bettinelli, *Phys. Chem. Chem. Phys.* **2**, 3203-3207 (2000).

234. C. A. Morrison, R. P. Leavitt, J. B. Gruber, N. C. Chang, *J. Chem. Phys.* **79**, 4758-4763 (1983).

235. G. A. Slack, S. L. Dole, V. Tsoukala, G. S. Nolas, *J. Opt. Soc. Am. B* **11**, 961-974 (1994).

236. S. Roy, W. Sigmund, F. Aldinger, *J. Mater. Res.* **14**, 1524-1531 (1999).

237. G. Schaack, J. A. Koningstein, *J. Opt. Soc. Am.* **60**, 1110-1115 (1970).

238. J. A. Capobianco, F. Vetrone, J. C. Boyer, A. Speghini, M. Bettinelli, *J. Phys. Chem. B* **106**, 1181-1187 (2002).

239. F. Vetrone, J. C. Boyer, J. A. Capobianco, A. Speghini, M. Bettinelli, *Chem. Mater.* **15**, 2737-2743 (2003).

240. P. Kisliuk, W. F. Krupke, J. B. Gruber, *J. Chem. Phys.* **40**, 3606-3610 (1964).

241. C. B. Layne, W. H. Lowdermilk, M. J. Weber, *Phys. Rev. B* **16**, 10-20 (1977).

242. M. A. Chamarro, R. Cases, *J. Lumin.* **46**, 59-65 (1990).

243. M. Pollnau, D. R. Gamelin, S. R. Lüthi, H. U. Güdel, M. P. Hehlen, *Phys. Rev. B* **61**, 3337-3346 (2000).

244. X. Chen, T. Nguyen, Q. Luu, B. Di Bartolo, *J. Lumin.* **85**, 295-299 (2000).

245. J. A. Capobianco, J. C. Boyer, F. Vetrone, A. Speghini, M. Bettinelli, *Chem. Mater.* **14**, 2915-2921 (2002).

246. E. Nakazawa, in *Phosphor Handbook* S. Shionoya, W. M. Yen, Eds. (CRC Press, Boca Raton, FL, 1999).

247. M. F. Joubert, S. Guy, B. Jacquier, *Phys. Rev. B* **48**, 10031-10037 (1993).

248. J. P. Wittke, I. Ladany, P. N. Yocom, *J. Appl. Phys.* **43**, 595-600 (1972).

249. F. Vetrone, J. C. Boyer, J. A. Capobianco, A. Speghini, M. Bettinelli, *J. Phys. Chem. B* **107**, 1107-1112 (2003).

250. D. F. de Sousa, L. F. C. Zonetti, M. J. V. Bell, R. Lebullenger, A. C. Hernandes, L. A. O. Nunes, *J. Appl. Phys.* **85**, 2502-2507 (1999).

251. L. F. Johnson, H. G. Guggenheim, T. C. Rich, F. W. Ostermayer, *J. Appl. Phys.* **43**, 1125-1137 (1972).

252. H. Kuroda, S. Shionoya, T. Kushida, *J. Phys. Soc. Japan* **33**, 125-141 (1972).

253. R. H. Page, K. I. Schaffers, P. A. Waide, J. B. Tassano, S. A. Payne, W. F. Krupke, *J. Opt. Soc. Am. B* **15**, 996-1008 (1998).

254. F. Vetrone, J. C. Boyer, J. A. Capobianco, A. Speghini, M. Bettinelli, *J. Appl. Phys.* **96**, 661-667 (2004).

255. G. Boulon, L. Laversenne, C. Goutaudier, Y.Guyot, M. T. Cohen-Adad, *J. Lumin.* **102-103**, 417-425 (2003).

256. F. Auzel, G. Baldacchini, L. Laversenne, G. Boulon, *J. Lumin.* **24**, 103-109 (2003).

257. T. Danger, J. Koetke, R. Brede, E. Heumann, G. Huber, B. H. T. Chai, *J. Appl. Phys.* **76**, 1413-1422 (1994).

258. A. Konrad, T. Fries, A. Gahn, F. Kummer, U. Herr, R. Tidecks, K. Samwer, *Mater. Sci. Forum* **343-346**, 494-499 (2000).

259. F. Vetrone, J. C. Boyer, J. A. Capobianco, A. Speghini, M. Bettinelli, *J. Mater. Res.* **19**, 3398-3407 (2004).

260. M. J. Weber, *Phys. Rev.* **157**, 262-272 (1967).

261. J. A. Capobianco, N. Raspa, A. Monteil, M. Malinowski, *J. Phys.: Condens. Matter* **5**, 6083-6090 (1993).

262. C. Maunier, J. L. Doualan, R. Moncorgé, A. Speghini, M. Bettinelli, E. Cavalli, in *Trends in Optics and Photonics*, Proceedings of Advanced Solid-State Lasers, Vol. 50 C. Marshall, Ed. (Optical Society of America, Seattle, WA, 2001).

263. P. Rambaldi, R. Moncorgé, J. P. Wolf, C. Pédrini, J. Y. Gesland, *Optics Commun.* **146**, 163-166 (1998).

264. F. Vetrone, J. A. Capobianco, J. C. Boyer, A. Speghini, M. Bettinelli, *J. Phys. Chem. B* **106**, 5622-5628 (2002).

265. J. A. Capobianco, F. Vetrone, J. C. Boyer, A. Speghini, M. Bettinelli, *Opt. Mater.* **19**, 259-268 (2002).

266. O. Guillot-Noël, B. Bellamy, B. Viana, D. Vivien, *Phys. Rev. B* **60**, 1668-1677 (1999).

267. B. Moine, C. Dujardin, H. Lautesse, C. Pedrini, C. M. Combes, A. Belski, P. Martin, J. Y. Gesland, *Mat. Sci. Forum* **239-241**, 245-248 (1997).

268. J. C. Boyer, F. Vetrone, J. A. Capobianco, A. Speghini, M. Bettinelli, *J. Phys. Chem. B* **108**, 20137-20143 (2004).

269. E. Cavalli, E. Zannoni, M. Bettinelli, A. Speghini, M. Tonelli, A. Toncelli, *J. Phys.: Condens. Matter* **12**, 4665-4674 (2000).

270. I. R. Martín, P. Vélez, V. D. Rodríguez, U. R. Rodríguez-Mendoza, V. Lavín, *Spectrochim. Acta Part A* **55**, 935-940 (1999).

271. J. P. van der Ziel, F. W. Ostermayer, L. G. Van Uitert, *Phys. Rev. B* **2**, 4432-4441 (1970).

272. M. D. Shinn, W. A. Sibley, M. G. Drexhage, R. N. Brown, *Phys. Rev. B* **27**, 6635-6648 (1983).

273. J. Wang, D. J. Simkin, *Phys. Rev. B* **52**, 3309-3314 (1995).

274. S. V. Sergeyev, B. Jaskorzynska, *Phys. Rev. B.* **62**, 15628-15633 (2000).

275. D. F. de Sousa, F. Batalioto, M. J. V. Bell, S. L. Oliveira, L. A. O. Nunes, *J. Appl. Phys.* **90**, 3308-3313 (2001).

276. D. Hreniak, W. Strek, *J. Alloy Compd.* **341**, 183-186 (2002).

277. C.-H. Lu, H.-C. Hong, R. Jagannathan, *J. Mater. Sci. Lett.* **21**, 1489-1492 (2002).

278. D. S. Gill, A. A. Anderson, R. W. Eason, T. J. Warburton, D. P. Shepherd, *Appl. Phys. Lett.* **69**, 10-12 (1996).

279. D. Sugak, A. Matkovskii, A. Durygin, A. Suchocki, I. Solskii, S. Ubizskii, K. Kopczynski, Z. Mierczyk, P. Potera, *J. Lumin.* **82**, 9-15 (1999).

280. J. A. Capobianco, P. Kabro, F. S. Ermeneux, R. Moncorgé, M. Bettinelli, E. Cavalli, *J. Appl. Phys.* **82**, 3983-3986 (1997).

281. T. Weber, W. Lüthy, H. P. Weber, *Appl. Phys. B* **B55**, 144-148 (1992).

282. S. R. Lüthi, M. Pollnau, H. U. Güdel, *Phys. Rev. B* **60**, 162-178 (1999).

283. R. D. Peacock, in *Structure and Bonding* J. D. Dunitz, P. Hemmerich, R. H. Holm, J. A. Ibers, C. K. Jørgensen, J. B. Neilands, D. Reinen, R. J. P. Williams, Eds. (Springer-Verlag, New York, 1975), vol. 22, pp. 83-122.

284. A. A. Kaminskii, *Laser Crystals: Their Physics and Properties* (Springer-Verlag, New York, 1990).

285. C. K. Jørgensen, R. Reisfeld, *J. Less-Common Met.* **93**, 107-112 (1983).

286. A. R. Devi, C. K. Jayasankar, *J. Non-Cryst. Solids* **197**, 111-128 (1996).

287. F. Vetrone, J. C. Boyer, J. A. Capobianco, A. Speghini, M. Bettinelli, *Nanotechnology* **15**, 75-81 (2004).

288. T. Luxbacher, H. P. Fritzer, R. Sabry-Grant, C. D. Flint, *Chem. Phys. Lett.* **241**, 103-108 (1995).

289. E. Cavalli, E. Bovero, A. Belletti, *J. Phys.: Condens. Matter* **14**, 5221-5228 (2002).

290. M. Inokuti, F. Hirayama, *J. Chem. Phys.* **43**, 1978-1989 (1965).

291. M. Bettinelli, G. Ingletto, *J. Lumin.* **43**, 115-119 (1989).

292. R. K. Watts, H. J. Richter, *Phys. Rev. B* **6**, 1584-1589 (1972).